POLITECNICO DI MILANO

Faculty of Industrial Engineering

Master of Science in Mechanical Engineering

Characterization of damage in Dry Automated Fiber Placement (DAFP) carbon/epoxy composites under tensile loading

Supervisor: Prof. Valter Carvelli

Co-supervisor: Prof. Stepan Lomov

M.Sc. thesis of:

Hossein Rastegarian Jahromi
Matr. 787435

Academic Year 2014 -2015

Acknowledgment

First and foremost, I would like to express the deepest gratitude to my supervisor, Prof. Valter Carvelli, for his excellent guidance, for providing me with an exceptional atmosphere for doing my research, and for helping me to carry out my research in the best possible way.

Furthermore, I would like to appreciate Prof. Stepan Lomov for guiding my research during the past year, providing me the opportunity to gain lots of academic experiences and to develop my knowledge especially during the first three months which I have been working on my thesis at Katholieke Universiteit Leuven, Belgium (Department of Material Engineering) as a visiting scholar.

Moreover, I would like to thank Dr. Li Li and Eng. Nghi Quoc Nguyen at the Department of Material Engineering, KU Leuven for their help in the past year.

Notably, I offer my sincerest appreciation to my parents and my brother for their unconditional love and support, both financially and emotionally throughout my M.Sc. studies.

Table of Contents

List of Figures

List of Tables

Abstract

The Dry Automated Fiber Placement (DAFP) process has good potential for manufacturing large composite structures and is used for large scale production. However, the DAFP process reveals uncertainties associated with the induced defects; e.g. gaps and overlaps. This study investigates the damage development in DAFP carbon/epoxy composites under tensile loading in two laminates (named CANAL QI and AP-PLY) with different layups, in different directions (0^0 and 90^0), and with or without intentional process induced defects. Therefore, laminates were cut into specimens, loaded in tension till different stages of loading so as to make possible studying the propagation of the damage utilizing two in-situ experimental techniques; Acoustic Emission (AE) and Digital Image Correlation (DIC). Consequently, the tensile mechanical properties as well as the full-field strain maps of the different tested specimens were achieved by DIC registration using Vic2D software. Moreover, the time and frequency domain features of the AE events were recorded beside the load data input from the tensile testing machine and then the AE energy and cumulative energy were plotted as a function of strain or stress. As a result, different strain thresholds, which are the points were there would be a change in the damage mechanisms, were determined for all the tested specimens. Furthermore, in order to have an idea about the compressive mechanical properties of the laminates some compression samples of each of the laminates were tested till fracture and compressive mechanical properties were obtained using DIC registration. Finally, the clustering analysis was performed on the AE features of the tested specimens and three general clusters were distinguished which can be correlated to different damage mechanisms. In order to verify the strain thresholds obtained from the AE graphs and the hypothesized damage mechanisms related to different AE clusters, future works should be concentrated on verification of the results achieved by AE registration by studying microstructural features of the internal structure using techniques such as Micro-Computed Tomography (μCT).

Keywords: Damage characterization; Dry Automated Fiber Placement (DAFP); carbon/epoxy composites; tensile loading; process-induced defects; Acoustic Emission (AE); Digital Image Correlation (DIC); clustering analysis.

1

Introduction

During the last 50 years, a number of industries such as the aerospace, automotive, renewable energy, sporting goods and military have worked hard to improve the quality of their products and processes in order to make them more reliable and to obtain advantages over competitors. To do so, companies have often chosen to use advanced composite materials rather than traditional materials because of their high strength/weight ratio, good fatigue life, and good impact resistance. For instance, future aircraft programs, such as the Boeing 787 and Airbus A350XWB (Figure 1-1), contain more than 50% by weight of advanced composite components. The major disadvantage of composite materials is the difficulties they present in the manufacturing process.

Figure 1-1: *Airbus A350XWB airframe. (Source: aerospace.honeywell.com)*

Highly consistent quality and cost-effective manufacture of advanced composites can be achieved through automation. It may therefore open up new markets and applications for composite products. The specific elements that combine to make up the overall cost reduction provided by composites automation are:

- *Reduction in labor hours per component.* Automation will provide a significant reduction in the labor hour content required to fabricate composite parts.
- *Reduction in material scrap rates.* Automated processes typically have a material scrap rate in the 3-10 percent range. This is compared to manual processes with scrap factors in a range of 20-40 percent. The reduced material scrap rate is a major contributor to the overall cost reduction provided by automation.
- *Reduction need for in-process inspection.* With a computer controlled machine laying up the prepreg materials, it is not necessary to have a quality assurance technician verify that each ply has been completed and the plies are the specified orientations.
- *Higher quality, repeatable quality parts.* Implementation of automation normally provides some improvement in quality and better process repeatability. This can contribute to the overall cost reduction provided by automation.

Automated **T**ape **L**aying **(ATL)** and **A**utomated **F**iber **P**lacement **(AFP)** are the two main technologies that are employed today to manufacture advanced composite laminates from unidirectional prepregs. ATL is employed to deliver wide prepreg tape onto a surface while automatically removing the ply backing. Layup speed, tape temperature, speed, and tape tension can be controlled during layup. AFP is similar to ATL but utilizes a band of narrow prepreg slices, which are collimated on the head and then delivered together.

The prepreg materials (carbon fiber materials preimpregnated with resins) have “tack” and the machines lay the materials onto a tool surface with compaction pressure. Each new ply “tacks” to the previous ply.

ATL and AFP systems are **C**omputer **N**umeric **C**ontrol **(CNC)** machine tools with programmable axis movements, rack and pinion and/or linear motor axis drives, and “delivery heads” to dispense the prepreg composite materials. The machines are programmed to follow the exact contour of the part tool and lay the prepreg materials onto the tool surface. Composites automation is primarily the “material delivery head” technology as there is nothing magic about machine tools. CNC machine tool technology has been used for many years.

ATL and AFP systems are normally used to fabricate aircraft structures such as:

1. Control surfaces (Flaps, ailerons and spoilers);
2. Nacelle structure (Fan cowl doors, thrust reversers and intake cowls);
3. Main wing structure (Spars, skins, ribs, stringers and fixed trailing edge);
4. Vertical/horizontal stabilizers (Skins, spars, ribs and stringers);
5. Fuselage structure (Skins and stringers); and
6. Aircraft tail cones. (Figure 1-2) [1]

Both ATL and AFP manufacturing processes will be described in detail later in this chapter.

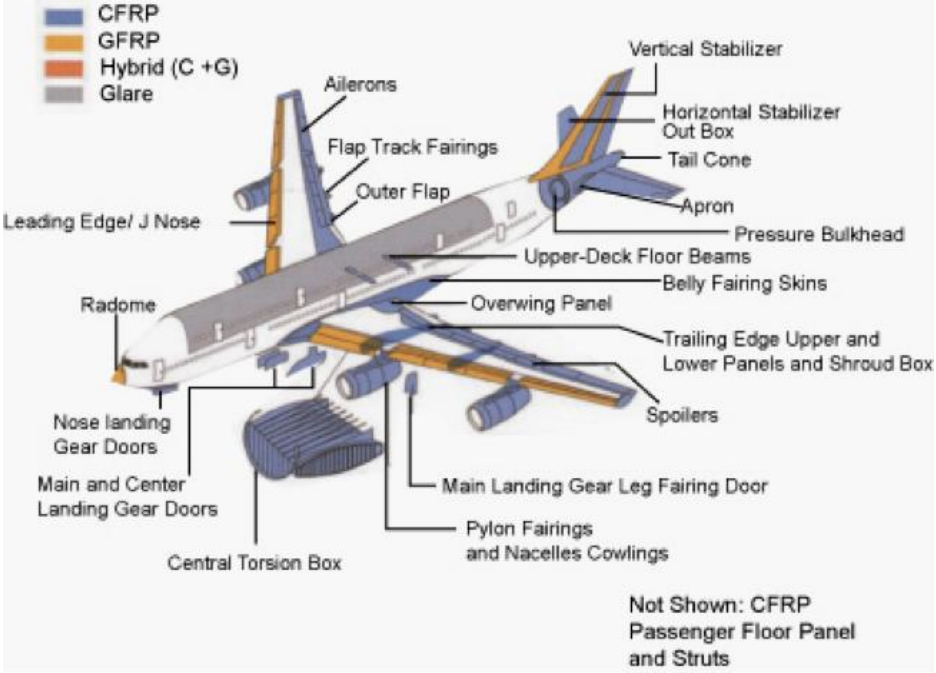

Figure 1-2: *Detailed aircraft structures. (Source: www.airliners.net)*

In the following sections the historical development and past research of both technologies are reviewed; with an emphasis on past issues in application and capability as well as their solution, including both thermoset and thermoplastic material layup. It is shown that past developments have moved away from simply emulating manual layup into the now unique layup procedures for ATL, and into the current AFP technology base. The state of the art for both technologies is discussed and current gaps in the understanding of both processes are highlighted. [2]

1.1. Automated Tape Laying (ATL)

1.1.1. Historical developments of ATL

1971	The earliest known reference to an ATL is a patent assigned to **Chitwood** and **Howeth**, describing a method of laminating composite tape onto a rotatable base-plate using CNC. [3]
1974	**Goldsworthy** described an automated system (Figure 1-3) delivering 76 *mm* wide tape over a curved surface where the head was able to rotate and withhold material to improve the part complexity that could be manufactured using ATL layup. [4]
1981	**Huber** noted that aerospace manufacturers and research institutions built most ATL systems as early as 1975 in-house, and as a result they were normally part of a component centered production system for a given aircraft program (Figure 1-4). [5]
1984	To address the issue of higher layup speeds, **Eaton** [6] and **Saveriano** [7] introduced a layup system with a lightweight head that dispensed tape over a rotatable surface, similar to the first patent of **Chitwood** and **Howeth** [3], at up to 60 *m/min*. At that time most ATL systems were **F**lat **T**ape **L**aminating **M**achines **(FTLM)**, which could only deliver tape onto a flat tool.
1984	**Coad et al.** [8] discussed a robotic pick-and-place system to overcome ATL's limitations regarding geometric complexity.
1984	**Stone** [9] introduced a commercial ATL system from Cincinnati Milacron (now Mag-Cincinnati). The system was capable of delivering tape over geometries with curvature up to 15^0 using an ultrasonic tracking system, to follow the contour of the mould, making it the first example of a **C**ontour **T**ape **L**aminating **M**achine **(CTLM)**.
1984	**Albus** [10] pointed out the limitations that robotic arms had during the middle of the 1980s, which were limited to speeds <60 *m/min* for layup applications, and that accuracy was the key to enable off-line programming. To address this issue most ATL systems became high-rail gantries resulting in heavy and stiff structures that were associated with very poor machine dynamics. [11]
1986	**Meier** [12] introduced a system that has formed the basis for all modern commercial single-phase ATL systems. Direct layup force control and head normality over curved surfaces was enabled by replacing the previous ultrasonic tracking system with force-controlled Z-and A-axes [13].

1986	**Grone et al.** [14] patented a method to finalize the end of a tape course cut under an oblique angle using a second flexible layup element. This method has since been modified by **Torres Martinez** [15] not only to finalize a tape course, but also to start a ply, and in particular to overcome the technical difficulties of first-ply attachment.
1987	To address the limitation of the prepreg layup, **Lewis** and **Romero** [16] introduced a layup system combined with significant software capability, to enable layup over a curved surface along a natural (the path a tape will take over a surface without friction) or geodesic path.
1988	**Grove** [17] proposed a model for the laser assisted heating of thermoplastic tape to enable direct layup and consolidation of thermoplastic materials, however, the focus of thermoplastic layup shifted quickly to AFP. Since the middle of the 1990s to the present day, further developments to ATL have thus been rather limited and were starting to be dominated by productivity requirements.
1989	**Grimshaw** [18] demonstrated an ATL system having a segmented layup shoe connected to a pressure chamber, enabling accurate layup pressure and improved ply alignment over contoured surfaces. In 1995 this approach was extended to multiple layup elements operating independently from the layup head. [19]
1991	Tape heating was introduced in the 1990s to overcome issues during layup of complex laminates, and also enable tack control for layup of large parts. Irradiation heating for thermoplastic layup was in use by 1991. [20]
1995	**Sarazin** and **Springer** [21] addressed the question of optimal processing conditions for thermoset tape, in the context of a cure-on-the-fly system, to effectively reduce post-curing. It was observed that the thermoset material only reached a limited degree of cure and that post-curing was still a necessity; that layup pressure was independent of the number of plies, and scaled weakly with the roller diameter and ply orientation. Finally, the authors concluded that a high layup pressure could result in delamination during layup, as the material is pushed and pulled apart in front of and behind the layup roller compressing the material onto the tool; however their study did not include tack, which could prevent such separation.
1996	**Benda** and **Stump** [22] discussed the joint development of a component and layup system, where a hot-air heating system was added to an ATL to enable

	tape attachment onto complex contours. Further changes included the layup roller diameter, which was reduced from 150 *mm* to 50 *mm* to improve dexterity when delivering tape onto contours with $>30^0$ curvature. To enable layup onto such complex geometries some tape tension was required to keep the plies aligned.
2008	**Torres Martinez** [23] introduced a system that combined at least two rolls of either 75, 150 or 300 *mm* wide material on one ATL head to potentially improve both productivity and layup dexterity, though this can also be considered an AFP layup system.
2008	**Forest-Liné** [24,25] developed a nesting technology for ATL layup, to improve productivity for large parts with small features. Ply patches are pre-cut in a separate operation, stored on a plybacking, and wound back onto a roll. Forest-Liné's system employ two separate head sides to deliver either the continuous ply course or small pre-cut prepreg patches, often referred to a twin (or dual)-phase layup, with conventional layup being single-phase layup.
2011	Despite the potential complexity limitations of ATL manufacture, it has recently received renewed interest due to the high productivity achievable for flat laminates [26]. After layup, flat laminates can be formed into the desired shape by hot drape forming [27], offering a cost competitive manufacturing route for large composite components and material with high prepreg areal weight, however forming may detrimentally affect the mechanical performance of the structure, e.g. due to fiber wrinkling.

Table 1-1: *Historical development of ATL*

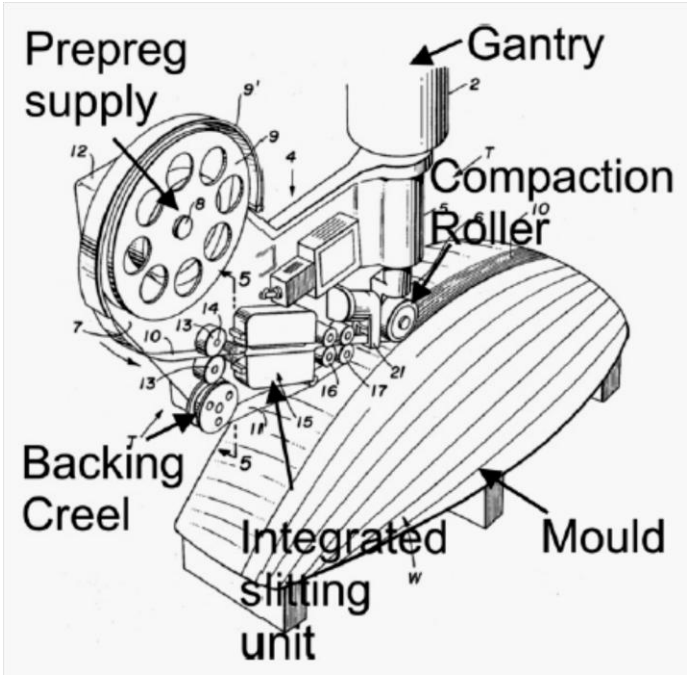

Figure 1-3: *Drawing of an ATL delivering slit tape over a curved surface* [4]

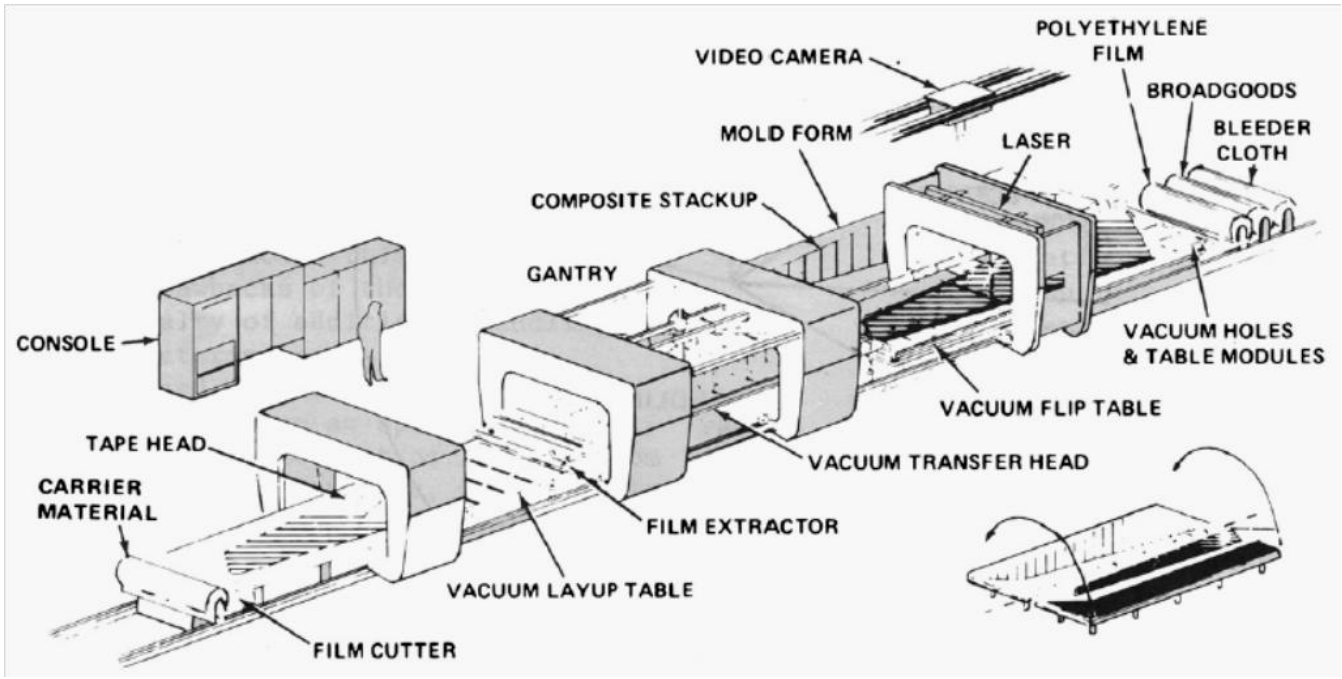

Figure 1-4: *Drawing of an early composite components manufacturing system.* [5] *The material is moved from left to right and material is applied to a mould using a bespoke tape layup head.*

1.1.2. ATL process description [30]

ATL is a process that is very amenable to large flat parts, such as wing skins. Tape layers usually lay-down either 3, 6, or 12 *in* wide unidirectional tape, depending on whether the application is for flat structure or mildly contoured structure. Automated tape layers are normally gantry style machines (Figure 1-5) which can contain up to 10 axes of movement [28]. Normally, 5 axes of movement are associated with the gantry itself and the other 5 axes with the delivery head movement. A typical tape layer consists of a large floor-mounted gantry with parallel rails, a cross-feed bar that moves on precision ground ways, a ram bar that raises and lowers the delivery head, and the delivery head that is attached to the lower end of the ram bar. Commercial tape layers can be configured to lay either flat or mildly contoured parts. Flat Tape Laying Machines (FTLM) are either fixed bed machines or open bay gantries, while Contour Tape Laying Machines (CTLM) are normally open bay gantries. The tool is rolled into the working envelope of the gantry, secured to the floor, and the delivery head is initialized onto the working surface.

The delivery heads (Figure 1-6) for both FTLM and CTLM are basically the same configuration and will normally accept 3, 6, or 12 *in* wide unidirectional tape. To facilitate the tape laying process, the unidirectional tape purchased for ATL applications is closely controlled for width and tack. FTLM uses either 6 or 12 *in* wide tape to maximize material deposition rates for flat parts, while most CTLMs are restricted to 3 or 6 *in* wide tape to minimize tracking errors (gaps and overlaps) when laying contoured parts. The term "CTLM" currently applies to mild contours that rise and fall at angles up to about 15%. More highly contoured parts normally are made by processes such as hand lay-up, filament winding, or fiber placement, depending on the geometry and complexity of the part. Material for ATL comes in large diameter spools, some containing almost 3000 lineal *ft* of material. The tape contains a backing paper that must be removed during the tape laying operation.

The spool of material is loaded onto the delivery head supply reel (reels as large as 25 *in.* in diameter are used) and threaded through the upper tape guide shoot and past the cutters. The material then passes through the lower tape guides, under the compaction shoe and onto a backing paper take-up reel. The backing paper is separated from the prepreg and wound onto a take-up roller. The compaction shoe makes contact with the tool surface and the material is laid onto the tool with compaction pressure. To insure uniform compaction pressure, the compaction shoe is segmented so that it follows the contour of the lay-up. The segmented compaction shoe is a series of plates that are air pressurized and conform to lay-up surface deviations, maintaining a uniform compaction pressure. The machine lays the tape according to the previously generated

NC program, cuts the material at the correct length and angle when a length (course) is completed, lays out tail, lifts off the tool, retracts to the course start position, and begins laying the next course. [29]

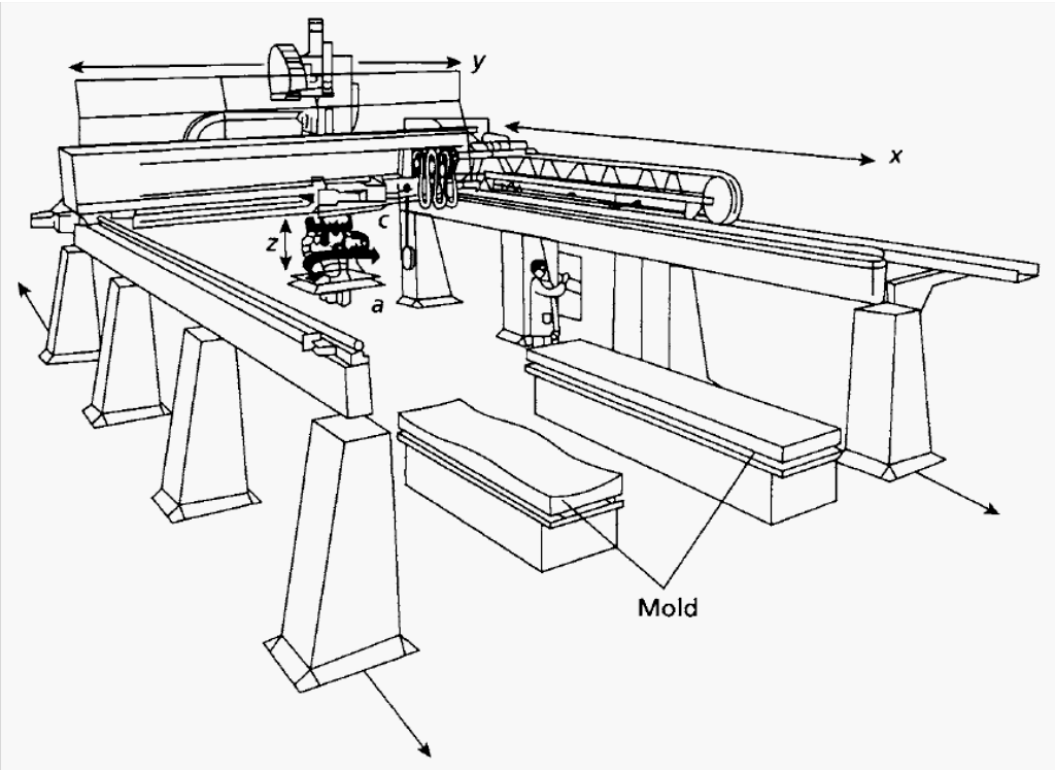

Figure 1-5: *Typical gantry style tape laying machine* [25]

Modern tape laying heads have optical sensors that will detect flaws during the tape laying process and send a signal to the operator. In addition, machine suppliers now offer a laser boundary trace in which the boundary of a ply can be traced by the operator to verify the correct position. Modern tape laying heads also contain a hot air heating system that will preheat the tape (27-44 ^{0}C) to improve the tack and tape-to-tape adhesion. Computer controlled valves maintain the temperature in proportion to the machine speed, i.e. if the head stops, the system diverts hot air flow to prevent overheating the material.

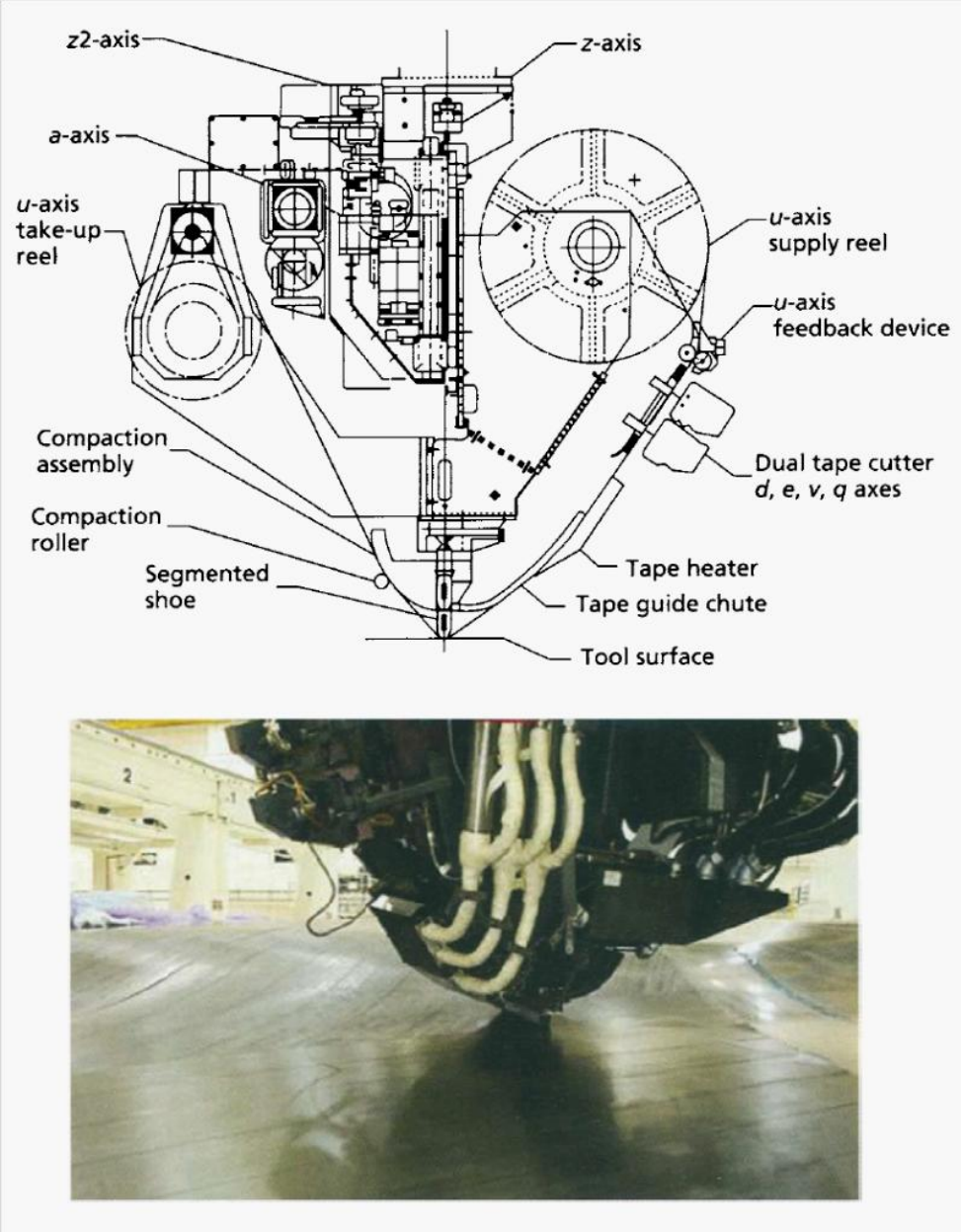

Figure 1-6: *Composite tape layer delivery head. (Source: The Boeing Company)*

Software to drive modern tape layers has improved dramatically in recent years. All modern machines are programmed off-line with systems that automatically compute the "natural path" for tape laying over a contoured surface. As each ply is generated, the software updates the surface geometry, eliminating the need for the designer to redefine the surface for each new ply. The software can also display detailed information about the fiber orientation of each course and

the predicted gaps between adjacent courses. Once the part has been programmed, the software will generate NC programs that optimize the maximum quantity of composite tape laid per hour.

Part size and design are key drivers for composite tape layer efficiency. As a general rule of thumb, bigger parts and simpler lay-ups are more efficient. This is illustrated in Figure 1-7 for a FTLM [29]. If the design is highly sculptured (lots of ply drop-offs), or the part size is small, the machine will spend a significant amount of time slowing down, cutting, and then accelerating back to full speed.

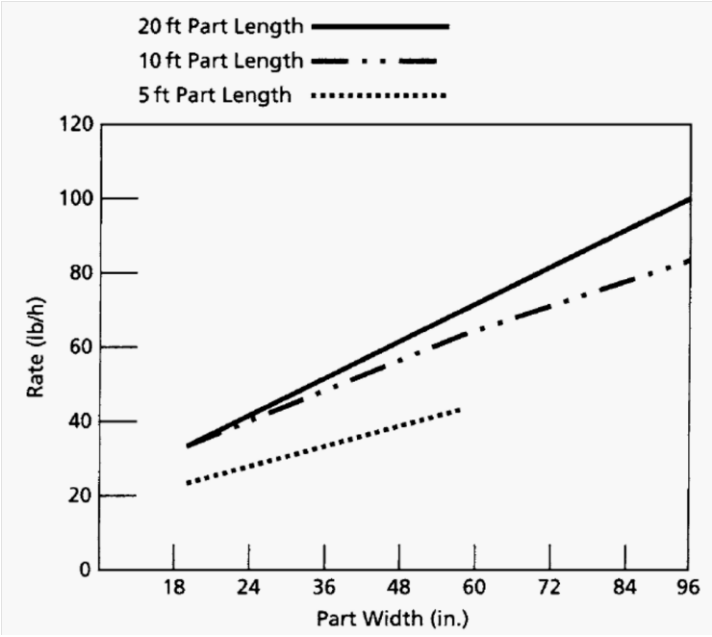

Figure 1-7: *Tape laying efficiency vs. part size graph [29]*

ATL systems are used for manufacturing of a variety of parts, such as tail planes, wing skins and the center wing box of the Airbus A380. The main manufacturers of aerospace ATL equipment are MAGCincinnati (USA), MTorres (Spain), and Forest Liné (France), although the latter was recently acquired by MAGCincinnati. GFM (Germany), Mikrosam (Macedonia), Entec (USA) and ATK (USA) supply ATL systems, but do not have a comparable number of installed systems. Ingersoll (USA) currently only supplies AFP systems, but has delivered ATL systems in the past.

1.2. Automated Fiber Placement (AFP)

1.2.1. Historical developments of AFP

1974	The **Goldsworthy** [4] patent described an ATL system but also highlighted the challenge of conforming a tape to a curved surface. To address this, the layup head had the ability to slit down the wide tape into 3.2 *mm* slices and then deliver those at individual speeds by keeping the additional material on the head. (Figure 1-8)
1980	AFP systems were commercially introduced towards the end of the 1980s, and were described as a logical combination of ATL and **F**ilament **W**inding **(FW)** [31]; by combining the differential payout capability of FW and the compaction and cut-restart capability of ATL.
1989	**Evans et al.** [32] initially overcame the limitations of **Goldsworthy**'s approach by keeping slit tape on separate bobbins, which were also individually driven.
1990	**Bullock** [33] demonstrated another type of AFP machine together with an offline programming system, and argued that offline programming was essential to AFP productivity as it directly affected machine production time. The AFP system controlled layup speed, pressure, temperature, and tape tension.
1990	**Barth** [34] showed an AFP system that made use of cooled creel houses to reduce prepreg tack, thus enabling reliable despoiling and improved layup reliability. Additionally, the **C**ompression **A**fter **I**mpact **(CAI)** strength of laminates manufactured by AFP and manual forming was evaluated, showing that mechanical properties of both were comparable.
1991	To enhance productivity, **Enders** [35] introduced an AFP system that could deliver up to 24 tows in a sequence. The system was uniquely tightly integrated into the **C**omputer-**A**ided **D**esign **(CAD)** system to address the earlier note [33] regarding AFP productivity.
1993	**Evans** [36] improved productivity by focusing on reliability, such as material changes, tape tolerances and intermittent debulking. More reliable layup over complex geometries was achieved by delivering the tows along a curvilinear path; this is often referred to as steering.
1995	The earliest approaches for developing thermoplastic layup were reported by **Grove** [17], **Mantell** and **Springer** [37,38], and **Sarazin** and **Springer** [21].

	These works identified a trade-off between layup pressure, temperature, and speed. Layup quality, mainly measured by interfacial healing and void age, was detrimentally affected by layup speed; and as discussed by **Bourban et al.** [39] the main limiting factor for thermoplastic layup was the amount of time required to heat the material above its melting point.
1997	A laser heating was also successfully developed by **Funck** and **Neitzel** [40], **Rosselli et al.** [41], and **Pistor et al.** [42]. **Goodmann et al.** [43], and **Burgess et al.** [44], similarly reported a method for curing photoactivated thermoset prepregs on the fly using an electron beam or **U**ltra **V**iolet **(UV)** light as a radiation source for faster processing and reduction of residual thermal stresses. Overall however, both thermoplastic and thermoset in-situ processing approaches achieved limited layup speeds, while also exhibiting reduced mechanical properties.
2006	**Grant** [1,45,46] described the change in focus for AFP layup from novel processes to addressing issues regarding affordability, process reliability, and productivity, and showed that AFP had mainly been employed in military and space programs until 2000. (Table 1-3)
2008	**Torres Martinez** [47] introduced an automated system for splicing the tows together, and this could improve productivity by reducing downtime for material refilling. **Oldani** [48] also introduced an automated system to detect layup errors, improving productivity by reducing the time for quality inspection after ply layup.
2008	To increase tack levels and further minimize layup errors infrared heating of thermoset tape was introduced by **Calawa** and **Nancarrow** [49] to allow faster heating and higher layup temperatures. Furthermore, **Hamlyn** and **Hardy** [50] introduced a system for rapidly exchanging layup heads and tools by keeping a second layup head ready for immediate layup, and this led reduced system downtime.
2008	Material delivery was improved by using systems that either reduced the feed length, or by minimizing the amount of redirects and twists in the tow using appropriate guide systems. [51]

Table 1-2: *Historical development of AFP*

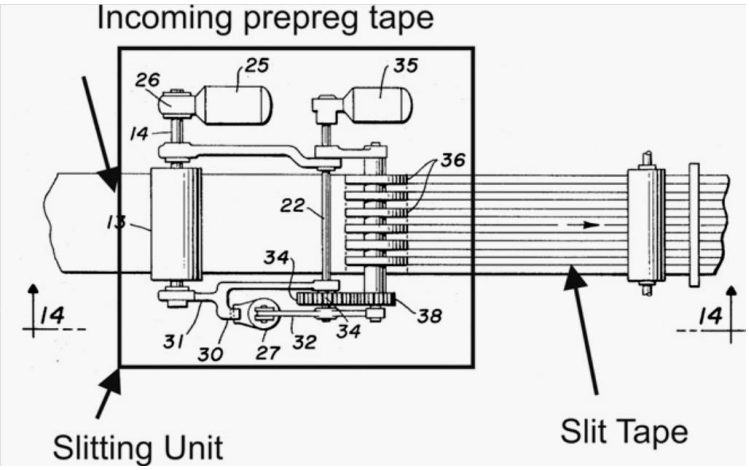

Figure 1-8: *Integrated slitting unit with individual tow pay-out from [4]. This can be interpreted as the first AFP concept.*

Aircraft Program	Components made by AFP
F-18 E/F	Inlet Duct, Aft Center Side Skins, Stabilator Skins
C-17 Globemaster	Fan Cowl Doors, Landing Gear Pods
Bell Agusta 609	Fuselage Panels
V-22 Osprey	Aft Fuselage, Side Skins, Drag Angle, Sponsons, Grips
Premier I	Fuselage Sections
Hawker Horizon	Fuselage Sections
F22 Raptor	Stabilator Pivot Shaft
Sea Launch	Payload Fairing

Table 1-3: *Overview of AFP applications in 2000, from [46]. AFP was mostly used for military applications.*

1.2.2. AFP process description [30]

In the late 1970s, Hercules Aerospace Co. (now Alliant Techsystems) developed the fiber placement process. Shown conceptually in Figure 1-9, it is a hybrid between filament winding and tape laying. A fiber placement, or tow placement, machine allows individual tows of prepreg to be placed by the head. The tension on the individual tows normally ranges from 0 up to about 2 *lb*. Therefore, true 0^0 (longitudinal) plies pose no problems. In addition, a typical fiber placement machine (Figure 1-10) contains 12, 24, or 32 individual tows that may be individually cut and then added back in during the placement process. Since the tow width normally ranges from 0.125 to 0.182 *in*, bands as wide as 1.50-5.824 *in* can be applied depending on whether a 12 or 32 tow head is used. The adjustable tension employed during this process also allows the machine to lay tows into concave contours, limited only by the diameter of the roller mechanism. This allows complicated ply shapes, similar to those that can be obtained by hand lay-up. In

addition, the head (Figure 1-12) contains a compliant compaction roller that applies pressure in the range of 10-400 *lb* during the process, effectively debulking the laminate during lay-up. Advanced fiber placement heads also contain heating and cooling capability. Cooling is used to decrease the towpreg tack during cutting, clamping, and restarting processes, while heating can be used to increase the tack and compaction during lay-down. For the current generation of fiber placement heads, a minimum convex radius of approximately 0.124 *in* and a minimum concave radius of 2 *in* are obtainable. One limitation of the fiber placement process is that there is a minimum course (or ply) length, normally about 4 *in*. This is a result of the cut-and-add process. A ply that is cut or added must then pass under the compliant roller, resulting in a minimum length that is dependent on the roller diameter. Fiber-placed parts are usually autoclave cured on carbon/epoxy, steel or low-expansion invar tools to provide dimensionally accurate parts. Typical applications for fiber placement are engine cowls, inlet ducts, fuselage sections, pressure tanks, nozzle cones, tapered casings, fan blades, and C-channel spars.

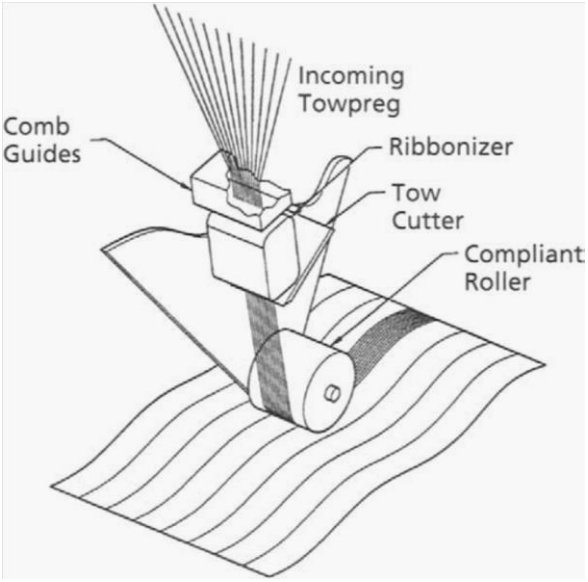

Figure 1-9: *Fiber placement process [30]*

Extensive testing has shown that the mechanical properties of fiber-placed parts can be essentially equivalent to hand layed-up parts [52]. Like hand layed-up parts, gaps and overlaps are typically controlled to 0.030 *in* or less. One difference between fiber placed and hand layed-up plies are the "stair-step" ply terminations obtained with fiber placement, since each tow is cut perpendicular to the fiber direction. Again, this stair-step ply termination has been shown to be equivalent in properties to the smooth transition you obtain with manual lay-up. In fact, some parts have been designed so that either fiber placement or manual hand lay-up may be used for

fabrication. Since the tows are added-in and taken-out as they are needed, there is very little wasted material; scrap rates of only 2-5% are common in fiber placement. In addition, since the head can "steer" the fiber tows, there is the potential for the design of highly efficient load-bearing structure.

The software required to program and control a fiber placement machine is even more complex than that required for an automated tape layer or modern filament winder. The software translates CAD part and tooling data into 7-axis commands, developing the paths and tool rotations for applying the composite tows to the part's curved and geometric features, while keeping the compaction roller normal to the surface. A simulator module confirms the part program with 3-D animation, while integrated collision avoidance post-processing of the NC program automatically detects interferences.

Modern fiber placement machines are extremely complex and can be very large installations. Most machines contain seven axes of motion (cross-feed, carriage traverse, arm tilt, mandrel rotation, mandrel wrist yaw, pitch, and roll). The larger machines are capable of handling parts up to 20 *ft* in diameter and 70 *ft* long, with mandrel weights up to 80000 *lb.* They typically contain refrigerated creels for the towpreg spools, towpreg delivery systems, and redirect mechanisms to minimize twist, and tow sensors to sense the presence or absence of a tow during placement.

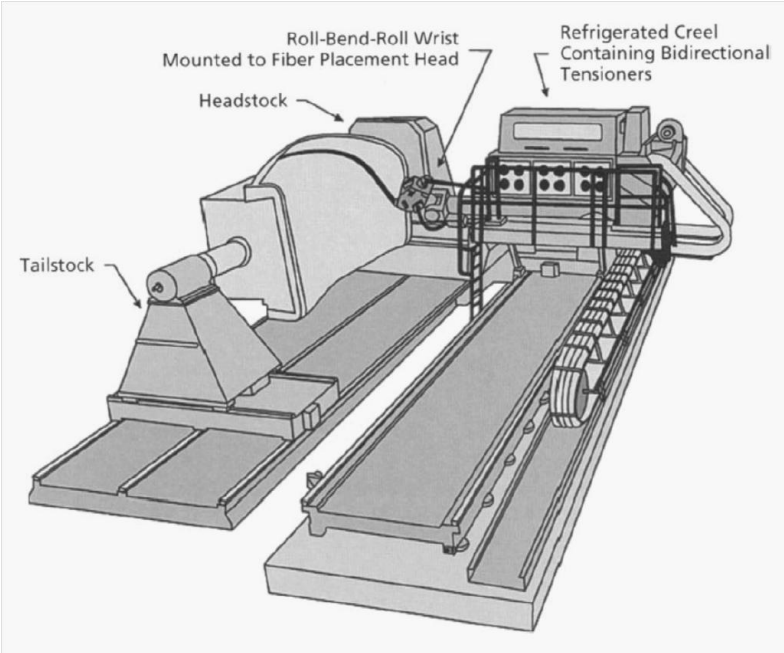

Figure 1-10: *Fiber placement machine [30]*

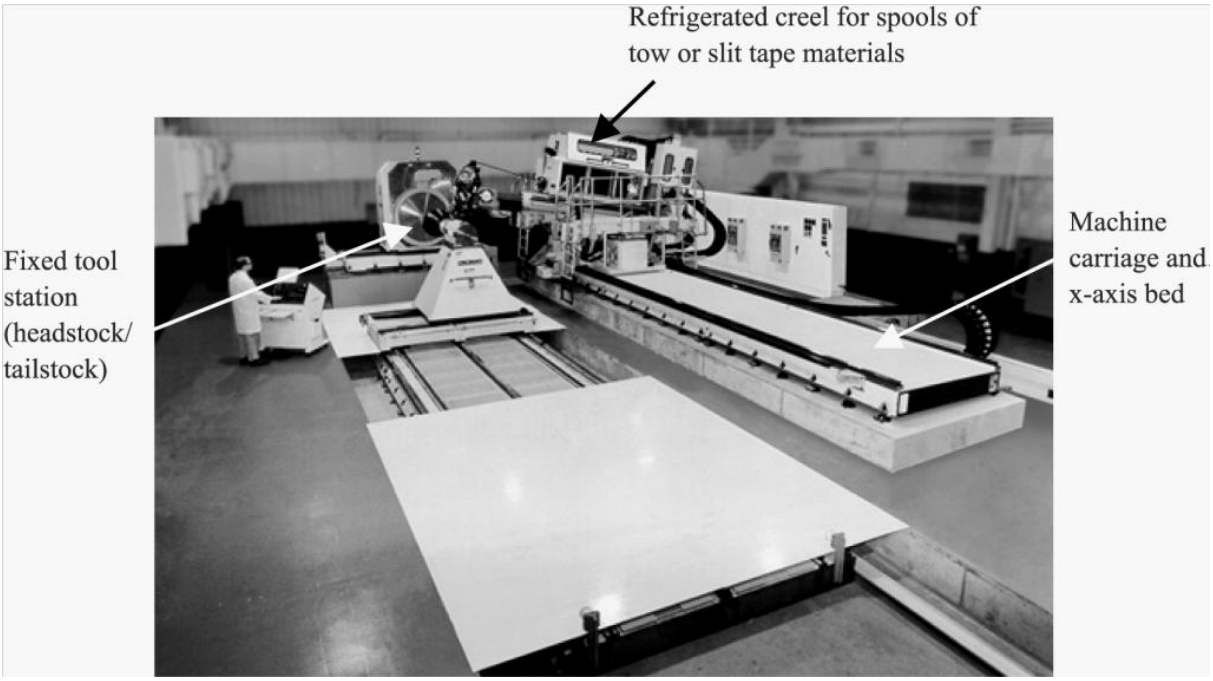

Figure 1-11: *Typical FP machine configuration (Cincinnati Machine Viper 3000) [1]*

Figure 1-12: *Fiber placement head. (Source: www.mag-ias.com)*

Although complex part geometries and lay-ups can be fabricated using fiber placement, the biggest disadvantages are that the current machines are very expensive, complex, and the lay-down rates are slow compared to most conventional filament winding operations.

The capability to automatically manufacture unsymmetrical laminates that can have locally changing fiber orientations makes AFP a lead technology for future developments in the areas of smart and tailored structures, and their application.

The main manufacturers of AFP systems are Automated Dynamics (USA), Accudyne (USA), MAGCincinatti (USA), Coriolis (France), Electroimpact (USA), Foster Miller/ATK (USA), Ingersoll (USA), Mikrosam (Macedonia) and MTorres (Spain). Automated Dynamics, Accudyne, Coriolis and Electroimpact supply their systems on industrial robots and gantries. Cincinnati, Foster Miller, Ingersoll, Mikrosam and MTorres use either column type or horizontal gantries. Robotic layup systems tend to have a lower initial capital expenditure and can be better tailored for specific applications. Gantry layup systems offer improved general productivity and reliability by handling more tows in the head.

1.3. Objectives and organization of the thesis

The ultimate goal of this research is to experimentally investigate the correlation between the damage patterns and the process induced defects in composite laminates produced by Dry Automated Fiber Placement (DAFP). The work followed an experimental methodology developed in the **C**omposite **M**aterials **G**roup **(CMG)** at KU Leuven. [53]

To arrive at this ultimate goal, the project is divided into two parts. First, tensile tests were performed till different load levels on samples which were cut from the laminates provided by NLR (The National Aerospace Laboratory), with and without defects, accompanied by the **A**coustic **E**mission **(AE)** registration and full-field strain mapping using **D**igital **I**mage **C**orrelation **(DIC)** to compare the effects of each type of defect. Furthermore, in order to study the compressive mechanical properties of the laminates, compression tests were carried out on samples without defects accompanied by full-field strain mapping (DIC). Consequently, the tensile and compressive mechanical properties of the laminates as well as the damage development during different steps of loading were studied.

Second, the clustering analysis of the AE signals were performed so as to determine the connection between the AE signal parameters and corresponding damage mode and to discriminate AE signals according to the nature of the damage events they originate from.

1.4. References

1. Grant C. Automated processes for composite aircraft structure. Industrial Robot: An International Journal 2006; 33(2): 117–21.
2. Lukaszewicz Dirk H-JA, Ward C, Potter KD. The engineering aspects of automated prepreg layup: History, present and future. Composites Part B: Engineering 2012; 43(3): 997-1009.
3. Chitwood BE, Howeth MS. Composite tape laying machine with pivoting presser member. Patent 4627886, 6th April 1971.
4. Goldsworthy WB. Geodesic path length compensator for composite-tape placement method. Patent US 3810,805, 14th May 1974.
5. Huber J. Automated lamination of production advanced composite aircraft structures. SAE International Congress and Exposition. Detroit, Michigan, USA; 1981.
6. Eaton HL. Cost effective tape laying. 29th National SAMPE symposium. Reno, Nevada, USA; 1984.
7. Saveriano JW. Automated contour tape laying of composite materials. 16th National SAMPE technical conference. Albuquerque, New Mexico, USA; 1984.
8. Coad CL, Werner SM, Dharan CKH. Design of a composite four-axis robot for prepreg layup. 29th National SAMPE symposium. Reno, Nevada, USA; 1984.
9. Stone KL. Automation in composite processing. 29th National SAMPE symposium. Reno, Nevada, USA; 1984.
10. Albus JS. Research issues in robotics. 16th National SAMPE technical conference. Albuquerque, New Mexico, USA; 1984.
11. Wang EL, Gutowsi T. Laps and gaps in thermoplastic composites processing. Composites manufacturing 1991; 2(2): 69–78.
12. Meier RA. An advanced control system for composite material placement. 31st International SAMPE symposium. Covina, California, USA; 1986.
13. Grone RJ, Grimshaw MN. Composite tape laying machine with pivoting presser member. Patent US 4627886, 30th May 1985.
14. Grone RJ, Schnell LR, Vearil L. Composite tape laying machine and method. Patent US 4557783, 5th December 1983.
15. Torres Martinez M. Tete enrubanneuse pour l'application de bande en materiau composite [Tape laying unit for depositing a band of composite material]. Patent EP 1097 799 A1, 9th May 2001[in Spanish].
16. Lewis HW, Romero JE. Composite tape placement apparatus with natural path generation means. Patent US 4696,707, 29th September 1987.

17. Grove SM. Thermal modeling of tape laying with continuous carbon fiber-reinforced thermoplastic. Composites 1988; 19(5): 367–75.
18. Grimshaw MN. Machine for applying composite and presser assembly therefore. Patent EP 0371289-A1, 8th November 1989.
19. Grimshaw MN, Hecht JR. Method and apparatus for laying composite material. Patent EP 0644040-A1, 8th November 1994.
20. Zaffiro JA, Cincinnati Milacron Inc. Control of radiation heating system for thermoplastic composite tape. Patent 5177340, 5th January 1993.
21. Sarazin H, Springer GS. Thermochemical and mechanical aspects of composite tape laying. Journal of Composite Materials 1995; 29: 1908–43.
22. Benda BJ, Stump KH. A case study of contoured tape laying. American Helicopter Society 52nd Annual Forum. Washington, DC, USA; 1996.
23. Torres Martinez M. Head for application of carbon-fiber strips and application method. Patent WO 2008/020094 A1, 21st February 2008.
24. Tillement PAH, Charra SRE. Device for separating and discharging trimmings cut in a pre-impregnated strip. Patent WO 2008/135645 A1, 13th November 2008.
25. Tillement PAH, Charra SRE. Composite lay-up head with a retractable device for separating a prepreg from its support tape. Patent WO 2008/142273 A2, 27th November 2008.
26. Larberg YR, Kermo M. On the interply friction of different generations of carbon/epoxy prepreg system. Composites Part A: Applied Science and Manufacturing 2011; 42(9): 1067–74.
27. Gutowski TG, Dillon G, Chey S, Li H. Laminate wrinkling scaling laws for ideal composites. Composites Manufacturing 1995; 6(3–4): 123–34.
28. Grimshaw MN. Automated Tape Laying. ASM Handbook Volume 21 Composites, ASM International 2001.
29. Grimshaw MN, Grant C, Diaz JML. Advanced Technology Tape Laying for Affordable Manufacturing of Large Composite Structures. 46th International SAMPE Symposium; 2001. p. 2484-94.
30. Campbell FC. Chapter 7 - Polymer Matrix Composites, In Manufacturing Technology for Aerospace Structural Materials. Elsevier Science, Oxford; 2006. p. 273-368.
31. Knight BW. The technique of filament winding. Composites; June 1970. p. 228–33.
32. Evans DO, Vaniglia MM, Hopkins PC. Fiber placement process study. 34th International SAMPE symposium. Covina, California, USA; 1989. p. 1822–33.

33. Bullock DE. Automated prepreg tow placement for composite structures. 35th International SAMPE symposium. Anaheim, California, USA; 1990.
34. Barth JR. Fabrication of complex composite structures using advanced fiber placement technology. 35th International SAMPE symposium. Anaheim, California, USA; 1990. p. 710–20.
35. Enders ML, Hopkins PC. Developments in the fiber placement process. 36th International SAMPE symposium. San Diego, California, USA; 1991. p. 778–90.
36. Evans DO. Design considerations for fiber placement. 38th International SAMPE symposium. Anaheim, California, USA; 1993. p. 170–81.
37. Mantell SC, Wang QL, Springer GS. Processing thermoplastic composites in a press and by tape laying – experimental results. Journal of Composite Materials 1992; 26(16): 2378–401.
38. Mantell SC, Springer GS. Manufacturing process models for thermoplastic composites, Journal of Composite Materials 1992; 26(16): 2348–77.
39. Bourban P, Bernet N, Zanetto J, Manson J. Material phenomena controlling rapid processing of thermoplastic composites. Composites Part A: Applied Science and Manufacturing 2001; 32(8): 1045–57.
40. Funck R, Neitzel M. Improved thermoplastic tape winding using laser or direct-flame heating. Composites Manufacturing 1995; 6(3-4): 189–92.
41. Rosselli F, Santare M, Guceri S. Effects of processing on laser assisted thermoplastic tape consolidation. Composites Part A: Applied Science and Manufacturing 1997; 28(12): 1023-33.
42. Pistor C, Yardimci M, Guceri S. On-line consolidation of thermoplastic composites using laser scanning. Composites Part A: Applied Science and Manufacturing 1999; 30(10): 1149-57.
43. Goodmann DL, Weidman DJ, Bryne CA, et al. Automated tape placement with in-situ electron beam cure: a viable process. 46th International SAMPE symposium. Long Beach, California, USA; 2001. p. 2127–39.
44. Burgess JW, Wilenski MS, Belvin HL, Cano RJ, Johnston NJ. Development of a cure-on-the-fly automated tape placement machine for electron curable prepregs. 46th International SAMPE symposium. Long Beach, California, USA; 2001. p. 2024–36.
45. Grant C, Martin J. Automated processing technology for composites: current status and vision for the future. 48th International SAMPE symposium. Long Beach, California, USA; 2003.

46. Grant C. Fiber placement process utilization within the worldwide aerospace industry. 45th International SAMPE symposium. Long Beach, California, USA; 2000. p. 709–20.
47. Torres Martinez M. Faserstreifenverbinder fuer Bandwickler. Patent DE 10 2008 010 424 A1, 2nd October 2008.
48. Oldani T. Increasing productivity in fiber placement processes. SAE aerospace manufacturing and automated fastening conference & exhibition. North Charleston, South Carolina, USA; 2008.
49. Calawa R, Nancarrow J. Medium wave infrared heater for high-speed fiber placement. SAE Aerofast. Los Angeles, California, USA; 2007.
50. Hamlyn A, Hardy Y. Fiber application machine with tool changing system. Patent WO 2008/149004 A1, 11th December 2008.
51. Hamlyn A, Hardy Y. Fiber application machine with fiber supply flexible tubes. Patent WO 2008/122709-A1, 28th February 2007.
52. Adrolino JB, Fegelman TM. Fiber Placement Implementation for the F/A-18 E/F Aircraft. 39th International SAMPE Symposium; 1994. p. 1602-16.
53. Lomov SV, Ivanov DS, Truong TC, Verpoest I, Baudry F, Vanden Bosche K, Xie H. Experimental methodology of study of damage initiation and development in textile composites in uniaxial tensile test, Composites Science and Technology 2008; 68(12): 2340-9.

2

Constituents and Composites Manufacturing

This research summarizes results of the study on damage development done into two laminate composites which were produced at NLR "The National Aerospace Laboratory" for the CANAL project[1]. These panels are named here as "CANAL QI" (Figure 2-1) and "AP-PLY" (Figure 2-2).

The preforms for both panels were manufactured using automated dry tow placement technique. The reinforcement material was "Tenax IMS65 E23 24K" dry unidirectional tape delivered by

[1] **CANAL**

Cre**A**ting **N**onconvention**A**l **L**aminates
Funding: European (7th RTD Framework Program)
Duration: 09/2013 - 08/2016
Background & policy context
Currently, no non-conventional laminates are known to be implemented in the industry, though research has shown promising results in virtual analysis and coupon testing. Variable stiffness laminates with curved fiber paths show an increase in buckling loads, as well as tailoring of natural frequencies for both panels and cylinders. Straight-fiber laminates with dispersed fiber angles show a promise for improved damage tolerance. A so-called AP-PLY multidirectional weave pattern can improve damage tolerance for any stacking sequence.

Objectives
The purpose of the CANAL project is to develop new **N**on-**C**onventional **L**aminate **(NCL)** configurations using Dry Fiber Placement (DFP) and the establishment of engineering tools to ensure implementation of the technology in the aerospace industry and other industries, such as automotive that can benefit from rapid and cost effective production of complex shaped and high-performance composite parts. Whereas up to now composite laminates usually consist of only 90, 0 and +/-45 degree layers, the development of Automated Fiber Placement technology has opened possibilities to divert from this limiting step in design and manufacturing. Whereas for large aircraft manufacturers like Airbus and Boeing it almost seems default to use composites and a high level of automated fabrication with e.g. AFP, it is also lucrative for the small aircraft industry and the transport industry in general.

Methodology
Both weight and cost reduction can be achieved using automated composite manufacturing like AFP. Further material cost reductions are achieved through use of dry fibers instead of more costly prepregs, in combination with **L**iquid **C**omposite **M**oulding **(LCM)** instead of costly autoclave curing. The reduction in weight and cost supported by novel non-conventional design and dry fiber placement and LCM manufacturing technique will further facilitate and speed up the introduction of composite lightweight structures in aerospace and other transport industries.

"Toho Tenax", with area density of 194 gsm (g/m^2), and ¼ in (6.25 mm) of width. These carbon fiber tows had no twist and were covered with 1.3% E23 binder powder to facilitate sufficient tackiness needed for the automated placement.

Figure 2-1: *CANAL QI panel*

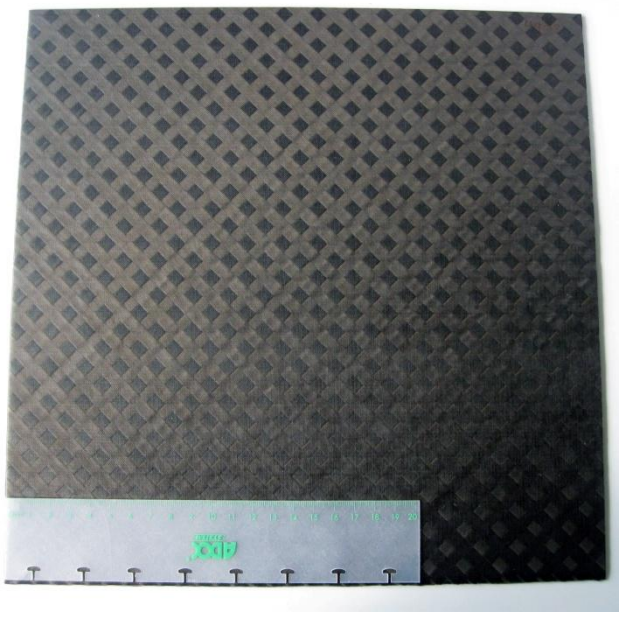

Figure 2-2: *AP-PLY panel*

The preforms were injected by vacuum infusion with autoclave using "PRISM EP2400 RESIN SYSTEM" produced by "Cytec". The resin system as well as the reinforcement material will be discussed in details in subsequent sections.

The "CANAL QI" panel had a quasi isotropic lay-up with 16 plies $[+45/0/-45/90/+45/0/-45/90]_s$. Each ply was 0.2 *mm* thick; therefore the nominal thickness of the plate was 3.2 *mm*. The dimensions of the plate were 400 *mm**400 *mm*. The intentional gap and overlap were placed in the second 0^0 ply by shifting the two pairs of successive tapes to lay aside (gap)/lay on each other (overlap) for a width of 1.5 *mm*. Orientations of the gap and overlap are shown in Figure 2-3 and Figure 2-4.

The "AP-PLY" panel had 10 plies $[(+45/-45)/0/(+45/-45)]_S$. Each ply was 0.2 *mm* thick; therefore the nominal thickness of the plate was 2 *mm*. The dimensions of the plate were 300 *mm**300 *mm*. This plate does not contain any intentional defects.

For both panels no process-induced defects (e.g. tolerance of angle in fiber placement) were reported. The minimal permissible tolerance between any two successive individual tapes shall be ±0.2 *mm*.

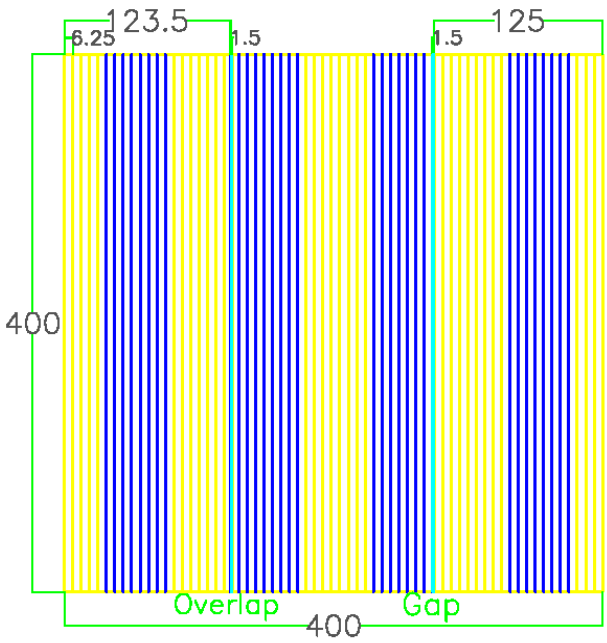

Figure 2-3: *Tows, gap, and overlap configuration in the second 0^0 ply; CANAL QI panel; dimensions are in mm.*

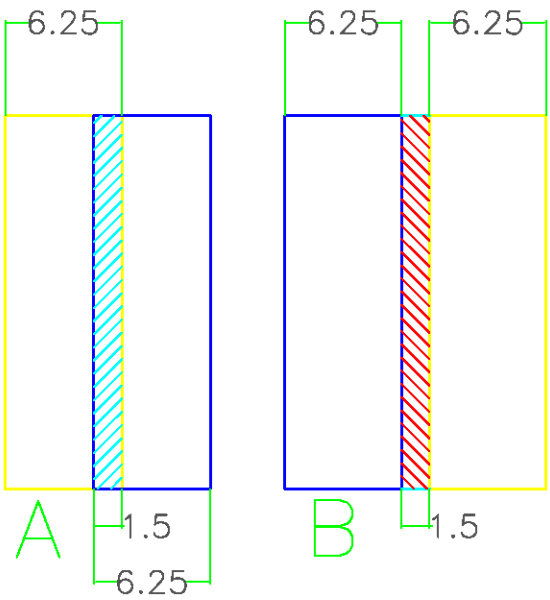

Figure 2-4: *Configurations of the two pairs of successive tows in the second 0^0 ply of the CANAL QI panel:* ***(A)*** *overlap, and* ***(B)*** *gap. Dimensions are in mm.*

2.1. Fibers and tows [1-2]

Carbon fibers are widely used for airframes and engines and other aerospace applications. High Modulus (HM, Type I), High Strength (HS, Type II) and Intermediate Modulus (IM, Type III) form the three broad categories of carbon fibers available commercially, shown in Table 2-1.

Property	HM, Type I	HS, Type II	IM, Type III
Specific Gravity	1.9	1.8	1.8
Tensile Modulus (GPa)	276-380	228-241	296
Tensile Strength (MPa)	2415-2555	3105-4555	4800
Ultimate Strain (%)	0.6-0.7	1.3-1.8	2.0
Coefficient of Thermal Expansion ($\times 10^{-6}\ mm^{-1}K^{-1}$)	-0.7	-0.5	N/A
Thermal Conductivity ($Wm^{-1}K^{-1}$)	64-70	8.1-9.3	N/A
Electrical Resistivity ($\mu\Omega\ m$)	9-10	15-18	N/A

Table 2-1: *Typical properties for the major types of commercial carbon fibers [1]*

Carbon fibers are made from organic precursor materials by a process of carbonization. The bulk of carbon fibers used in aerospace and other structural applications are made from

polyacrylonitrile (PAN) fibers [3]. Carbon fibers are also made from various forms of pitch [4]. Early carbon fibers were manufactured from rayon; however, these fibers have been gradually phased out due to their low carbon yield (20-25%) and their generally poorer mechanical properties compared to PAN and pitch-based carbon fibers.

TENAX IMS65 E23 24K is a PAN-based carbon fiber. PAN is an acrylic textile fiber produced by wet or dry spinning of the basic polymer or copolymer. Dry spinning produces round smooth fibers whereas wet spinning (extrusion into a coagulating bath) produces a variety of cross-sections, including dog-bone, elliptical, and kidney-shaped. There are some advantages in the non-circular cross-sections; for example, the larger relative surface area improves effective bonding. The fibers are stretched during the spinning process. The greater is the stretch, the smaller is the fiber diameter and the higher is the preferred orientation of the molecular chain along the fiber axis, resulting in a stiffer carbon fiber when processed. PAN fiber tows typically contain around 10^4 fibers, although much larger or smaller tows are also produced. The finished carbon fibers are between 5-10 μm in diameter.

Figure 2-5 schematically illustrates the process of conversion of the PAN fibers into carbon fibers. The PAN is first stabilized in air at around 250 $°C$ by oxidation to form a thermally stable ladder polymer, having a high glass transition temperature (T_g), which is resistant to melting at the higher temperatures. The cyclic groups in the ladder polymer are rather similar in molecular structure to the carbon basal plane, except that they also contain nitrogen and hydrogen atoms. The fibers are maintained under tension to prevent them from contracting during oxidation and, through the resulting deformation, to align further the ladder structure with the fiber axis.

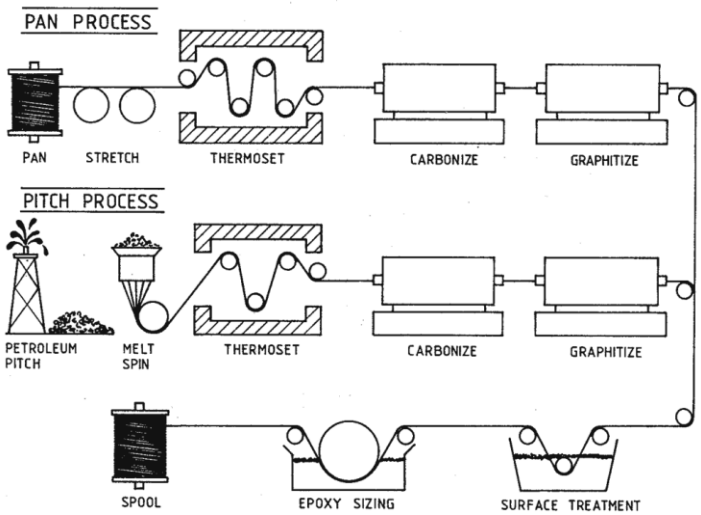

Figure 2-5: *Schematic illustration of the process used to make carbon fibers from PAN or Pitch. [2]*

The next step in the process is carbonization 1200-1600 $°C$ in an inert nitrogen atmosphere. This removes the nitrogen, oxygen, and hydrogen from the ladder.

As the heat treatment proceeds, benzene aromatic rings link to form polynuclear aromatic fragments, with the basal planes aligned along the fiber axis. Gradually the aromatic network transforms to mainly carbon atoms and becomes denser through cross-linking with the evolution of N_2 through open pores in the fiber. At 120 $°C$ the transformation to carbon is almost complete and closed pores remain in the fiber. Finally, at around 1500-1600 $°C$ the strength of the fiber reaches its peak.

After heat treatment at 1500-1600 $°C$ the strain capability of the fibers is then over 1.5% with an intermediate value of the Young's modulus of around 240 GPa.

If higher modulus is required, which will be at the expense of strength and strain capability, the fibers undergo a final graphitization stage of heat treatment up to 2500 $°C$. This treatment is generally carried out in a clean and more inert atmosphere, such as argon, to prevent the formation of flaws through chemical reactions and/or local graphitization. Strain capacity is then reduced to around 0.7% and the Young's modulus up to 380 GPa.

The strength of carbon fibers depends on: **(1)** the type of precursor used, **(2)** the processing conditions during manufacturing (such as fiber tension and temperatures), and **(3)** the presence of flaws and defects. Flaws in the carbon fiber microstructure include internal pits and inclusions, external gouges, scratches, and stuck filament residues, as well as undesirable characteristics such as striations and flutes. These flaws can have a considerable impact on the fiber tensile strength, but little effect, if any, on modulus, conductivity or thermal expansion [5]. Carbon fibers usually have a slightly negative coefficient of thermal expansion that becomes more negative as the modulus E increases. One consequence of using high- and ultrahigh-modulus carbon fibers is the increased possibility of matrix microcracking during processing or environmental exposure due to the larger mismatch in the coefficients of thermal expansion between the fibers and the matrix.

Carbon fibers with a wide range of strength and moduli are available from a number of producers. PAN-based carbon fibers having strengths ranging from 3500 to 7000 MPa and moduli ranging from 200 to 310 GPa with elongations of up to 2% are commercially available. Standard-modulus PAN fibers have good properties and lower cost, while higher-modulus PAN fibers cost more because high processing temperatures are required. Heating the fibers to 980 $°C$ yields PAN fibers containing 94 % carbon and 6 % nitrogen, while heating to 1260 $°C$ removes

the nitrogen and raises the carbon content to around 99.7%. Higher processing temperatures increase the tensile modulus by refining the crystalline structure and the 3D nature of the structure. The diameter of carbon fibers usually ranges from 0.3 to 0.4 *mm*. Carbon fibers are provided in untwisted bundles of fibers called "tows." Tow sizes can range from as small as 1,000 fibers per tow up to >200,000 fibers per tow. A typical designation of "12k tow" indicates that the tow contains 12,000 fibers. Normally, as the tow size decreases, the strength and cost increases. For aerospace structures, normal tow sizes are 3k, 6k, 12k, and 24k, with 3k and 6k being the most prevalent for woven cloth and 12k and 24k for unidirectional tape. The costs of carbon fibers are dependent on the manufacturing process, the type of precursor used, the final mechanical properties and the tow size. The maximum use temperature for carbon and graphite fibers in an oxidizing atmosphere is 500 *°C*.

The ideal engineering material would have high strength, high stiffness, high toughness and low weight. Carbon fibers combined with polymer matrices meet these criteria more closely than any other material. Carbon fibers are elastic to failure at normal temperatures, creep resistant and not susceptible to failure, chemically inert, except in strong oxidizing environments or in contact with certain molten metals, and have excellent damping characteristics. Some disadvantages of carbon fibers are: they are brittle and have low impact resistance; they have low strains to failure; their compressive strengths are less than their tensile strengths; and they are relatively expensive compared to glass fibers.

“TENAX®-E IMS65 E23 24K 830tex” which was used in this study, is a family of intermediate modulus, aerospace-grade carbon fibers manufactured in Japan and Germany for use as reinforcements in high performance composites. These fibers are produced from poly-acrylonitrile (PAN) precursor and are surface treated to promote adhesion to organic matrix polymers. The epoxy-based sizing materials are designed to aid in handling. [6]

Figure2-6: *TENAX®-E IMS65 E23 24K 830tex; Net Weight: 1122 g, Length: 1352 m; (Source: Toho Tenax Europe)*

The specifications offered by "Toho Tenax" are mentioned in Table 2-2.

Typical Fiber Properties	Value (SI)
Tensile Strength	6000 MPa
Tensile Modulus	290 GPa
Poisson's Ratio	0.236
Elongation	1.90%
Density	1.78 g/cc
Linear Density with Sizing	840 tex (g/km)
Number of Filaments	24 K
Thermal Expansion Coefficient	-0.1×10^{-6} K^{-1}
Sizing Level	1.30%
Filament Diameter	4.97369 μm
Electric Resistance	1.5 $\Omega.cm$

Table 2-2: *Typical Tenax IMS65 24K fiber properties [6]*

2.2. Resin [2]

The matrix holds the fibers in their proper position, protects the fibers from abrasion, transfers loads between fibers, and provides interlaminar shear strength. A properly chosen matrix also provides resistance to heat, chemicals and moisture; it has a high strain-to-failure; and it cures at as low a temperature as possible and yet has a long pot or out-time life and is not toxic. The most prevalent thermoset resins used for composite matrices are polyesters, vinyl esters, epoxies, bismaleimides, polyimides and phenolics.

Epoxy resin matrices are high performance matrix systems for primarily continuous fiber composites. They can be used at temperatures up to 120-135 ^{0}C. Moreover, they have better high temperature performance than polyesters and vinyl esters.

Matrices for polymeric composites can be either thermosets or thermoplastics. Thermoset resins usually consist of a resin (e.g., epoxy) and a compatible curing agent. When the two are initially mixed they form a low-viscosity liquid that cures as a result of either internally generated (exothermic) or externally applied heat. The curing reaction forms a series of cross-links between the molecular chains so that one large molecular network is formed, resulting in an intractable solid that cannot be reprocessed on reheating. On the other hand, thermoplastics start as fully reacted high-viscosity materials that do not cross-link on heating. On heating to a

high enough temperature, they either soften or melt, so they can be reprocessed a number of times.

The first consideration in selecting a resin system is the service temperature required for the part. The glass transition temperature (T_g) is a good indicator of the temperature capability of the matrix. For a polymeric material, T_g is the temperature at which it changes from a rigid glassy solid into a softer, semi-flexible material. At this point the polymer structure is still intact but the cross-links are no longer locked in position. A resin should never be used above its T_g unless the service life is very short (e.g., a missile body). A good rule of thumb is to select a resin in which T_g is 10 ^0C higher than the maximum service temperature. Since most polymeric resins absorb moisture, which lowers the T_g, it is not unusual to require that the T_g be as much as 38 ^0C higher than the service temperature. It should be noted that different resins absorb moisture at different rates and the saturation levels can be different; therefore, the specific resin candidate must be evaluated for environmental performance. Most thermoset resins are fairly resistant to solvents and chemicals.

In general, the higher is the temperature performance required, the more brittle and less damage tolerant is the matrix. Toughened thermoset resins are available but are more expensive and their T_g's are typically lower. High-temperature resins are also more costly and more difficult to process. Temperature performance is difficult to quantify because it is dependent on time at temperature, but it is important to thoroughly understand the environment in which the matrix is expected to preform.

Although the fiber selection usually dominates the mechanical properties of the composite, the matrix selection can also influence performance. Some resins wet out and adhere to fibers better than others, forming a chemical and/or mechanical bond that affects the fiber-to-matrix load transfer capability. The matrix can also microcrack during cure or inservice. Resin-rich pockets and brittle resin systems are susceptible to microcracking, especially when the processing temperatures are high and the use temperatures are low, since this condition creates a very large difference in thermal expansion between the fibers and the matrix. Again, toughened resins help in preventing microcracking but often at the expense of elevated temperature performance.

The selection of a matrix material can profoundly affect the processing conditions. The following factors should be considered when selecting a resin matrix:

- ***Pot-life or working-life*:** This is the time period that a matrix has when the handling characteristics remain suitable for the intended use. Typically, pot-life refers to neat

resins (unreinforced) and working life refers to prepregs (reinforced). A long pot-life is desired for processes that use neat resin, such as wet filament winding, resin transfer molding and pultrusion. A short pot-life requires frequent resin bath changes and increased scrapped material. A short pot-life can also negatively affect the quality of the part in a wet process by decreasing fiber wet-out.

- ***Shelf-life:*** This is the length of time a matrix material can be stored for under certain environmental conditions while meeting all performance and handling requirements. Thermoset prepreg materials are generally stored in a freezer and have a 6-12 month shelf life before recertification is required. Thermoset materials, whose part A (resin) and part B (curing agent) are supplied in separate containers; generally have longer (~2 years) shelf lives at room temperature. Although not as reactive as a prepreg, viscosity and chemical changes occur over time. Refrigeration slows down the process and extends the shelf life.
- ***Viscosity:*** The viscosity of an uncured resin can be described as its resistance to flow. It is measured in terms of flow, using water as the standard, which has a viscosity of 1 cP (centipoises). Viscosity requirements depend on the process but, typically, the lower the viscosity the easier it is to process and the better the wetability of the matrix to fiber. As a resin is heated, the viscosity initially drops and then rises as the chemical reactions proceed until it sets up or gels. For wet processing of thermosets, typically viscosities of less than 1000 cP are preferred. A thermoset is typically considered gelled when it reaches a viscosity of 100 000 cP.
- ***Cure time:*** For thermoset resins, the cure time is the time it takes for the cross-linking reactions to take place. Typically, higher-T_g resins require longer cure times. Epoxies generally have cure times of 2-6 h at elevated temperatures. A post-cure may not be required for some epoxies, polyesters and vinyl esters; therefore, elimination of postcure requirements should be evaluated as a way to decrease processing costs. Higher-T_g resins, such as bismaleimides and polyimides, require longer cure cycles and post-cures. Post-curing further develops higher-temperature mechanical properties and improves the T_g of the matrix for some epoxies, bismaleimides and polyimides. Very short cure times are desired for some processes, such as compression molding and pultrusion. Cure temperatures can range from 120 ^0C to 180 ^0C for epoxies.

PRISM™ EP2400 [7], which was used in this study, is a single part, 180 ^0C curing, and toughened liquid epoxy resin system offering simple and flexible processing with the damage tolerance required for composite primary structure.

PRISM EP2400 has an optimized low viscosity/temperature profile allowing injections at temperatures from $70\,^{0}C$ without the need for excessive heating of resin transfer pipework or high injection pressures. After injection, the resin viscosity decreases to below 20 cP, helping to ensure full fiber wetting.

PRISM EP2400 offers a dry T_g (storage modulus intercept) of 179 ^{0}C and an exceptional wet T_g of 163 ^{0}C following a two-hour cure at 180 ^{0}C.

Features and Benefits of this resin system are as follows:

- One-part toughened resin system specifically developed for ease of processing primary aircraft structures
- Suitable for processing via RTM (Resin Transfer Molding), VaRTM (Vacuum Assisted Resin Transfer Molding), CAPRI (Controlled Atmospheric Pressure Resin Infusion)
- Two-hour 180 ^{0}C cure giving service temperature of >120 ^{0}C
- Exceptional "wet" T_g of 163 ^{0}C
- Injectable at 70 ^{0}C
- Wide processing window; 10 hours at <300 cP at 100 ^{0}C
- <100 cP initial injection viscosity
- Minimum viscosity of 20 cP at 120 ^{0}C
- Excellent compression strength and damage tolerance
- Compliance with FAR "Federal Aviation Regulations"/JAR "Joint Aviation Regulations" Flammability, Smoke and Toxicity
- High strain enhances fatigue and microcrack resistance
- Shelf-life >12 months at -18 ^{0}C and out-life >28 days at 22 ^{0}C
- Low reactivity; No special shipping requirements

The suggested applications are primary structure applications requiring superior toughness, low viscosity and extended pot-life

- Stringer Stiffened Box Covers
- Fuselage and Window Frames
- Pressure Bulkheads
- Passenger and Cargo Door Structures
- Engine Containment Cases
- Hinge/Brackets/Fittings

Property	Specimen Conditioning	Value
Cured Resin Density, g/cm^{-3}	Room Temperature, Dry	1.24
Tensile Strength, MPa	Room Temperature, Dry	95
Tensile Modulus, GPa	Room Temperature, Dry	3.4
Tensile Strain, %	Room Temperature, Dry	7.2
Flexural Strength, MPa	Room Temperature, Dry	164
Flexural Modulus, GPa	Room Temperature, Dry	3.6
Strain Energy Release, $G_{IC}, J\ m^{-2}$	Room Temperature, Dry	279
Fracture Toughness, $MPa\ m^{1/2}$	Room Temperature, Dry	0.96
CTE, $\times 10^{-6}\ C^{-1}$	Room Temperature, Dry	60.5
Dry T_g, ^0C	Room Temperature, Dry	179
Wet T_g, ^0C	Wet, 48 Hour Water Boil	163

Table 2-3: *Neat resin characteristics [7]*

2.3. Manufacturing process

As it was mentioned previously, after the dry automated fiber placement the preforms of the two panels were injected by vacuum infusion with autoclave. The manufacturing processes of ATL and AFP were described in chapter 1.

Dry Automated Fiber Placement (DAFP) is an adaptation of prepreg AFP, using dry tapes instead of slit prepreg tapes:

- Several suppliers now offer dry fiber tapes with suitable binders, designed to be used on current AFP machines to create dry preforms. These dry tapes are analogous to slit prepreg tape, but with no resin. There is a small amount of binder powder on the tape surface to hold the dry tapes together with the application of heat and pressure.
- Preforms are produced using many passes of narrow bands of dry tape that are consolidated as it is placed, just like AFP.
- Resin is later infused to the preform using **V**acuum **A**ssisted **R**esin **I**nfusion **M**olding **(VARIM)**.
- Conceptually DAFP is very similar to AFP, using the same basic equipment and design practices.

Figure 2-7: *DAFP using AFP with dry fiber tapes at NLR. (Source: www.nlr.nl)*

The VARIM is a technique that uses vacuum pressure to drive resin into a laminate. Materials are laid dry into the mold and the vacuum is applied before resin is introduced. Once a complete vacuum is achieved, resin is literally sucked into the laminate via carefully placed tubing. This process is aided by an assortment of supplies and materials.

In a typical hand lay-up, reinforcements are laid into a mold and manually wet out using brushes, rollers, or through other means. An improvement on that method is to use a vacuum bag to suck excess resin out of the laminate. Vacuum bagging greatly improves the fiber-to-resin ratio, and results in a stronger and lighter product.

Vacuum infusion provides a number of improvements over traditionally vacuum bagged parts. These benefits include:

- Better fiber-to-resin ratio
- Less wasted resin
- Very consistent resin usage
- Unlimited set-up time
- Cleaner process

Vacuum infusion offers a better fiber-to-resin ratio than vacuum bagging. A typical hand lay-up usually results in excess of 100% fabric weight by resin. Resin alone is very brittle, so any excess will actually weaken the part. Vacuum bagging can reduce this number significantly; however, it is still not ideal and can lead to additional problems.

While vacuum bagging certainly improves on the hand lay-up, there is still a hand lay-up involved. Because of this, the laminate will always begin in an oversaturated state. Vacuum pressure will remove much of the excess resin, but the amount removed still depends on a variety of variables including reinforcement, resin, time factors, and others.

Vacuum infusion takes a different approach, in that a vacuum is drawn while the materials are still dry. From that point, resin is infused using vacuum pressure. Rather than starting with excess and drawing resin out, vacuum infusion starts with none and pushes resin in. Ideally, any excess resin that is introduced will eventually be sucked out into the vacuum line. As a result, only the minimum amount of resin is introduced. This lowers weight, increases strength, and maximizes the properties of fiber and resin. Parts constructed using vacuum infusion can approach prepreg levels of resin content.

Due to the nature of vacuum infusion, resin usage becomes very predictable. While a standard lay-up varies in resin content due to the human variable, vacuum infusion is remarkably consistent. Even when creating a large product, resin usage will be predictably similar upon repeated attempts. This results in less wasted resin, and more importantly, less wasted money.

Vacuum infusion provides another valuable benefit: time. A frequent problem that can arise in vacuum bagging is the time factor. Many resins have a pot-life of about 30 minutes, though there are certainly some that offer work times of up to 2 hours. Even so, that time limit is extremely critical in vacuum bagging applications. Large projects can easily approach the 2 hour mark, and even small, seemingly simple projects can quickly turn frantic when a pesky leak in the vacuum seal cannot be found. Also, depending on when the bag is applied, the amount of resin removed can vary from part to part.

Vacuum infusion, however, offers unlimited set-up time. Because the vacuum is applied while reinforcements are still dry, there is no resin clock to work against. After the bag is applied, leaks can be patiently sought out. If something is not sitting properly, simply release vacuum and readjust. No time constraints are introduced until it is decided that it is time to infuse the resin. Until that moment, changes can be made again and again.

Finally, vacuum infusion is a much cleaner process. There are no brushes or rollers, and therefore no splashing or spattering. No one will be required to hover over an open mold, saturating a laminate by hand, trying not to drip on himself. In addition, there are less resin fumes to contend with. Because the only fumes radiate from the resin reservoir, they are somewhat containable. Vacuum infusion process provides a cleaner, safer, and friendlier work environment, though it is still important to work in a well ventilated area and wear a respirator and other appropriate safety equipment.

Like any laminating process, vacuum infusion process is not without its drawbacks. When attempting infusion for the first time, it is important to keep the following ideas in mind.

- Complicated set-up
- Easy to ruin a part
- Trial and error

Though set-up is time-limit free, it is somewhat more complicated. Vacuum bagging requires the placement of only the vacuum tubing. Vacuum infusion requires not only vacuum tubes but resin inlets as well, not to mention in-bag extensions of these tubes. Placement of these vacuum and resin lines varies from part to part, and there is no one way to set them up. These considerations must be evaluated prior to lay-up, or else the part could be ruined.

This leads into the next pitfall; it is very easy to destroy a part. Typically, once infusion begins, there is little that can be done to correct any errors. For example, if a leak were to occur, even the smallest amount of air introduced could be potentially fatal to a part. It would probably result in resin pooling, undersaturation, or even a complete stoppage of resin flow. Though there are certainly some cases where problems can be corrected, it should not be expected. The best protection from disaster is careful planning.

Due to the complexity and ease of error, vacuum infusion should be viewed as a trial-and-error process. The best mindset to have when attempting vacuum infusion for the first time is that a few parts (or more than a few) will be ruined before getting it right. The trick is to carefully document each attempt in order to learn from each trial. Keep track of the resin flow rates. Determine where the resin is reluctant to go and find a way to get it there. Even the smallest modifications can yield drastically different results. Practice with small quantities and inexpensive materials before undertaking full-scale projects. The key is learning from mistakes. This is especially the case when working with larger projects requiring multiple vacuum and resin lines. In a manufacturing environment, it is recommended that at least 6 months are set aside for testing and preparation. [8]

As indicated earlier, VARIM is a composite manufacturing process to produce high-quality large-scale components. In this process, dry preform fabrics are placed in an open mould and a plastic vacuum bag is placed on the top of the mould. The one-sided mould is connected with a resin source and a vacuum pump. The liquid resin infuses into the reinforcing fibers thanks to the vacuum drawn through the mould. Curing and de-moulding steps follow the impregnation process to finish the product. The main steps of the process are:

1. A dry fabric or preform and accompanying materials such as release films, peel plies are laid on tool surface.
2. The preform is sealed with a vacuum bag and the air is evacuated by a vacuum pump.
3. Liquid resin with hardener from an external reservoir is drawn into the component by vacuum.
4. The liquid resin with hardener is infused into the preform until complete impregnation.
5. Curing and de-moulding steps follow the impregnation to finish the product. [9]

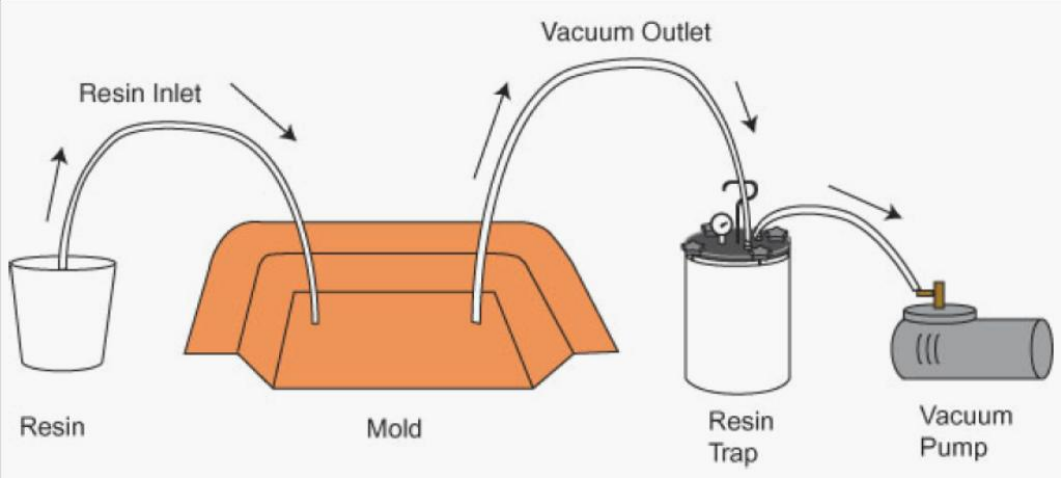

Figure 2-8: *General sequence of events that comprises vacuum infusion. [8]*

Figure 2-9 shows the schematic of VARIM process. In the VARIM process, the preform is loaded in the mould and resin is infused under vacuum. The impregnated preform is then cured in an autoclave. During cure an external pressure is applied in order to achieve required fiber volume fraction and better compaction, especially at cocured joints and thicker regions. [10]

The growing use of complex composite parts combined with the desire for structural integration has made it increasingly more difficult for aerospace manufacturers to build parts using cost-effective automated tape lay-up and advanced fiber placement. Resin infusion offers the potential for weight and cost savings through lower part counts and the elimination of many post-manufacturing processes. Current high-performance, injectable resin systems suitable for

primary structure applications are very limited. Not anymore. Introducing PRISM® EP2400 resin infusion system.

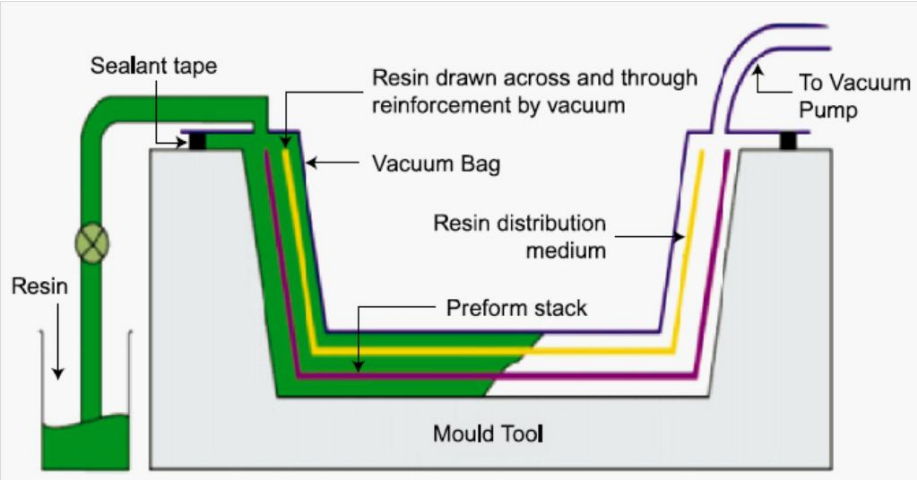

Figure 2-9: *Schematic of VARIM process. [10]*

This unique, one-part toughened epoxy system represents a step forward in resin infusion capability, delivering primary structure level performance without limiting reinforcement or processing type. With PRISM EP2400 resin, manufacturers no longer face trade-offs between performance and processing; they get resin infusion without compromise.

Reasons for choosing PRISM EP2400 resin infusion system:

- High Mechanical Toughness: Meets aerospace performance requirements for primary structure applications
- Single Part System: Simplifies manufacturing process reducing quality concerns
- Low Injection Viscosity: Compatible with all major infusion processes and textile configurations enabling manufacturing flexibility and design/weight optimization
- Extended Pot Life: Enables manufacture of large complex integrated structures that reduce part count and save weight
- Low Reactivity: No transportation restrictions resulting in lower shipping costs
- Low Cure Temperature: Suitable for out-of-autoclave processing lowering capital, tooling and manufacturing costs [11]

2.4. References

1. Baker A, Dutton S, Kelly D. Composite materials for aircraft structures. 2nd edition. American Institute of Aeronautics & Astronautics; 2004.
2. Campbell FC. Chapter 2 - Fibers and reinforcements: The string that provides the strength, In Manufacturing Processes for Advanced Composites. Elsevier Science, Amsterdam; 2003. p. 39-62.
3. Shindo A. Polyacrylonitrile (PAN)-Based Carbon Fibers, In Comprehensive Composite Materials, Volume 1. Elsevier, Cambridge; 2000.
4. Diefendorfe RJ. Pitch Precursor Carbon Fibers, In Comprehensive Composite Materials, Volume 1. Elsevier, Cambridge; 2000.
5. David A. Advances in UHM Carbon Fibers. SAMPE Journal. March/April 1987.
6. TENAX®- E IMS65 E23 24K 830tex Data Sheet. Toho Tenax America, Inc.
7. PRISM™ EP2400 RESIN SYSTEM Technical Data Sheet. Cytec Engineered Materials, Inc.
8. Vacuum Infusion – The Equipment and Process of Resin Infusion. http://www.composites.ugent.be/home_made_composites/documentation/FibreGlast_Vacuum_infusion_process.pdf
9. Goren A, Atas C. Manufacturing of polymer matrix composites using vacuum assisted resin infusion molding. Materials Science and Engineering 2008; 34(2): 117-20.
10. Kundan Kumar Verma, BL Dinesh, Kailash Singh, Kotresh M Gaddikeri, V Srinivasa, Ramesh Kumar, Ramesh Sundaram. Development of Vacuum Enhanced Resin Infusion Technology (VERITy) Process for Manufacturing of Primary Aircraft Structures. Journal of the Indian Institute of Science 2013; 93(4).
11. PRISM™ EP2400 Resin Infusion System Data Sheet. Cytec Engineered Materials, Inc.

3

Experimental Techniques and Planning

3.1. Sample preparation for mechanical characterization

3.1.1. CANAL QI plate

As it was previously mentioned the dimensions of the CANAL QI panel were 400*400*3.2 *mm*. As long as the geometrical specifications were concerned, the location of the intentional defects (gap and overlap) in the second 0^0 ply was depicted in Figure 2-1. Moreover, NLR has also provided the ultrasonic C-scan inspection of the plate since the plate contained a relatively large spot which can be located using the reported C-scan image. A brief description of the ultrasonic inspection concepts and definitions as well as the reported C-scan images of the CANAL QI will be presented in the next section.

3.1.1.1. Ultrasonic C-scan inspection [1]

Ultrasonic Inspection: Ultrasonic inspection (conventional) is a primary technique for the inspection of composite and metal aircraft components. The technique makes use of high-frequency sound waves that are introduced into the material of interest. Because air is not an adequate transmitting medium for ultrasonic waves, a coupling medium such as water or gel has to be used between the transducer and the material. At interfaces of different materials a part of the sound beam is reflected and the other part is transmitted into the material. The reflection and transmission signals can be displayed and analyzed on a scope. Depending on the material condition attenuation of the sound beam due to the microstructure or local defects can occur. The time difference between reflected signals gives information about the "defect" depth in the material.

Immersion Technique: The test specimen is herewith totally immersed in water. The water provides a good and constant coupling between transducer and the test specimen. This technique provides the highest sensitivity of inspection because of the possibility of applying focused transducers. (Figure 3-1)

Pulse Echo Method (PE): One transducer acts both as transmitter and receiver. With this method the ultrasonic signal transmits the full specimen thickness twice. When a defect is present in the material (most cases) there will be a reduction of the backwall amplitude. (Figure 3-2)

Attenuation Measurement: Hereby the amplitude differences of the transmitted signal are monitored and an electronic gate is positioned on this signal. Attenuation measurements can be performed during pulse echo-, reflector plate- and through transmission methods.

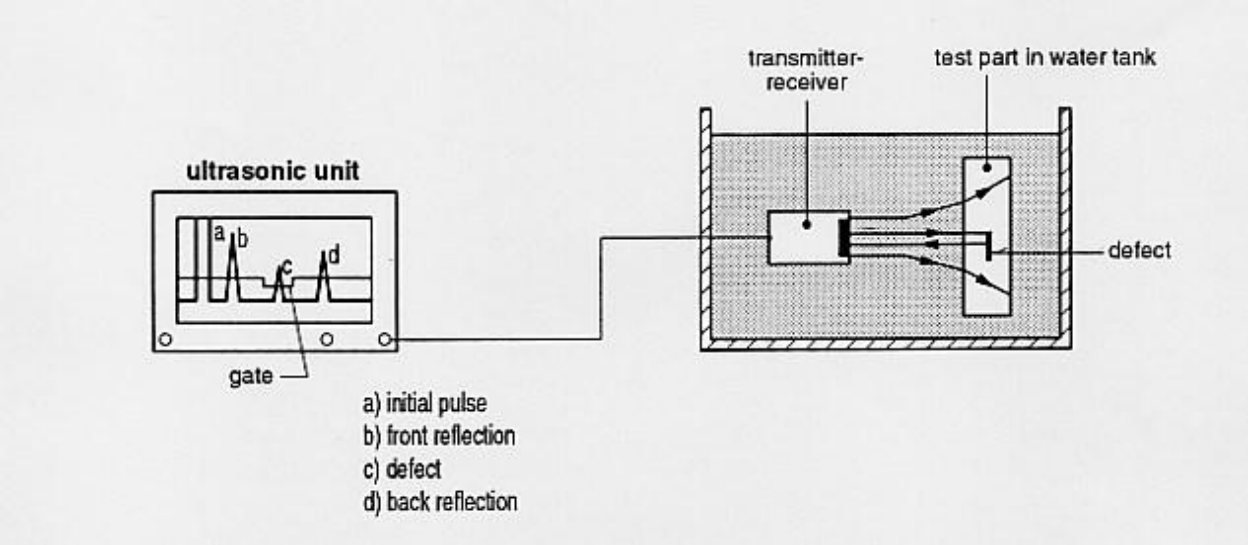

Figure 3-1: *Immersion technique [1]*

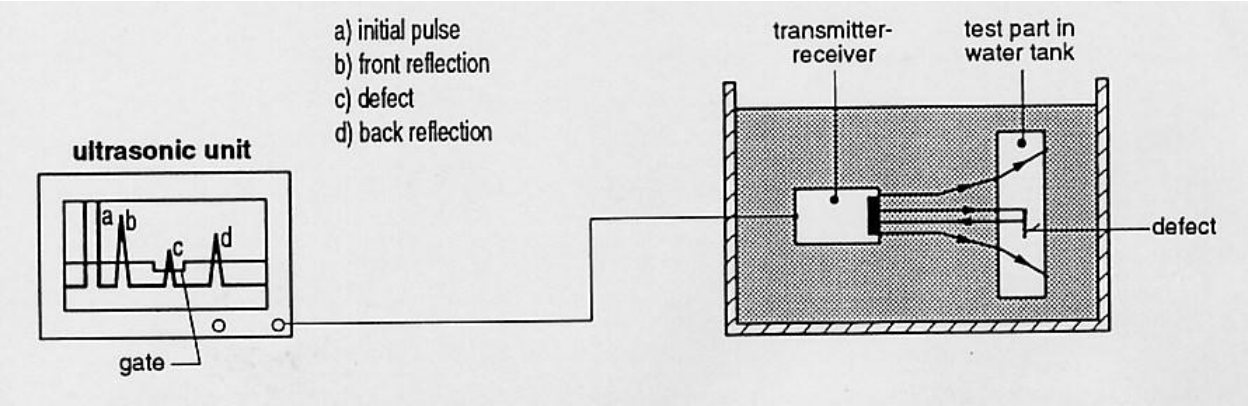

Figure 3-2: *Pulse-Echo method [1]*

Reflection Measurement: Hereby the amplitude of the reflected signal(s) is monitored. The electronic gate is placed between the **F**ront **R**eflection (**FR**) and the **B**ackwall **R**eflection (**BR**). At areas of sound material there are only some "noise" signals but no relevant reflection signals within the gate. When a defect is present in the material there will be a clear reflection peak, which triggers the gate. The reflection measurements are less suitable to determine the overall quality of the material but give good results for local defect detection, characterisation and sizing.

Reflector Plate Method (DTT): One transducer acts both as transmitter and receiver. Behind the specimen of interest a glass plate is positioned. The reflection signal received from the glass plate can be clearly separated from the signals of the specimen. This results in an easier set-up and transducer optimisation. With this method a double through transmission of the ultrasound beam is established. This results in a full coverage throughout the thickness of the specimen, including flaws close to the front or back surface. (Figure 3-3)

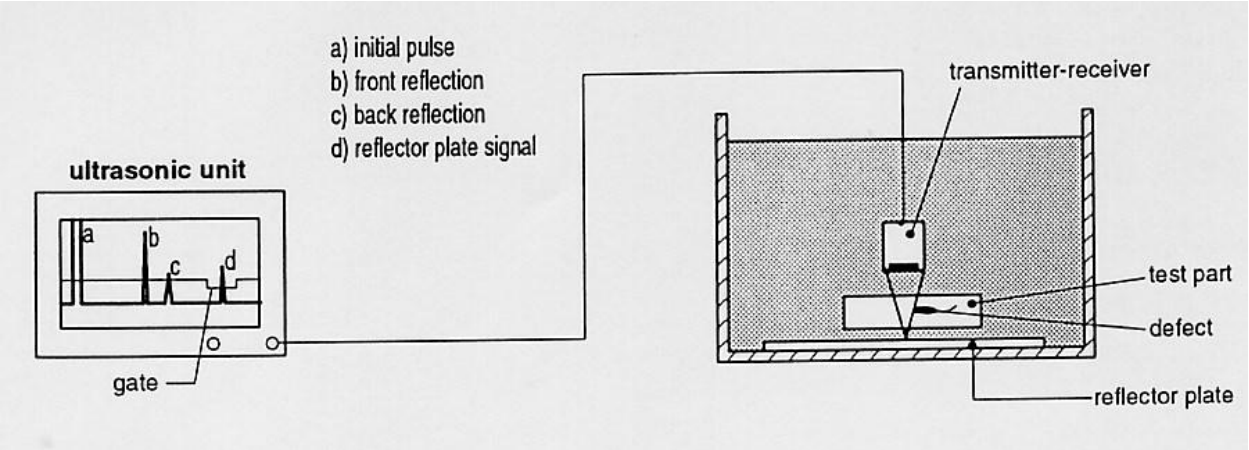

Figure 3-3: *Reflector plate method [1]*

Inspection Parameters:

Frequency	5 *MHz*
Focus of ultrasonic beam	RP
Reflector plate distance	4 *mm*
Index	1 *mm*
Scan size	420*420 *mm*
Scan speed	250 (*mm/s*)

Table 3-1: *Inspection parameters [1]*

Reporting: The following inspection results were supplied:

- A 16-colour attenuation C-scan plot (reflector plate); (Figure 3-4)
- A 16-colour reflection C-scan plot ; (Figure 3-5)
- Cross-sectional scan (B-scans); (Figure 3-6).

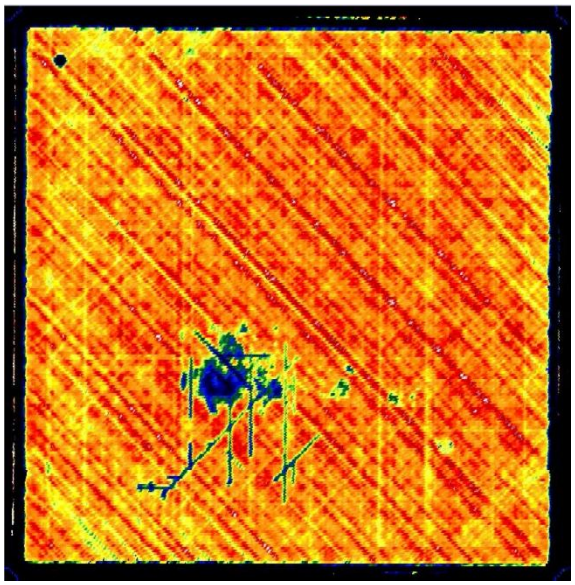

Figure 3-4: *Attenuation reflector plate C-scan [1]*

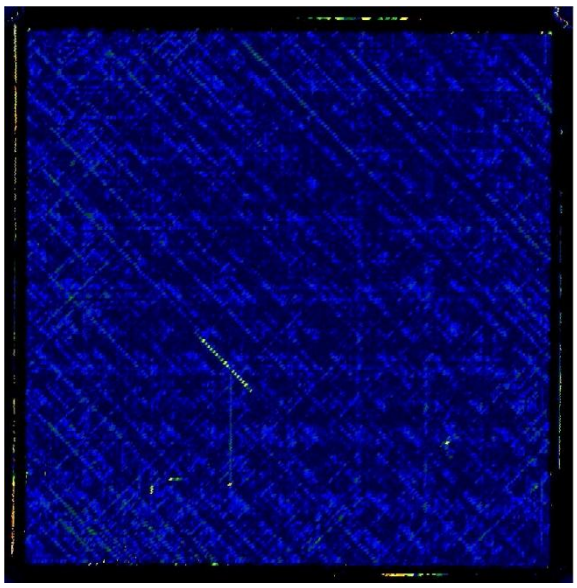

Figure 3-5: *Reflection C-scan [1]*

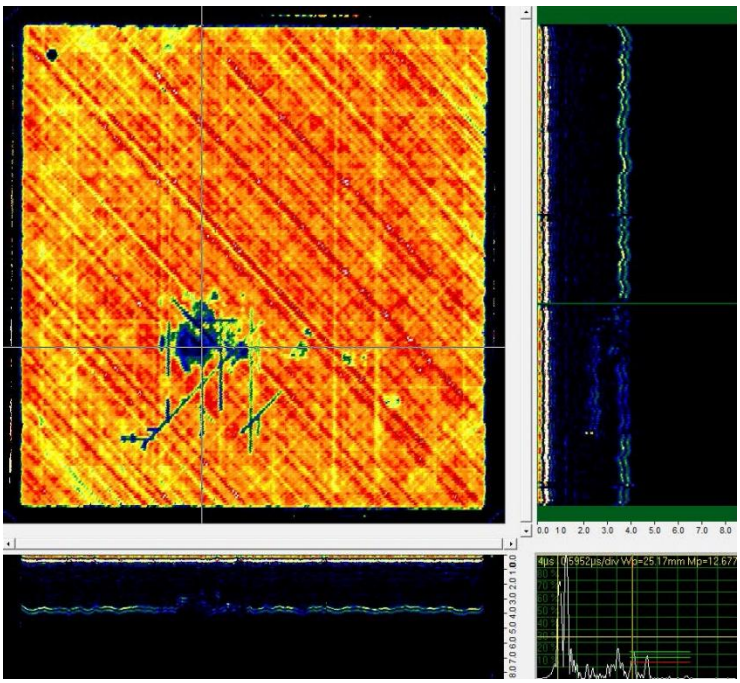

Figure 3-6: *Volume scan with cross sectional views [1]*

3.1.1.2. Specimen planning on the plate

In order to achieve the maximum number of tensile and compressive specimens, several considerations were taken into account. First, regarding the ASTM D3039 / D3039M-14 [2] and ASTM D3410 / D3410M-03 [3], the recommended tensile specimen size for the balanced and symmetric fiber orientation is 250 *mm* (overall length) by 25 *mm* (width) and the recommended compressive specimen size for the specially orthotropic fiber orientation is 140-155 *mm* (overall length) by 25 *mm* (width). (Figures 3-8,3-9)

The spot area was determined as a rectangle which covers all the defects (dark blue regions in Figure 3-4) using the C-scan image and an appropriate scale in Auto CAD. This area must be excluded from the specimens plan as far as possible. (Figure 3-7)

Regarding the facts that the priority was having maximum number of tensile specimens (with and without defects) and we must have specimens in both 0^0 and 90^0 directions and gap and overlap strips were placed along the 0^0 direction, the optimum specimen plan drawing is depicted in Figure 3-7. The test coupons were sawn with a water-cooled diamond saw.

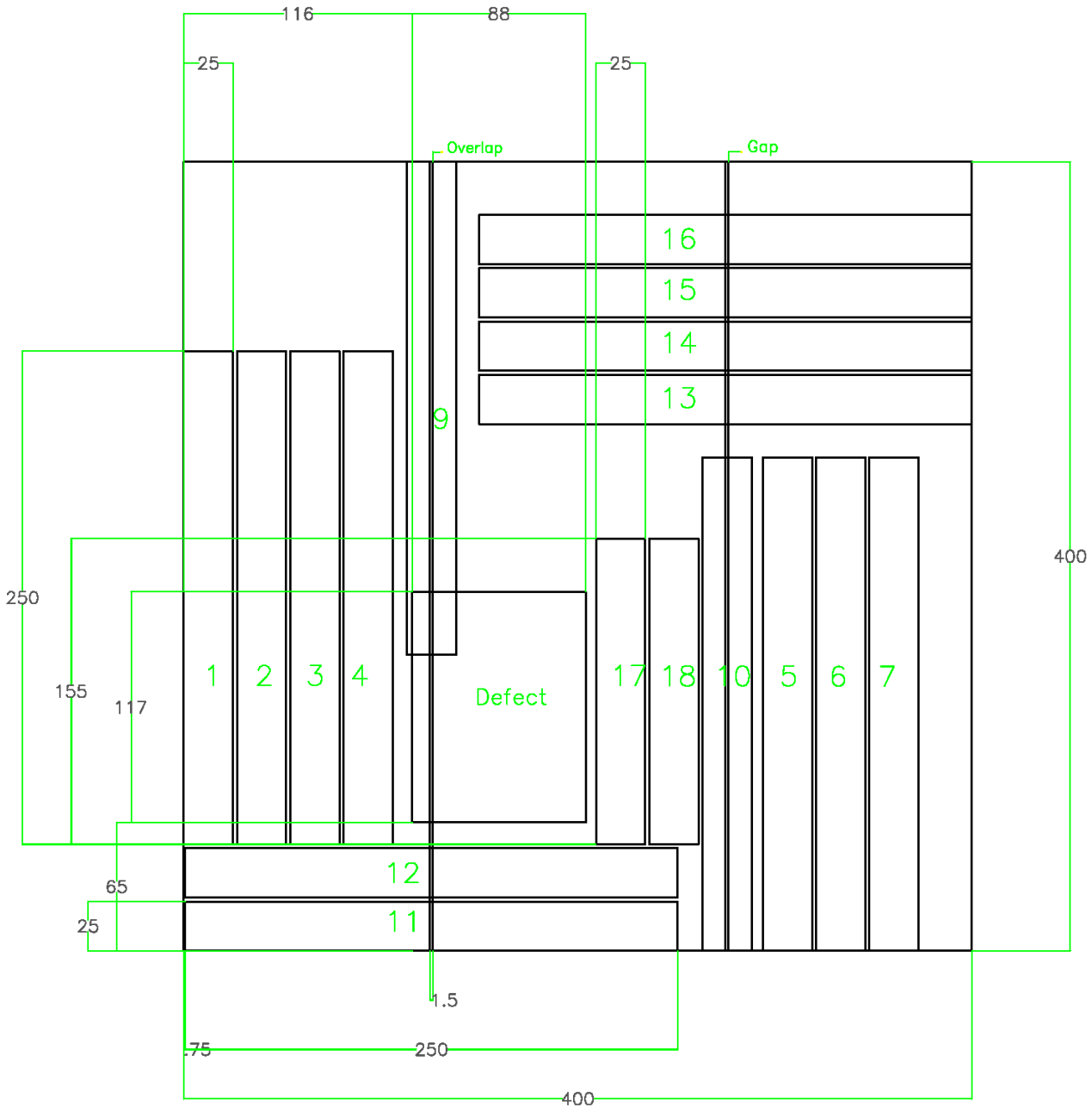

Figure 3-7: *Drawing of the specimens plan for CANAL QI panel; all dimensions are in mm.*

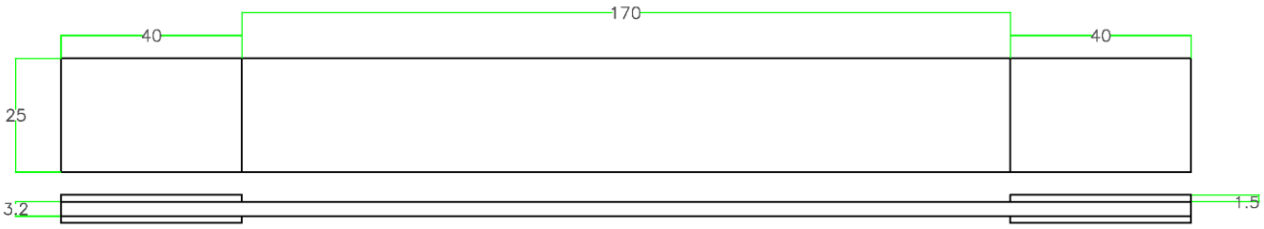

Figure 3-8: *Tensile specimen dimensions (CANAL QI), all dimensions are in mm.*

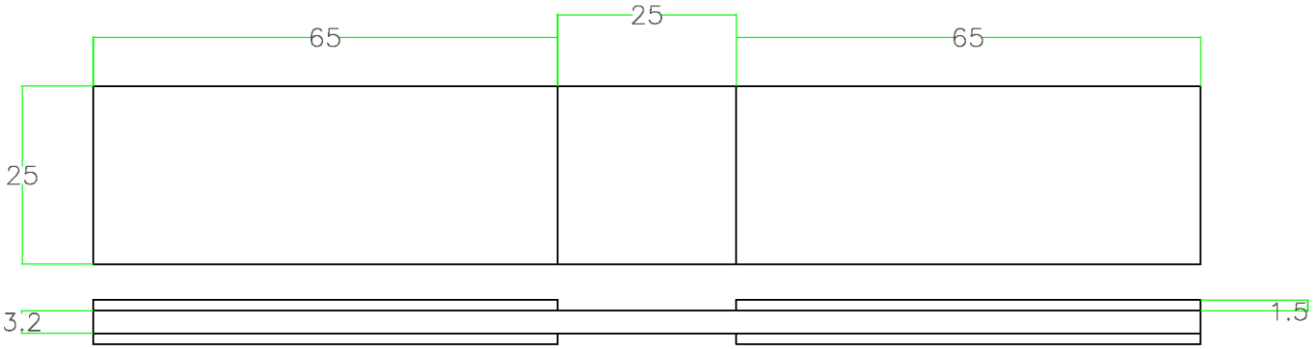

Figure 3-9: *Compressive specimen dimensions (CANAL QI), all dimensions are in mm.*

Specimen Number	Specimen Orientation	Defects (if any)
1	0^0	Without defects
2	0^0	Without defects
3	0^0	Without defects
4	0^0	Without defects
5	0^0	Without defects
6	0^0	Without defects
7	0^0	Without defects
9	0^0	With overlap
10	0^0	With gap
11	90^0	With overlap
12	90^0	With overlap
13	90^0	With gap
14	90^0	With gap
15	90^0	With gap
16	90^0	With gap

Table 3-2: *Tensile specimens list; CANAL QI panel*

Specimen Number	Specimen Orientation	Defects (if any)
17	0^0	Without defects
18	0^0	Without defects

Table 3-3: *Compressive specimens list; CANAL QI panel*

3.1.1.3. Adding end tabs

When performing quasi-static tests on fiber-reinforced materials, the use of end tabs is often necessary to prevent clamp failure. The ASTM D3039 / D3039M-14 [2], states that tabs are not required, but the need to use tabs should be determined by the experiments themselves. If acceptable failure modes occur with reasonable frequency, then there is no need to change the gripping method. However, if grips are required, the standard gives some recommendations considering the tab dimensions. Summarized, a continuous glass fiber-reinforced polymer with $[+45^{0}/-45^{0}]_{ns}$ laminate configuration should be used, the length should be about 50 *mm* and the bevel angle should be 7 or 90 degrees, depending on the stacking sequence of the test material. When gripping the test specimen, the grip should overhang the beveled portion of the tab by approximately 10 to 15 *mm*. It is also stated that 'sufficient' lateral pressure should be used to avoid slipping.

Therefore, for the tensile specimens end tabs with the dimensions of 40*25*1.5 *mm* with the bevel angle of 90^0 were used. Moreover, according to the ASTM D3410 / D3410M-03 [3], for the compressive specimens end tabs with the dimensions of 65*25*1.5 *mm* with the bevel angle of 90^0 were used.

The end tab material was glass fiber-reinforced epoxy matrix with $[+45^{0}/-45^{0}]_{ns}$ laminate configuration. End tabs were attached to the specimen using the epoxy glue. Adhesive selection is no less important than tabbing material selection. The adhesive must be able to transmit the required load into the test specimen through shear and must withstand the compressive force applied by the grips. Furthermore, the adhesive must be suitable for use at the desired test temperature, and the required cure temperature of the adhesive must not exceed the acceptable exposure temperature for both the test panel and the tabbing material. The adhesive layer may be designed to further minimize stress concentrations at the tab terminations. Other desirable features include workability, storage requirements (out-time), and be readily available at a reasonable cost.

After adding end tabs, in order to cure the adhesive specimens were put in the autoclave press with the temperature set at 100 ^{0}C. Specimens were put under hot press for one hour. Subsequently, specimens were ready to be tested.

3.1.2. AP-PLY plate

As it was previously mentioned the dimensions of the AP-PLY panel were 300*300*2 *mm*. No intentional and process defects were reported by NLR.

3.1.2.1. Specimen planning on the plate

Regarding the facts that the priority was having maximum number of tensile specimens and we must have tensile specimens in both 0^0 and 90^0 directions, the optimum specimen plan drawing is depicted in Figure 3-10. The test coupons were sawn with a water-cooled diamond saw. Since we needed enough space to clamp the plate under the diamond saw during cutting, it was not possible to cut 8 tensile specimens (4 in 0^0 direction and 4 in 90^0 direction) with the standard dimensions of 25*250 *mm* mentioned in ASTM D3039 / D3039M-14 [2]. Therefore, it was decided to reduce the gauge length from 170 *mm* to 150 *mm* and consequently having tensile specimens of 230 *mm* of overall length. Due to this clamping issue, we could not have compressive specimens in 90^0 direction and we decided to cut more compressive specimens in 90^0 direction instead.

3.1.2.2. Adding end tabs

Due to the geometric limitations and the space needed to clamp the plate under the diamond saw, the overall length of the tensile samples were reduced to 230 *mm* compared with CANAL QI samples and consequently the gauge length was reduced to 150 *mm*. All the specifications of the end tabs are the same as those of the CANAL QI samples.

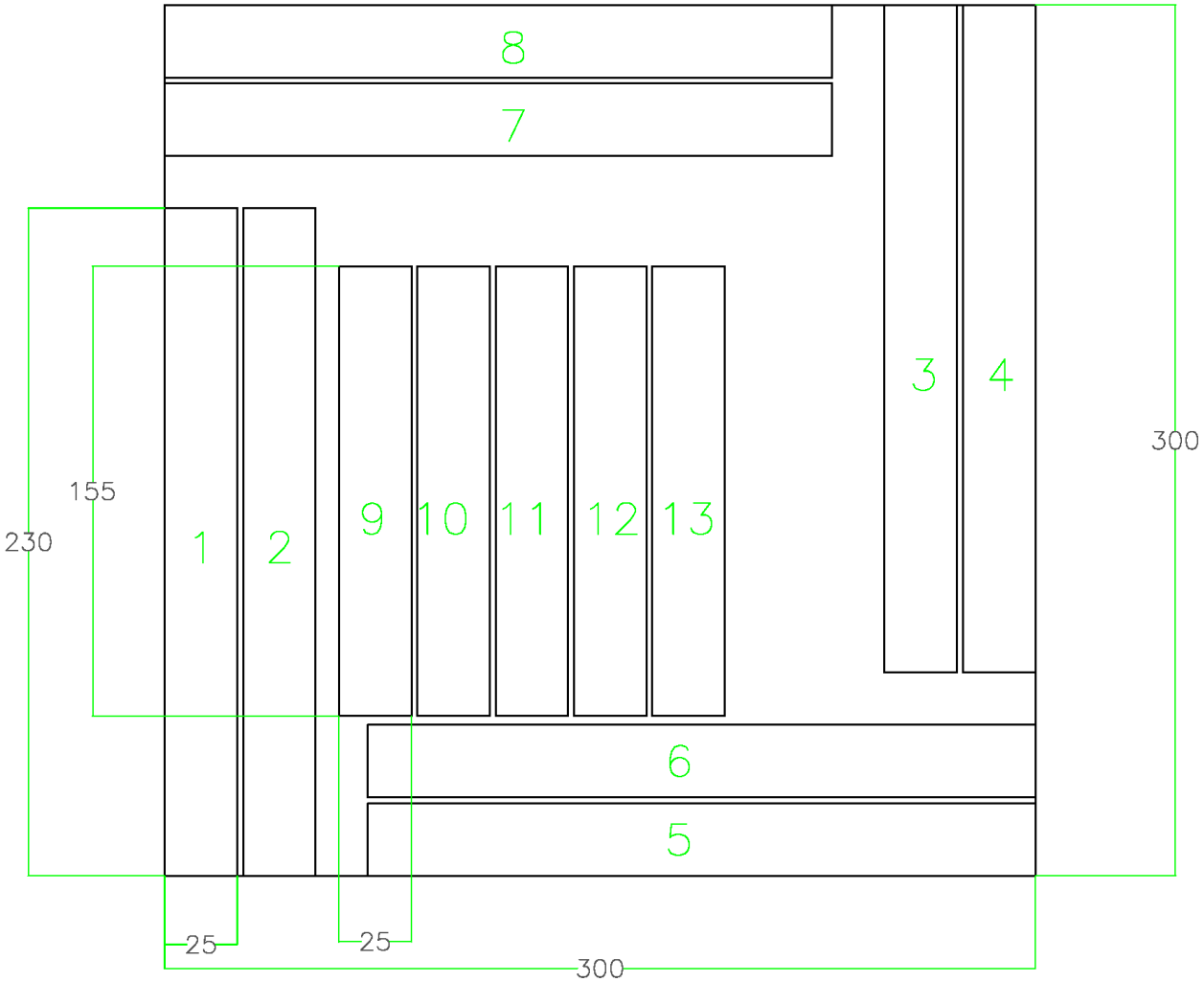

Figure 3-10: *Drawing of the specimens plan for AP-PLY panel; all dimensions are in mm.*

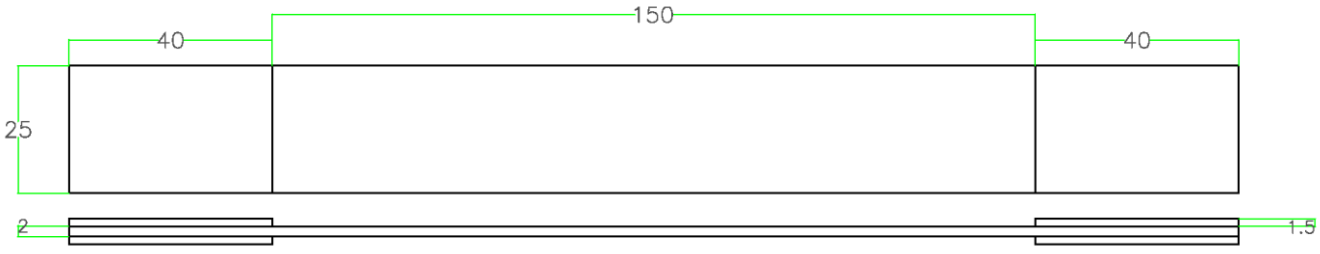

Figure 3-11: *Tensile specimen dimensions (AP-PLY), all dimensions are in mm.*

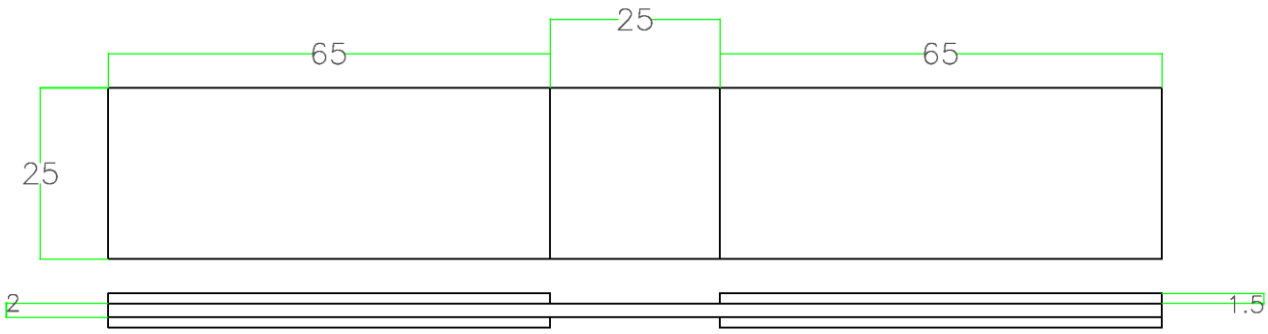

Figure 3-12: *Compressive specimen dimensions (AP-PLY), all dimensions are in mm.*

Specimen Number	Specimen Orientation	Defects (if any)
1	90^0	Without defects
2	90^0	Without defects
3	90^0	Without defects
4	90^0	Without defects
5	0^0	Without defects
6	0^0	Without defects
7	0^0	Without defects
8	0^0	Without defects

Table 3-4: *Tensile specimens list; AP-PLY panel*

Specimen Number	Specimen Orientation	Defects (if any)
9	90^0	Without defects
10	90^0	Without defects
11	90^0	Without defects
12	90^0	Without defects
13	90^0	Without defects

Table 3-5: *Compressive specimens list; AP-PLY panel*

3.2. Quasi-static tensile test

Tension testing under ASTM D3039 / D3039M-14 [2] has become a well-accepted standard for testing of high-modulus and high-strength composites. The standard defines a tabbed, straight, flat specimen of high aspect ratio. The tabs, with a beveled entry into the test section, are added to the specimen to allow for substantial clamping forces at the grip. These tabs are typically made

from G-10 glass/epoxy and are adhered using a high-strength epoxy. In general, this standard is appropriate for almost any composite form.

Both mechanical and hydraulic grips may be used for ASTM D3039 / D3039M-14 [2]. The clamping pressure on wedge-type mechanical grips is generally proportional to the applied loads. This reduces the potential for crushing the specimen in the tabbed area. Hydraulic grips add more versatility, since the clamping force is independent of the load, although care must be taken to avoid specimen crushing. [5]

Tensile test is one of the most common testing procedures: it ensures well-controlled plane stress - plane strain state of sample and the set up allows to follow damage phenomena with acoustic emission and to monitor deformation of the sample with full field optical surface strain measurement (during the test the strain field in the center region of the sample is reasonably homogeneous). Samples were tested on a standard Instron 4505 machine in displacement control and with a load cell of 100 *kN*. Samples were loaded at a constant rate of 2 *mm/min*. Since the machine has finite (not infinite) stiffness, during testing of a material with a high stiffness one would expect a significant deviation of the registered distance between the clamps from the actual distance. This may result in inaccurate strain values. To avoid this we use *strain mapping* measurements on the surface of a sample. When making stress-strain graphs, stress values from the Instron machine are used in combination with strain values from the *strain mapping*.

The Instron 4500 series of universal testing instruments are electro-mechanical devices employing the latest technology in order to provide the optimum in materials testing systems. The Instron 4505 (Figure 3-13) is comprised of a floor mounted frame and a front panel connected to a tower (microprocessor based control console). The 4505 frame has a maximum load capacity of 100 *kN*. Specimens to be tested are secured between grips and fixtures. Tension and compression testing can be carried out either above or below the moving crosshead. Other specifications of Instron 4505 are listed in Table 3-6. [4]

After stress-strain curves are plotted, modulus can be calculated by selecting the same range of data in the beginning period for all the samples. Stress-strain curves of the samples tested till final fracture also provide the ultimate stress σ_{ult} as the maximum stress level reached during the test and the ultimate strain ε_{ult} as the strain corresponding to σ_{ult}. Poisson's ratio (ϑ_{12}) was determined by calculating longitudinal (ε_{11}) and transverse (ε_{22}) strains using the Digital Image Correlation (DIC) which will be discussed later.

The tests were performed up to different strain levels: initial strain (ε_1) when first microcracks appear; intermediate strain (ε_2) for different failure mode transitions; ultimate strain (ε_{ult}). These levels were determined from **A**coustic **E**mission **(AE)** measurements as will be discussed further.

Testing speed range	0.001 – 1000 *mm/min*
Maximum crosshead travel	1336 *mm*
Clearance between columns	575 *mm*
Machine compliance	125 *kN/mm* (Nominal axial stiffness)
Test modes available	Tension, Compression, Flexure, Shear, and Reverse Stress cyclic testing

Table 3-6: *Instron 4505 specifications [4]*

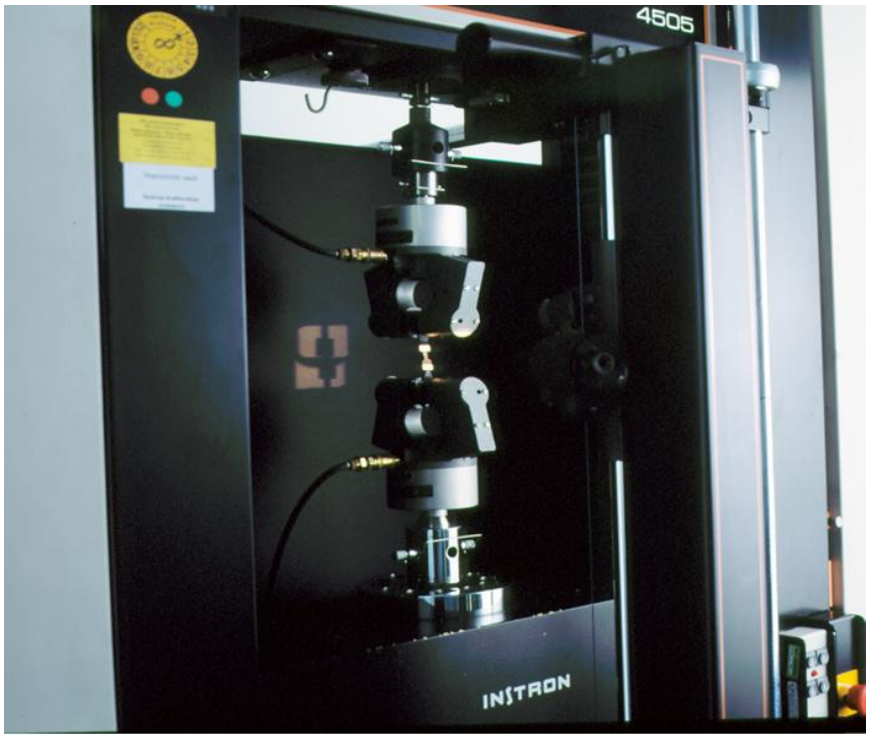

Figure 3-13: *Instron 4505. (Source: www.instron.us)*

3.3. Quasi-static compression test

Compression testing of composites has received a considerable amount of attention and has proven to be more complicated than tension testing [6]. Since the compressive strength (in the

fiber direction) is generally lower than the tensile strength, and since there is a desire to use a larger fraction of the ultimate load capacity, there is a need to characterize the compressive strength accurately. Because relatively thin specimens are desired, buckling may occur if the unsupported length is too large. Therefore, in general, most compression tests are designed such that the specimen fails due to true compressive failure of the material and not due to Euler buckling. There are three methods [3,7,8] of introducing compressive loading into the specimen: via shear through end tabs (ASTM D 3410), by direct end loading (ASTM D 695), and by bending of a composite sandwich panel (ASTM D 5476). The latter is rarely used since the specimens are typically large, difficult to manufacture, and expensive. Additionally, there is a concern that prevails among the composites community that the compressive failure strength may be artificially elevated by the presence of the core being bonded along the entire face sheet.

Introducing the compressive load via shear through end tabs is similar to the way loads are introduced in tensile tests, except that the loads are of opposite sign and therefore the wedges in the grips are inverted. Testing of thin specimens may lead to buckling if the slenderness ratio is too high.

Samples were tested on a standard Instron 4505 machine (specifications are mentioned in Table 3-6) in displacement control and with a load cell of 250 *kN*. Samples were loaded at a constant rate of 1.5 *mm/min*. Since the machine has finite (not infinite) stiffness, during testing of a material with a high stiffness one would expect a significant deviation of the registered distance between the clamps from the actual distance. This may result in inaccurate strain values. To avoid this we use *strain mapping* measurements on the surface of a sample and on both sides using two cameras. When making stress-strain graphs, stress values from the Instron machine are used in combination with strain values from the *strain mapping*.

Compression tests were performed based on ASTM D3410/D3410M-03 [3]. After stress-strain curves were plotted, elasticity modulus was calculated by selecting the same range of data in the beginning period for all the samples. Stress-strain curves also provide the ultimate compressive strength $\sigma_{ult,comp}$ as the minimum stress level reached during the test and the ultimate compressive strain $\varepsilon_{ult,comp}$ as the strain corresponding to $\sigma_{ult,comp}$. Poisson's ratio (ϑ_{12}) was determined by calculating longitudinal (ε_{11}) and transverse (ε_{22}) strains using the DIC which will be discussed later. All the samples were tested till final fracture without AE and only with DIC (strain mapping), since our purpose is to investigate the compressive mechanical properties.

3.4. Full field strain mapping by Digital Image Correlation (DIC)

The term Digital Image Correlation refers to the class of noncontacting methods that acquire images of an object, store images in digital form, and perform image analysis to extract full-field shape and deformation measurements. Within the broad field of image analysis, digital image correlation (i.e., matching is performed using image correlation metrics) is generally considered a subset of digital image registration techniques. Digital image correlation (i.e., matching) has been performed with many types of object-based patterns, including lines, grids, dots, and random arrays. One of the most commonly used approaches employs random patterns and compares subregions throughout the image to obtain a full field of measurements.

One of the earliest papers to propose the use of computer-based image acquisition and deformation measurements in material systems was by **Peters** and **Ranson** in 1981 [9]. Using the fact that changes in images can be described by the same continuum concepts that govern the deformation of small areas on a surface; an approach was proposed to relate measurable image deformations to object deformations. For use in the field of experimental mechanics, these original concepts have been refined and incorporated into numerical algorithms to extract object deformations from an image sequence. The resulting algorithms and software have been used successfully to obtain surface deformations in a wide variety of applications. The historical development of DIC is summarized in Table 3-7.

1981	For 2D, through-thickness averaged, ultra-sound applications, **Ranson** and **Peters** [9] proposed an approach for conversion of digitized ultra-sound images into estimates for local surface displacements. Initial experiments completed in 1985 by recording and comparing laser speckle images obtained from strained metallic specimens.
1983	**Sutton** and **Wolters** [10]; **Cheng** and **Sutton** [11] developed non-linear least squares approach using first-order gradients in a matching function to obtain local displacements quickly and accurately.
1985	**TC Chu et al.** [12] using a DAGE MTI analog camera to record images of a speckle pattern at 8 bits, demonstrated conclusively that the method could be used to measure deformations (translations, rotations, and strain)
1993	**Luo**, **Chao**, and **Sutton** [13] developed a simple stereo-vision system and verified the ability to make local strain and deformation measurements in cracked material.
1999	**Bay et al.** [14] extended 2D and 3D methods to volumetric images and performed DIC on volumetric elements on the interior of the material. The

	technique requires a tomographic imaging facility and is limited to those materials providing sufficient contrast during tomographic imaging.

Table 3-7: *Historical developments of DIC technique.*

Today, the technology is being used to measure **(a)** 3-D surface shape and deformations using a variety of illumination sources for a wide range of material systems, with size scales ranging from tens of meters to the microscale, **(b)** 2-D surface deformations at the nanoscale using atomic force microscopy and scanning electron microscopy, **(c)** interior deformation measurements through volumetric imaging of biological and porous materials using technology such as computer aided tomography, and **(d)** dynamic/impact behavior of materials using high speed camera systems. With increasing processor speed and improved computational software, the method has been extended for use in areas such as automatic inspection, system control, and real-time structural assessment.

For image-correlation-based measurement purposes, modern scientific-grade digital cameras are generally used to **(a)** obtain high-quality images on the sensor plane, **(b)** perform onboard digitization of the intensity at each sensor location, and **(c)** transfer the digital data to a storage location. [15]

Digital Image Correlation is based on the maximization of a correlation coefficient that is determined by examining pixel intensity array subsets on two or more corresponding images and extracting the deformation mapping function that relates the images (Figure 3-14). An iterative approach is used to minimize the 2D correlation coefficient by using non-linear optimization techniques. The cross correlation coefficient r_{ij} is defined as:

$$r_{ij} = 1 - \frac{\sum_i \sum_j \left[F(x_i, y_j) - \bar{F}\right]\left[G(x_i^*, y_j^*) - \bar{G}\right]}{\sqrt{\sum_i \sum_j \left[F(x_i, y_j) - \bar{F}\right]^2 \sum_i \sum_j \left[G(x_i^*, y_j^*) - \bar{G}\right]^2}}$$

where $F(x_i, y_j)$ is the pixel intensity or the gray scale value at a point (x_i, y_j) in the undeformed image, $G(x_i^*, y_j^*)$ is the gray scale value at a point (x_i^*, y_j^*) in the deformed image. (Figure 3-14a) $\bar{F}$ and $\bar{G}$ are mean values of the intensity matrices F and G. The coordinates or grid points (x_i, y_j) and (x_i^*, y_j^*) are related by the deformation that occurs between the two images. If the motion is perpendicular to the optical axis of the camera, then the relation between (x_i, y_j) and (x_i^*, y_j^*) can be approximated by a 2D affine transformation such as:

$$x^* = x + u + \frac{\partial u}{\partial x}\Delta x + \frac{\partial u}{\partial y}\Delta y$$

$$y^* = y + v + \frac{\partial v}{\partial x}\Delta x + \frac{\partial v}{\partial y}\Delta y$$

In the current case, u and v are translations of the center of the sub-image in the X and Y directions, respectively. The distances from the center of the sub-image to the point (x,y) are denoted by Δx and Δy. Therefore, the correlation coefficient r_{ij} is a function of displacement components (u, v) and displacement gradients: [16]

$$\frac{\partial u}{\partial x}, \frac{\partial u}{\partial y}, \frac{\partial v}{\partial x}, \frac{\partial v}{\partial y}$$

The **S**quared **S**um of **D**ifferences **(SSD)** is just one of many optimization criteria that can be used for template matching, and indeed, the digital image correlation method owes its name to the use of the normalized cross-correlation criterion [15]. After Image matching, strains, rotations, displacement rate, etc. are calculated by means of Continuum Solid Mechanics models.

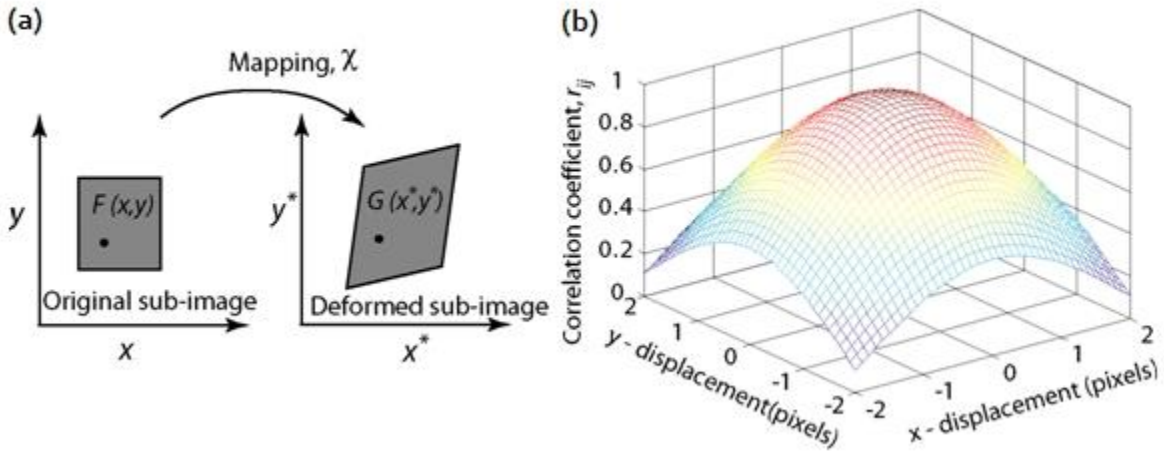

Figure 3-14: *Basic concept of DIC. [16]*

Strain mapping is a system of measuring surface strain by means of correlation of subsequent digital images taken of a sample before, after, and during loading. Image analysis software can be used consistently and repeatedly to obtain surface deformations with **(a)** an accuracy of ±0.01 pixels or better for in-plane displacement components and **(b)** point-to-point accuracy of ±100 με for the in-plane surface strains. This accuracy has been established using the VIC-2D software (LIMESS Messtechnik und Software Gmbh) based on a wide range of experimental and simulation studies. This accuracy is achievable even when the object is subjected to in-plane rigid-body rotations from $+180^0$ to -180^0 and arbitrary amounts of in-plane rigid-body

translations since these motions do not corrupt the strain measurements. Parameters of the strain mapping device (LIMESS Q-400-2D) are reported in Table 3-8.

Cameras	12 bit grayscale 1392*1040 pixels - fire wire
Lens focus distance	16 mm
Measurement rate	15 $frames/s$
Exposure time	40 μs to 15 min
Measurement field size	10 mm^2 to 100 m^2
Accuracy for displacements	0.01 Pixel
Accuracy for strain	200 µstrains (=0.02%)
Software	LIMESS Vic2D
Correlation subset	21 Pixels
Correlation step	5 Pixels
Strain window	5 Pixels

Table 3-8: *Technical specifications of LIMESS Q-400-2D. (Source: www.limess.com)*

To achieve a reference pattern, which can be identified by the image correlation software, a centric rectangular region on the surface of the samples was first painted with a black and white random speckle. As the tensile and compressive tests proceeded, the LIMESS camera took subsequent images every 500ms (Figure 3-15). The software determined the local displacement and strain components by comparing each picture with the initial image corresponding to the undeformed state. Changes in the displacement of the speckle dots can be identified to quantify the deformation of the sample, as this speckle pattern deforms with the sample under loading. This allows the software to produce a strain field. The strain mapping system is used also as an optical extensometer, with a precision of about 0.01% strain: local strain components can be averaged over an area of interest (normally a square zone of the sample) to have global strain components.

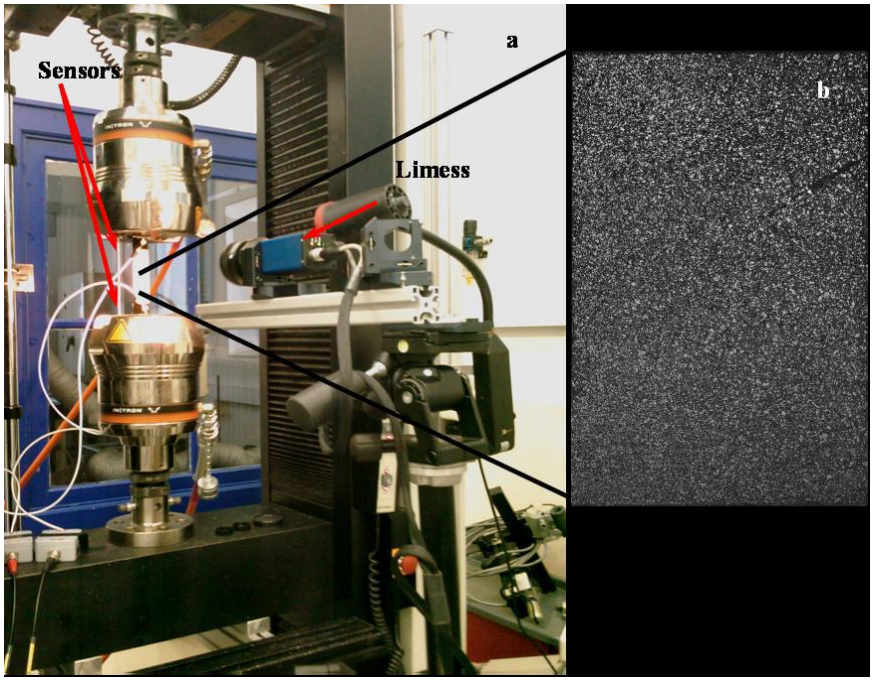

Figure 3-15: (a) *Set-up of the strain mapping system, acoustic emission sensors, and Instron machine;* ***(b)*** *Black and white speckles on the sample.*

3.5. Acoustic Emission (AE)

Acoustic emission testing (AE) has become a recognized nondestructive test (NDT) method commonly used to detect and locate faults in mechanically loaded structures and components. AE can provide comprehensive information on the origination of a discontinuity (flaw) in a stressed component and also provides information pertaining to the development of this flaw as the component is subjected to continuous or repetitive stress.

Discontinuities in components release energy as the component is subjected to mechanical loading or stress. This energy travels in the form of high-frequency stress waves. These waves or oscillations are received with the use of sensors (transducers) that in turn convert the energy into a voltage. This voltage is electronically amplified and with the use of timing circuits is further processed as AE signal data. Analysis of the collected data comprises the characterization of the received voltage (signals) according to their source location, voltage intensity and frequency content.

The major difference between the AE method of NDT and the other NDT methods is that this method is passive, whereas the others, in a sense, are for the most part active. With ultrasonic,

radiographic or the other NDT methods, the source of information is derived by creating some effect in or on the material by external application of energy or compounds. AE relies on energy that is initiated within the component or material under test.

The origination of the method is attributed to J. Kaiser in the 1950s. The sounds emitted during crack growth became an issue of scientific investigation during the 1960s. As the technology developed, AE became accepted as a NDT method. Separating the useful information from the background noise was the challenge to the instrument developers. Maturity of the technology led to the ongoing investigation into the micromechanical processes that produce these emissions within various materials. The historical development of the AE technique is summarized in Table 3-9.

1928	**Abram Joffe** observed the noise generated by deformation process of Salt and Zinc crystals. " The Physics of Crystals" [17]
1936	**Friedrich Forster** and **Erich Scheil** conducted experiments that measured small voltage and resistance variations caused by sudden strain movements caused by martensitic transformations.
1948	**Warren P. Mason**, **Herbert J. McSkimin** and **William Shockley** suggested measuring AE to observe the moving dislocations by means of the stress waves they generated.
1950	**D.J. Millard** performed twinning experiments on single crystal wires of cadmium. The twinning was detected using a rochelle salt transducer.
1950	**Josef Kaiser** used tensile tests to determine the characteristics of AE in engineering materials. The result from his investigation was the observation of the irreversibility phenomenon that now bears his name, the Kaiser Effect.
1954	**Bradford H. Schofield** investigated the application of AE in the field of materials engineering and the source of AE. He concluded that AE is mainly a volume effect and not a surface effect.
1957	**Clement A. Tatro**, after performing extensive laboratory studies, suggested using AE as a method to study the problems of behavior of engineering metals. He also foresaw the use of AE as an NDT method.
1961	The first AE test in USA was conducted in the Aerospace industry to verify the integrity of the Polaris rocket motor for the U.S Navy. After noticing audible sounds during hydrostatic testing it was decided to test the rocket using contact microphones, a tape recorder and sound level analysis equipment.
1963	**Dunegan** suggested the use of AE for examination of high pressure vessels.

1965	At the National Reactor Testing Station, researchers were looking for a NDT method for detecting the loss of coolant in a nuclear reactor. Acoustic Emission was applied successfully.
1969	**Dunegan** founded the first company that specializes in the production of AE equipment.
Today	AE Non-Destructive Testing used practically in all industries around the world for different types of structures and materials.

Table 3-10: *Historical developments of AE technique.*

The technology involves the use of ultrasonic sensors (20 *kHz*–1 *MHz*) that listen for the sounds of material and structural failure. Acoustic emission frequencies are usually in the range of 150–300 *kHz*, which is above the frequency of audible sound. Crack growth can be detected and located with the use of this technology. AE technology is also becoming commonly applicable to nondestructive testing for structural integrity of structures made from composite materials [24].

AE is a continuous testing process that does not require the disassembly of a structure or sample for testing, since it is carried out on an entire structure under its in-service loading [18,19,20]. If defects are present, AE sensors will detect the defect propagation as the acoustic emissions produced travel away from the source [21]. These AE signals are collected by stationary piezoelectric sensors and subsequently measured and amplified (Figure 3-16) [20-23]. Piezoelectric sensors are critical to AET because they convert the mechanical AE waves into electrical voltages. The electrical signals generated by the piezoelectric sensors are output to equipment for processing and later displayed for interpretation [20-23]. As the discontinuity or defect approaches a critical size, the AE count rate will increase to warn of an impending instability and failure. (The rate at which acoustic emissions are produced is directly related to the microstructure and deformation mode of the material.)

When setting up an acoustic emissions test, material loading is crucial. AET is typically performed on in-use structures using an array of sensors, since the in-service loading applies enough stress to cause the already present defects to propagate [22]. Performing AET on in-service structures requires the addition of sensors only; these sensors do not cause the defect to propagate since they apply no additional external stimuli. Simply put, AET detects already present defects, defects that would grow whether AE sensors were connected to the structure or not. For this reason, AET is considered a NDT method.

An important feature of AET is its irreversibility; if the material is loaded to a given stress level, unloaded, and reloaded, no emissions will be noted upon reloading unless the previous loading

has been exceeded or further damage is present. Until this point the material will behave elastically. This behavior is referred to as the Kaiser Effect and directly results from the fact that AE are closely related to plastic deformation and fracture. This irreversibility has important practical considerations and is the reason AET detects already present flaws [18,19].

AE testing exploits the Kaiser Effect as a means for determining the stress at which damage occurs. As damage accumulates from continued use, the Kaiser Effect breaks down (i.e., acoustic emissions are detected at lower stress levels). This is known as the Felicity Effect. The Felicity Ratio is used to denote the percentage of full loading (or maximum previous loading) at which the first AE are detected.

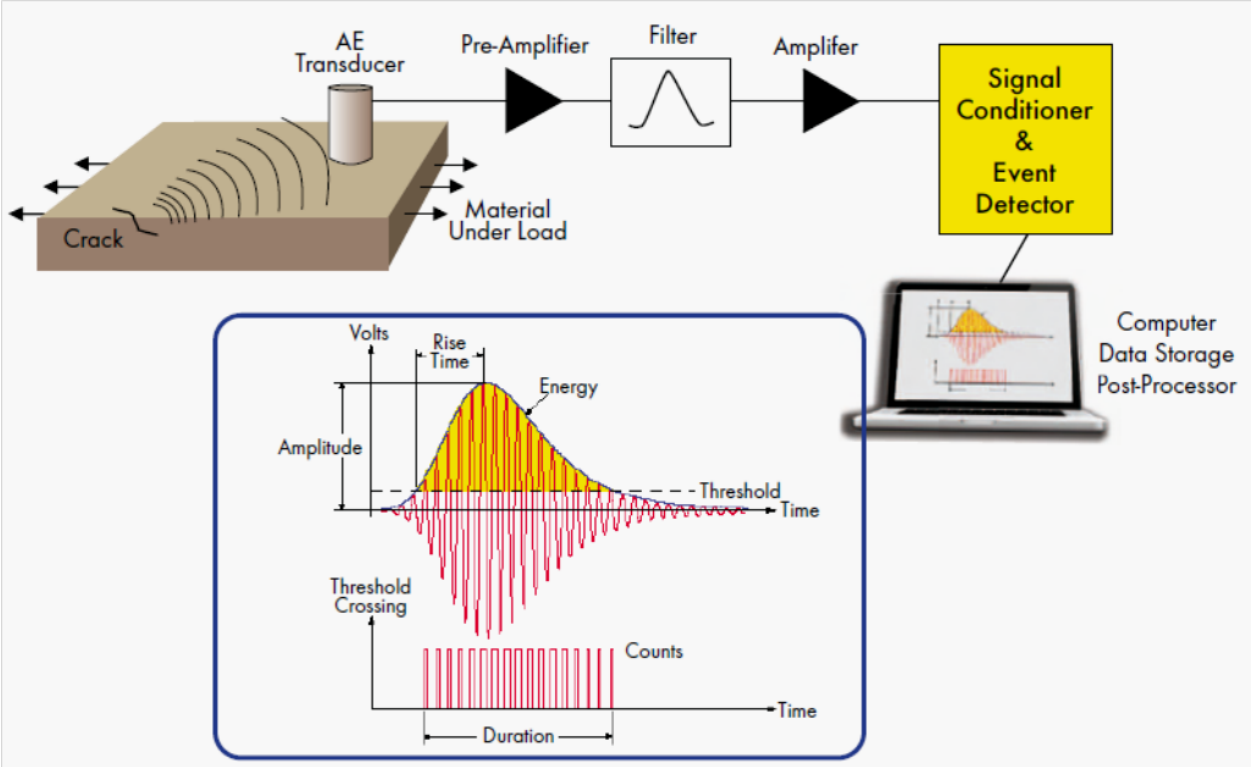

Figure 3-16: *A basic AE test set-up and sample output.*

The definition of the AE features which are depicted in Figure 3-16 are as follows:

- **Amplitude** in AE testing refers to the largest voltage present in the signal waveform. It is one of the most important measures of signal height. It is fundamental because for a signal to be detected, its amplitude must exceed a predetermined threshold. Amplitude is usually measured in dB, a decibel scale running from 0 to 100. 0 dB is defined as amplitude of one microvolt at the preamplifier input.

- **Duration** is the length of time from the first threshold crossing to the last, measured in microseconds. The relationship between duration and amplitude tells the user about the signal's shape.
- **Energy** is the area under the voltage–time envelope. This is another important measure of signal size and is the most widely used measure of AE activity. When a structure produces many emissions in response to loading, the energies of the individual signals can be added to produce a total amplitude. Of all the techniques that have been used to describe emission quantity in a single number, this has been the most successful.
- **Counts** are the comparator output pulses corresponding to the threshold crossings. A single hit may provide only a few counts or it might furnish hundreds of counts, depending on the size and shape of the signal. For the electronics designer, this is the easiest measurement to make, and in the early years of AE, "counts" were the most common way to describe and report AE quantities. During the 1980s, energy replaced counts as the preferred measure of AE activity. However, counts are still useful for data interpretation; used in conjunction with amplitude or duration, they can give valuable information on signal shape.
- **Rise time** is the time interval from the first threshold crossing to the maximum amplitude. [24]

Due to the sample deformation during the test there is an energy build-up in the material. When the material undergoes permanent deformation such as microcracking, this energy is released in the form of acoustic waves. By registering the waves the growth of damage in the material can be followed. In the present setup of the tensile test, two AE sensors are used that are situated at the boundaries of the gauge length region. In the course of the experiment, the energy of AE events is registered and the dependency "cumulative energy of AE events vs. tensile strain" is produced. Changes of rate of generation of AE events, reflected by the change of slope of the diagram, indicate change in damage mechanisms in the sample, as discussed further in the report. Signals occurred outside of the sensors are filtered out by the AE system (AMSY-5, Vallen Systems Gmbh, Figure 3-17 - see details in Table 3-10) using by a suitable calibration procedure. This procedure had to be repeated for each sample due to the highly anisotropic nature of the constituent materials and the inevitable distance variation of the sensors which had obviously to be placed each time. Since the AE sensors are very sensitive, they have to be removed before the final failure of the sample. This makes it impossible to study the very last stage of damage development. [25]

Software	Vallen AMSY-5
Amplifiers	Vallen AEP4
Amplification	34 *dB*
Discrimination time	0.4 *ms*
Rearm time	3.2 *ms*
Bandwidth	25 *kHz* to 1.6 *MHz*
Sampling rate	5 *MHz*
Sensors	Digital wave B-1025
Sensor diameter	9.3 *mm*

Table 3-10: *Technical specifications of Vallen AMSY-5 [25]*

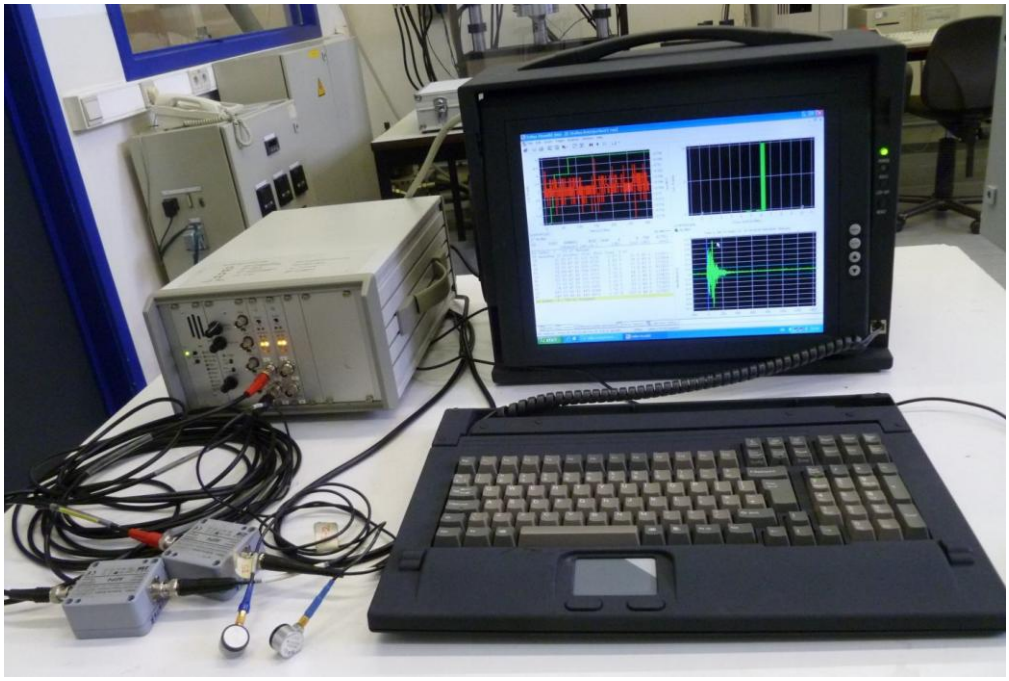

Figure 3-17: *Vallen AMSY-5 at KU Leuven*

3.6. References

1. Ultrasonic C-scan inspection on specimen 4910, Project Number: ST1237-06-WI-004-0-AFB, AV- Structures Testing & Evaluation, National Aerospace Laboratory 'NLR'.
2. ASTM D3039 / D3039M-14. Standard Test Method for Tensile Properties of Polymer Matrix Composite Materials. ASTM International, West Conshohocken, PA; 2014.
3. ASTM D3410 / D3410M-08. Standard Test Method for Compressive Properties of Polymer Matrix Composite Materials with Unsupported Gage Section by Shear Loading. ASTM International, West Conshohocken, PA; 2008.
4. Instron Universal Testing Instruments Instructions – Models 4505 and 4507 Load Frames, Instron Inc.
5. Sharpe WNJ. Springer Handbook of Experimental Solid Mechanics. Springer US; 2008.
6. Adams DF. Mechanical Test Fixtures, In: Manual on Experimental Methods of Mechanical Testing of Composites. Society for Experimental Mechanics. Fairmont, Lilburn; 1998. p. 87–100.
7. ASTM D695-10. Standard Test Method for Compressive Properties of Rigid Plastics. ASTM International, West Conshohocken, PA; 2010.
8. ASTM D5467 / D5467M-97. Standard Test Method for Compressive Properties of Unidirectional Polymer Matrix Composites Using a Sandwich Beam. ASTM International, West Conshohocken, PA; 2010.
9. Peters WH, Ranson WF. Digital imaging techniques in experimental stress analysis. Optical Engineering 1981; 21(3): 427–32.
10. Sutton MA, Wolters WJ, Peters WH, Ranson WF, McNeil SR. Determination of displacements using an improved digital correlation method. Image Vision Computing 1983; 1(3): 133-9.
11. Sutton MA, Cheng M, Peters WH, Chao YJ, McNeil SR. Application of an optimized digital image correlation method to planar deformation analysis. Image Vision Computing 1986; 4(3): 143-50.
12. Chu TC, Ranson WF, Sutton MA, Peters WH. Applications of digital image correlation techniques to experimental mechanics. Experimental Mechanics 1985; 25(3): 232–45.
13. Luo PF, Chao YJ, Sutton MA, Peters WH. Accurate measurement of three-dimensional deformations in deformable and rigid bodies using computer vision. Experimental Mechanics 1993; 33(2): 123- 32.
14. Bay BK, Smith TS, Fyhrie DP, Saad M. Digital volume correlation: Three-dimensional strain mapping using X-ray tomography. Experimental Mechanics 1999; 39(3): 217-26.

15. Sutton MA, Orteu JJ, Shreier HW. Image Correlation for Shape, Motion and Deformation Measurements: Basic Concepts, Theory and Applications. Springer US, 2009.
16. http://en.wikipedia.org/wiki/Digital_image_correlation
17. Joffe AF. The Physics of Crystals. Loeb, 1st edition, 1928, McGraw-Hill Book Company, Inc.
18. Huang M, Jiang L, Liaw PK, Brooks CR, Seeley R, Klarstrom DL. Using Acoustic Emission in Fatigue and Fracture Materials Research. Journal of Materials 1998; 50(11).
19. Pollock AA. Acoustic Emission Inspection. Metals Handbook, Volume 17: Nondestructive Evaluation and Quality Control, ASM International; 1989.
20. Filho PF. Acoustic Emission Testing in Composite Materials. Proceedings from World Conference on Non-Destructive Testing 1992; (13): 40-5.
21. Hellier CJ. Handbook of Nondestructive Evaluation, McGraw-Hill, 2001.
22. Pollock AA. Loading and Stress in Acoustic Emission Testing. Materials Evaluation; March 2004.
23. Filho PF. The Effectiveness of Flaw Detection Caused by Cracking using Acoustic Emission Technique. Proceedings of ECNDT 2006, 9th European Conference on NDT. Berlin, Germany; 2006.
24. Grosse CU, Ohtsu M. Acoustic Emission Testing. Springer US; 2008.
25. AMSY-5 Introduction to AE Testing. Vallen Systems Gmbh, Inc.

4

Quasi-Static Tensile Test Results

4.1. Mechanical tensile properties

As it was previously mentioned, tensile tests were performed based on ASTM D3039 [1]. This test method determines the in-plane tensile properties of polymer matrix composite materials reinforced by high modulus fibers. The composite material forms are limited to continuous fiber or to discontinuous fiber-reinforced composites in which the laminates are balanced and symmetric with respect to the test direction.

The tensile test coupon which is a thin flat strip of material having a constant rectangular cross section is mounted in the grips of a mechanical testing machine and monotonically loaded in tension while recording the force. The ultimate strength of the material can be determined from the maximum force carried before failure. If the coupon strain is monitored with strain or displacement transducers then the stress-strain response of the material can be determined, from which the ultimate tensile strain, tensile modulus of elasticity, and Poisson's ratio can be derived.

This test method is designed to produce tensile property data for material specifications, research and development, quality assurance, and structural design and analysis. Factors that influence the tensile response and should therefore be reported include the following: material, methods of material preparation and lay-up, specimen stacking sequence, specimen preparation, specimen conditioning, environment of testing, specimen alignment and gripping, speed of testing, and volume percent reinforcement. Properties, in the test direction, which may be obtained from this test method, include the following:

- Ultimate tensile strength
- Ultimate tensile strain
- Tensile chord modulus of elasticity
- Poisson's ratio

Along the factors which influence the tensile response, material, methods of material preparation and lay-up, specimen stacking sequence, specimen preparation, and specimen conditioning have

been explained previously. Regarding the test environment, the test temperature was 20 ^{0}C and humidity was 50%. Speed of testing was controlled by constant crosshead speed of 2 mm/min.

Each head of the testing machine shall carry one grip for holding the test specimen so that the direction of force applied to the specimen is coincident with the longitudinal axis of the specimen. The grips shall apply sufficient lateral pressure to prevent slippage between the grip face and the coupon. Since tabs were used the grips should be long enough that they overhang the beveled portion of the tab by approximately 10 to 15 mm. It is highly desirable to use grips that are rotationally self-aligning to minimize bending stresses in the coupon. Furthermore, poor system alignment can be a major contributor to premature failure, to elastic property data scatter, or both. [1]

Volume percent reinforcement (fiber volume fraction) has not been discussed yet in the context. Consequently, the test methods to determine the fiber volume fraction as well as the results for both of the materials are discussed in the next section.

4.1.1. Determination of the fiber content

The fiber volume fraction was measured using the combustion test according to ASTM D3171 standard [2]. The following procedure was adopted:

- Several samples of comparable sizes for each material were prepared according to the dimensions and weight restrictions of the applied standard.
- Each sample was put in a ceramic crucible and they were pre-dried in the oven at 150 ^{0}C overnight (at least for 12 hours).
- The crucible was weighted with and without the sample. Consequently, the weight of the specimen was calculated by subtracting the two values.
- A furnace was preheated till its core was red hot (about 500 ^{0}C)
- A ceramic crucible containing the sample was replaced in the hot furnace
- Burning process steps were done at 400 ^{0}C for different periods of time and after each step the crucible containing the sample was taken out of the furnace, put in a desiccator, allowed to cool to room temperature, and weighed. Considering the fact that after each step a certain amount of matrix was burnt out, therefore the weight of the sample was decreasing continuously.
- Finally the fiber weight fraction was calculated by dividing the weight of the sample after the final step by initial weight of the sample.

- In order to calculate the fiber volume fraction we need the density of the fiber as well as the density of the composite. We already had the fiber density from the fiber data sheet which was mentioned in Table 2-2. The composite density was calculated using "Sartorius Density Determination Kit" at MTM department; KU Leuven. [3] The density of the CANAL QI material was reported to be 1.49 $^{g}/_{cm^3}$ and for the AP-PLY panel 1.5 $^{g}/_{cm^3}$.

$$V_r = \frac{M_f}{M_i} \times 100 \times \frac{\rho_c}{\rho_r} \quad 4\text{-}1$$

M_f: Final mass of the specimen after combustion
M_i: Initial mass of the specimen before combustion
ρ_c: Density of the composite specimen
ρ_r: Density of the fiber

	Mass [g]												
Sample Number	**Sample + CR**	**CR**	**Sample**	**1 2h 400°C**	**2 1h 400°C**	**3 1h 400°C**	**4 3h 400°C**	**5 1h 400°C**	**6 1h 400°C**	**7 1h 400°C**	**8 1h 400°C**	**Fiber Weight Fraction**	**Fiber Volume Fraction [%]**
C1	26.9431	26.2472	0.6959	26.7178	26.7087	26.698	26.6706	26.6669	26.6647	26.6638	26.6629	0.597	50.00
C2	27.4737	26.8231	0.6506	27.2693	27.2597	27.2512	27.2171	27.2141	27.2115	27.2108	27.2099	0.595	49.77
C3	27.0817	26.3124	0.7693	26.8468	26.8334	26.8205	26.7885	26.7863	26.7833	26.7831	26.7823	0.611	51.13
											Average		**50.30**
											Standard Deviation		**0.73**

Table 4-1: *Fiber volume fraction calculation; CANAL QI panel*

	Mass [g]											
Sample Number	**Sample + CR**	**CR**	**Sample**	**1 2h 400°C**	**2 1h 400°C**	**3 1h 400°C**	**4 3h 400°C**	**5 1h 400°C**	**6 1h 400°C**	**7 1h 400°C**	**Fiber Weight Fraction**	**Fiber Volume Fraction [%]**
A1	27.0113	26.6262	0.3851	26.8866	26.8828	26.8763	26.8594	26.8570	26.8568	26.8568	0.599	50.46
A2	26.9058	26.5357	0.3701	26.7873	26.7797	26.7735	26.7598	26.7581	26.7575	26.7575	0.599	50.50
A3	26.7177	26.3163	0.4014	26.5911	26.5834	26.5753	26.5594	26.5570	26.5562	26.5562	0.598	50.36
										Average		**50.44**
										Standard Deviation		**0.07**

Table 4-2: *Fiber volume fraction calculation; AP-PLY panel*

Therefore, the average fiber volume fraction for both CANAL QI and AP-PLY panels are more or less the same, 50.30% for CANAL QI and 50.44% for AP-PLY.

4.1.2. Tensile test planning

Since limited amount of test coupons of each plate were available and the main purpose was to investigate damage development during tensile loading, samples had to be tested until different levels of strain. In this study, we planned to test the samples until two strain levels; first one a bit

more than the threshold strain which was defined as regards to the AE cumulative energy vs. strain curve in order to study the damage initiation and the other one at a higher strain level less than ultimate tensile strain so as to study the damage development during loading.

First, we needed an approximation of the ultimate tensile strain and stress for each of the laminates as well as an approximation of the threshold strain on AE cumulative energy vs. strain curve. Therefore, since CANAL QI laminate was quasi-isotropic, one sample without defects in 0^0 direction (sample 5) was tested till failure with AE sensors which were removed before final rupture and full-field strain registration using DIC. For the AP-PLY panel, one specimen was tested in 0^0 direction (sample 5) and one in 90^0 direction (sample 1) until failure.

Considering: **(a)** amount of available specimens, **(b)** the data derived from the stress vs. strain and AE cumulative energy vs. strain diagrams, and **(c)** the two strain levels which were decided for each of the materials, tensile tests planning were summarized as follows:

Specimen Number	Specimen Orientation	Defects (if any)	Planned Strain/Load
1	0^0	Without defects	1% - 37.3 *kN*
2	0^0	Without defects	1% - 37.3 *kN*
3	0^0	Without defects	1% - 37.3 *kN*
4	0^0	Without defects	0.6% - 22.4 *kN*
5	0^0	Without defects	Till failure
6	0^0	Without defects	0.6% - 22.4 *kN*
7	0^0	Without defects	Reserved
9	0^0	With overlap	1% - 37.3 *kN*
10	0^0	With gap	1% - 37.3 *kN*
11	90^0	With overlap	1% - 37.3 *kN*
12	90^0	With overlap	0.6% - 22.4 *kN*
13	90^0	With gap	0.6% - 22.4 *kN*
14	90^0	With gap	0.6% - 22.4 *kN*
15	90^0	With gap	1% - 37.3 *kN*
16	90^0	With gap	1% - 37.3 *kN*

Table 4-3: *Tensile tests planning; CANAL QI specimens*

Specimen Number	Specimen Orientation	Defects (if any)	Planned Strain/Load
1	90^0	Without defects	Till failure
2	90^0	Without defects	1.2% - 7.45 kN
3	90^0	Without defects	1.2% - 7.45 kN
4	90^0	Without defects	0.8% - 4.97 kN
5	0^0	Without defects	Till failure
6	0^0	Without defects	1.2% - 21.95 kN
7	0^0	Without defects	1.2% - 21.95 kN
8	0^0	Without defects	0.8% - 14.94 kN

Table 4-4: *Tensile tests planning; AP-PLY specimens*

4.1.3. Tensile properties report

Tensile tests were performed on INSTRON 4505 from which the load and displacement were obtained. The displacement of the crosshead can't be used to calculate the strain of the tensile sample, because the tensile apparatus is not infinitely rigid. This would lead to an incorrect (higher) strain. To overcome this problem, the strain was measured using strain mapping as explained in the previous chapter. The Vic2D software gives the strain in the loading direction as a function of load and time. Consequently, tensile stress vs. strain curve was drawn for each sample after the DIC analysis using Vic2D.

From the stress-strain curves of the samples which were tested until fracture, ultimate tensile stresses and strains were attained.

Regarding ASTM 3039, [1] tensile chord modulus of elasticity and Poisson's ratio were derived in the strain interval of 1000 μstrains and 3000 μstrains using the following formulas:

$$E^{chord} = {\Delta\sigma}/{\Delta\varepsilon_l} \qquad 4\text{-}2$$

$$\vartheta = -{\Delta\varepsilon_t}/{\Delta\varepsilon_l} \qquad 4\text{-}3$$

$\boldsymbol{E^{chord}}$: Tensile chord modulus of elasticity; GPa

$\Delta\boldsymbol{\sigma}$: Difference in applied tensile stress between the two strain points which correspond to the previously mentioned strain values

$\Delta\boldsymbol{\varepsilon_l}$: Difference between the two longitudinal strain points (nominally 0.002)

$\boldsymbol{\vartheta}$: Poisson's ratio

$\Delta\boldsymbol{\varepsilon_t}$: Difference in lateral strains between the two longitudinal strain points

Stress vs. strain diagrams, elasticity modulus vs. strain diagrams, longitudinal and transversal strain maps for all the tensile samples will be depicted later in Appendix A.

4.1.3.1. CANAL QI tensile properties summary

A. 0^0 Specimens without defects

Specimen Number	Width (mm)	Thickness (mm)	Cross Section Area (mm^2)	Elasticity Modulus (GPa)	Poisson's Ratio	Maximum Measured Load (kN)	Maximum Measured Strain	Maximum Stress (MPa)	Ultimate Tensile Strength (MPa)	Ultimate Tensile Strain
1	25.07	3.65	91.51	44.50	0.341	37.64	0.0096	411.34	-	-
2	25.05	3.64	91.18	45.20	0.359	37.43	0.0092	410.50	-	-
3	25.08	3.56	89.28	43.61	0.289	37.57	0.0098	420.79	-	-
4	25.05	3.56	89.18	45.56	0.316	23	0.0057	257.91	-	-
5	24.97	3.53	88.14	47.08	0.300	56.57	0.0145	641.80	641.8	1.45%
6	25.07	3.53	88.50	46.52	0.348	22.91	0.0056	258.89	-	-
		Average		45.41	0.3255					
		Standard Deviation		1.277	0.028					

Table 4-5: *Tensile properties summary; CANAL QI; 0^0 specimens without defects*

B. 0^0 Specimen with overlap

Specimen Number	Width (mm)	Thickness (mm)	Cross Section Area (mm^2)	Elasticity Modulus (GPa)	Poisson's Ratio	Maximum Measured Load (kN)	Maximum Measured Strain	Maximum Stress (MPa)
9	25.05	3.55	88.93	44.46	0.323	37.5	0.0096	421.69

Table 4-6: *Tensile properties summary; CANAL QI; 0^0 specimen with overlap*

C. 0^0 Specimen with gap

Specimen Number	Width (mm)	Thickness (mm)	Cross Section Area (mm^2)	Elasticity Modulus (GPa)	Poisson's Ratio	Maximum Measured Load (kN)	Maximum Measured Strain	Maximum Stress (MPa)
10	25.06	3.53	88.46	49.96	0.370	37.62	0.0094	425.27

Table 4-7: *Tensile properties summary; CANAL QI; 0^0 specimen with gap*

D. 90^0 Specimen with overlap

Specimen Number	Width (mm)	Thickness (mm)	Cross Section Area (mm^2)	Elasticity Modulus (GPa)	Poisson's Ratio	Maximum Measured Load (kN)	Maximum Measured Strain	Maximum Stress (MPa)
11	25.12	3.61	91.51	47.26	0.320	37.65	0.0088	415.18
12	25.12	3.58	91.18	46.08	0.279	23.18	0.0058	257.76
			Average	46.67	0.300			

Table 4-8: *Tensile properties summary; CANAL QI; 90^0 specimens with overlap*

E. 90^0 Specimen with gap

Specimen Number	Width (mm)	Thickness (mm)	Cross Section Area (mm^2)	Elasticity Modulus (GPa)	Poisson's Ratio	Maximum Measured Load (kN)	Maximum Measured Strain	Maximum Measured Stress (MPa)
13	25.20	3.59	90.47	45.59	0.261	23.04	0.0059	254.68
14	25.06	3.53	88.46	44.98	0.295	23.03	0.0059	260.34
15	25.04	3.59	89.89	43.89	0.237	37.32	0.0096	415.16
16	25.06	3.56	89.21	45.50	0.236	37.55	0.0093	420.90
		Average		44.99	0.257			
		Standard Deviation		0.781	0.0277			

Table 4-9: *Tensile properties summary; CANAL QI; 90^0 specimens with gap*

4.1.3.2. AP-PLY tensile properties summary

A. 90^0 Specimens without defects

Specimen Number	Width (mm)	Thickness (mm)	Cross Section Area (mm^2)	Elasticity Modulus (GPa)	Poisson's Ratio	Maximum Measured Load (kN)	Maximum Measured Strain	Maximum Stress (MPa)	Ultimate Tensile Strength (MPa)	Ultimate Tensile Stress
1	25.10	2.17	54.47	18.22	0.377	11.8	0.0184	216.64	216.64	1.84%
2	25.06	2.12	53.13	20.12	0.411	7.6	0.008316	143.05	-	-
3	24.95	2.08	51.9	17.86	0.42	7.67	0.0085	147.80	-	-
4	25.05	2.05	51.35	17.01	0.312	5.17	0.0061	100.68	-	-
		Average		18.30	0.380					
		Standard Deviation		1.314	0.049					

Table 4-10: *Tensile properties summary; AP-PLY; 90^0 specimens*

B. 0^0 Specimens without defects

Specimen Number	Width (mm)	Thickness (mm)	Cross Section Area (mm^2)	Elasticity Modulus (GPa)	Poisson's Ratio	Maximum Measured Load (kN)	Maximum Measured Strain	Maximum Stress (MPa)	Ultimate Tensile Strength (MPa)	Ultimate Tensile Stress
5	24.95	2.14	53.39	36.73	0.743	34.76	0.01897	651.02	651.02	1.9%
6	25.05	2.14	53.61	32.97	0.723	22.38	0.01324	417.48	-	-
7	25.08	2.07	51.92	31.32	0.719	22.43	0.01302	432.05	-	-
8	25.05	2.06	51.60	33.99	0.685	14.97	0.00848	290.10	-	-
		Average		33.75	0.718					
		Standard Deviation		2.27	0.024					

Table 4-11: *Tensile properties summary; AP-PLY; 0^0 specimens*

From the calculated tensile properties the following observations have been made:

- The tensile properties (elasticity modulus and Poisson's ratio) of the CANAL QI specimen 9; oriented in 0^0 direction with overlap, are more or less the same as those of the specimens in the same direction without defects.
- The tensile properties (elasticity modulus and Poisson's ratio) of the CANAL QI specimen 10; oriented in 0^0 direction with gap, are significantly higher than those of the specimens in the same direction without defects.

- The average tensile properties (elasticity modulus and Poisson's ratio) of the CANAL QI specimens oriented in 90^0 direction with overlap are higher than those of the specimens in the same direction with gap.
- The average tensile properties (elasticity modulus and Poisson's ratio) of the AP-PLY specimens oriented in 0^0 direction are much higher (about 85% higher) than those of the specimens oriented in 90^0 direction. This was somehow quite predictable since the AP-PLY laminate was not quasi-isotropic.

4.1.4. Classical Laminate Theory (CLT) predictions

Using engineering constants of carbon fiber (Table 2-2) and epoxy resin (Table 2-3) and the fiber volume fractions measured in the combustion tests (Tables 4-1, 4-2), elastic constants of a single unidirectional **(UD)** lamina: **(1)** Longitudinal Young's modulus, E_1 **(2)** Transverse Young's modulus, E_2 **(3)** Major Poisson's ratio, v_{12} **(4)** In-plane shear modulus, G_{12} can be calculated according to the Chamis formulas and the results are reported in Table 4-12 for the CNAL QI panel and in Table 4-13 for the AP-PLY panel:

$$V_m = 1 - V_f \quad 4\text{-}4$$

$$E_1 = E_f V_f + E_m V_m \quad 4\text{-}5$$

$$E_2 = \frac{E_f E_m}{V_f E_m + V_m E_f} \quad 4\text{-}6$$

$$G_{12} = \frac{G_f G_m}{V_f G_m + V_m G_f} \quad 4\text{-}7$$

$$v_{12} = V_f v_f + V_m v_m \quad 4\text{-}8$$

$\boldsymbol{V_m}$: Matrix volume fraction
$\boldsymbol{V_f}$: Fiber volume fraction
$\boldsymbol{E_f}$: Young's modulus of the fiber
$\boldsymbol{E_m}$: Young's modulus of the matrix
$\boldsymbol{G_f}$: Shear modulus of the fiber
$\boldsymbol{G_m}$: Shear modulus of the matrix
$\boldsymbol{v_f}$: Poisson's ratio of the fiber
$\boldsymbol{v_m}$: Poisson's ratio of the matrix

E_1 (GPa)	E_2 (GPa)	G_{12} (GPa)	v_{12}
148	6.76	2.84	0.29

Table 4-12: *Elastic constants of a single UD ply; CANAL QI panel*

E_1 (GPa)	E_2 (GPa)	G_{12} (GPa)	v_{12}
148	6.78	2.85	0.29

Table 4-13: *Elastic constants of a single UD ply; AP-PLY panel*

Laminate engineering constants are another way of defining laminate stiffnesses. Showing equation 4-9 in short notation:

$$\begin{bmatrix} N_x \\ N_y \\ N_{xy} \\ M_x \\ M_y \\ M_{xy} \end{bmatrix} = \begin{bmatrix} A_{11} & A_{12} & A_{16} & B_{11} & B_{12} & B_{16} \\ A_{12} & A_{22} & A_{26} & B_{12} & B_{22} & B_{26} \\ A_{16} & A_{26} & A_{66} & B_{16} & B_{26} & B_{66} \\ B_{11} & B_{12} & B_{16} & D_{11} & D_{12} & D_{16} \\ B_{12} & B_{22} & B_{26} & D_{12} & D_{22} & D_{26} \\ B_{16} & B_{26} & B_{66} & D_{16} & D_{26} & D_{66} \end{bmatrix} \begin{bmatrix} {\varepsilon_x}^0 \\ {\varepsilon_y}^0 \\ {\varepsilon_{xy}}^0 \\ {\kappa_x}^0 \\ {\kappa_y}^0 \\ {\kappa_{xy}}^0 \end{bmatrix} \qquad 4\text{-}9$$

$$\begin{bmatrix} [N] \\ [M] \end{bmatrix} = \begin{bmatrix} [A] & [B] \\ [B] & [D] \end{bmatrix} \begin{bmatrix} [\varepsilon^0] \\ [\kappa^0] \end{bmatrix} \qquad 4\text{-}10$$

The $[A]$, $[B]$, and $[D]$ matrices are called the extensional, coupling, and bending stiffness matrices respectively. The extensional stiffness matrix $[A]$ relates the resultant in-plane forces $[N]$ to the in-plane strains $[\varepsilon^0]$, and the bending stiffness matrix $[D]$ relates the resultant bending moments $[M]$ to the plate curvatures $[\kappa^0]$. The coupling stiffness matrix $[B]$ couples the force and moment terms to the midplane strains and midplane curvatures.

$$A_{ij} = \sum_{k=1}^{n} \left[\left(\bar{Q}_{ij}\right)\right]_k (h_k - h_{k-1}) \,, i = 1,2,6;\ j = 1,2,6 \qquad 4\text{-}11$$

$$B_{ij} = \frac{1}{2} \sum_{k=1}^{n} \left[\left(\bar{Q}_{ij}\right)\right]_k \left({h_k}^2 - {h_{k-1}}^2\right) \,, i = 1,2,6;\ j = 1,2,6 \qquad 4\text{-}12$$

$$C_{ij} = \frac{1}{3} \sum_{k=1}^{n} \left[\left(\bar{Q}_{ij}\right)\right]_k \left({h_k}^3 - {h_{k-1}}^3\right) \,, i = 1,2,6;\ j = 1,2,6 \qquad 4\text{-}13$$

where $\left[\left(\bar{Q}_{ij}\right)\right]_k$ is the stiffness of the k^{th} layer.

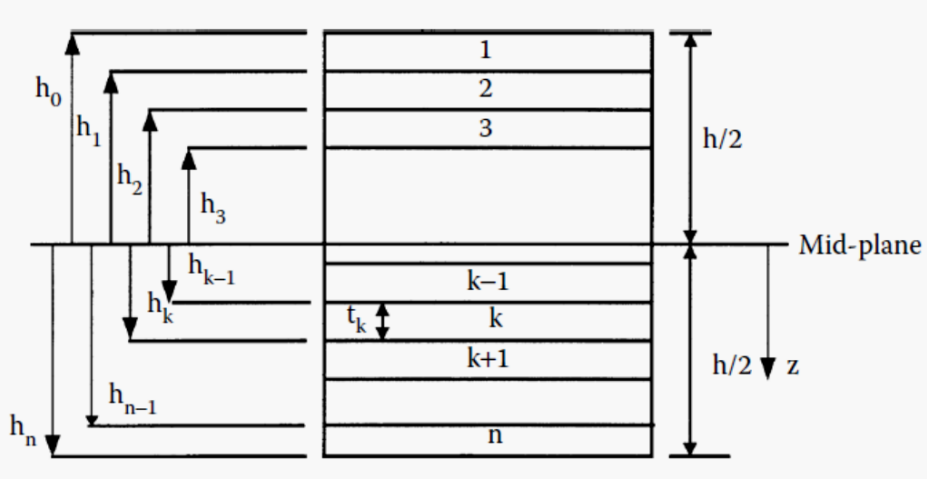

Figure 4-1: *Coordinate location of plies in a laminate.*

Inverting equation 4-10 gives:

$$\begin{bmatrix}[\varepsilon^0]\\ [\kappa^0]\end{bmatrix} = \begin{bmatrix}[A^*] & [B^*]\\ [C^*] & [D^*]\end{bmatrix}\begin{bmatrix}[N]\\ [M]\end{bmatrix} \qquad 4\text{-}14$$

where $\begin{bmatrix}[A^*] & [B^*]\\ [C^*] & [D^*]\end{bmatrix} = \begin{bmatrix}[A] & [B]\\ [B] & [D]\end{bmatrix}^{-1}$ and $[C^*] = [B^*]^T$.

The $[A^*]$, $[B^*]$, and $[D^*]$ matrices are called the extensional compliance matrix, coupling compliance matrix, and bending compliance matrix respectively.

For a symmetric laminate like both of the laminates that we had, $[B] = 0$ and it can be shown that $[A^*] = [A]^{-1}$ and $[D^*] = [D]^{-1}$. Then, from Equation:

$$\begin{bmatrix}{\varepsilon_x}^0\\ {\varepsilon_y}^0\\ {\varepsilon_{xy}}^0\end{bmatrix} = \begin{bmatrix}{A_{11}}^* & {A_{12}}^* & {A_{16}}^*\\ {A_{12}}^* & {A_{22}}^* & {A_{26}}^*\\ {A_{16}}^* & {A_{26}}^* & {A_{66}}^*\end{bmatrix}\begin{bmatrix}N_x\\ N_y\\ N_{xy}\end{bmatrix} \qquad 4\text{-}15$$

The preceding equations allow us to define effective in-plane moduli in terms of the extensional compliance matrix $[A^*]$ as follows (h is the thickness of the laminate):

$$E_x = \frac{1}{h{A_{11}}^*} \qquad 4\text{-}16$$

$$E_y = \frac{1}{h{A_{22}}^*} \qquad 4\text{-}17$$

$$G_{xy} = \frac{1}{hA_{66}^{*}} \quad 4\text{-}18$$

$$v_{xy} = \frac{-A_{12}^{*}}{A_{11}^{*}} \quad 4\text{-}19$$

$$v_{yx} = \frac{-A_{12}^{*}}{A_{22}^{*}} \quad 4\text{-}20$$

$\boldsymbol{E_x}$: Effective in-plane longitudinal modulus
$\boldsymbol{E_y}$: Effective in-plane transverse modulus
$\boldsymbol{G_{xy}}$: Effective in-plane shear modulus
$\boldsymbol{v_{xy}}, \boldsymbol{v_{yx}}$: Effective in-plane Poisson's ratios [4]

E_x (GPa)	E_y (GPa)	G_{xy} (GPa)	v_{xy}	v_{yx}
51.6	51.6	18.2	0.28	0.28

Table 4-14: *Elastic constants of the CANAL QI laminate [5]*

E_x (GPa)	E_y (GPa)	G_{xy} (GPa)	v_{xy}	v_{yx}
37.5	20.8	30.8	0.86	0.48

Table 4-15: *Elastic constants of the AP-PLY laminate [5]*

It is seen that the longitudinal and transverse Young's moduli E_x and E_y are slightly over predicted in comparison with the measured ones. For the CANAL QI laminate the predicted effective in-plane Poisson's ratios are slightly smaller and for AP-PLY laminate are slightly greater in comparison with the measured values.

4.2. Damage investigation

In this section, different steps in the data processing of the tensile tests are explained. It is explained how to get the final stress-strain curve with AE events and cumulative energy curve, starting from the raw data. The raw data consists of three data series:

- Load and displacement from the tensile testing machine (INSTRON 4505)
- Full-field strain maps by DIC analysis (LIMESS Q-400-2D and Vic2D software)
- AE events with corresponding energy and load at which they occurred.

The damage investigation methodology combines mechanical testing with acoustic emission registration, AE clustering analysis, and DIC full-field surface strain mapping. The energy of AE events registered by AE device and the associated loading level allow to obtain and to plot the

dependency of cumulative energy of AE events vs. tensile stress, from which damage initiation thresholds can be determined based on the following observations. At the very beginning of the test no acoustic events are registered; starting from a certain load threshold, low energy events start to occur with low frequency. Then the frequency of events increases sharply and the energy content reaches higher levels. This is reflected by the increase of the slope of the cumulative AE event energy curve (the energy was negligible before). At some higher level of the applied stress, a second "knee" on the AE cumulative energy curve may appear.

According to these observations, the processing of these results allowed to determine: **(1)** the AE threshold strain $\varepsilon_{min}$for which the first AE event occurs, i.e. low energy acoustic events start to appear; **(2)** the first damage threshold strain ε_1 at the first increase of the slope of the cumulative AE energy curve; **(3)** the second damage threshold strain ε_2 at the second "knee" on the AE cumulative energy curve.

The damage thresholds are very important properties of a composite. A change in the rate of AE event accumulation indicates a switch to another damage mechanism. Moreover, the first event damage threshold and/or the first damage initiation threshold could be used for determining a long-term durability of the material. The second damage threshold is also characteristic of the material; it can be considered as the basis for determining a shorter-term durability design stress limit. A further characteristic parameter is the density of AE events, i.e. the number of events.

4.2.1. Acoustic emission registrations

4.2.1.1. State of art

Williams and **Lee** [5]	They early introduced the acoustic emission to monitor the failure of composites.
Groot et al. [6] **Yu et al.** [7]	Performed the failure detection of the composites by determining the real-time acoustic frequency.
Woo and **Choi** [8]	They explored the failure process for the single-edge-notched laminated composites by studying the high-amplitude acoustic emission events.
Giordano et al. [9]	They performed the quantitative failure analysis on the polymer composites by acoustic emission.
Mizutania et al. [10] **Bohse** [11] **Zhuang and Yan** [12] **Bussiba et al.** [13] **Ramirez-Jimenez et al.** [14]	They studied several typical microscopic damage and failure mechanisms of composites using acoustic emission.

Benmedakhene et al. [15] **Hill et al.** [16] **Johnson** and **Gudmundson** [17] **Bakhtiary Davijani et al.** [18] **Scholey et al.** [19] **Gutkin et al.** [20]	They explored the failure mechanisms including the matrix cracking and delamination of composite laminates using acoustic emission.
Loutas and **Kostopoulos** [21] **Sasikumar et al.** [22] **Oliveira** and **Marques** [23]	They performed the health monitoring research of composites using acoustic emission and artificial neural network.
Czigany [24]	He proved that it's possible to correlate the acoustic emission features such as the number of events, the amplitude and energy to the physical properties (e.g., fiber orientation and fiber content).
Rosa et al. [25]	He gave a literature review on the application of acoustic emission for the natural fiber composites including the damage evolution and failure mechanisms detection.
Valentin et al. [26] **Berthelot** and **Rhazi** [27]	They have studied amplitude distribution of acoustic emission signals collected from various tests on unidirectional and cross-ply carbon/epoxy composites. Both studies reveal contradictory amplitude ranges for the failure modes observed. Longitudinal matrix microcracking is characterized by high amplitude signals, and fiber fracture by low amplitude signals in [26], but this is in marked contrast to [27], which reports that high amplitude signals are associated with fiber failure and low amplitude signals with transverse/longitudinal matrix cracking and delamination.
Ni and **Iwamoto** [28]	They show that the amplitude of AE signals is greatly affected by sensor distance, and conclude that the peak frequency of AE signals, which is not affected by sensor distance, is a more reliable characteristic.
Loutas and **Kostopoulos** [29] **Qi** [30]	The **D**iscrete **W**avelet **T**ransform **(DWT)** has been used to identify AE signals based on the energy contained in each level of decomposition and the frequency range of this level. From AE signals recorded during tensile tests on cross-ply notched laminates,

	three failure modes are identified with wavelet levels centered at: 300 kHz for fiber failure; 250 *kHz* for fiber–matrix debonding and 110 *kHz* for matrix cracking. [30]

Table 4-16: *Damage investigation using AE, state of art*

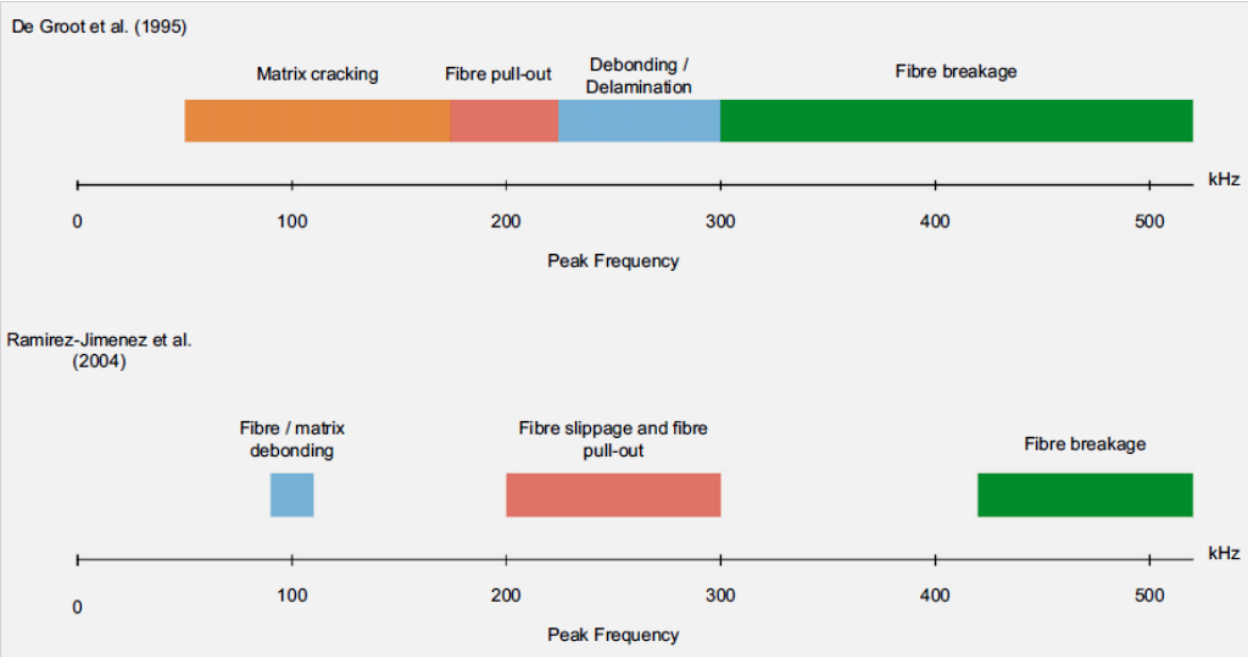

Figure 4-2: *Frequency ranges related to different damage mechanisms defined by* ***de Groot et al.*** *[6] for carbon/epoxy composites and* ***Ramirez-Jimenez et al.*** *[14] for glass/polypropylene composites.*

4.2.1.2. Experiments

Damage in a material develops in stages. This is reflected in acoustic emission measurements that record the amount of energy released during the loading. Sudden changes in the accumulated energy indicate that the material transitions to a new type of damage (transverse cracking, delaminations, fiber breakage, etc) or at least undergoes qualitatively different changes in damage development. By stopping the test at such characteristic strain levels or just beyond, one can examine the type of damage in the material and link it to the loading level. The type of damage in the material, on the other hand, can be related to the microstructural features and, possibly, to defects of manufacturing.

From collected AE data the following observations have been made:

- At the very beginning of the test, few events of low energy occur with low frequency. Then the frequency of events increases sharply and the energy content reaches higher levels.

This is reflected by the increase of the slope of the cumulative AE event energy curve. It is noted that the sudden increase in the cumulative energy is associated with the events of higher energy. The cumulative energy vs. strain curves for all of the samples will be illustrated later in Appendix A.

- Despite significant AE activity that is indicative of internal damage in the materials (in terms of transverse cracks, fiber breakage, etc), no visible changes are noted in the stress strain curves. The latter show linear behavior. This can be explained by the fact that 90°-carbon yarns contribute less than 5% to the stiffness of the composite. In the case of glass fibers, for example, the stress-strain curves show visible deviation from linear behavior at the first jump in AE cumulative energy showing permanent changes in the material. The deviation in the case of glass fibers is noticeable due to the fact that 90°- yarns in glass fiber reinforced composites contribute more than 20% of the composite stiffness.
- AE activity is increased in the course of the loading (less events in the beginning and more towards the end).
- The AE curves of accumulated energy as a function of strain for different specimens with same conditions (sample direction and defect types) show small scatters for CANAL QI samples and relatively large scatters for AP-PLY samples (Figures 4-3;6).

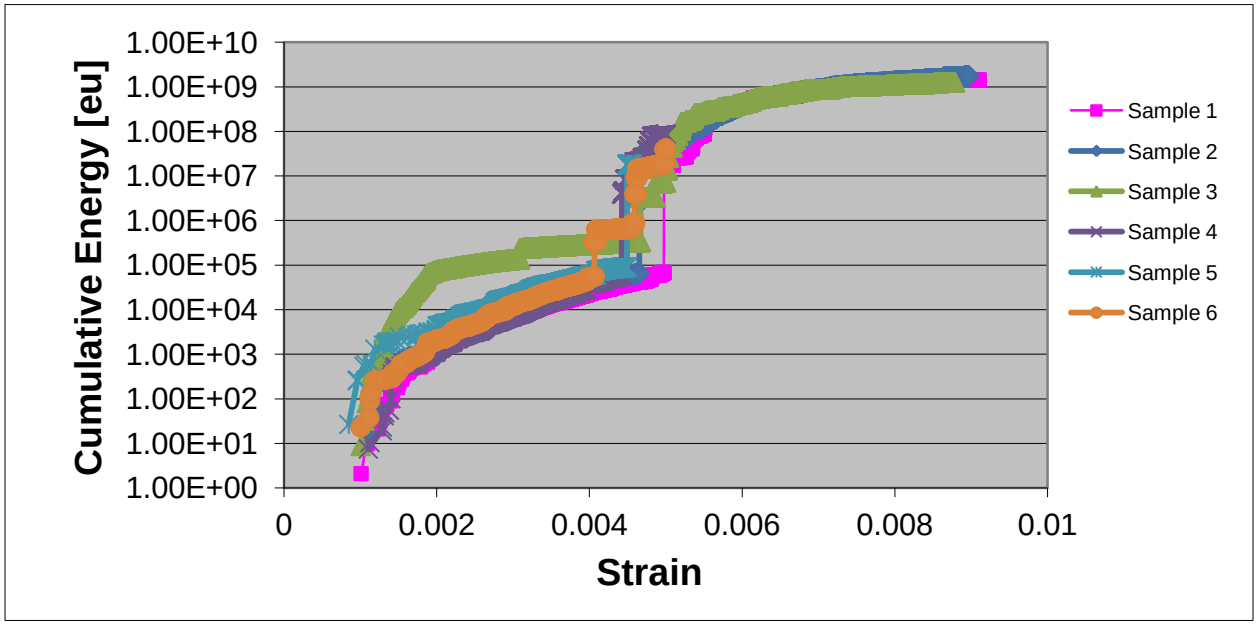

Figure 4-3: *Small scatter in AE curves of accumulated energy vs. strain for CANAL QI specimens without defects in 0^0 direction*

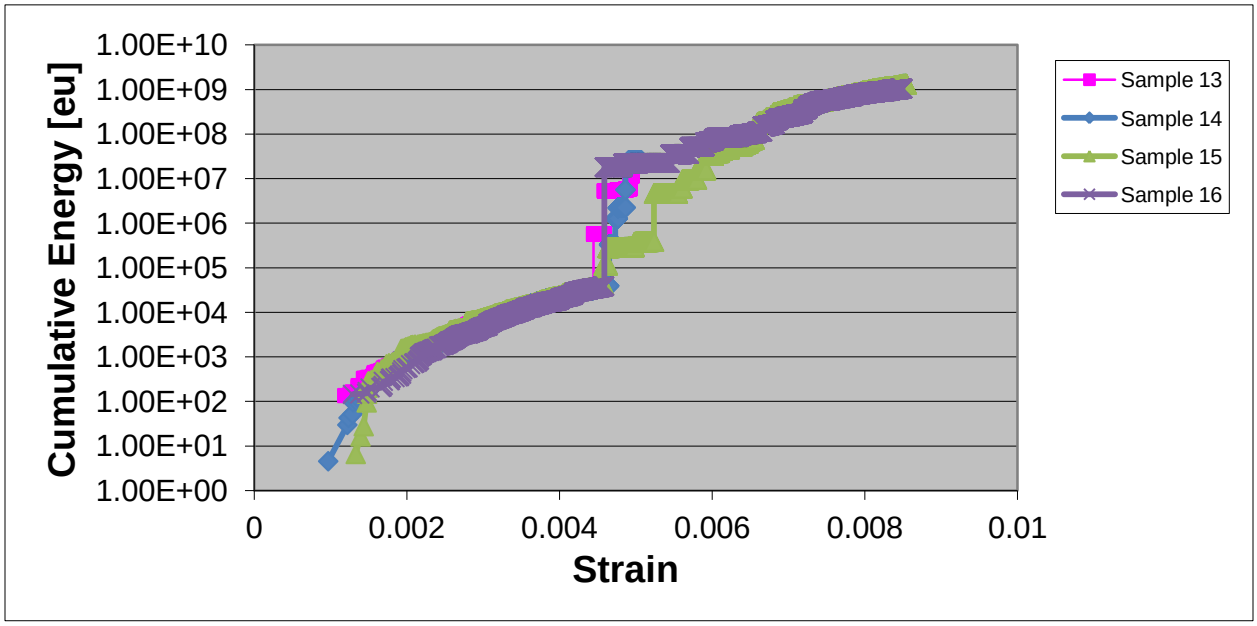

Figure 4-4: *Small scatter in AE curves of accumulated energy vs. strain for CANAL QI specimens with gaps in 90^0 direction*

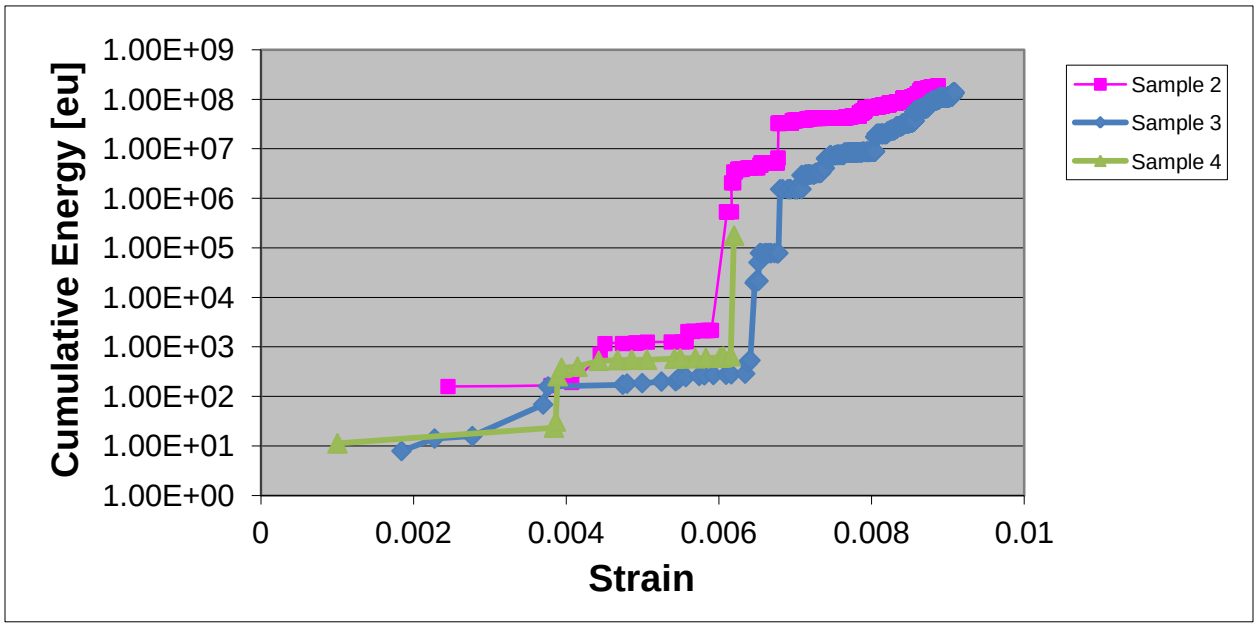

Figure 4-5: *Relatively large scatter in AE curves of accumulated energy vs. strain for AP-PLY specimens without defects in 90^0 direction*

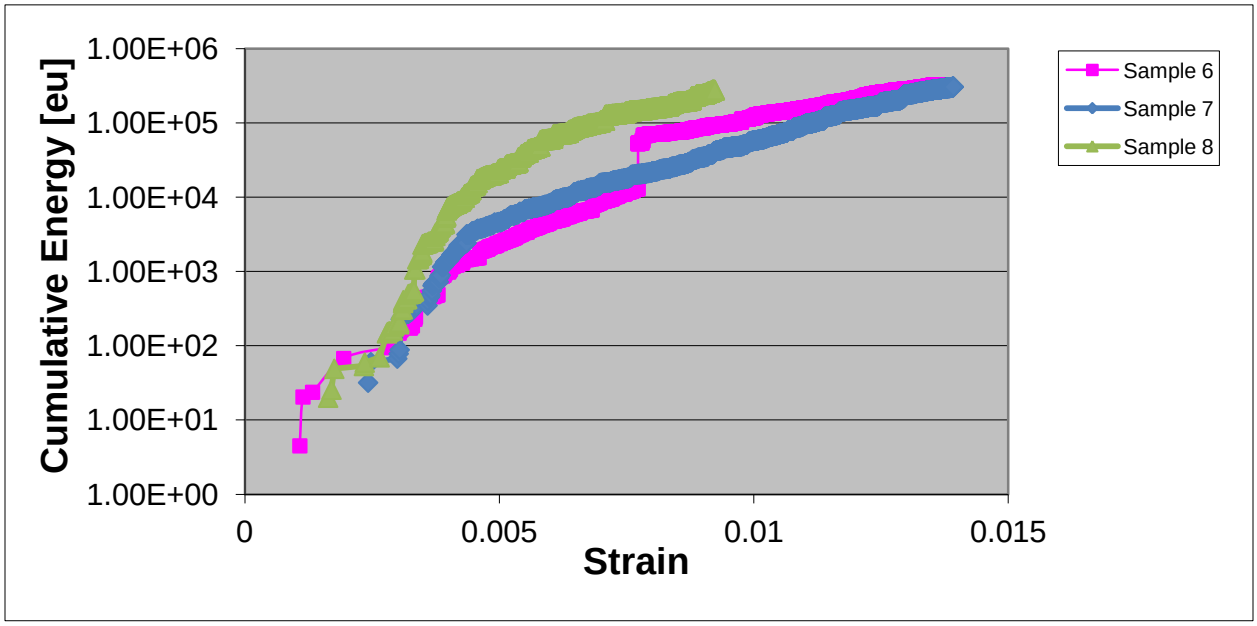

Figure 4-6: *Relatively large scatter in AE curves of accumulated energy vs. strain for AP-PLY specimens without defects in 0^0 direction*

The step-wise changes in the AE diagrams with the appearance of high energy events are related to certain changes in the damage evolution. In the present work we will identify three characteristics strain levels: ε_{min} for which the first AE event occurs, i.e. low energy acoustic events start to appear; $\varepsilon_1$is the first damage threshold strain at the first increase of the slope of the cumulative AE energy curve; and ε_2 is the second damage threshold strain at the second "knee" on the AE cumulative energy curve. These characteristic thresholds for damage initiation and propagation have been identified for each tested specimen by means of the respective AE cumulative energy curve. The first event threshold has been simply defined evaluating the stress level of the first registered acoustic emission event, independently of its energy level. First and second damage thresholds have been instead evaluated considering the levels of applied loads at which abrupt discontinuities ("jumps") of the AE cumulative energy curve occur. More specifically, definition of the first and second damage thresholds has been performed plotting the The identified strain thresholds are shown in Figure 4.5 – 4.6 for both CANAL QI and AP-PLY specimens.

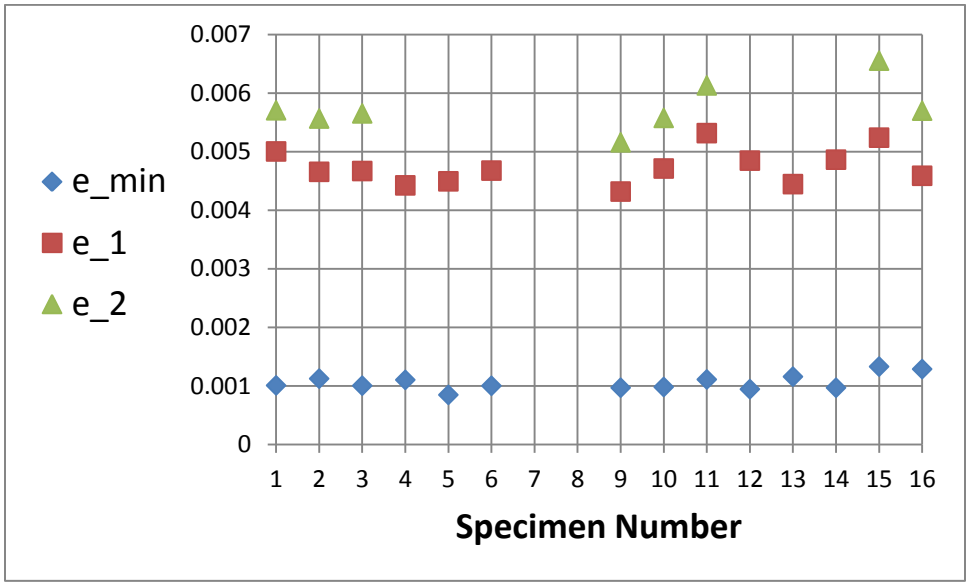

Figure 4-7: *Characteristic strains for all tested samples; CANAL QI*

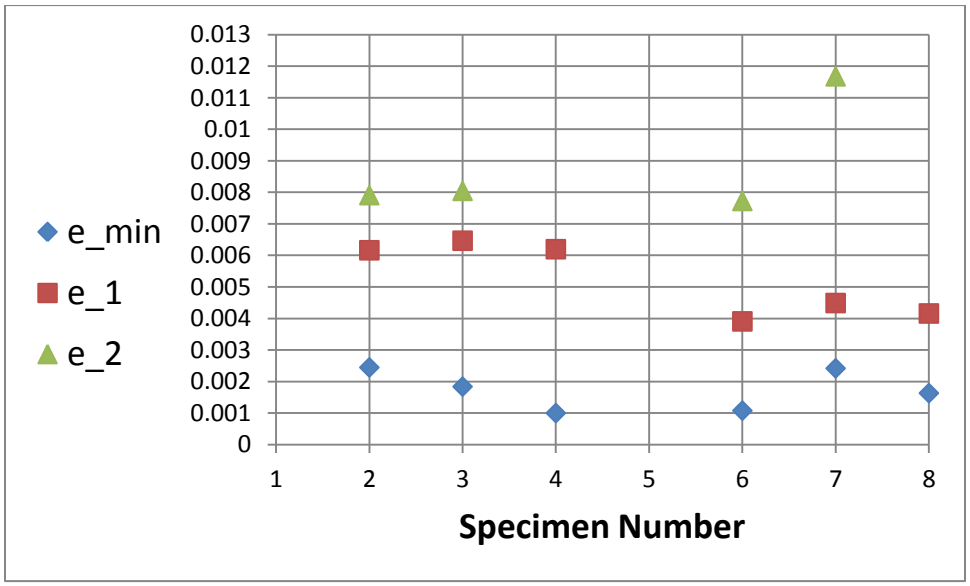

Figure 4-8: *Characteristic strains for all tested samples; AP-PLY*

In relation to the material failure, the difficulty is the definition of what exactly is understood by ‘‘the damage initiation’’. As the inter-fiber transversal cracks may be created by coalescence of the ‘‘crescent’’ debonding on the individual fibers, the definition of ‘‘initiation’’ is rather fuzzy. Traditionally the damage initiation strain to be an indication of appearance of a crack, which connects several debonded fibers. In reality such a transversal crack develops fast into a crack through the whole thickness of the yarn.

The onset of steady generation of higher energy AE events, on the other hand, is often treated as appearance of transversal inter-fiber cracks. The AE events ''heard'' before could be interpreted as micro-debonding events.

4.2.2. DIC full field strain registration

In mechanical testing of structural materials usually only two points based strain measurement devices or strain gages are utilized. Such measurements do not deliver much useful information concerning strain concentration and decohesion of materials. This information may be delivered when using optical methods of strain measurements. One of the methods, which became widely used in recent years due to development of PC computers and image acquisition methods and devices, is Digital Image Correlation.

The aim of presented investigation was to perform DIC measurements during uniaxial tensile tests for determination of Young's modulus and Poisson's ratio (during elastic range of loading) and to obtain full-field strain maps different stages of loading.

The repeatability of the tensile tests of different categories of specimens for both of the laminates are depicted in Figures 4-9; 12 which show an acceptable scatter range. According to the tensile test results summary of the CANAL QI panel which was reported in section 4.1.3.1., for the samples tested in the 0^0 direction, the Young's modulus and the Poisson's ratio of the sample with gap are slightly higher than those for the samples without defects. Furthermore, the Young's modulus and the Poisson's ratio of the sample with overlap are slightly lower than those of the samples without defects. For the samples tested in the 90^0 direction, the averaged values of Young's modulus and the Poisson's ratio for the samples with gap are slightly lower than those for the samples with overlap.

According to the tensile test results summary of the AP-PLY panel which was reported in section 4.1.3.2., the averaged values of Young's modulus and Poisson's ratio for the samples tested in 0^0 direction are about 47% higher than the values for the samples tested in 90^0 direction.

The longitudinal and transversal strain maps, stress vs. strain curves, and elasticity modulus vs. strain curves for all the tested specimens are illustrated in Appendix A.

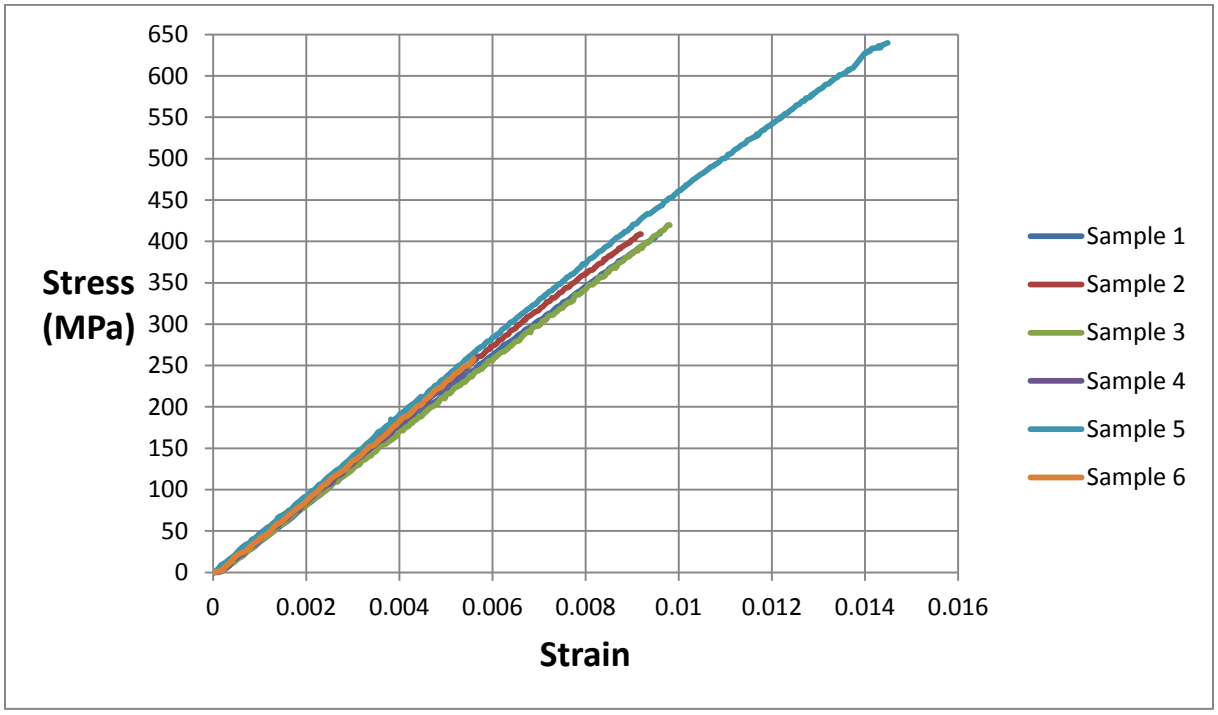

Figure 4-9: *Stress vs. strain curves for CANAL QI specimens without defects oriented in 0^0 direction*

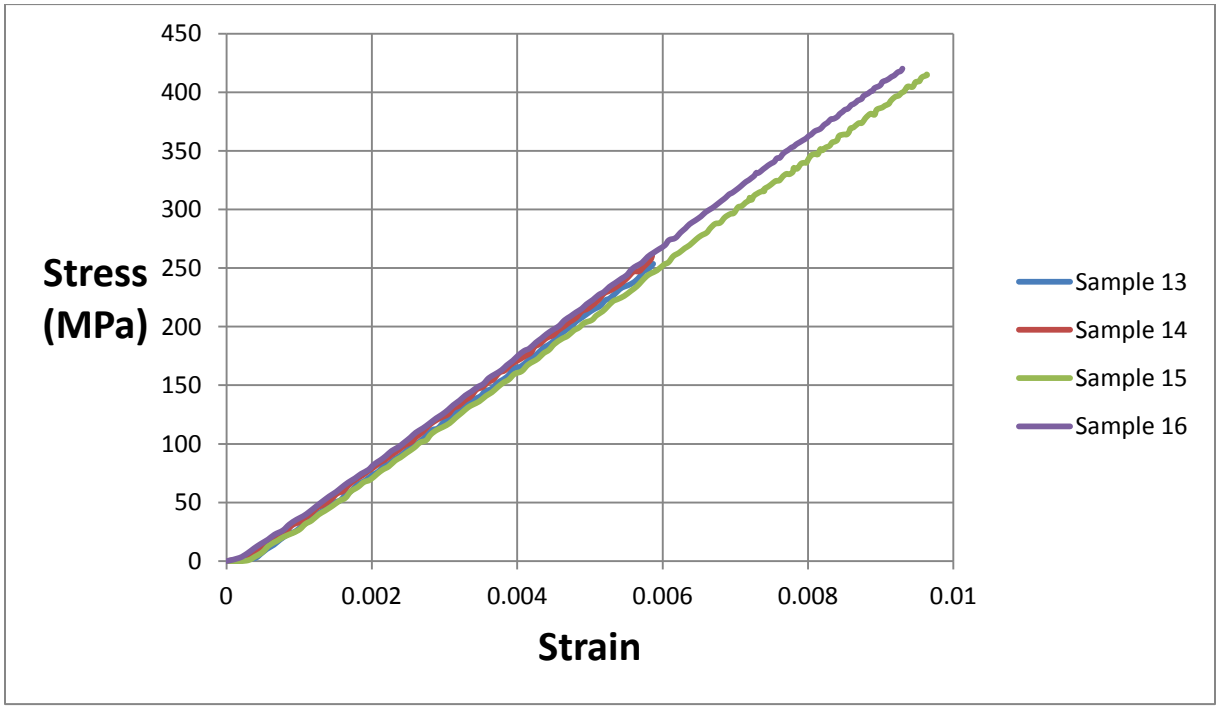

Figure 4-10: *Stress vs. strain curves for CANAL QI specimens with gaps oriented in 90^0 direction*

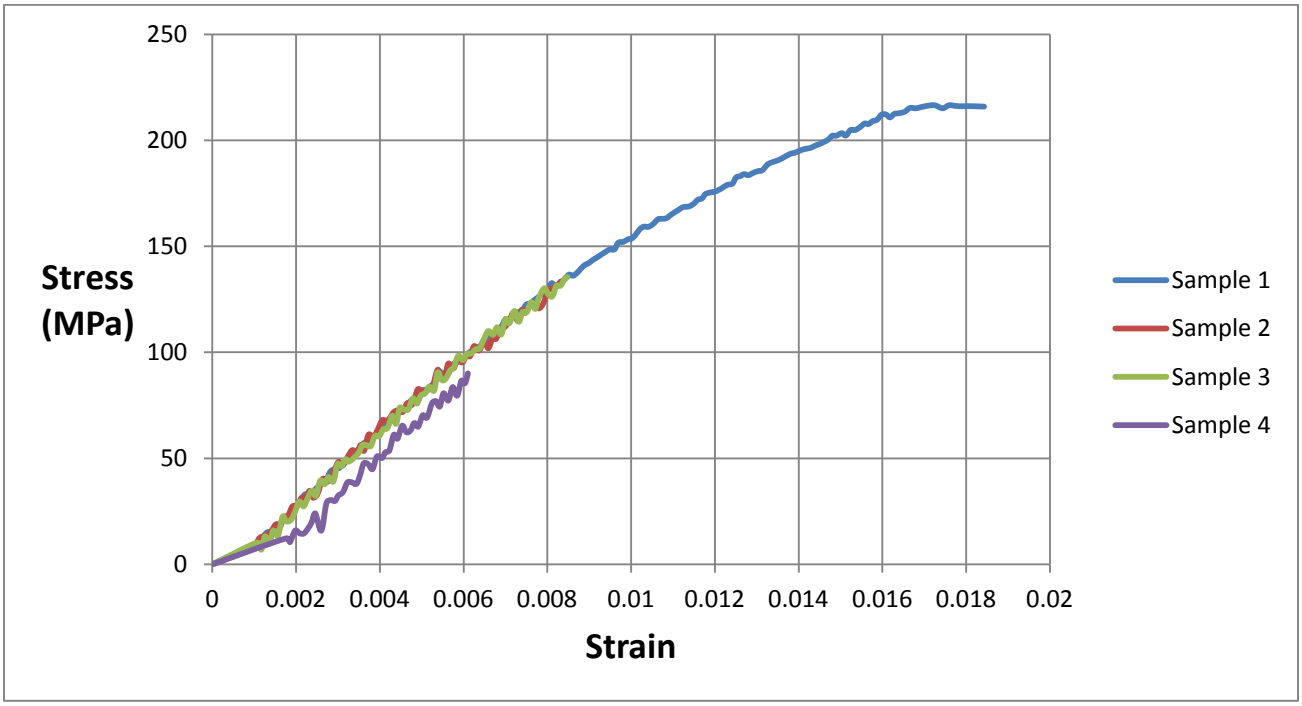

Figure 4-11: *Stress vs. strain curves for AP-PLY specimens without defects oriented in 90^0 direction*

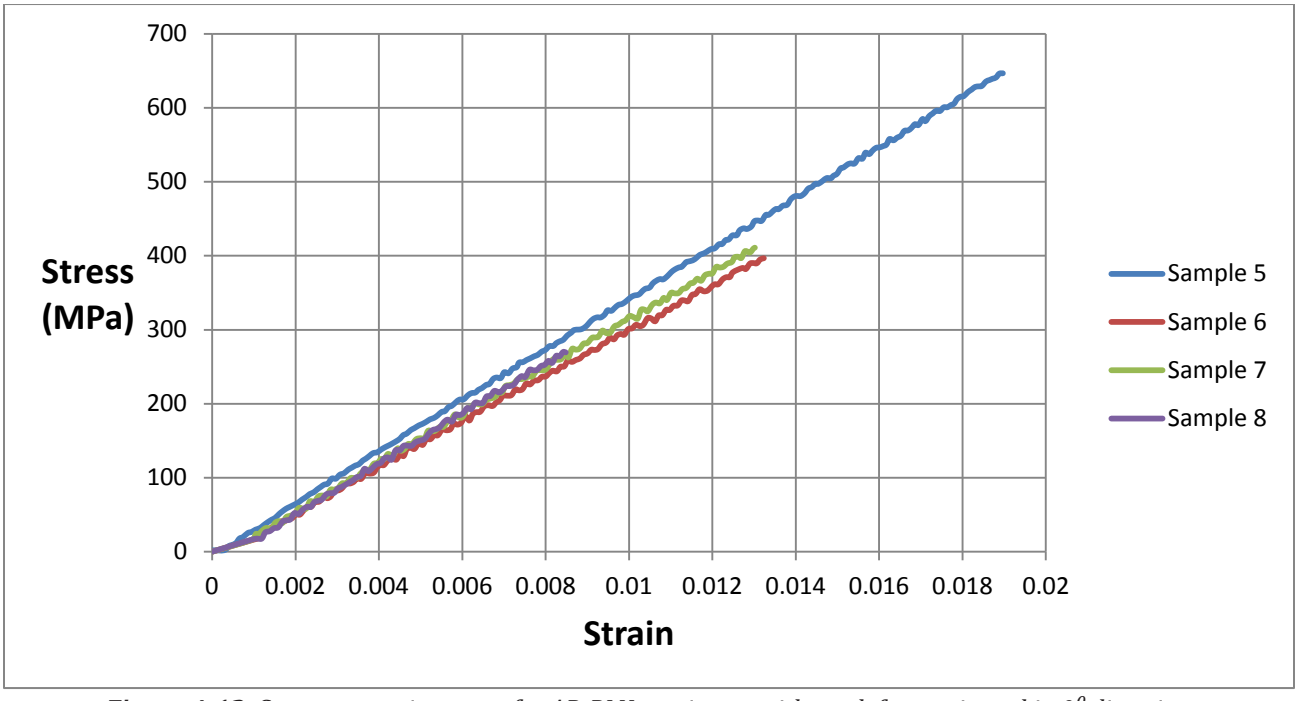

Figure 4-12: *Stress vs. strain curves for AP-PLY specimens without defects oriented in 0^0 direction*

4.3. References

1. ASTM D3410 / D3410M-08. Standard Test Method for Compressive Properties of Polymer Matrix Composite Materials with Unsupported Gage Section by Shear Loading. ASTM International, West Conshohocken, PA; 2008.
2. ASTM D3171-11. Standard Test Methods for Constituent Content of Composite Materials. ASTM International, West Conshohocken, PA; 2011.
3. Sartorius YDK 01, YDK 01-0D, YDK 01LP Density Determination Kit User's Manual, Sartorius AG, Goettingen, Germany; September 1998.
4. Kaw AK. Mechanics of Composite Materials. 2nd Edition, CRC Press; 2005.
5. Williams Jr JH, Lee SS. Acoustic emission monitoring of fiber composite materials and structures. Journal of Composite Materials 1978; 12(4): 348–70.
6. De Groot PJ, Wijnen PAM, Janssen RBF. Real-time frequency determination of acoustic emission for different fracture mechanisms in carbon/epoxy composites. Composites Science and Technology 1995; 55(4): 405–12.
7. Yu YH, Choi JH, Kweon JH, Kim DH. A study on the failure detection of composite materials using an acoustic emission. Composite Structures 2006; 75(1–4): 163–9.
8. Woo SC, Choi NS. Analysis of fracture process in single-edge-notched laminated composites based on the high amplitude acoustic emission events. Composites Science and Technology 2007; 67(7–8): 1451-8.
9. Giordano M, Calabro A, Esposito C, D'Amorec A, Nicolais L. An acoustic emission characterization of the failure modes in polymer-composite materials. Composites Science and Technology 1998; 58(12): 1923–8.
10. Mizutania Y, Nagashima K, Takemoto M, Ono K. Fracture mechanism characterization of cross-ply carbon-fiber composites using acoustic emission analysis. NDT & E International 2000; 33(2): 101–10.
11. Bohse J. Acoustic emission characteristics of micro-failure processes in polymer blends and composites. Composites Science and Technology 2000; 60(8): 1213–26.
12. Zhuang XM, Yan X. Investigation of damage mechanisms in self-reinforced polyethylene composites by acoustic emission. Composites Science and Technology 2006; 66(3–4): 444–9.
13. Bussiba A, Kupiec M, Ifergane S, Piat R, Bohlke T. Damage evolution and fracture events sequence in various composites by acoustic emission technique. Composite Science and Technology 2008; 68(5): 1144–55.
14. Ramirez Jimenez CR, Papadakis N, Reynolds N, Gan TH, Purnell P, Pharaoh M. Identification of failure modes in glass/polypropylene composites by means of the

primary frequency content of the acoustic emission event. Composites Science and Technology 2004; 64(12): 1819–27.
15. Benmedakhene S, Kenane M, Benzeggagh ML. Initiation and growth of delamination in glass/epoxy composites subjected to static and dynamic loading by acoustic emission. Composites Science and Technology 1999; 59(2): 201–8.
16. Hill R, Brooks R, Kaloedes D. Characterization of transverse failure in composites using acoustic emission. Ultrasonics 1998; 36(1–5): 517–23.
17. Johnson M, Gudmundson P. Experimental and theoretical characterization of acoustic emission transients in composite laminates. Composites Science and Technology 2001; 61(10): 1367–78.
18. Davijani AAB, Hajikhani M, Ahmadi M. Acoustic Emission based on sentry function to monitor the initiation of delamination in composite materials. Materials & Design 2011; 32(5): 3059–65.
19. Scholey JJ, Wilcox PD, Wisnom MR, Friswell MI. Quantitative experimental measurements of matrix cracking and delamination using acoustic emission. Composites: Part A 2010; 41(5): 612–23.
20. Gutkin R, Green CJ, Vangrattanachai S, Pinho ST, Robinson P, Curtis PT. On acoustic emission for failure investigation in CFRP: pattern recognition and peak frequency analyses. Mechanical Systems and Signal Processing 2011; 25(4): 1393–407.
21. Loutas TH, Kostopoulos V. Health monitoring of carbon/carbon, woven reinforced composites: Damage assessment by using advanced signal processing techniques. Part I: Acoustic emission monitoring and damage mechanisms evolution. Composites Science and Technology 2009; 69(2): 265–72.
22. Sasikumar T, Rajendraboopathy S, Usha KM, Vasudev ES. Failure strength prediction of unidirectional tensile coupons using acoustic emission peak amplitude and energy parameter with artificial neural networks. Composites Science and Technology 2009; 69(7–8): 1151–55.
23. De Oliveira R, Marques AT. Health monitoring of FRP using acoustic emission and artificial neural networks. Computers and Structures 2008; 86(3–5): 367–73.
24. Czigany T. Special manufacturing and characteristics of basalt fiber reinforced hybrid polypropylene composites: Mechanical properties and acoustic emission study. Composites Science and Technology 2006; 66(16): 3210–20.
25. De Rosa LM, Santulli C, Sarasini F. Acoustic emission for monitoring the mechanical behavior of natural fiber composites: a literature review. Composites: Part A 2009; 40(9): 1456–69.

26. Valentin D, Bonniau P, Bunsell AR. Failure mechanism discrimination in carbon fiber-reinforced epoxy composites. Composites 1983; 14: 345–51.
27. Berthelot JM, Rhazi J. Acoustic emission in carbon fiber composites. Composites Science and Technology 1990; 37: 411–28.
28. Ni QQ, Iwamoto M. Wavelet transform of acoustic emission signals in failure of model composites. Engineering Fracture Mechanics 2002; 69: 717–28.
29. Loutas TH, Kostopoulos V, Ramirez Jimenez C, Pharaoh M. Damage evolution in center-holed glass-polyester composites under quasi-static loading using time-frequency analysis of acoustic emission monitored waveforms. Composites Science and Technology 2006; 66: 1366–75.
30. Qi G. Wavelet-based AE characterization of composite materials. NDT&E International 2000; 33: 133–44.

5

Quasi-Static Compression Test Results

5.1. Mechanical compression properties

The quasi-static compression tests were performed based on ASTM D341 [1]. This test method determines the in-plane compressive properties of polymer matrix composite materials reinforced by high-modulus fibers. The composite material forms are limited to continuous-fiber or discontinuous-fiber reinforced composites for which the elastic properties are specially orthotropic with respect to the test direction. This test procedure introduces the compressive force into the specimen through shear at wedge grip interfaces. This type of force transfer differs from the procedure in Test Method D695 where compressive force is transmitted into the specimen by end-loading, Test Method D6641 where compressive force is transmitted by combined shear and end loading, and Test Method D5467 where compressive force is transmitted by subjecting a honeycomb core sandwich beam with thin skins to four-point bending.

This test method is applicable to composites made from unidirectional tape, wet-tow placement, textile (for example, fabric), short fibers, or similar product forms. Some product forms may require deviations from the test method.

A flat strip of material having a constant rectangular cross section, as shown in the specimen drawings of Figure 3-9 and Figure 3-12, is loaded in compression by a shear force acting along the grips. The shear force is applied via wedge grips in a specially-designed fixture shown in Figure 5-1 and Figure 5-2.

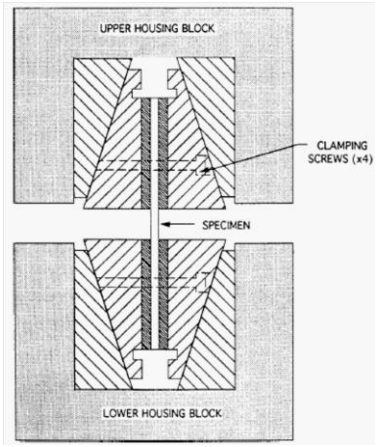

Figure 5-1: *Schematic of compression test fixture*

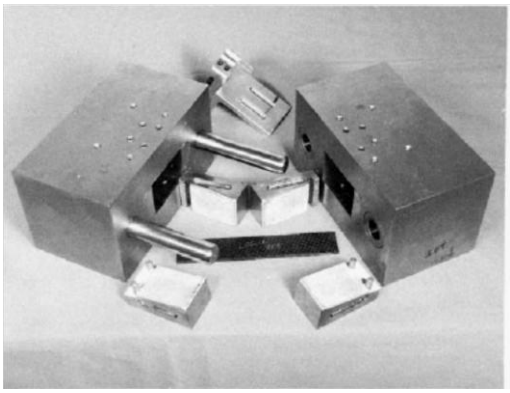

Figure 5-2: *Compression test fixture*

To obtain compression test results, the specimen is inserted into the test fixture which is placed between the platens of the testing machine and loaded in compression. (Figure 5-3) The ultimate compressive stress of the material, as obtained with this test fixture and specimen, can be obtained from the maximum force carried before failure. Strain is monitored with strain mapping using DIC, so the stress-strain response of the material can be determined, from which the ultimate compressive strain, the compressive modulus of elasticity, and Poisson's ratio in compression can be derived.

This test method is designed to produce compressive property data for material specifications, research and development, quality assurance, and structural design and analysis. Factors that influence the compressive response and should therefore be reported include the following: material, methods of material preparation and layup, specimen stacking sequence, specimen preparation, specimen conditioning, environment of testing, specimen alignment and gripping,

speed of testing, time at temperature, and volume percent reinforcement. Properties, in the test direction, that may be obtained from this test method include:

- Ultimate compressive strength,
- Ultimate compressive strain,
- Compressive modulus of elasticity, and
- Poisson's ratio in compression

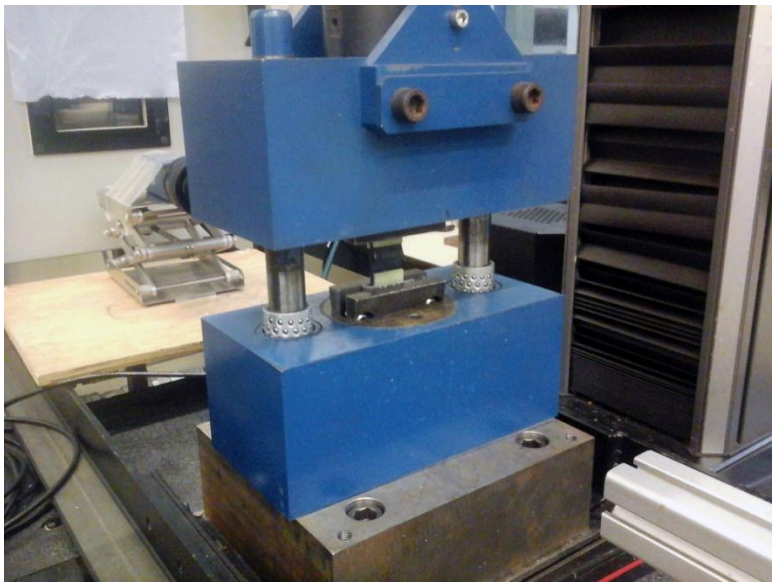

Figure 5-3: *Compression specimen in the test fixture*

Along the factors which influence the tensile response, just one of the factors are different from those mentioned for the quasi-static tensile tests mentioned in section 4.1. which is the testing speed. Speed of testing was controlled by constant crosshead speed of 50 *mm/min*.

Compression test results generated by this test method are sensitive to the alignment of the specimen with respect to the longitudinal axis of the wedges in the test fixture. Specimen alignment can be accomplished by using an alignment jig or gage block that mechanically holds the specimen captive outside the fixture housing blocks or by using a custom jig or machinist's square for a specimen inserted into wedge grips already in the fixture housing blocks.

Longitudinal strain shall be simultaneously measured on opposite faces of the specimen to allow for a correction as a result of any bending of the specimen and to enable detection of Euler (column) buckling. Back-to-back strain measurement shall be made for all the specimens. (Figure

5-4) Therefore, both faces of the specimens were speckled and two cameras were used for strain mapping on opposite faces of the specimens.

Figure 5-4: *Back-to-back strain measurement*

As it was depicted in Figure 3-9 and Figure 3-12, end tabs were added to specimens and pieces of emery cloth were used for better gripping conditions and to prevent slip.

All the samples were tested till fracture. From the stress-strain curves of these samples, ultimate tensile stress and ultimate tensile strain were attained. If compressive modulus or ultimate compressive strain is to be calculated, we have to determine the average compressive strain at each required data point using Equation 5-1 and Equation 5-2, respectively, and report the results to three significant figures.

$$\varepsilon_i{}^c = \frac{\varepsilon_{1i}+\varepsilon_{2i}}{2} \quad 5\text{-}1$$

$$\varepsilon^{cu} = \frac{\varepsilon_1{}^{cu}+\varepsilon_2{}^{cu}}{2} \quad 5\text{-}2$$

$\boldsymbol{\varepsilon_i{}^c}$: Average compressive strain at i^{th} data point
$\boldsymbol{\varepsilon_{1i}}$: Gage-1 compressive strain at i^{th} data point
$\boldsymbol{\varepsilon_{2i}}$: Gage-2 compressive strain at i^{th} data point

$\boldsymbol{\varepsilon^{cu}}$: Average ultimate compressive strain
$\boldsymbol{\varepsilon_1{}^{cu}}$: Gage-1 ultimate compressive strain
$\boldsymbol{\varepsilon_2{}^{cu}}$: Gage-2 ultimate compressive strain

Compressive chord modulus of elasticity and compressive Poisson's ratio were derived in the strain interval of 1000 μstrains and 3000 μstrains using the following formulas:

$$E^{chord} = \Delta\sigma / \Delta\varepsilon_l \qquad 5\text{-}3$$

$$\vartheta = -\Delta\varepsilon_t / \Delta\varepsilon_l \qquad 5\text{-}4$$

$\boldsymbol{E^{chord}}$: Compressive chord modulus of elasticity; *GPa*
$\Delta\boldsymbol{\sigma}$: Difference in applied compressive stress between the two strain points which correspond to the previously mentioned strain values
$\Delta\boldsymbol{\varepsilon_l}$: Difference between the two longitudinal strain points (nominally 0.002)
$\boldsymbol{\vartheta}$: Poisson's ratio
$\Delta\boldsymbol{\varepsilon_t}$: Difference in lateral strains between the two longitudinal strain points

Stress vs. strain diagrams, longitudinal and transversal strain maps for all the compressive samples will be depicted further in the quasi-static compressive appendix.

5.1.1. CANAL QI compressive properties summary

Specimen Number	Width (mm)	Thickness (mm)	Cross Section Area (mm^2)	Maximum Compressive Load (N)	Ultimate Compressive Strain	Ultimate Compressive Strength (MPa)	Compressive Modulus of Elasticity (GPa)	Compressive Poisson's Ratio
17	25.04	3.54	88.64	-39697.3	**-0.01077**	**-447.84**	**45.74**	**0.338**
18	25.06	3.47	86.96	-44384.8	**-0.01308**	**-510.42**	**46.18**	**0.366**
				Average	**-0.011925**	**-479.13**	**45.96**	**0.352**

Table 5-1: *Compressive properties summary; CANAL QI*

5.1.2. AP-PLY compressive properties summary

Specimen Number	Width (mm)	Thickness (mm)	Cross Section Area (mm^2)	Maximum Compressive Load (N)	Ultimate Compressive Strain	Ultimate Compressive Strength (MPa)	Compressive Modulus of Elasticity (GPa)	Compressive Poisson's Ratio
10	25.06	2.15	53.88	-11230.5	-0.01263	-208.44	19.15	0.499
11	25.01	2.16	54.02	-13525.4	-0.0174	-250.37	18.95	0.441
12	25.02	2.21	55.29	-13037.1	-0.01477	-235.78	19.16	0.446
13	24.99	2.12	52.98	-11767.6	-0.0143	-222.12	20.00	0.443
			Average		**-0.01478**	**-229.178**	**19.315**	**0.45725**
			Standard Deviation		0.001976	18.00525	0.466798	0.027909

Table 5-2: *Compressive properties summary; AP-PLY*

5.2. References

1. ASTM D3410 / D3410M-08, “Standard Test Method for Compressive Properties of Polymer Matrix Composite Materials with Unsupported Gage Section by Shear Loading”, ASTM International, West Conshohocken, PA, 2008.

6

Acoustic Emission Clustering

6.1. Introduction

Acoustic Emission (AE) registration is an important non-destructive technique for detecting and identifying damage initiation and propagation. The phenomenon of acoustic emission in Carbon Fiber Reinforced Polymers (CFRP) has been extensively studied (see, for example, [1-5]). Cluster analysis of AE events was applied to CFRP as well [6-8].

Amplitude-based classification of AE events using time domain features (mainly peak amplitude and energy) have been studied for unidirectional and cross-ply laminates [9-11]. Different conclusions had been made on damage mechanisms associated with peak amplitude. In [9] and [10], matrix cracking was found to be associated with low amplitude signals, fiber-matrix debonding correlated to medium amplitude events, and fiber rupture corresponded to high amplitude events. This classification contradicts the one proposed in [11], which suggests that high amplitude signals originate from matrix cracking, and low amplitude signals from fiber breakage. Evolution of cumulative energy of AE events is widely used for identification of damage initiation and propagation thresholds (e.g. [3,4,12]).

AE events cluster analysis based on both time and frequency features showed that peak frequency of an AE signal can represent specific damage types [8, 13]. The low frequency range is normally related to matrix cracking, while high frequency is correlated with fiber breakage, but the frequency range for delamination and fiber-matrix debonding varies in different studies [8, 13]. **De Groot et al.** [13] and **Gutkin et al.** [8] investigated carbon/epoxy laminates in different tests and obtained similar results of frequency bands for fiber-matrix debonding (medium frequency range from 200 to 300 *kHz*) and fiber breakage (high frequency over 300 *kHz*). These authors give different frequency ranges for the same damage modes. Matrix cracking was related to the 50-180 *kHz* frequency range in [13], while the range was below 50 *kHz* in [8]. Fiber pull-out corresponds to frequencies around 200 *kHz* in [13] but more than 500 *kHz* in [8]. Delamination related AE events lie in a higher frequency range from 220 to 300 *kHz* in De Groot et al. [13] than 50 to 150 *kHz* in **Gutkin et al.** [8]. **Sause et al.** [7] identified natural clusters of acoustic emission signals for unidirectional GFRP and CFRP composites using an approach

proposed in [6], and found that a frequency feature (weighted frequency) can distinguish occurrence of matrix cracking, interfacial failure and fiber breakage. According to [7], accumulated AE signal amplitudes reflect intensity of the damage, whilst the frequency feature identifies the damage type.

The goals of this study is to find out if AE events in carbon/epoxy composites manufactured by automated dry fiber placement can be represented with the same cluster construction as for unidirectional or cross-ply carbon/epoxy counterparts, and whether generic cluster bounds can be established for carbon/epoxy composites manufactured by automated dry fiber placement. Comparison of these statistics with numbers of high-frequency AE events will provide additional grounds for identification of the high frequency events.

6.2. Cluster analysis methods

Feature selection is a procedure of extracting the features which are good for classification. 'Good features' are such that objects from the same class have similar feature values and objects from different classes have different values. The goal of feature selection is to find the subset of parameters which eliminate irrelevant and redundant features while keeping relevant features in order to improve clustering efficiency and quality. Existence of irrelevant features in the data set may degrade clustering quality and consume more memory and computational time. In addition, different subset of relevant features may produce different clustering, which will greatly help discovering different hidden patterns in the AE data [14]. For unsupervised feature selection there exist the following methods: maximum variance, Laplacian score, spectral feature selection method and multi-cluster feature selection method. Laplacian score [15, 16] it is an advanced variance analysis. It not only prefers those features with larger variances which have more representative power, but also prefers selecting features with stronger locality preserving ability. A key assumption in Laplacian score is that data from the same class are close to each other. Here algorithms from [15] are used to calculate the value of Laplacian score for each feature.

Principle component analysis (PCA) is an orthogonal linear transformation that can transform multidimensional AE data into lower dimensions with a new coordinate system, with a set of uncorrelated features, that is, the principal components [17]. It is an effective and useful multivariate analysis method which is usually used to reduce dimensionality of a large data set to enable better analysis and visualization of data [18, 19]. PCA projects the input data (AE signal parameters) on the new coordinates (called principal components) with maximum variance in the data set. Based on the covariance matrix of the dataset the ordered orthogonal basis is

created, with its first eigenvectors having the direction of the largest variance of the data. Let A be the matrix, composed of these eigenvectors, then the principal components are expressed as $Pd_i = \sum a_{ij}\, \bar{p}_j$; where $\bar{p}_j$ are the initial set of the normalized AE signal parameters.

K-means++ [20] is a modified way of choosing centers for the k-means algorithm, which is a centroid based and an iterative algorithm. It follows a simple and easy way to classify a given data set through a certain k number of clusters fixed a priori, in which k centroids are spread throughout the data and the data samples are allocated to the centroid which is closest. Let *D(x)* denote the shortest distance from a data point to the closest center we have already chosen. Then k-means++ initiation algorithm was defined as follows. Firstly, choose a center at random (uniform distribution) from among the data points. Then compute *D(x)* for each data point *x*, make sure that the distance between *x* and the nearest center has been chosen. After that, use weighted probability distribution $\frac{D(x)^2}{\sum_{x\epsilon\chi} D(x)^2}$ to choose one new data point at random as a new center, which satisfy that its probability proportional to *D(x)*, where χ is the input data set. Repeat the last two steps until k centers have been chosen.

In this study we use two clustering evaluation indices, which are the mostly used in literature: Silhouette coefficient [8] and Davies–Bouldin index [21,22,23]. Silhouette coefficient combines ideas of both cohesion and separation. It measures how distinct or well-separated a cluster is from other clusters. The Silhouette coefficient for an individual point is given by:

$$SC = \frac{1}{N}\sum_{i=1}^{N} \frac{b(x)-a(x)}{\max\{a(x),b(x)\}} \qquad 6\text{-}1$$

where *a(x)* is the average distance of point x to all other vectors in the same cluster, it measures how closely related are objects in a cluster, *b(x)* is the average distance of point *x* to the vectors in other clusters and it aims to find the minimum among the clusters. *SC* is between -1 and 1. The score is higher when clusters are dense and well separated, which relates to a standard concept of a cluster.

The Davies–Bouldin criterion is based on a ratio of within cluster and between-cluster distances:

$$DB = \frac{1}{k}\sum_{i=1}^{k} \max\{D_{i,j}\}, \quad D_{i,j} = \frac{\bar{d}_i+\bar{d}_j}{d(c_i,c_j)} \qquad 6\text{-}2$$

where $D_{i,j}$ is the within-to-between cluster distance ratio for the *i*th and *j*th clusters. In mathematical terms, $\bar{d}_i$ is the average distance between each point in the *i*th cluster and the centroid of the *i*th cluster. $\bar{d}_j$ is the average distance between each point in the *i*th cluster and the

centroid of the *j*th cluster. $d(c_i, c_j)$ is the Euclidean distance between the centroids of the *i*th and *j*th clusters. The maximum value of $D_{i,j}$ represents the worst case within-to-between cluster ratio for cluster *i*. The clustering algorithm that produces a collection of clusters with the smallest Davies–Bouldin index is considered the best algorithm based on this criterion. Both Silhouette coefficient and Davies–Bouldin index combine cohesion and separation, but Davies–Bouldin index related to the cluster centroids.

In the present work the cluster analysis is performed based on MatLab R2014a routines from Statistics toolbox.

According to [6,18,19,21,24], nine originally recorded AE features were used to start the clustering analysis **(1)** peak amplitude (PA), **(2)** duration (D), **(3)** rise time (RT), **(4)** peak frequency (PF), **(5)** counts (CNT), **(6)** energy (E), **(7)** frequency centroid of gravity (FCoG, which is the frequency where the areas of the frequency spectrum below and above the FCOG are the same), **(8)** RA value (rise time divided by peak amplitude) and **(9)** weighted peak frequency (WF, which is square root of peak frequency multiplied by the frequency centroid of gravity). All AE features are normalized to range from 0 to 1 before data analysis.

The energy and cumulative energy graphs vs. strain for different categories of tensile specimens (see Appendix A) as well as the distribution of AE events amplitude and frequency for individual tests show that AE energy and amplitude pattern is qualitatively stable for CANAL QI and AP-PLY specimens in 0^0 and 90^0 test directions. Therefore, the repeatability of AE data is quite satisfactory.

Figure 6-1 shows the average Laplacian score of each AE feature for the representative specimens. It is obvious that PA, D, E, PF, FCoG, RA value and WF have higher values of Laplacian score for different tests, which means that they are good features and have the ability of clustering the AE data.

Figure 6-2 compares the correlation of nine AE features with peak amplitude and peak frequency. It can be seen that duration and counts are highly correlated to PA; E and RT are less dependent on PA, and the correlation coefficients of PF, FCoG, and WF with PA are around zero, which means that they are almost independent from PA. Weighted frequency is highly correlated to peak frequency, whereas frequency of centroid is less dependent. However, Laplacian score of E, RT are less than that for D, thus they do not have the ability to cluster the AE signals.

Four AE parameters entering the cluster analysis are peak amplitude (PA), peak frequency (PF), duration (D), and frequency of the centroid of gravity (FCoG). Peak frequency is the frequency

with the highest Fast Fourier transform magnitude, and frequency of the centroid of gravity, which is also called frequency centroid, is defined as:

$$F_{CoG} = \int f.\overline{U}(f)df \,/\, \int \overline{U}(f)df, \qquad 6\text{-}3$$

where *f* is the frequency in the spectrum, *U(f)* is the magnitude of the corresponding frequency [6]. The definition of these two frequency parameters is illustrated in Figure 6-3. Principal Component Analysis (PCA) and k-means ++ algorithm were used to cluster the AE events in this study [25]. Silhouette Coefficient (SC) and Davies-Bouldin index (DB) were used to evaluate the cluster validity, with higher SC and lower DB indicating better cluster quality.

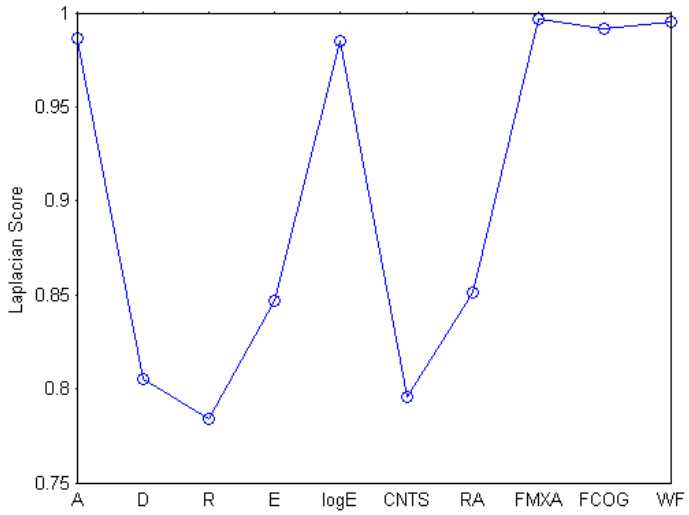

CANAL QI 4

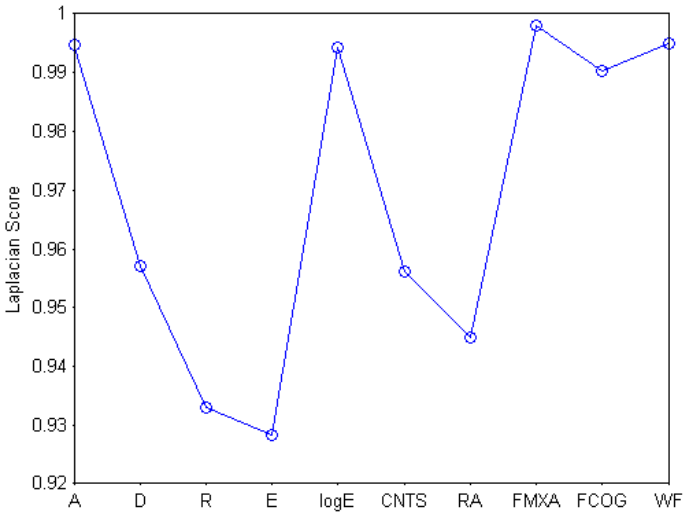

CANAL QI 15

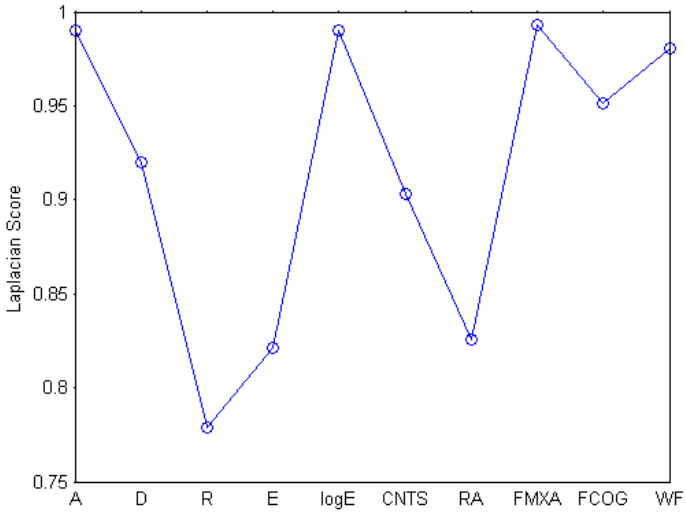

AP-PLY 2

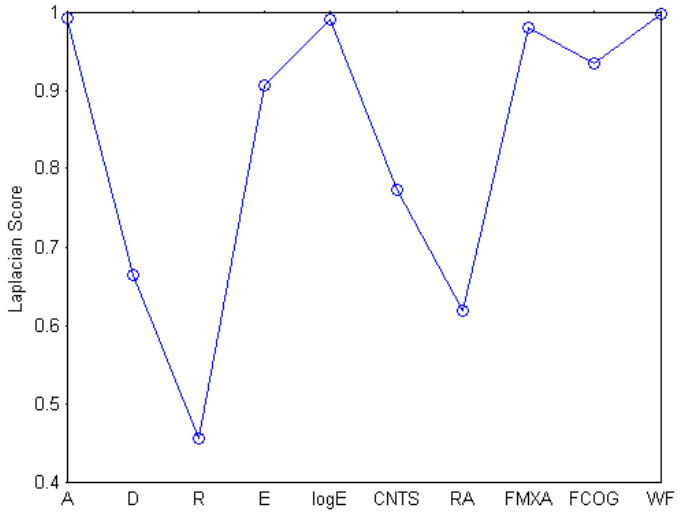

AP-PLY 7

Figure 6-1: *Feature selection using Laplacian Score values for all the representative specimens*

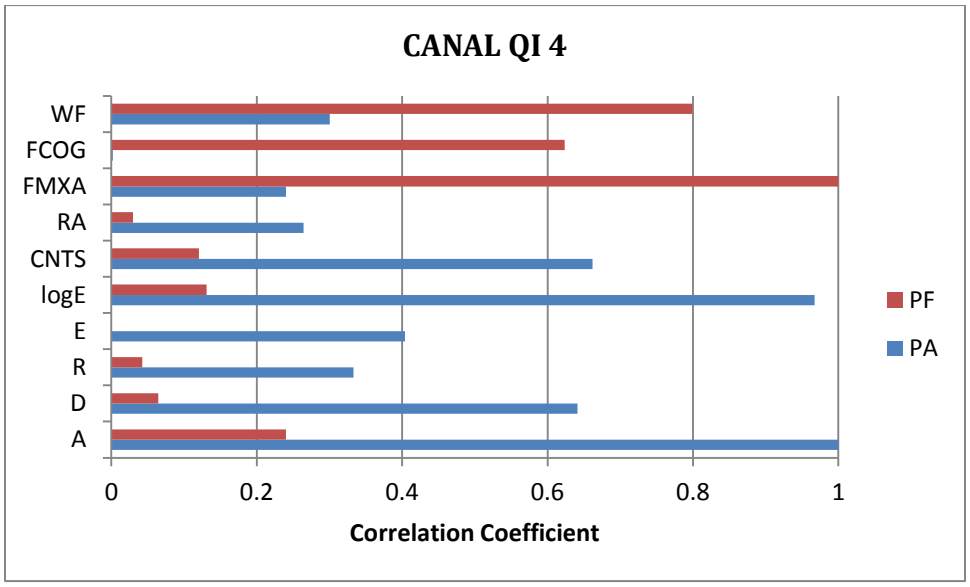

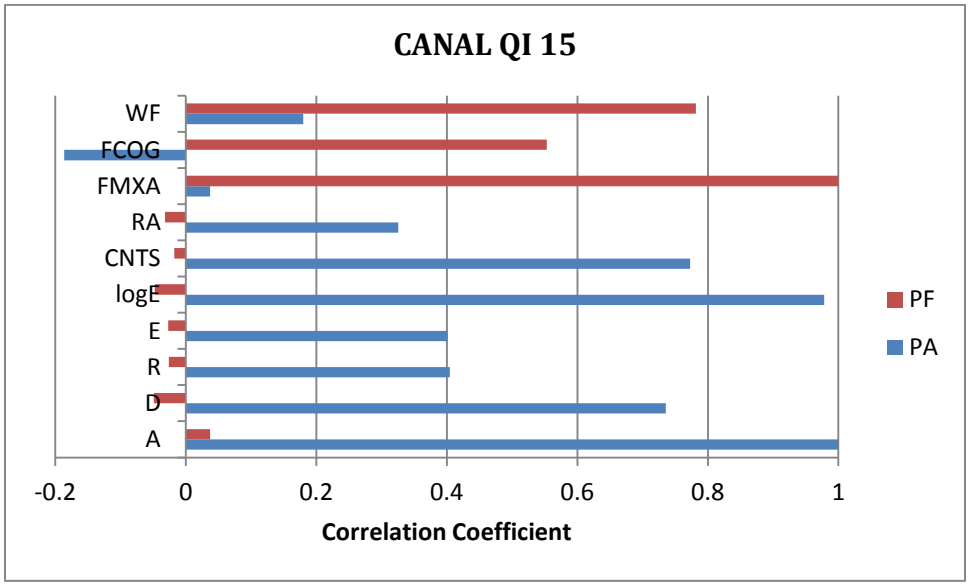
CANAL QI 15
WF
FCOG
FMXA
RA
CNTS
logE
E
R
D
A
-0.2
0
0.2
0.4
0.6
0.8
1
Correlation Coefficient
PF
PA

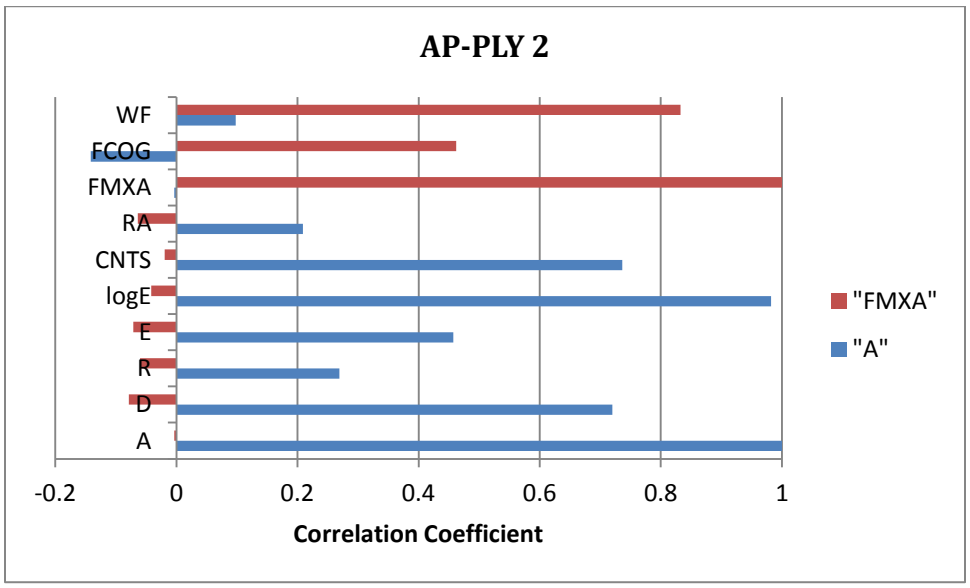
AP-PLY 2
WF
FCOG
FMXA
RA
CNTS
logE
E
R
D
A
-0.2
0
0.2
0.4
0.6
0.8
1
Correlation Coefficient
"FMXA"
"A"

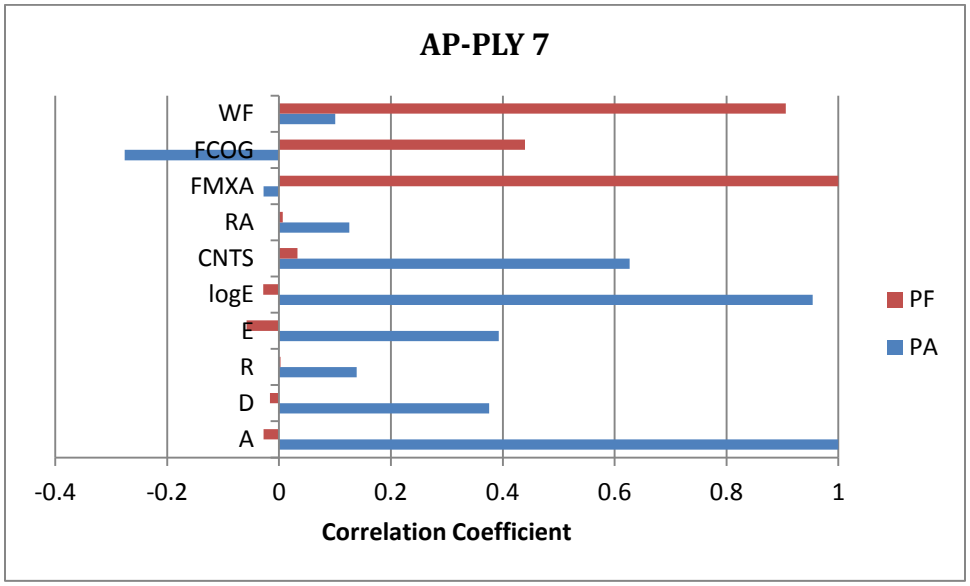

Figure 6-2: *Correlation coefficient of AE parameters with PA and PF for representative specimens*

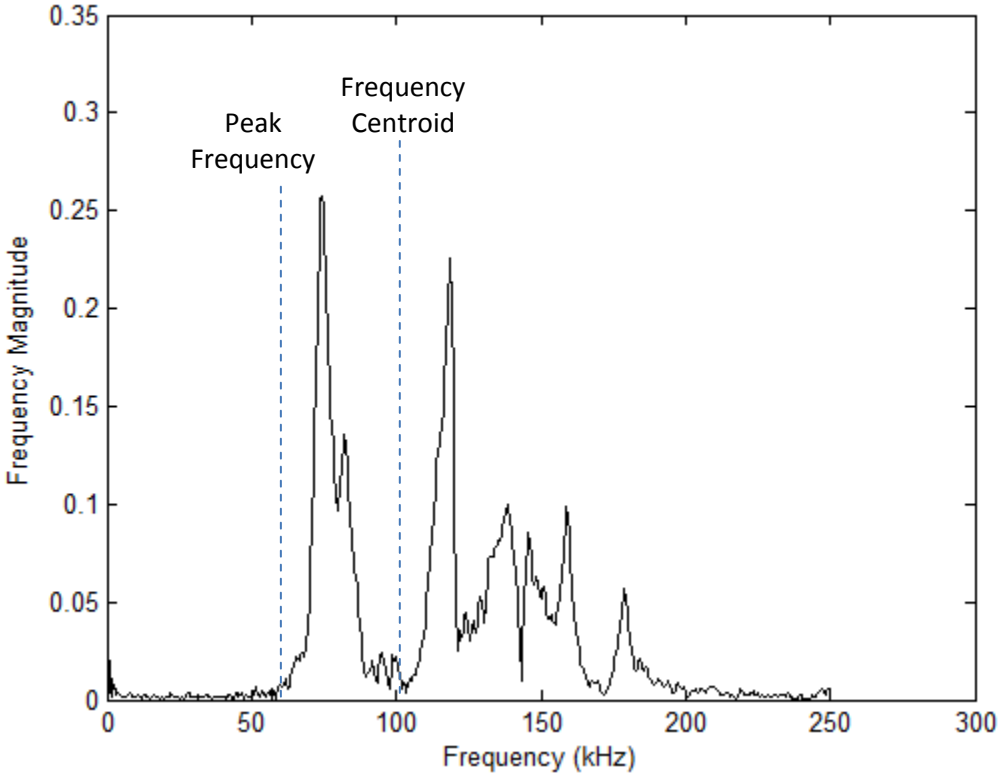

Figure 6-3: *AE frequency features; peak frequency and frequency centroid; in the spectrum of a typical AE signal*

The index of cluster evaluation used is Silhouette coefficient and Davies–Bouldin index defined in Equations 6-1 and 6-2 respectively. The number of cluster k is calculated using the range from 1 to 10 for all the test specimen data sets. The higher Silhouette coefficient and the lower Davies–Bouldin index mean better number of clusters. Figure 6-4 shows the optimal number of clusters for representative specimens. The cluster validity estimations for all the tested specimens are summarized in Table 6-1. It can be seen that the Silhouette coefficients for all the tested specimens are good and acceptable (0.6 < SC < 0.9). The DB index is always less than 1, and proved the clustering quality for all tests.

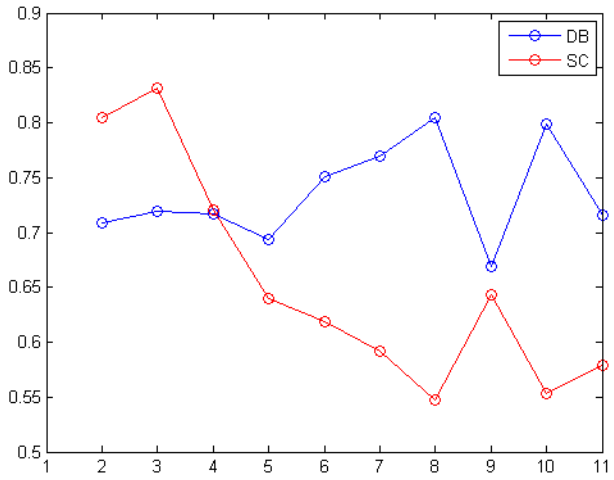

CANAL QI 4

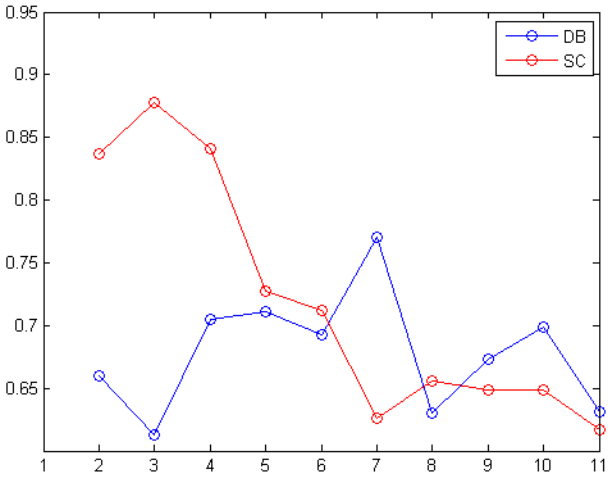

CANAL QI 15

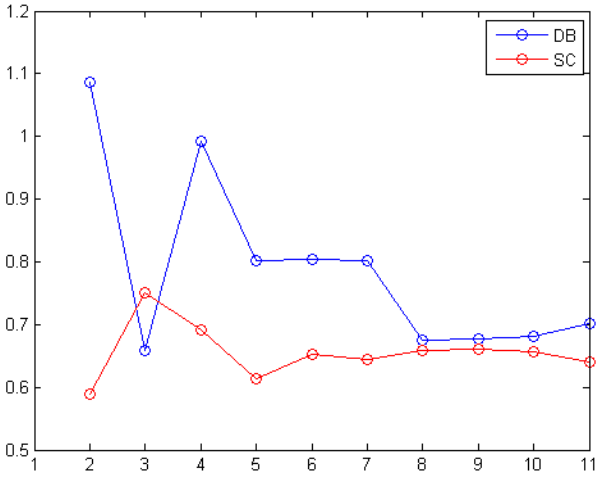

AP-PLY 2

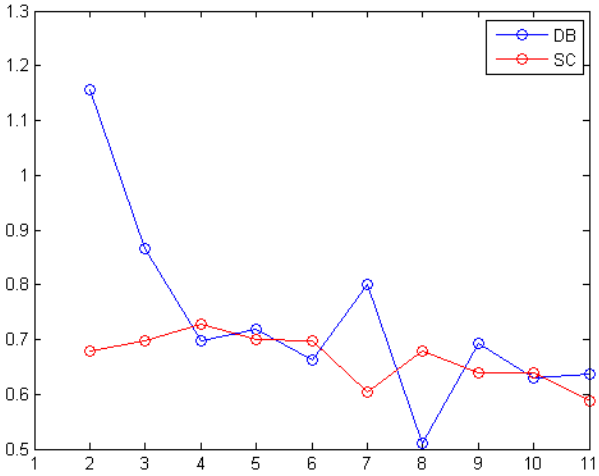

AP-PLY 7

Figure 6-4: *The number of clusters evaluated by Silhouette coefficient and Davies–Bouldin index*

				Percentage of events in each cluster				
Sample	**Number of Events**	**SC**	**DB - Index**	**CL1**	**CL2**	**CL3**	**CL4**	**CL5**
C1	16675	0.7175	0.8611	0.7334	0.2666	0	0	0
C2	18605	0.7213	0.8102	0.4793	0.4159	0.1049	0	0
C3	24770	0.6039	0.8019	0.3911	0.2225	0.1785	0.1486	0.0593
C4	4179	0.8318	0.6754	0.5793	0.39	0.0306	0	0
C5	4074	0.8499	0.5012	0.8456	0.1544	0	0	0
C6	4135	0.8594	0.5951	0.6034	0.3966	0	0	0
C9	20225	0.8373	0.6308	0.5638	0.4362	0	0	0
C10	12410	0.7983	0.7153	0.5551	0.4449	0	0	0
C11	9698	0.6752	0.8649	0.6357	0.3288	0.0355	0	0
C12	2750	0.8576	0.5042	0.8022	0.1978	0	0	0
C13	2773	0.88	0.4694	0.8154	0.1846	0	0	0
C14	2634	0.8902	0.4585	0.6917	0.3083	0	0	0
C15	12552	0.8775	0.6126	0.5956	0.3429	0.0615	0	0
C16	11876	0.8445	0.6368	0.6573	0.2594	0.0833	0	0
A2	1968	0.7366	0.6884	0.4548	0.4121	0.1331	0	0
A3	1470	0.7593	0.6369	0.5109	0.3537	0.1354	0	0
A4	261	0.7646	0.5249	0.6322	0.2261	0.0728	0.069	0
A6	6490	0.9101	0.4047	0.7529	0.2471	0	0	0
A7	6017	0.7272	0.62	0.5252	0.3058	0.1614	0.0076	0
A8	3060	0.698	0.7302	0.5337	0.2634	0.1846	0.0183	0

Table 6-1: *Clustering by k-means++ for all specimens.*

6.3. Clustering analysis

The variance percentage and cumulative variance of each principal AE component for representative samples are shown in Figure 6-5 (a). It can be seen that the first two principal components can explain roughly more than two-thirds of the total variance, so the two components can visualize the AE data. This is confirmed by Figure 6-6, in which clusters are well separated by the projection of the first two principal components. For different specimen types, the main AE features corresponding to the first two principal components vary. The principal components which are defined by the principle component analysis (PCA) algorithm are expressed as:

$$\mathrm{Pdi} = \lambda 1 \times \mathrm{PA} + \lambda 2 \times \mathrm{D} + \lambda 3 \times \mathrm{PF} + \lambda 4 \times \mathrm{FCoG}, \qquad 6\text{-}4$$

where $i = 1, 2, 3, 4$, refers to four principal components Pd1… Pd4, and λ1… λ4 refer to principal component coefficients. The values of λ's for different specimens are summarized in Table 6-2 and the contribution of the four AE parameters to the principal component is shown in Figure 6-5 (b). For CANAL QI and APPLY specimens, the largest coefficient in the first principal component is the third element, corresponding to peak frequency; for the second principal component, though coefficient of first element, related to peak amplitude, is the largest coefficient. Therefore peak frequency and peak amplitude can represent Pd1 and Pd2 respectively for CANAL QI and APPLY samples. This is evidenced by the good separation of AE events by the corresponding AE parameters for CANAL QI and APPLY specimens in Figure 6-7.

Figure 6-7 shows different clusters separated by the amplitude and frequency features, the validity of the clusters is summarized in Table 6-1, and the clusters are referred as CL1, CL2, CL3, CL4, and CL5. For CANAL QI specimens which were tested along 0^0 direction, mainly three clusters are separated by peak amplitude and peak frequency. CL1 has a lower peak amplitude and lower peak frequency, in the zone of 40-65 dB and 0-300 kHz; CL2 has more or less the same peak amplitude range (40-65 dB) and a broad peak frequency range 0-550 kHz; AE events in CL3 have broad peak amplitude range (65-100 dB) and almost the same peak frequency range as CL2, 0-550 kHz.

For CANAL QI specimens which were tested in 90^0 direction, there are three clusters separated by the peak amplitude and peak frequency. CL1 has a peak amplitude range of 40-65 dB and a frequency range of 0-250 kHz; CL2 has a peak amplitude range of 40-80 dB and a higher peak frequency compared to CL1, 300-550 kHz; CL3 has a broad range of peak frequency 0-550 kHz and the same peak amplitude range as CL1, 40-65 dB.

For APPLY specimens which were tested in 90^0 direction, there are mainly three clusters separated by the peak amplitude and peak frequency. CL1 has a peak amplitude range of 40-70 dB and a frequency range of 0-250 kHz; CL2 has the same peak amplitude range as CL1 and a higher peak frequency range compared to CL1, 250-450 kHz; CL3 has a broad range of peak frequency 100-450 kHz and the peak amplitude range of 70-100 dB.

For APPLY specimens which were tested in 0^0 direction, there are mainly four clusters separated by the peak amplitude and peak frequency. CL1 has a peak amplitude range of 40-50 dB and a frequency range of 100-250 kHz; CL2 has the same peak amplitude range as CL1 and a higher peak frequency range compared to CL1, 250-400 kHz; CL3 has a broad range of peak frequency 100-450 kHz and the peak amplitude range of 50-70 dB. CL4 has the same peak frequency range as CL3 and the peak amplitude range of 70-100 dB.

Cluster bounds for CANAL QI and AP-PLY specimens in different orientations are classified in Table 6-3.

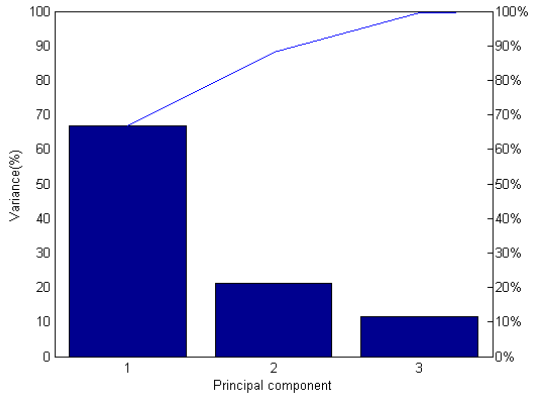

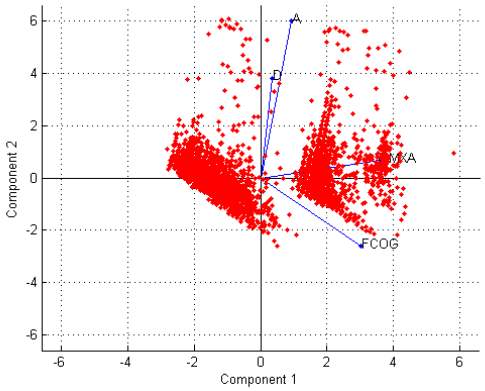

CANAL QI 4

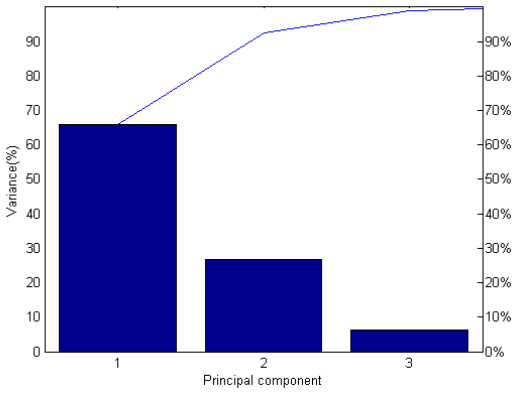

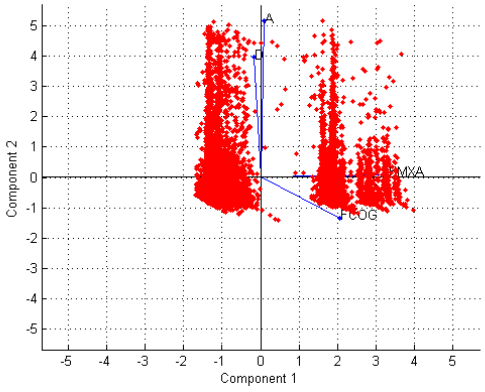

CANAL QI 15

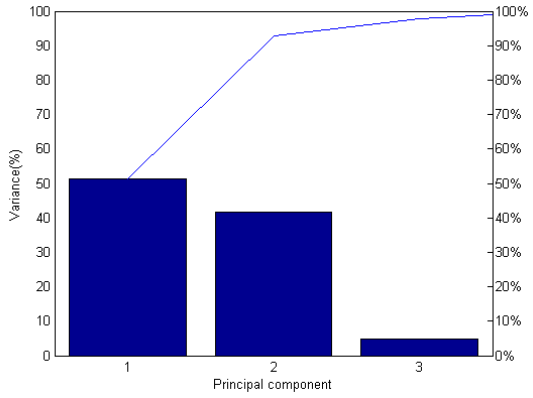

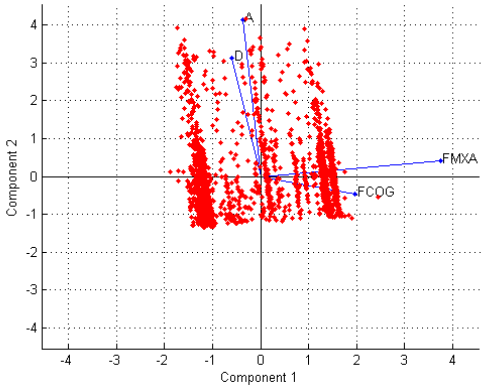

AP-PLY 2

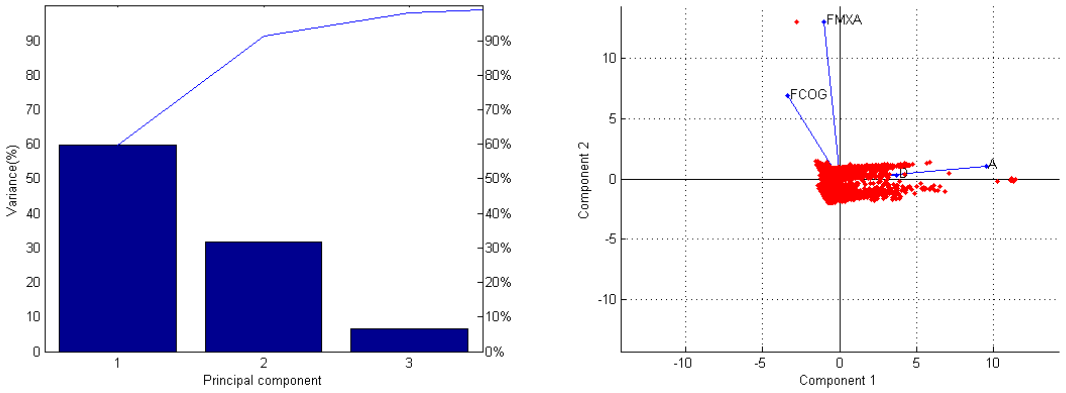

AP-PLY 7

Figure 6-5: *Variance and cumulative variance of each principal component for the representative samples* ***(a)*** *and the component coefficients of AE parameters to the first two principal components* ***(b)***.

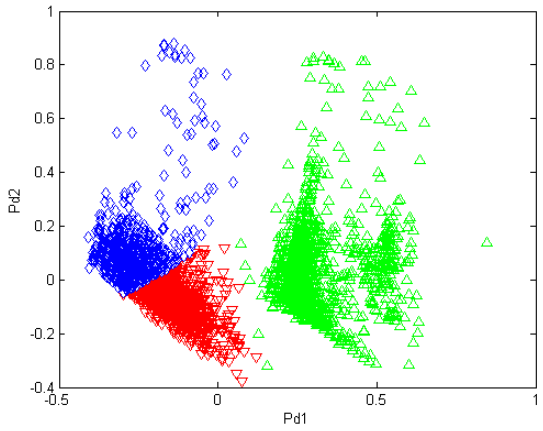

CANAL QI 4

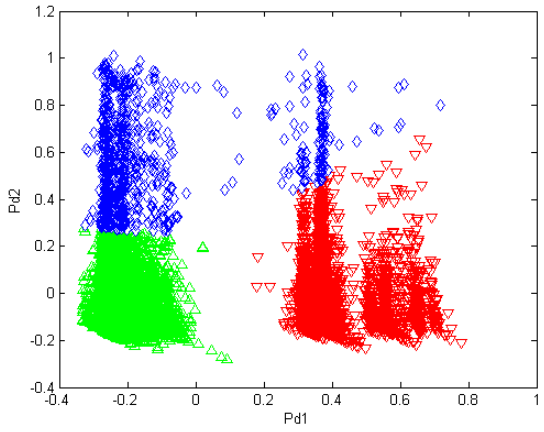

CANAL QI 15

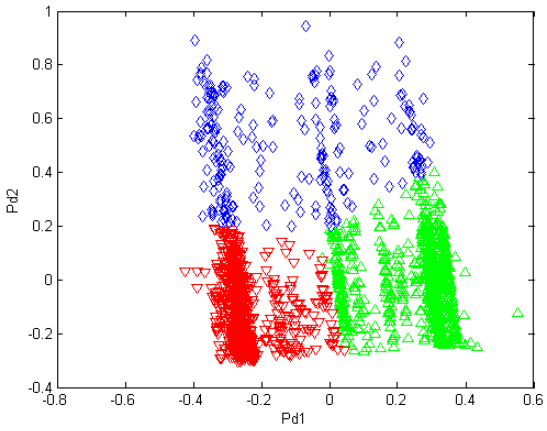

AP-PLY 2

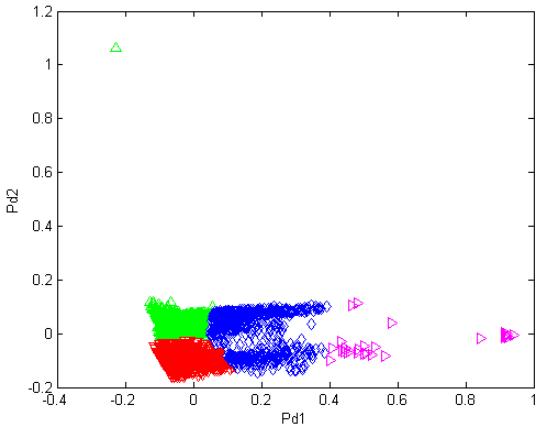

AP-PLY 7

Figure 6-6: *PCA projection of k-means ++ clustering for the CANAL QI and APPLY representative samples*

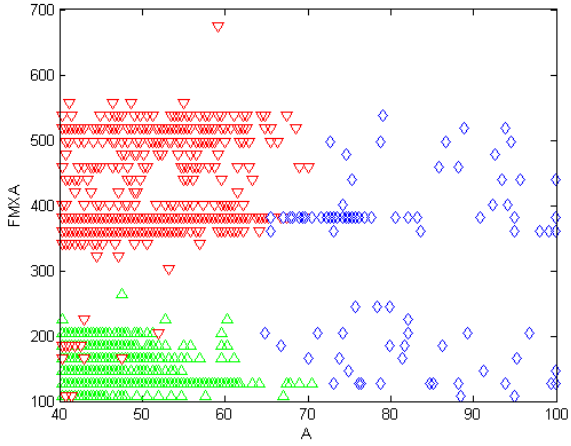

CANAL QI 4

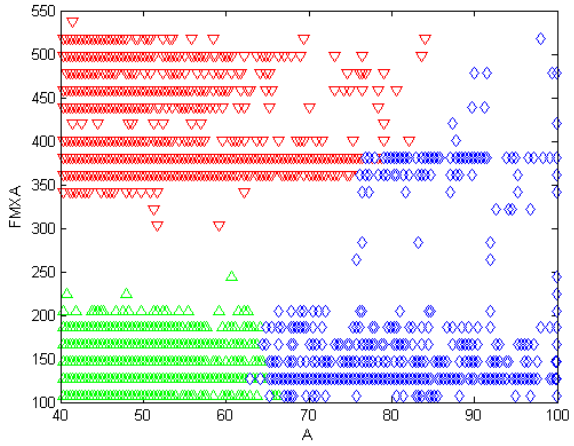

CANAL QI 15

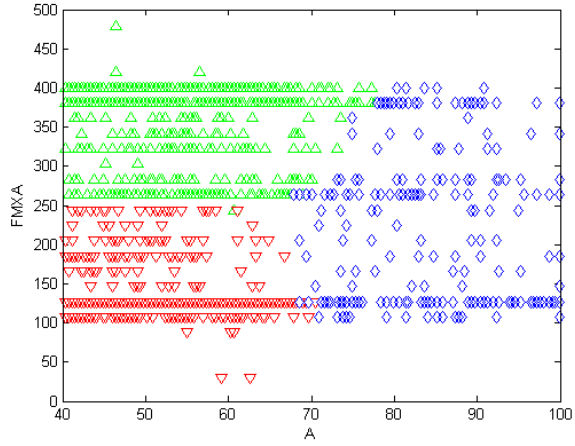

AP-PLY 2

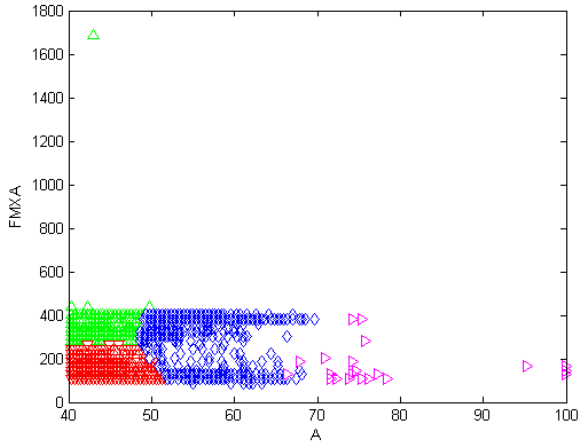

AP-PLY 7

Figure 6-7: *Cluster results separated by amplitude vs. frequency for CANAL QI and APPLY representative specimens*

	CANAL QI 4		CANAL QI 15		APPLY 2		APPLY 7	
	Pd1	Pd2	Pd1	Pd2	Pd1	Pd2	Pd1	Pd2
λ1	0.928395	**5.983902**	0.081064	**5.173544**	-0.376	**4.144132**	1.075955	**9.568458**
λ2	0.34893	3.807184	-0.18141	3.974413	-0.59124	3.13925	0.305639	3.739086
λ3	**3.597147**	0.656358	**3.302432**	0.098495	**3.744804**	0.409111	**12.96586**	-0.99324
λ4	3.005253	-2.60657	2.046404	-1.33915	1.974581	-0.45745	6.845821	-3.35936

Table 6-2: *The principal component coefficients for four AE parameters*

	Cluster bounds	Peak Amplitude Range (*dB*)	Peak Frequency Range (*kHz*)
CANAL QI, 0°	**Cluster 1**	40-65	0-300
	Cluster 2	40-65	0-550
	Cluster 3	65-100	0-550
CANAL QI, 90°	**Cluster 1**	40-65	0-250
	Cluster 2	40-65	0-550
	Cluster 3	40-80	300-550
AP-PLY, 90°	**Cluster 1**	40-70	0-250
	Cluster 2	40-70	250-450
	Cluster 3	70-100	100-450
AP-PLY, 0°	**Cluster 1**	40-50	100-250
	Cluster 2	40-50	250-400
	Cluster 3	50-70	100-450
	Cluster 4	70-100	100-450

Table 6-3: *Cluster bounds for CANAL QI and AP-PLY specimens in different directions*

6.4. Discussion

In order to primarily correlate the resulted clusters with different damage mechanisms, three general clusters for all the tested specimens were compared with peak amplitude distribution and peak frequency band which represents different damage mechanisms in carbon fiber composite materials in literature [2,5,8,9,19,22]. Cluster 1 have similar distribution with A-type signal as discussed in [19,22], which corresponds to matrix cracking. Similarly, Cluster 2 with the same amplitude distribution as Cluster 2 and wider frequency range relates to fiber-matrix debonding (B-type signal) [19]. Cluster 3 with higher peak frequency more than 300 *kHz* and a broad amplitude range have similar amplitude distribution with D-type signal which relates to delamination. High frequency can also be an indication of fiber breakage, given by different authors. [6-13] This correspondence should be confirmed and detailed in the future works.

6.5. References

1. Bourchak M, Farrow I, Bond I, Rowland C, Menan F, Acoustic emission energy as a fatigue damage parameter for CFRP composites. International Journal of Fatigue 2007; 29(3): 457-70.
2. Bourchak M, Khan A, Badr SA, Harasani W. Acoustic emission characterization of matrix damage initiation in woven CFRP composites. Materials Sciences & Applications 2013; 4(9): 509-15.
3. De Greef N, Gorbatikh L, Godara A, Mezzo L, Lomov SV, Verpoest I. The effect of carbon nanotubes on the damage development in carbon fiber/epoxy composites. Carbon 2011; 49(14): 4650-64.
4. Bogdanovich AE, Karahan M, Lomov SV, Verpoest I. Quasi-static tensile behavior and damage of carbon/epoxy composite reinforced with 3D non-crimp orthogonal woven fabric. Mechanics of Materials 2013; 62: 14-31.
5. Lomov SV, Karahan M, Bogdanovich A, Verpoest I. Monitoring of acoustic emission damage during tensile loading of 3D woven carbon/epoxy composites. Textile Research Journal; 2014: 0040517513519510.
6. Sause M, Gribov A, Unwin A, Horn S. Pattern recognition approach to identify natural clusters of acoustic emission signals. Pattern Recognition Letters 2012; 33(1): 17-23.
7. Sause M, Müller T, Horoschenkoff A, Horn S. Quantification of failure mechanisms in mode-I loading of fiber reinforced plastics utilizing acoustic emission analysis. Composites Science and Technology; 72(2): 167-74.
8. Gutkin R, Green C, Vangrattanachai S, Pinho S, Robinson P, Curtis P. On acoustic emission for failure investigation in CFRP: Pattern recognition and peak frequency analyses. Mechanical Systems and Signal Processing, Volume 25, Issue 4, 2011, Pages: 1393-1407.
9. Valentin D, Bonniau P, Bunsell A. Failure mechanism discrimination in carbon fibre-reinforced epoxy composites, Composites 1983; 14(4): 345-51.
10. Liu P, Chu J, Liu Y, Zheng J. A study on the failure mechanisms of carbon fiber/epoxy composite laminates using acoustic emission. Materials & Design 2012; 37: 228-35.
11. Berthelot J, Rhazi J. Acoustic emission in carbon fibre composites. Composites Science and Technology 1990; 37(4): 411-28.
12. Lomov SV, Ivanov D, Truong T, Verpoest I, Baudry F, Vanden Bosche K, et al. Experimental methodology of study of damage initiation and development in textile composites in uniaxial tensile test. Composites Science and Technology 2008; 68(12): 2340-9.

13. De Groot PJ, Wijnen PA, Janssen RB. Real-time frequency determination of acoustic emission for different fracture mechanisms in carbon/epoxy composites. Composites Science and Technology 1995; 55(4): 405-12.
14. Li L, Lomov SV, Yan X, Carvelli V. Cluster analysis of acoustic emission signals for 2D and 3D woven glass/epoxy composites. Composite structures 2014; 116: 286–99.
15. Alelyani S, Tang J, Liu H. Feature selection for clustering: a review. In: Aggarwal Charu, Reddy Chandan, editors. Data clustering: algorithms and applications. CRC Press; 2013.
16. He X, Cai D, Niyogi P. Laplacian score for feature selection. Advances in Neural Information Processing Systems 2005; p. 14.
17. Cai D, Zhang C, He X. Unsupervised feature selection for multi-cluster data. Proceedings of the 16th ACM SIGKDD international conference on knowledge discovery and data mining. ACM; 2010. p. 333–42.
18. Jolliffe I. Principal component analysis. Wiley Online Library; 2005.
19. Marec A, Thomas J-H, El Guerjouma R. Damage characterization of polymer based composite materials: multivariable analysis and wavelet transform for clustering acoustic emission data. Mechanical Systems and Signal Processing 2008; 22: 1441–64.
20. Pashmforoush F, Fotouhi M, Ahmadi M. Acoustic emission-based damage classification of glass/polyester composites using harmony search k-means algorithm. Reinforced Plastic and Composites 2012; 31: 671–80.
21. Arthur D, Vassilvitskii S. K-means++: the advantages of careful seeding. In: Proceedings of the eighteenth annual ACM-SIAM symposium on discrete algorithms: Society for Industrial and Applied Mathematics; 2007. p. 1027–35.
22. Godin N, Huguet S, Gaertner R. Integration of the Kohonen's self-organizing map and k-means algorithm for the segmentation of the AE data collected during tensile tests on cross-ply composites. NDT & E International 2005; 38: 299–309.
23. Maulik U, Bandyopadhyay S. Performance evaluation of some clustering algorithms and validity indices. The IEEE Transactions on Pattern Analysis and Machine Intelligence 2002; 24: 1650–4.
24. Wang G, Wang Z, Chen W, Zhuang J. Classification of surface EMG signals using optimal wavelet packet method based on Davies–Bouldin criterion. Medical & Biological Engineering & Computing 2006; 44: 865–72.
25. Godin N, Huguet S, Gaertner R, Salmon L. Clustering of acoustic emission signals collected during tensile tests on unidirectional glass/polyester composite using supervised and unsupervised classifiers. NDT & E International 2004; 37: 253–64.

7

Conclusions

7.1. Summary of the results and critical remarks

7.1.1. Tensile mechanical properties obtained by DIC full-field strain registration

One of the aims to perform the tensile tests was to investigate and compare the tensile mechanical properties such as elasticity modulus and Poisson's ratio of the different test specimens oriented in different directions; with or without manufacturing defects. Consequently, the following observations have been made:

- Since the CANAL QI laminate was quasi-isotopic and as it was expected from Classical Laminate Theory (CLT), the obtained mechanical properties in 0^0 and 90^0 directions were quite close.
- The tensile properties of the CANAL QI specimen oriented in 0^0 direction with overlap are more or less the same as those of the specimens in the same direction without defects.
- The tensile properties of the CANAL QI specimen oriented in 0^0 direction with gap are significantly higher than those of the specimens in the same direction without defects.
- The average tensile properties of the CANAL QI specimens oriented in 90^0 direction with overlap are higher than those of the specimens in the same direction with gap.
- The average tensile properties of the AP-PLY specimens oriented in 0^0 direction are notably higher (about 85% higher) than those of the specimens oriented in 90^0 direction. This was somehow quite predictable since the AP-PLY laminate was not quasi-isotropic.
- Comparing the theoretical values for the mechanical properties obtained by Classical Laminate Theory (CLT) with the measured values, it is seen that the longitudinal and transverse Young's moduli E_x and E_y are slightly over predicted by CLT. For the CANAL QI laminate the predicted effective in-plane Poisson's ratios are slightly smaller and for AP-PLY laminate are slightly greater in comparison with the measured values.

7.1.2. Damage investigation by AE registration

From collected AE data the following observations have been made:

- At the very beginning of the test, few events of low energy occur with low frequency. Then the frequency of events increases sharply and the energy content reaches higher levels. This is reflected by the increase of the slope of the cumulative AE event energy curve. It is noted that the sudden increase in the cumulative energy is associated with the events of higher energy.
- Despite significant AE activity that is indicative of internal damage in the materials (in terms of transverse cracks, fiber breakage, etc), no visible changes are noted in the stress strain curves. The latter show linear behavior. This can be explained by the fact that 90°-carbon yarns contribute less than 5% to the stiffness of the composite. In the case of glass fibers, for example, the stress-strain curves show visible deviation from linear behavior at the first jump in AE cumulative energy showing permanent changes in the material. The deviation in the case of glass fibers is noticeable due to the fact that 90°- yarns in glass fiber reinforced composites contribute more than 20% of the composite stiffness.
- AE activity is increased in the course of the loading (less events in the beginning and more towards the end).
- The AE curves of accumulated energy as a function of strain for different specimens with same conditions (sample direction and defect types) show small scatters for CANAL QI samples and relatively large scatters for AP-PLY samples.
- The step-wise changes in the AE diagrams with the appearance of high energy events are related to certain changes in the damage evolution. We have identified three characteristics strain levels for all the tested specimens: ε_{min} for which the first AE event occurs, i.e. low energy acoustic events start to appear; $\varepsilon_1$is the first damage threshold strain at the first increase of the slope of the cumulative AE energy curve; and ε_2 is the second damage threshold strain at the second "knee" on the AE cumulative energy curve.
- The changes in damage mechanism related to these step-wise changes in the AE diagrams should be investigated and detailed by visualizing the damage propagation in the internal structure and studying the microstructure features of the specimens using techniques such as **M**icro-**C**omputed **T**omography **(µCT)** in the future works.

7.1.3. AE clustering analysis

The clustering analysis of AE during tensile loading of Dry Automated Fiber Placement (DAFP) carbon/epoxy composites, loaded in 0^0 and 90^0 directions leads to the following conclusions valid for both directions and for both of the laminates; CANAL QI and AP-PLY:

- AE events can be discriminated in generally three clusters based on peak amplitude, peak frequency, frequency of centroid of gravity and duration. Peak amplitude (PA) and peak frequency (PF) are the most important parameters in this discrimination. Moreover, for all the studied test variants the boundaries of the clusters in PA–PF coordinates are the same and given in Table 6-3. **Cluster1** corresponds to low frequency low amplitude events, **Cluster 2** – moderate frequency, low amplitude, **Cluster 3** – moderate to high frequency, high amplitude.
- The order of the events number in the clusters during the whole test is as follows:
  Cluster 1 > Cluster 2 > Cluster 3
- The correspondence between the AE events in the clusters and the damage mode can be hypothesized based on literature data, as follows: Cluster 1 – matrix cracking, Cluster 2 – fiber/matrix debonding, Cluster 3 –delamination and fiber breakage. This correspondence should be confirmed and detailed in the future work.

7.2. Open issues and future developments

Since investigating the changes in damage mechanisms between different strain thresholds and in correspondence with different clusters obtained by AE clustering analysis, as well as studying the effects of manufacturing defects (gaps and overlaps) in the damage development would only be possible by visual observation of the microstructural features of the internal structure, the future works should be concentrated on verification of the results achieved by AE registration by studying microstructural features of the internal structure using techniques such as Micro-Computed Tomography (μCT).

The μCT investigation allows following the initiation and propagation of damage, monitoring the position and the direction of cracks formed at different loading stages. The evolution of damage could be followed also correlating damage patterns to characteristic thresholds evaluated by means of AE curves.

Appendix A

Quasi-Static Tensile Test Graphs

A.1. CANAL QI specimens

A.1.1. 0^0 specimens without defects

A.1.1.1. Specimens 1, 2, 3

I. Stress vs. Strain curves obtained by DIC analysis

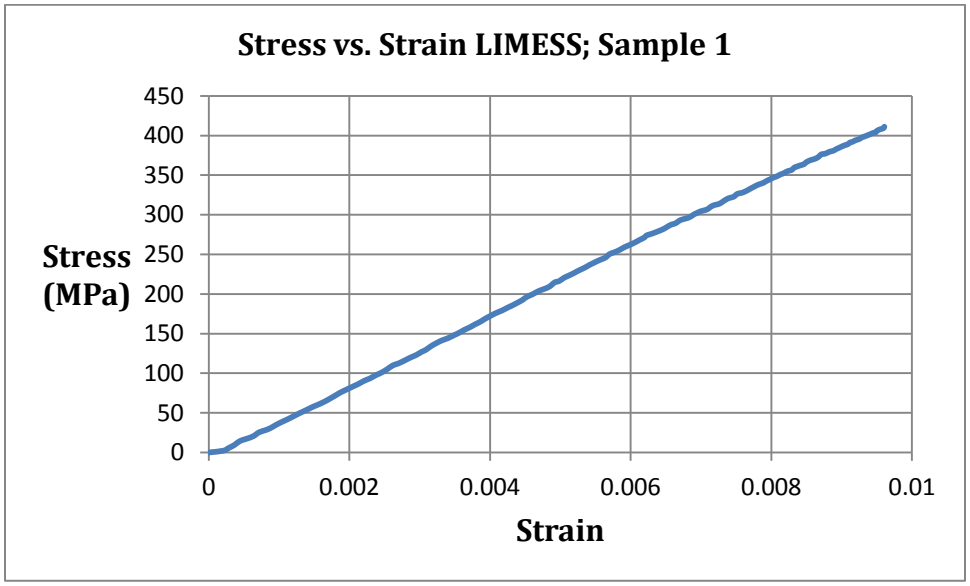

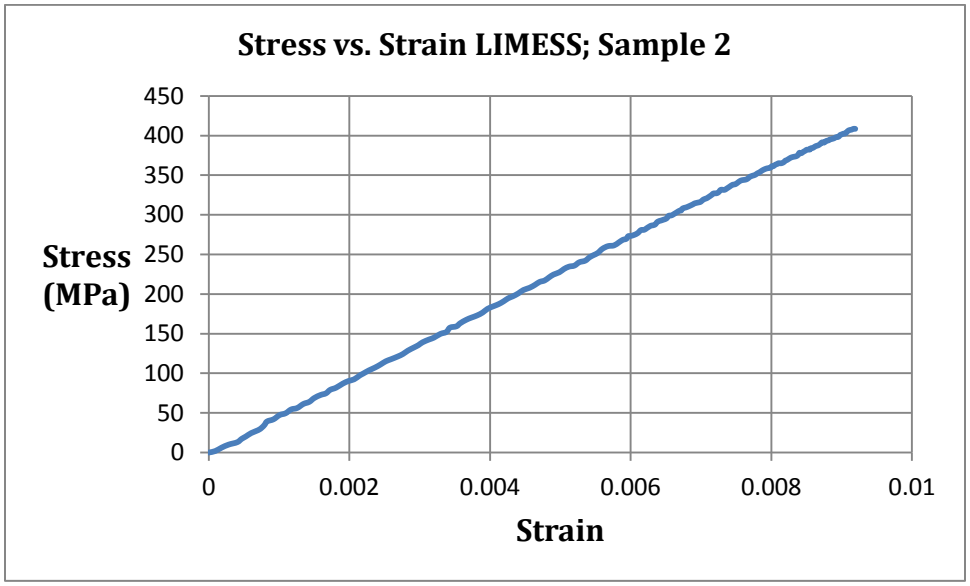
Stress vs. Strain LIMESS; Sample 2
Stress (MPa)
450
400
350
300
250
200
150
100
50
0
0
0.002
0.004
0.006
0.008
0.01
Strain

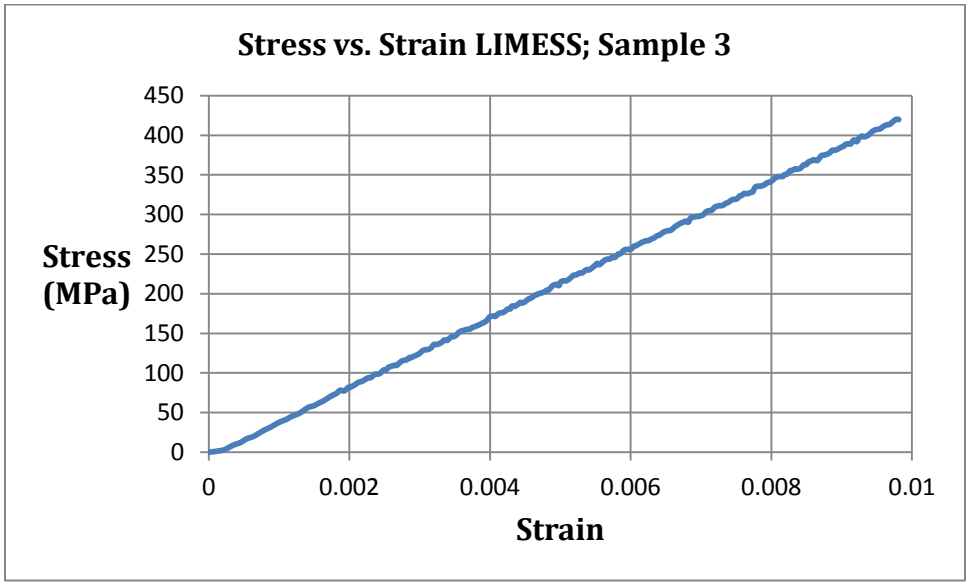
Stress vs. Strain LIMESS; Sample 3
Stress (MPa)
450
400
350
300
250
200
150
100
50
0
0
0.002
0.004
0.006
0.008
0.01
Strain

II. Elasticity Modulus vs. Strain curves obtained by DIC analysis

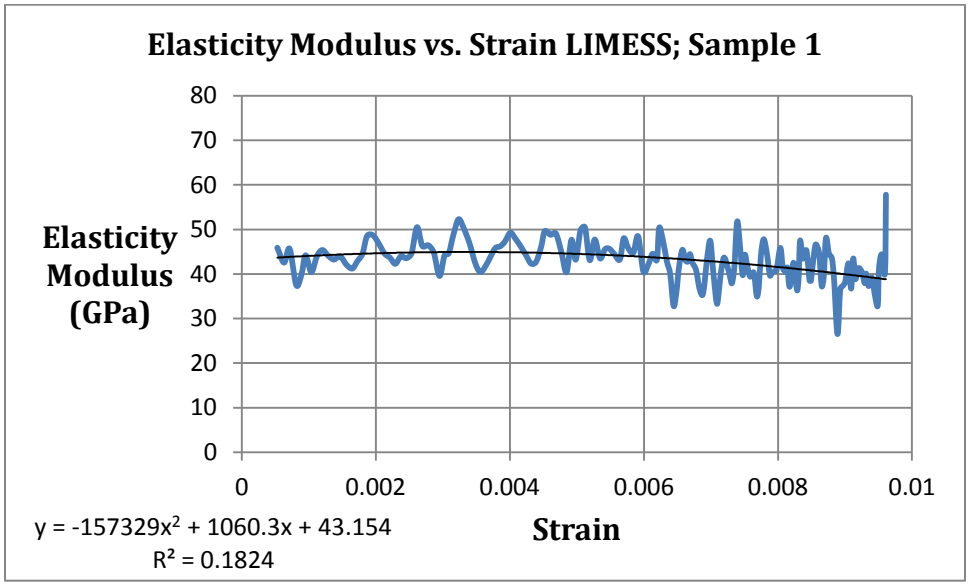

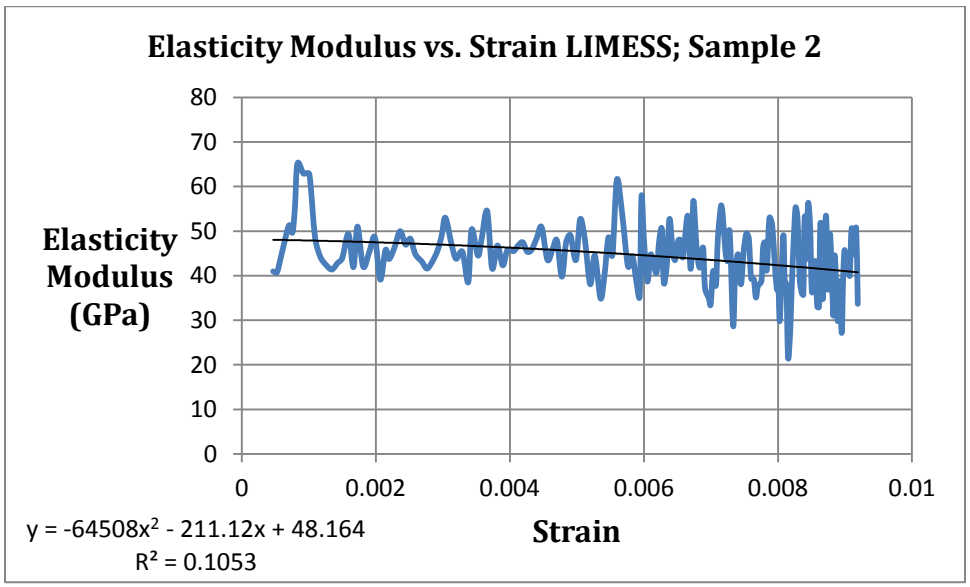

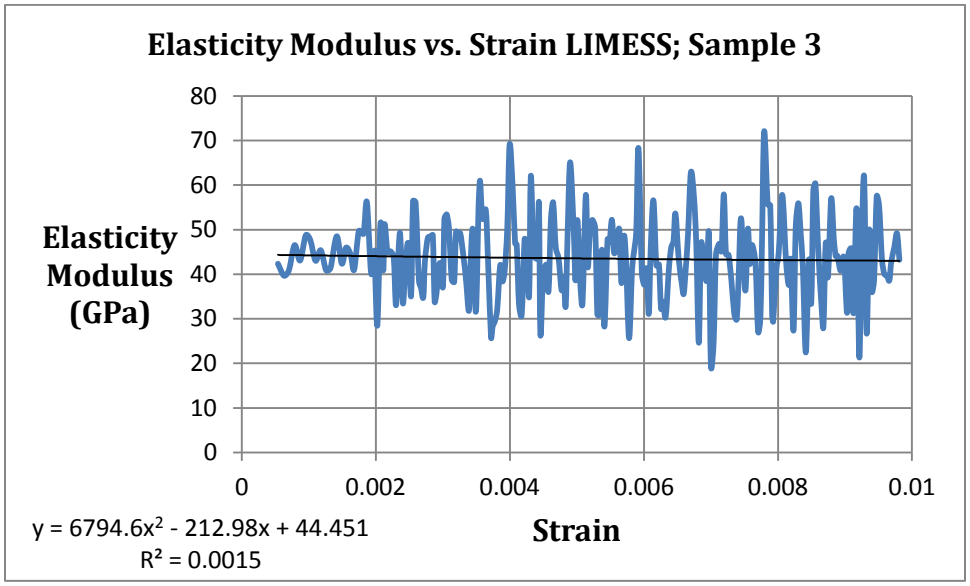

III. Energy – Cumulative Energy – Stress vs. Strain curves obtained by AE analysis

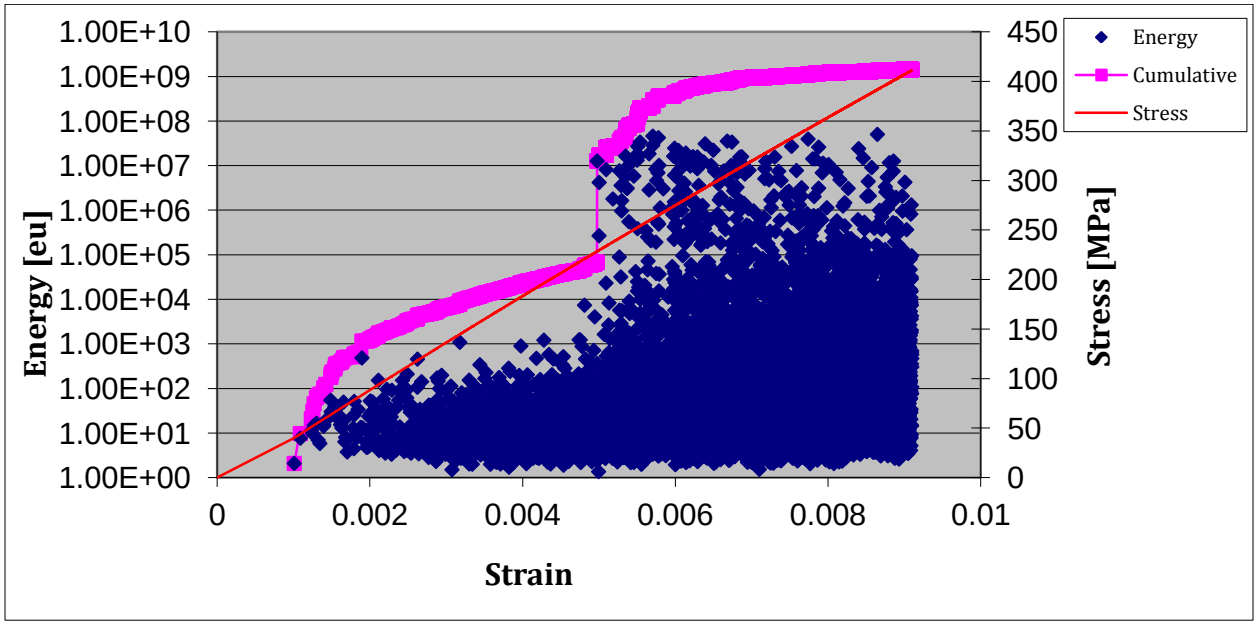

Sample 1

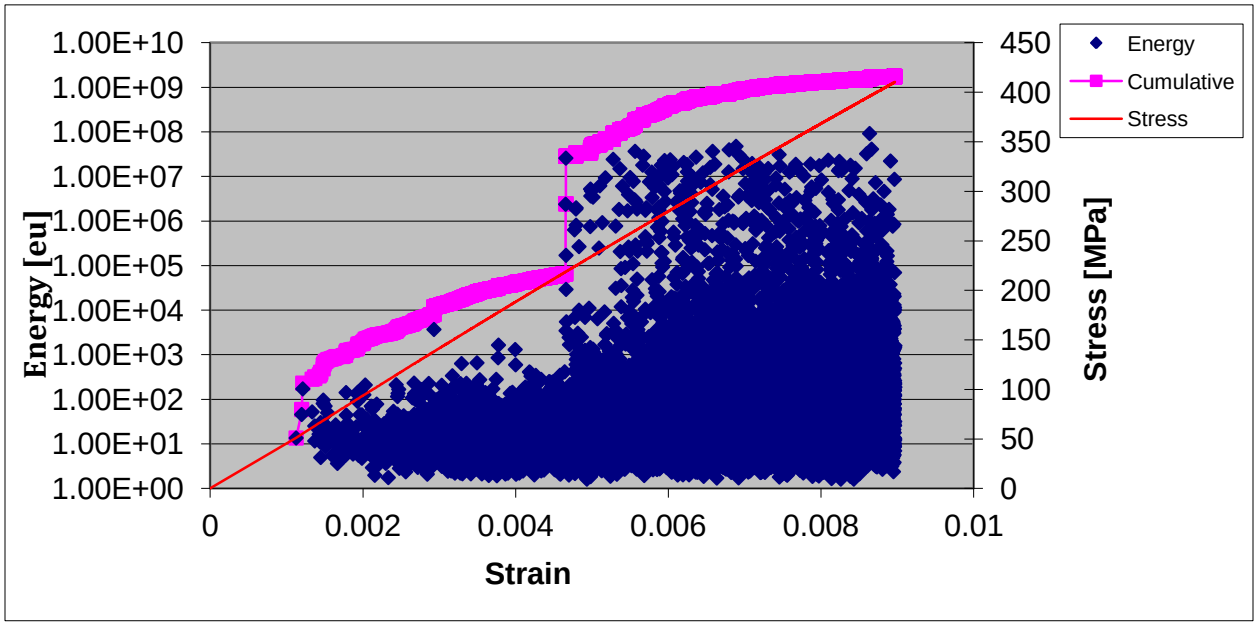

Sample 2

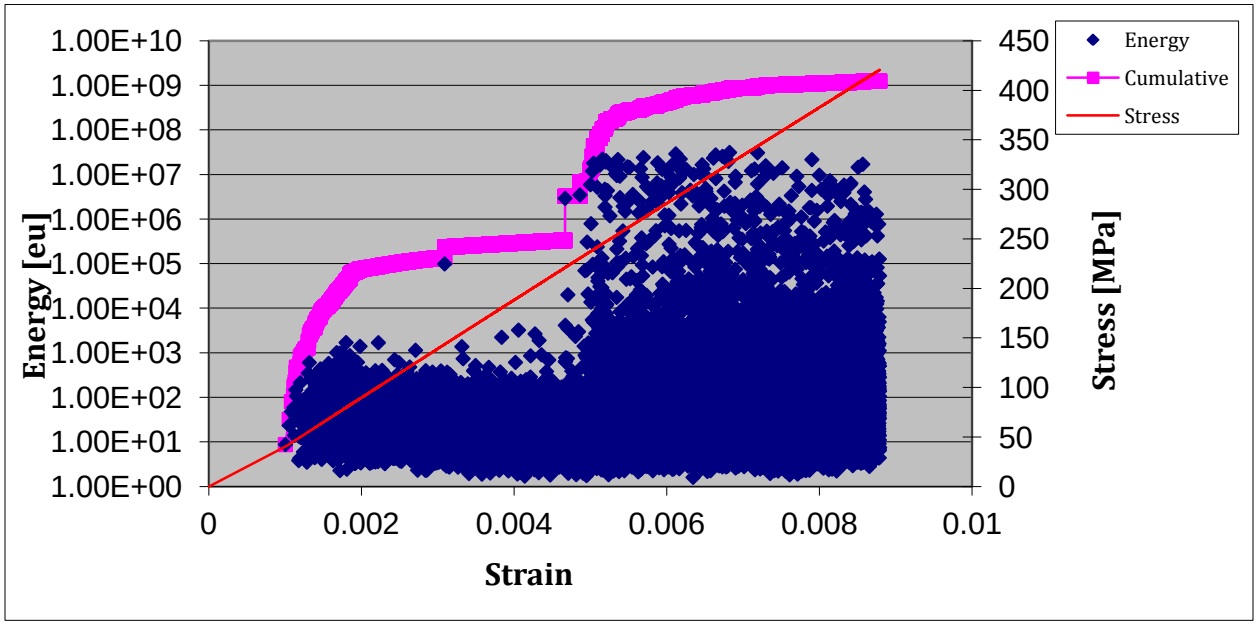

Sample 3

IV. DIC Longitudinal and Transverse Strain Maps at Maximum Strain Level

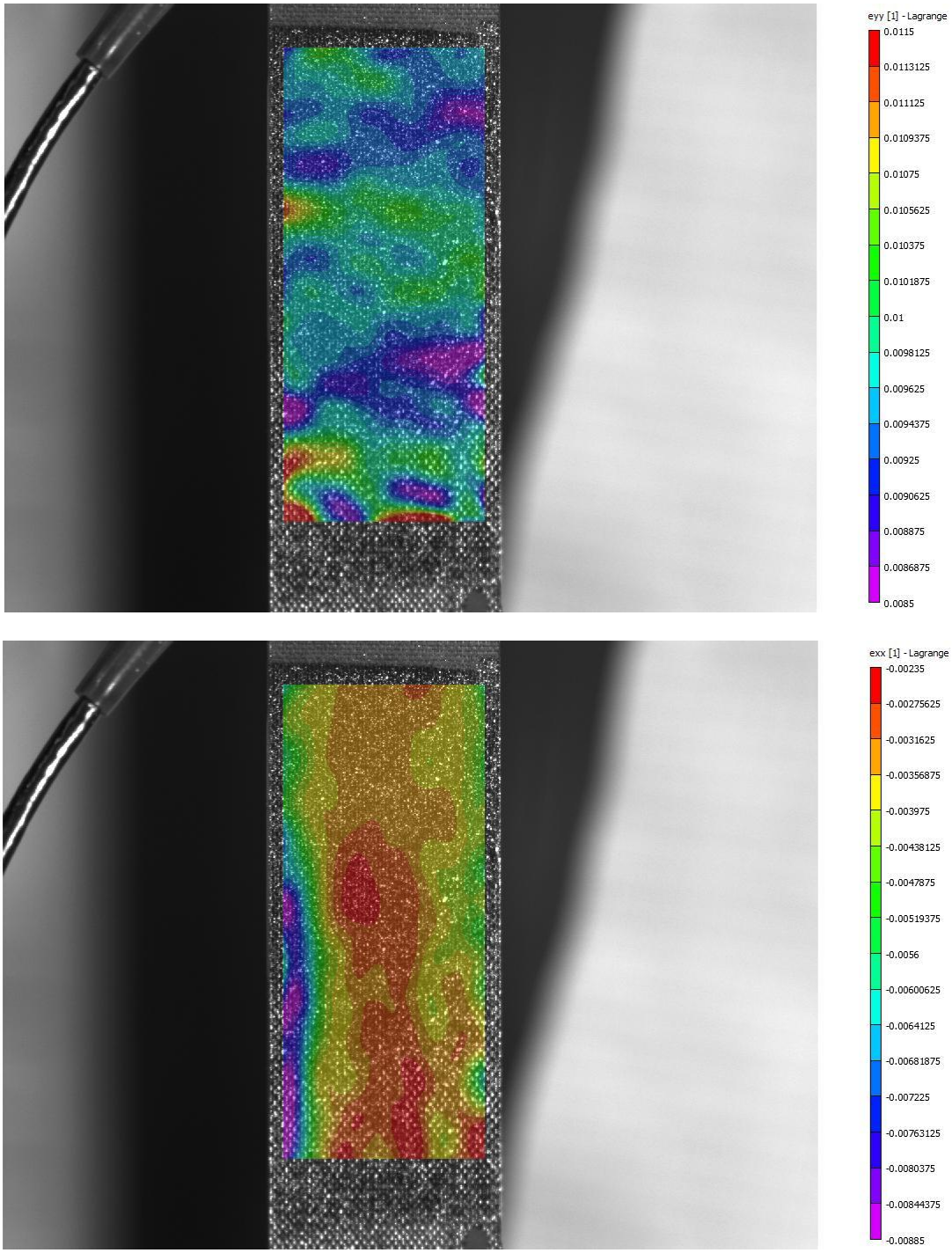

Sample 1 – *Longitudinal and Transversal Strain Maps*

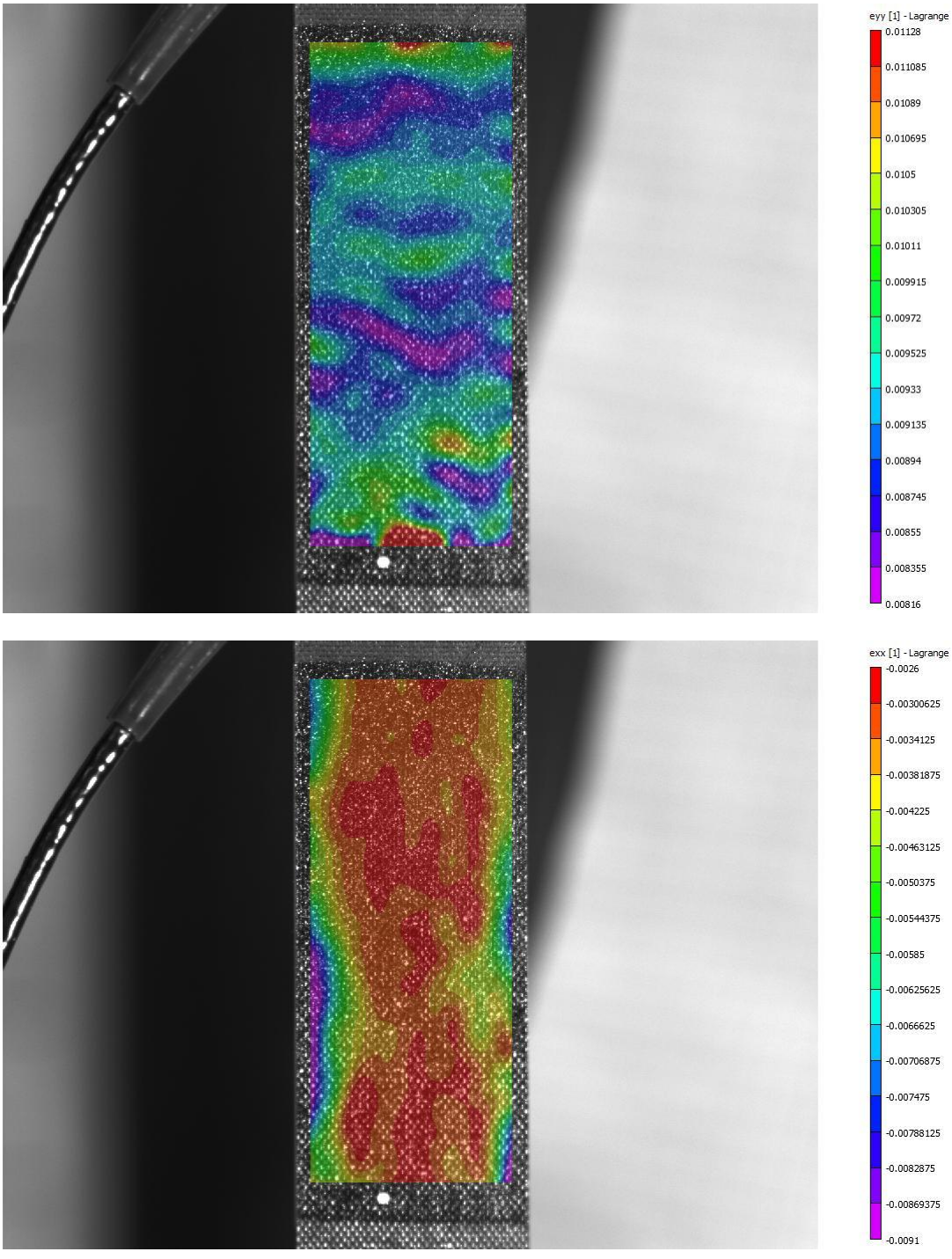

Sample 2 – Longitudinal and Transversal Strain Maps

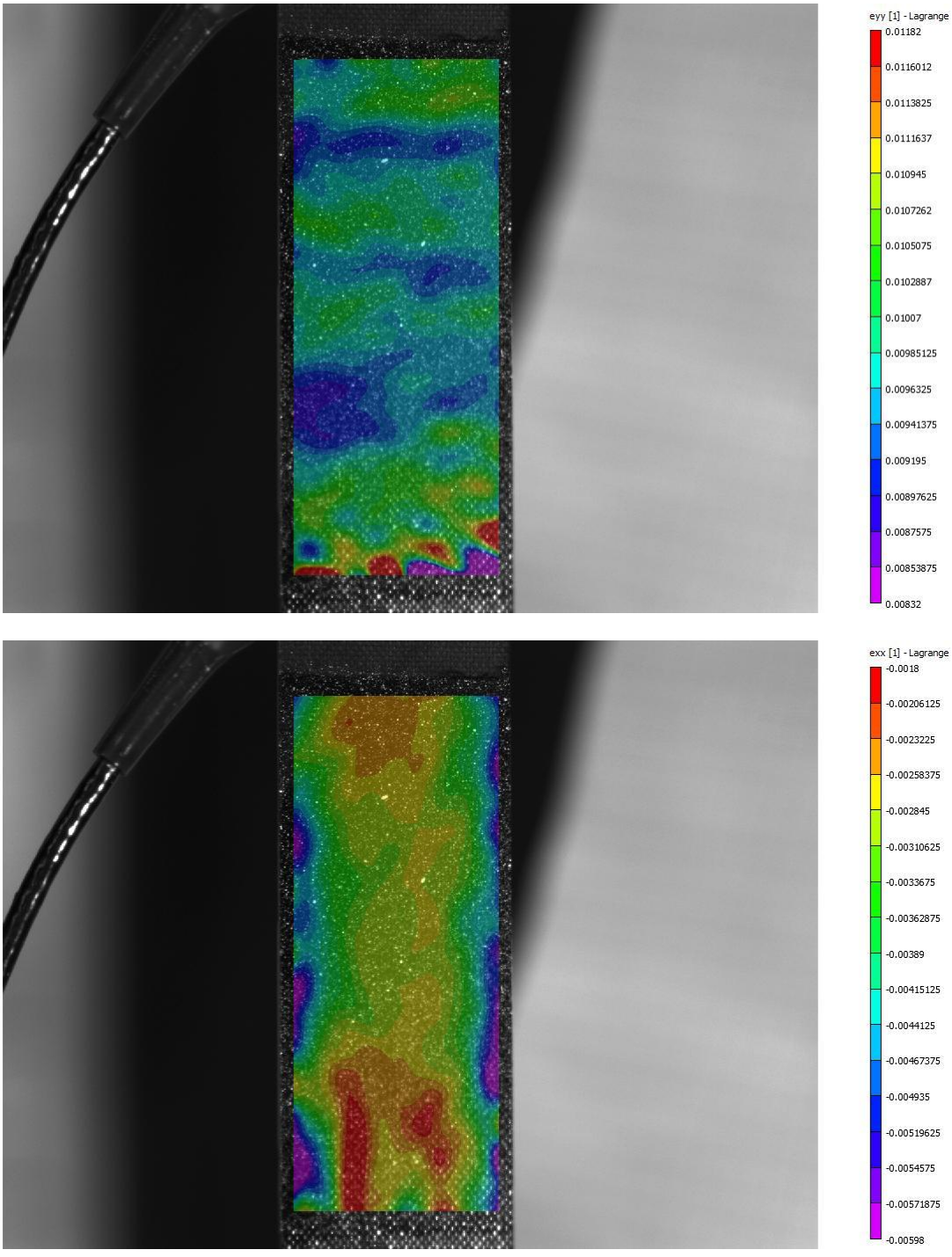

Sample 3 – *Longitudinal and Transversal Strain Maps*

A.1.1.2. Specimens 4, 6, 5

I. Stress vs. Strain curves obtained by DIC analysis

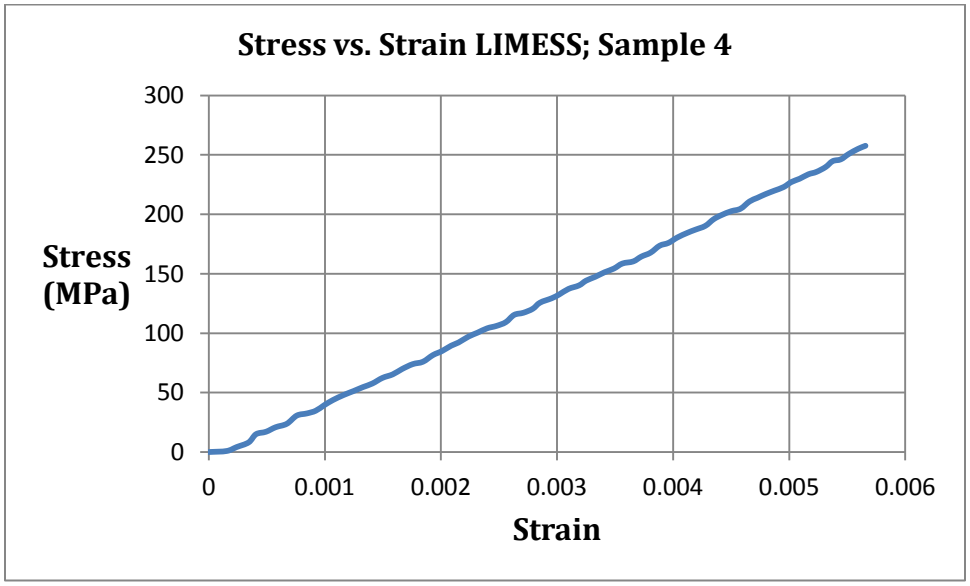

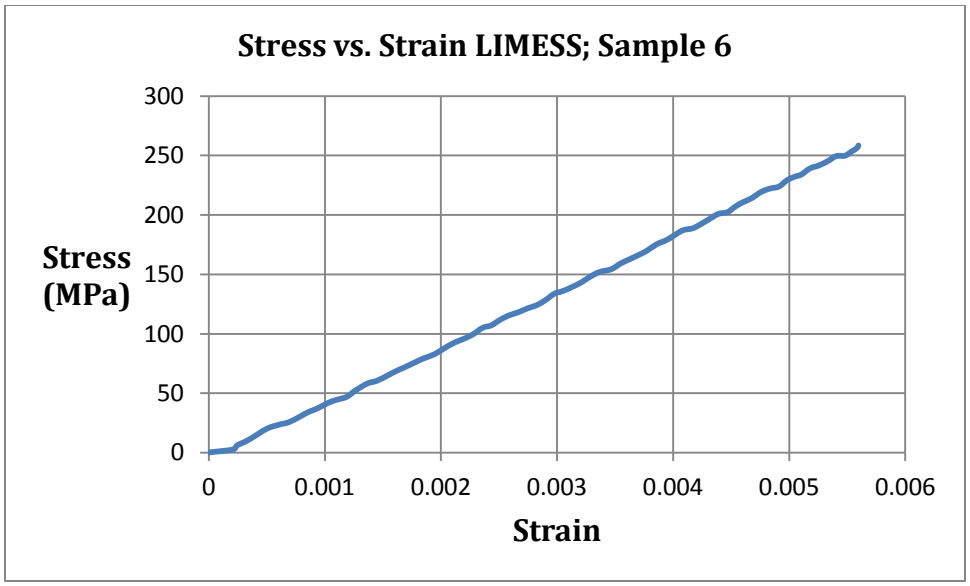

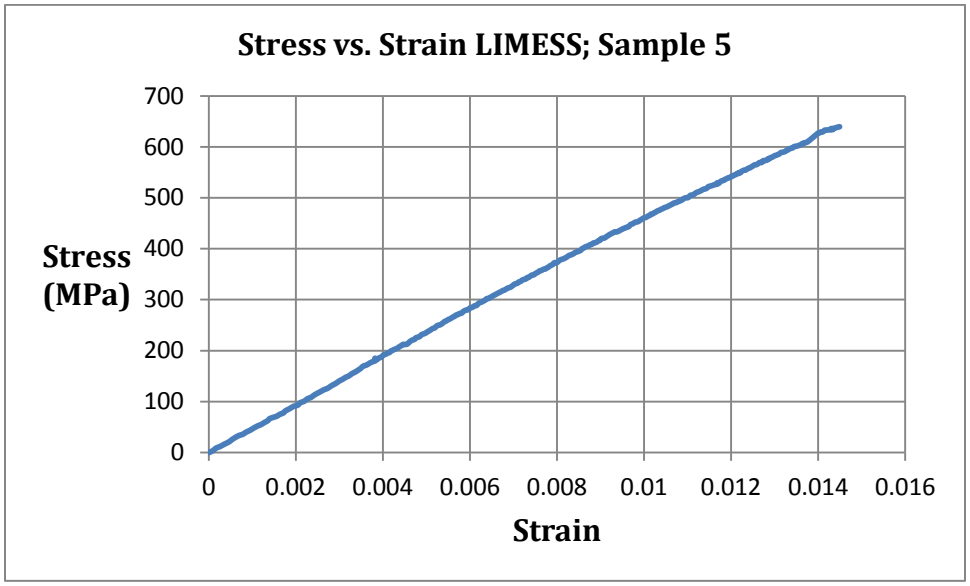

II. Elasticity Modulus vs. Strain curves obtained by DIC analysis

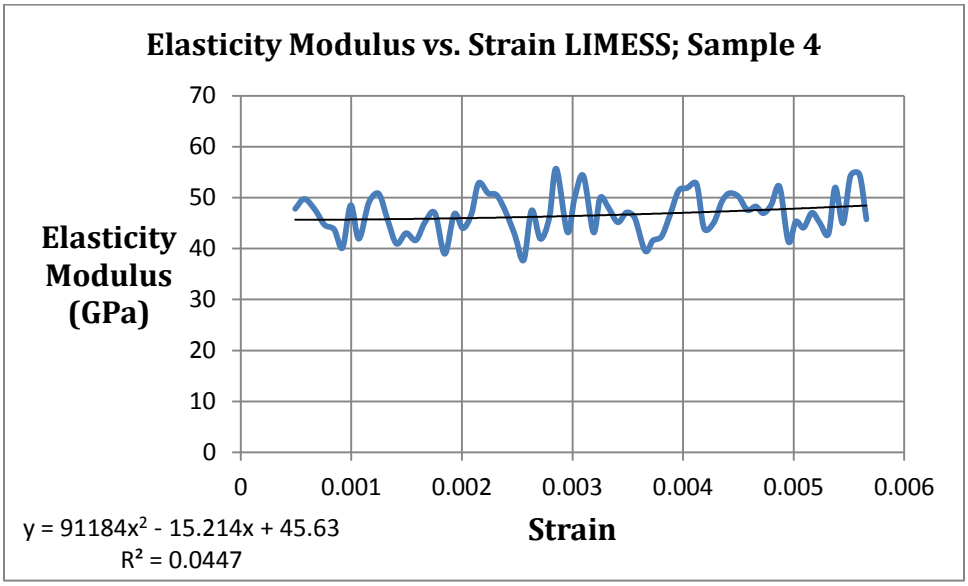

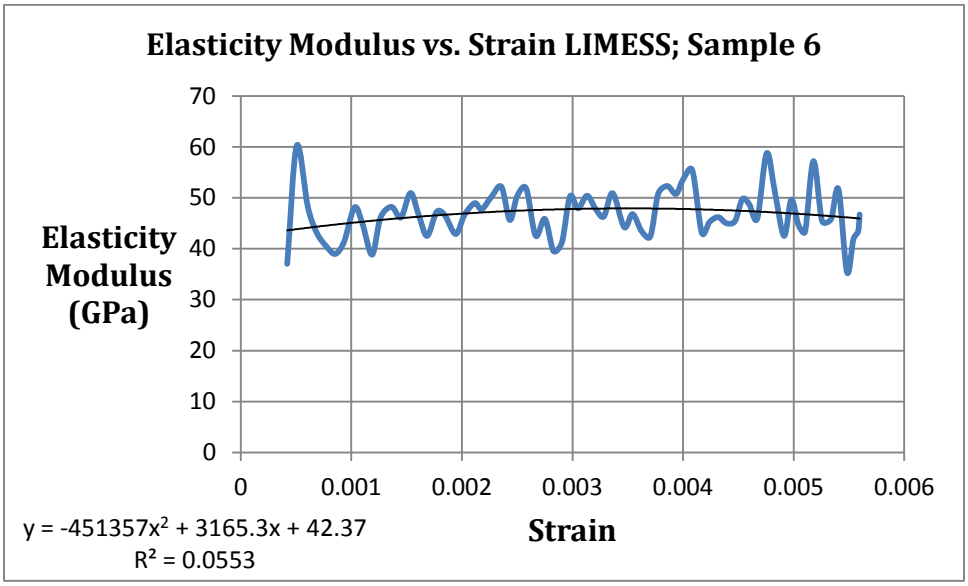
Elasticity Modulus vs. Strain LIMESS; Sample 6
Elasticity Modulus (GPa)
70
60
50
40
30
20
10
0
0
0.001
0.002
0.003
0.004
0.005
0.006
Strain
y = -451357x² + 3165.3x + 42.37
R² = 0.0553

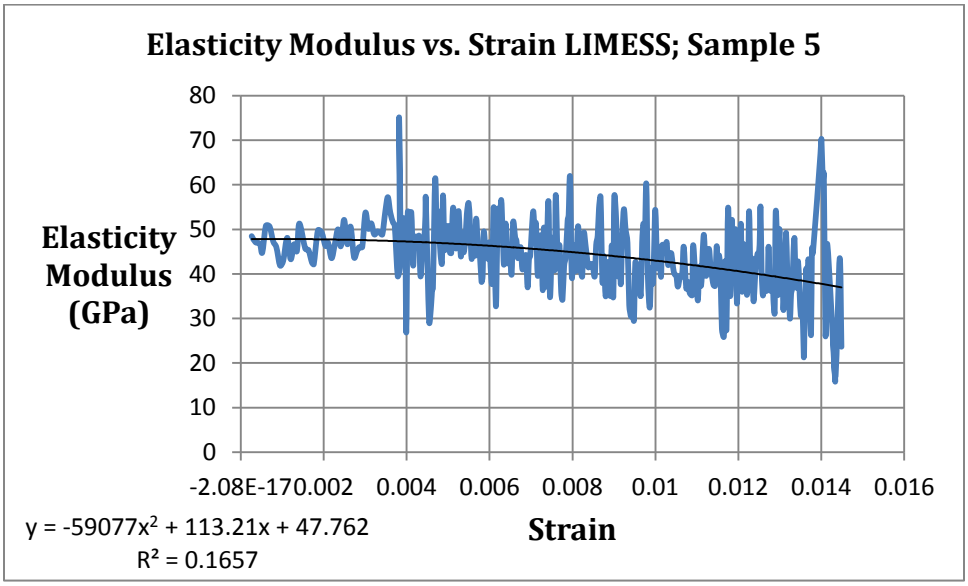
Elasticity Modulus vs. Strain LIMESS; Sample 5
Elasticity Modulus (GPa)
80
70
60
50
40
30
20
10
0
-2.08E-17
0.002
0.004
0.006
0.008
0.01
0.012
0.014
0.016
Strain
y = -59077x² + 113.21x + 47.762
R² = 0.1657

III. Energy – Cumulative Energy – Stress vs. Strain curves obtained by AE analysis

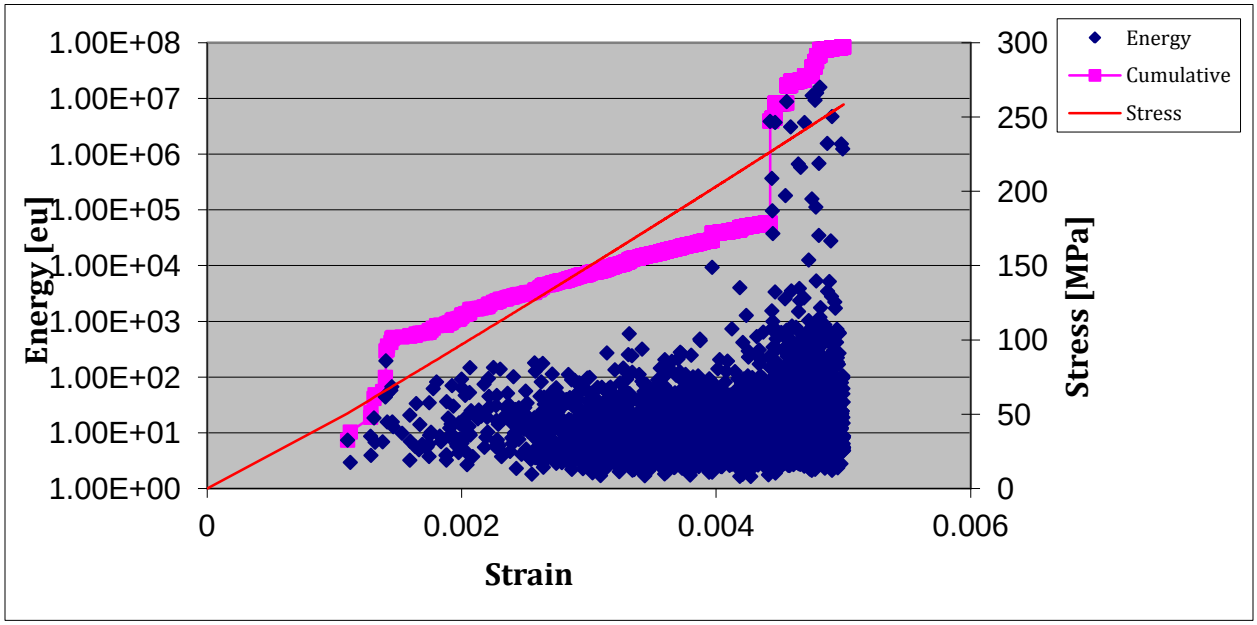

Sample 4

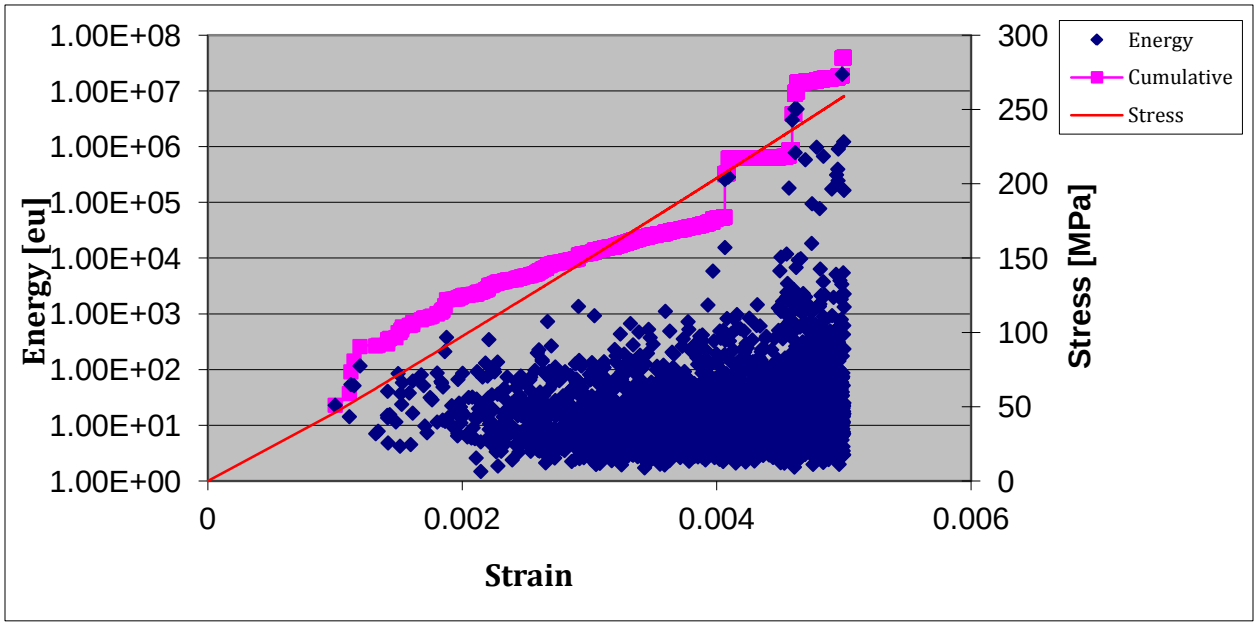

Sample 6

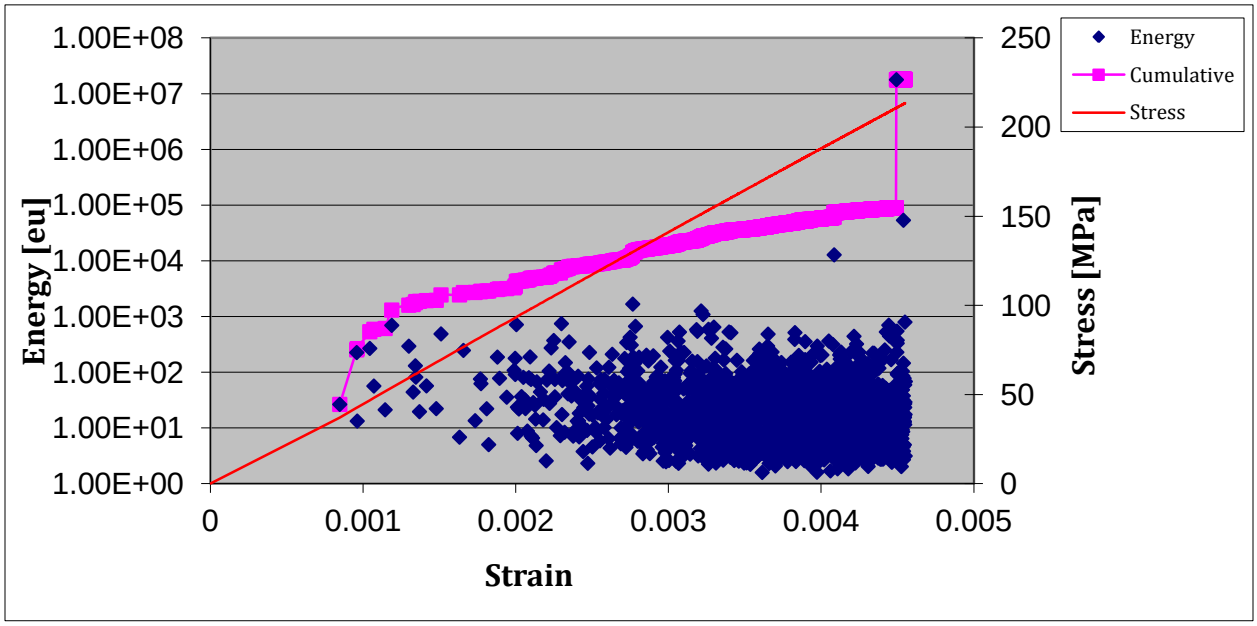
1.00E+08
1.00E+07
1.00E+06
1.00E+05
1.00E+04
1.00E+03
1.00E+02
1.00E+01
1.00E+00
Energy [eu]
250
200
150
100
50
0
Stress [MPa]
0
0.001
0.002
0.003
0.004
0.005
Strain
Energy
Cumulative
Stress

Sample 5

IV. DIC Longitudinal and Transverse Strain Maps at Maximum Strain Level

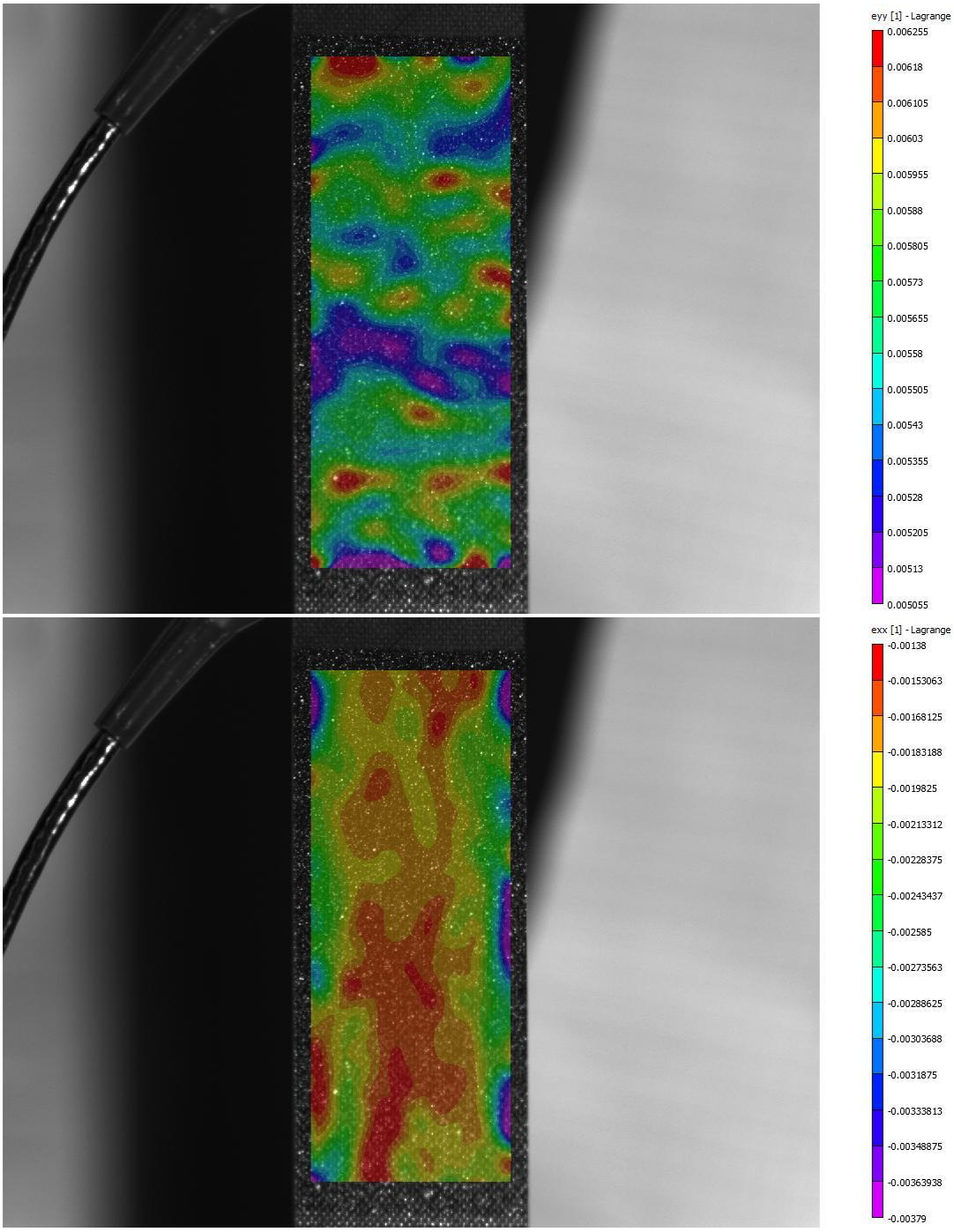

Sample 4 – *Longitudinal and Transversal Strain Maps*

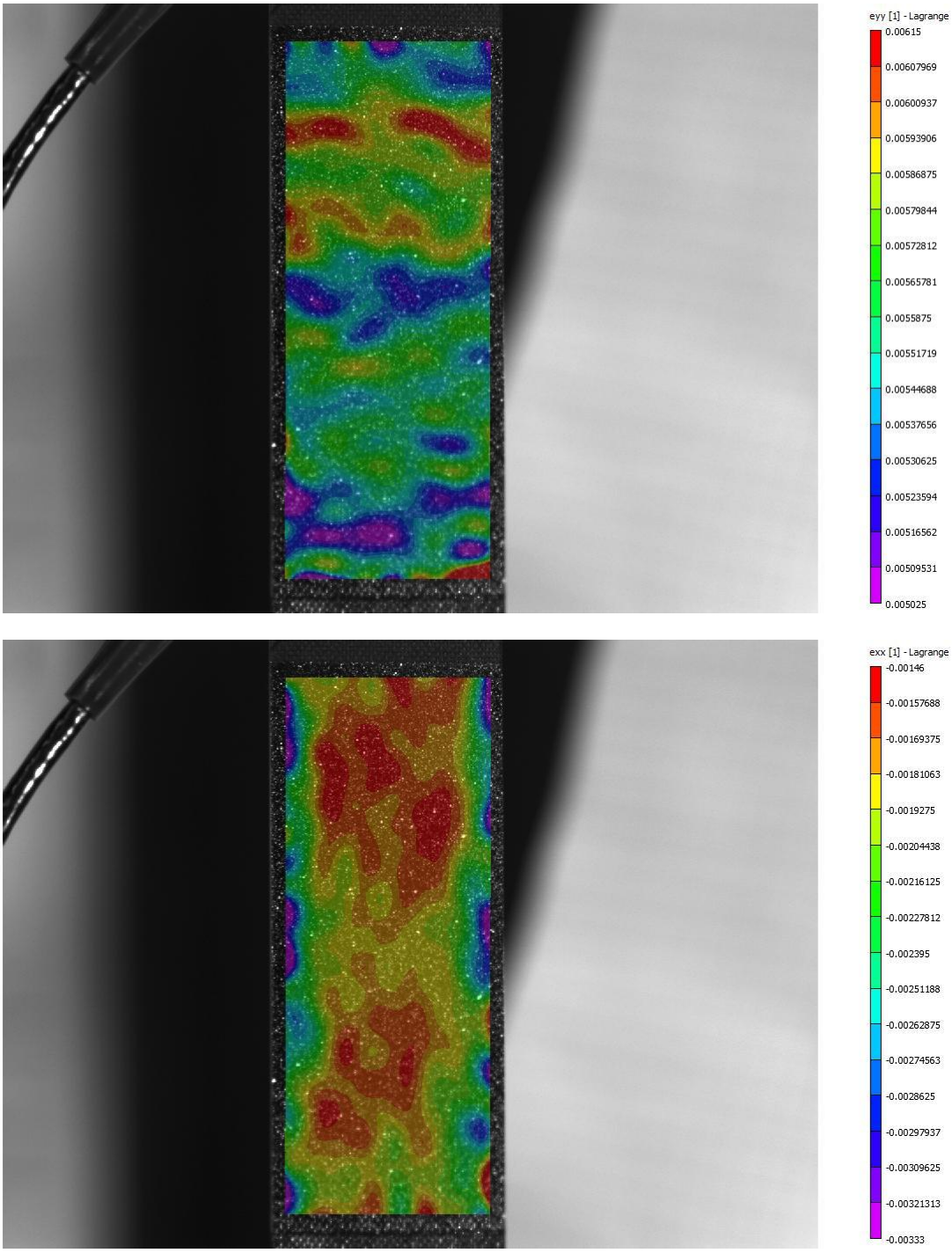

Sample 6 – *Longitudinal and Transversal Strain Maps*

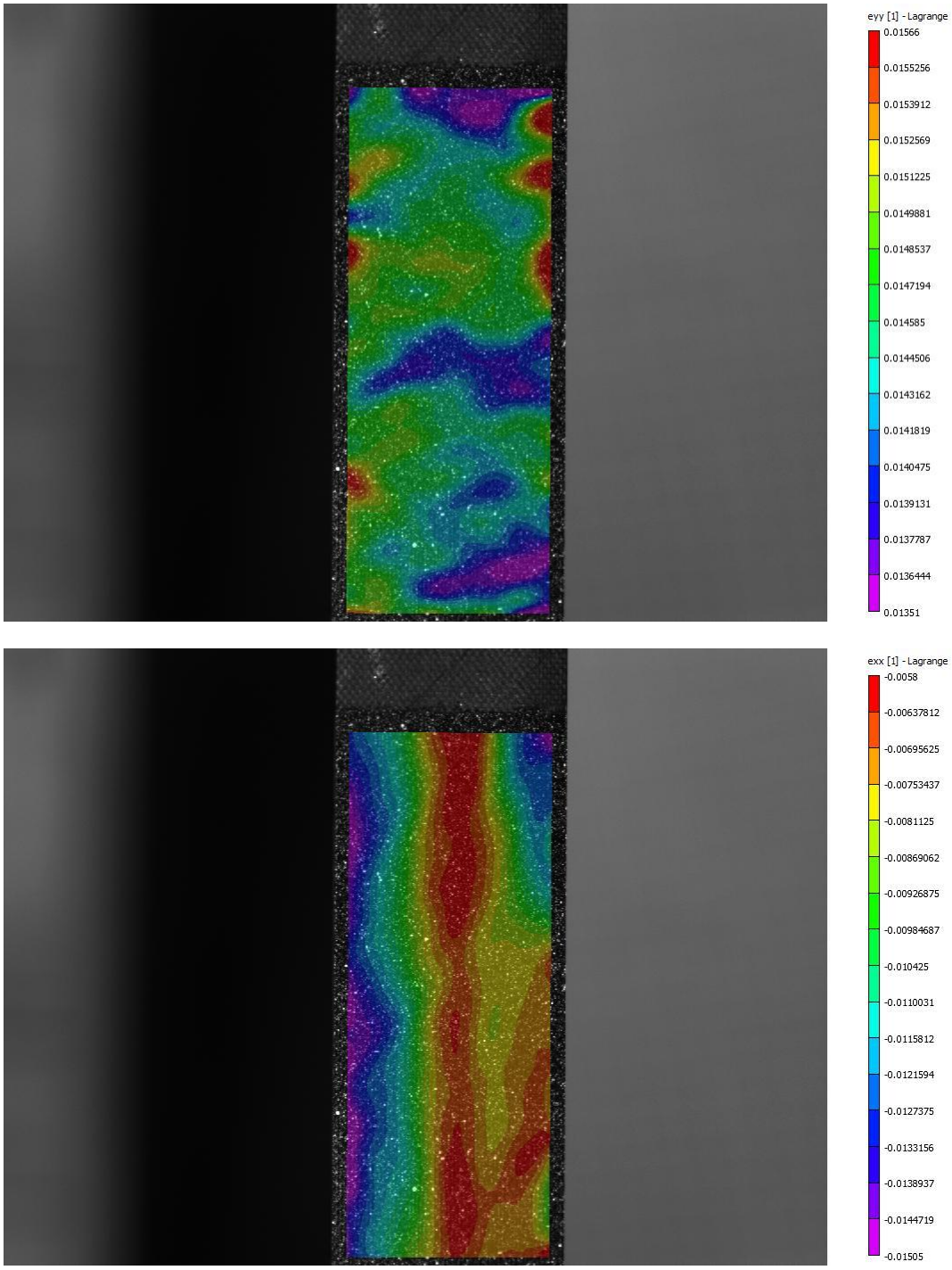

Sample 5 – *Longitudinal and Transversal Strain Maps*

A.1.2. 0^0 specimen with overlap (specimen 9)

I. Stress vs. Strain curves obtained by DIC analysis

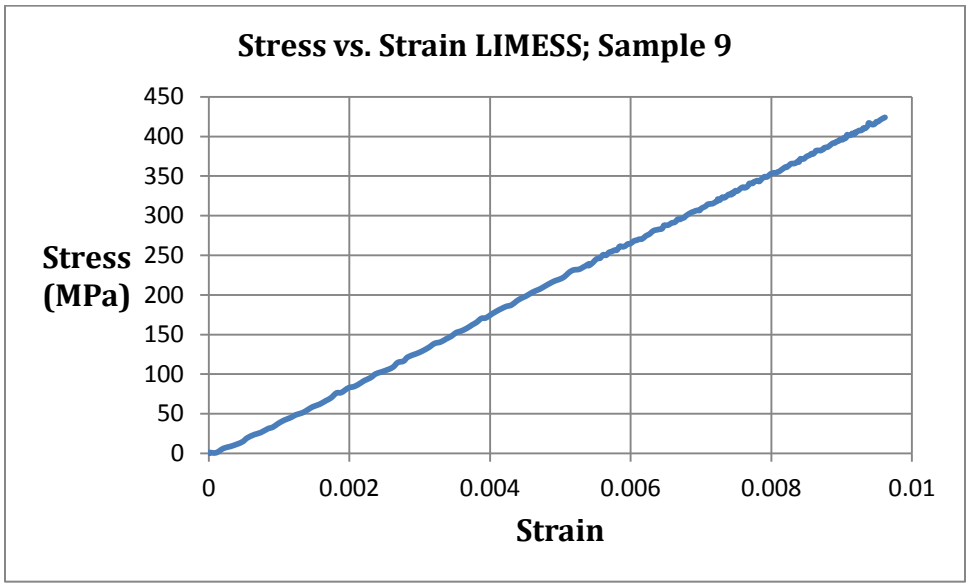

II. Elasticity Modulus vs. Strain curves obtained by DIC analysis

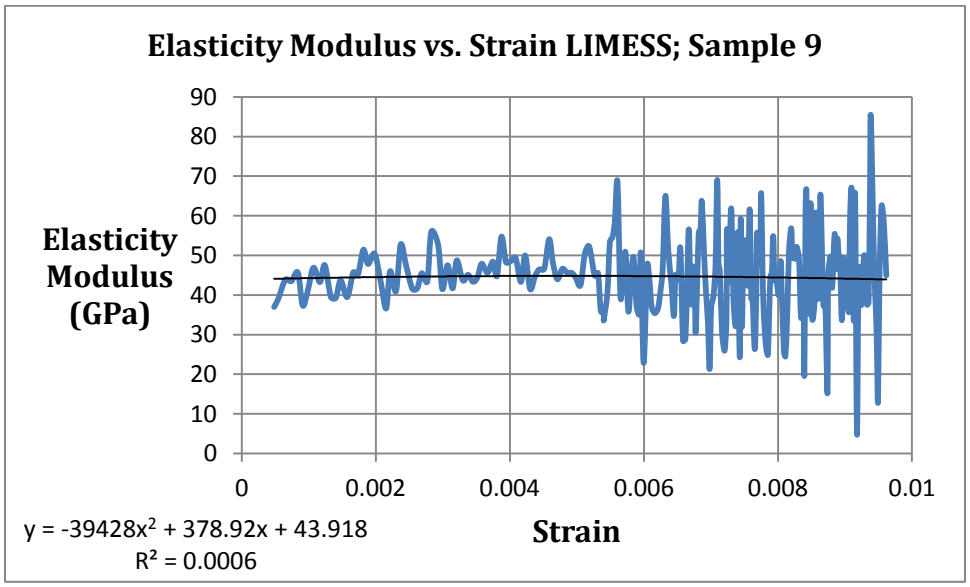

III. Energy – Cumulative Energy – Stress vs. Strain curves obtained by AE analysis

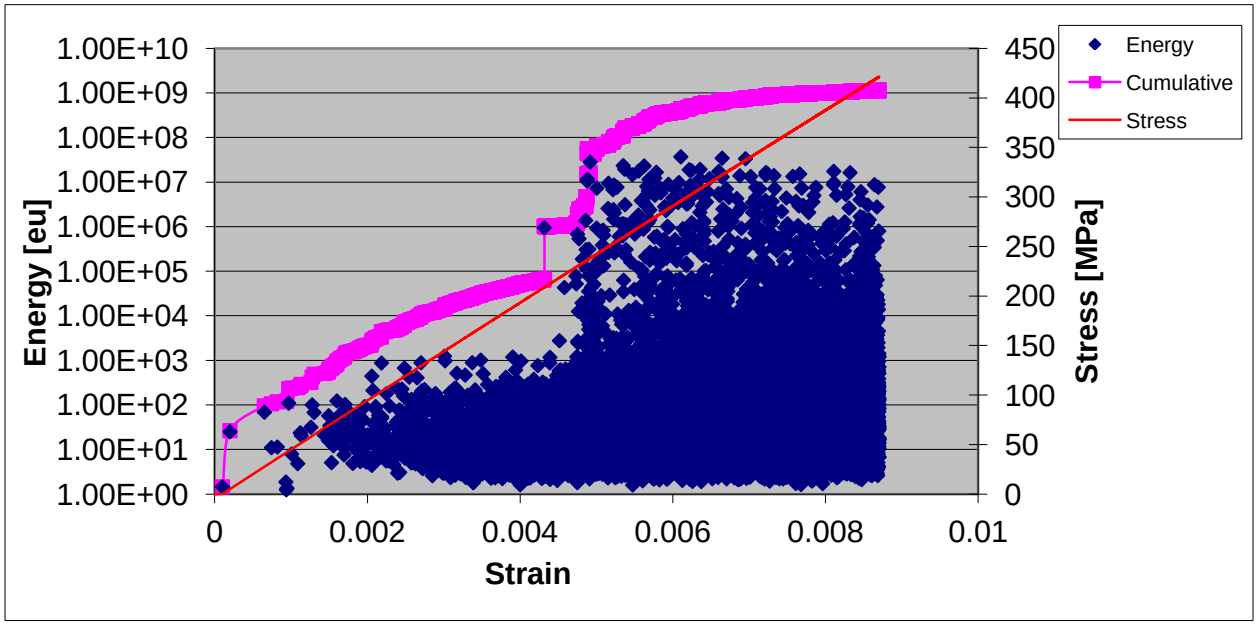

IV. DIC Longitudinal and Transverse Strain Maps at Maximum Strain Level

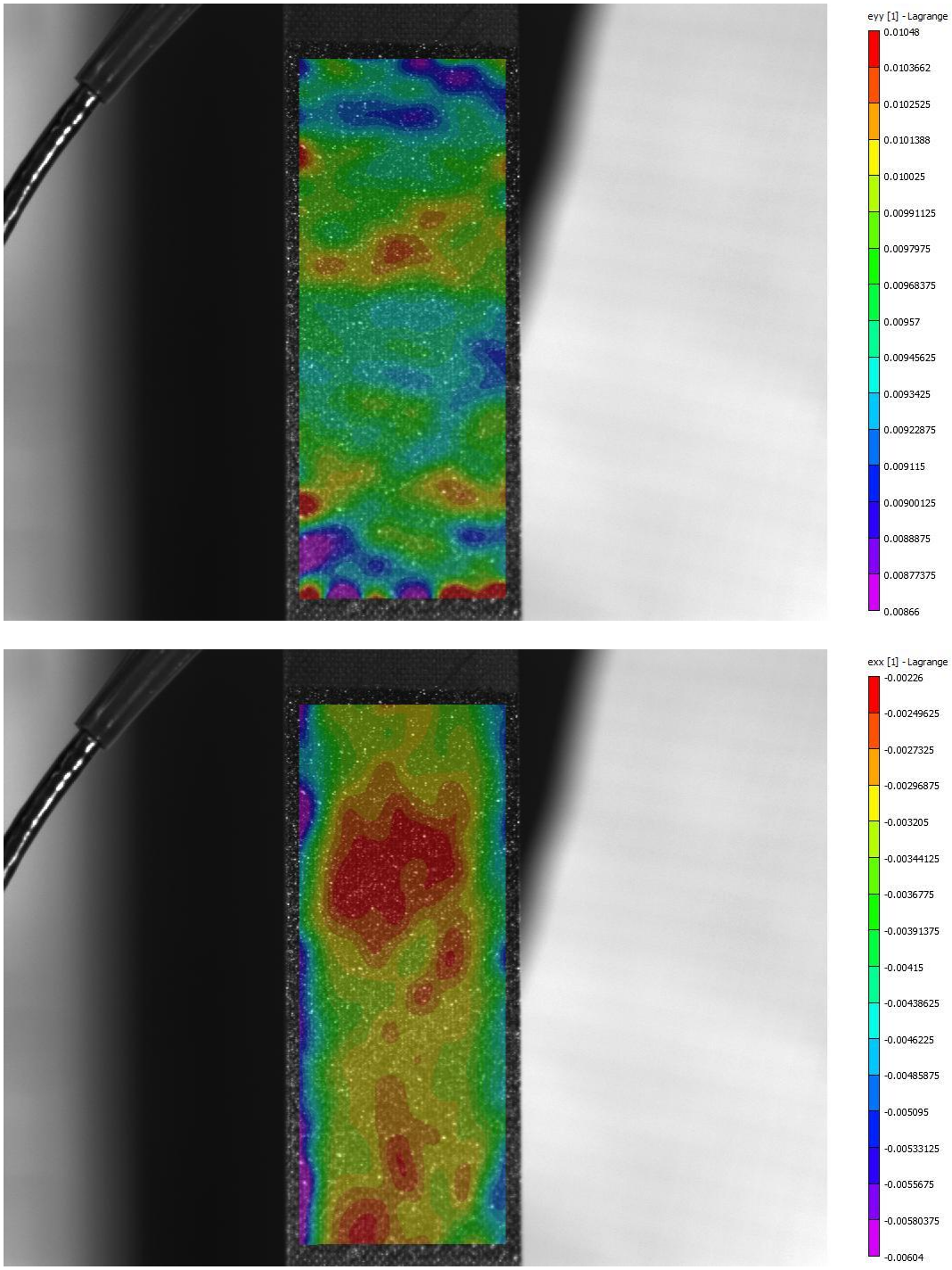

Sample 9 – *Longitudinal and Transversal Strain Maps*

A.1.3. 0^0 specimen with gap (specimen 10)

I. Stress vs. Strain curves obtained by DIC analysis

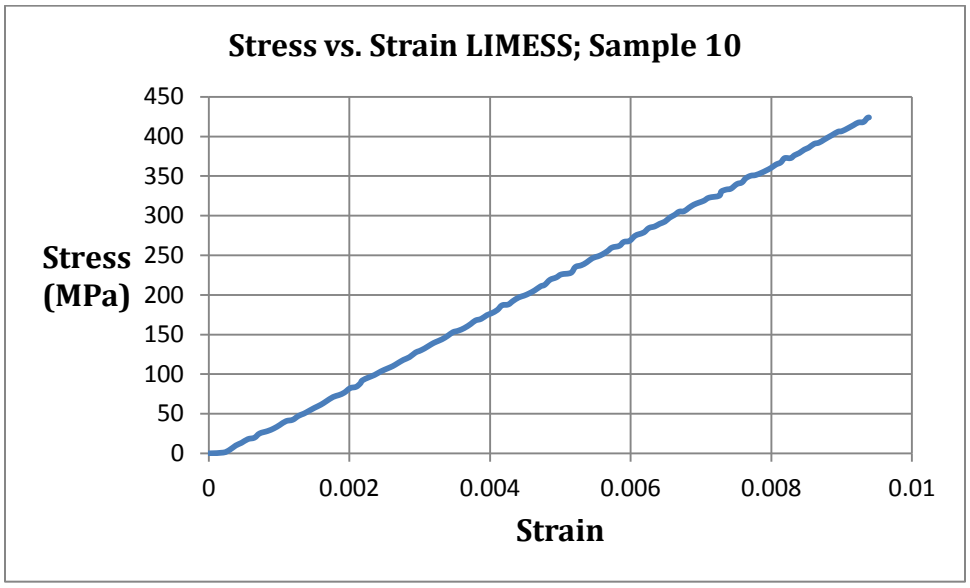

II. Elasticity Modulus vs. Strain curves obtained by DIC analysis

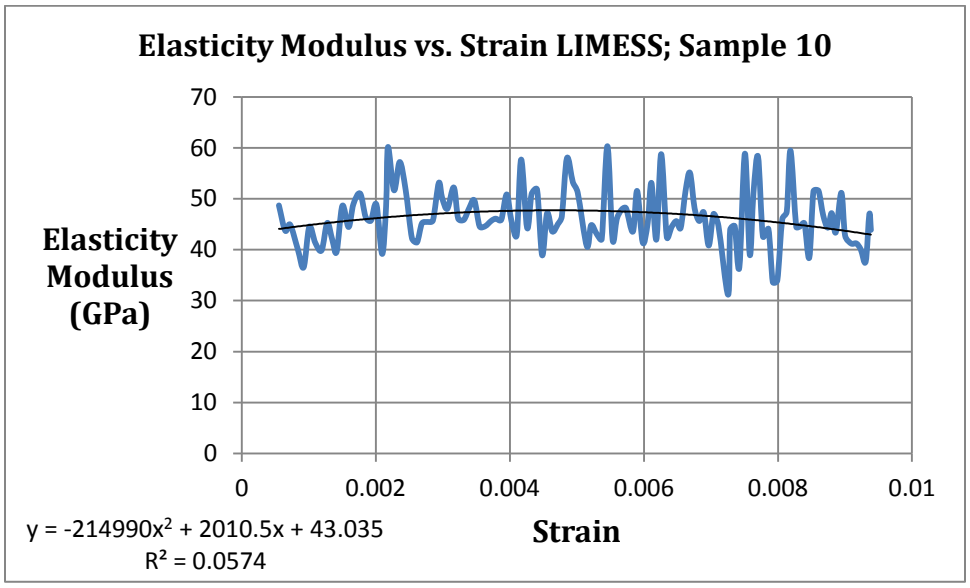

III. Energy – Cumulative Energy – Stress vs. Strain curves obtained by AE analysis

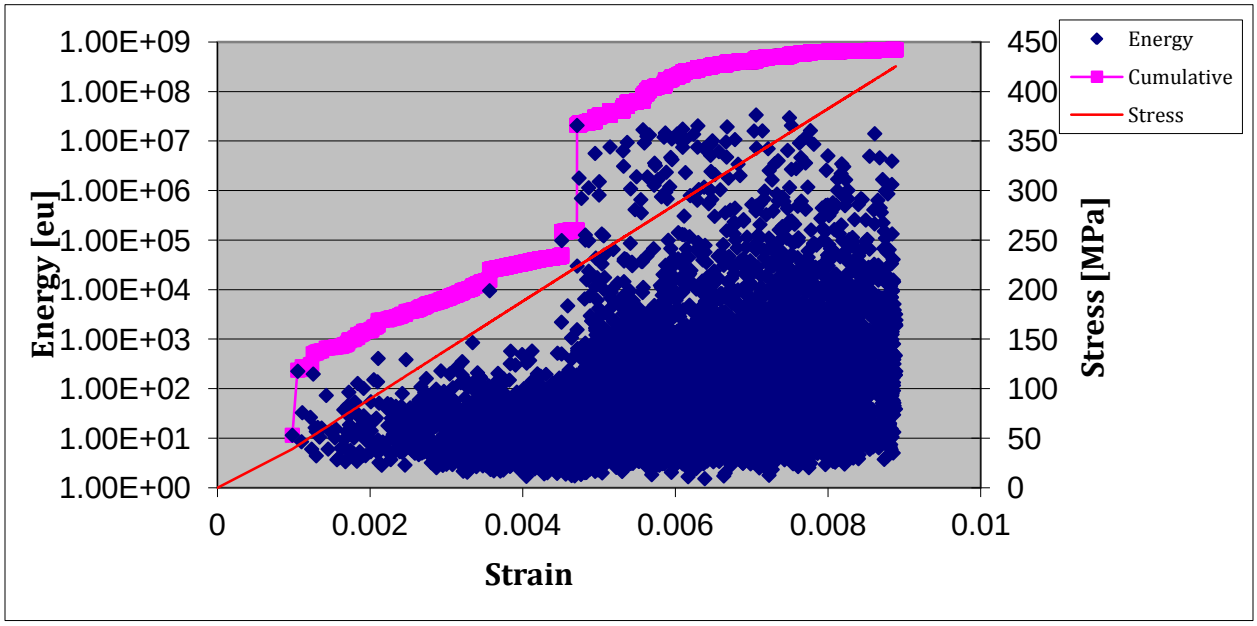

Sample 10

IV. DIC Longitudinal and Transverse Strain Maps at Maximum Strain Level

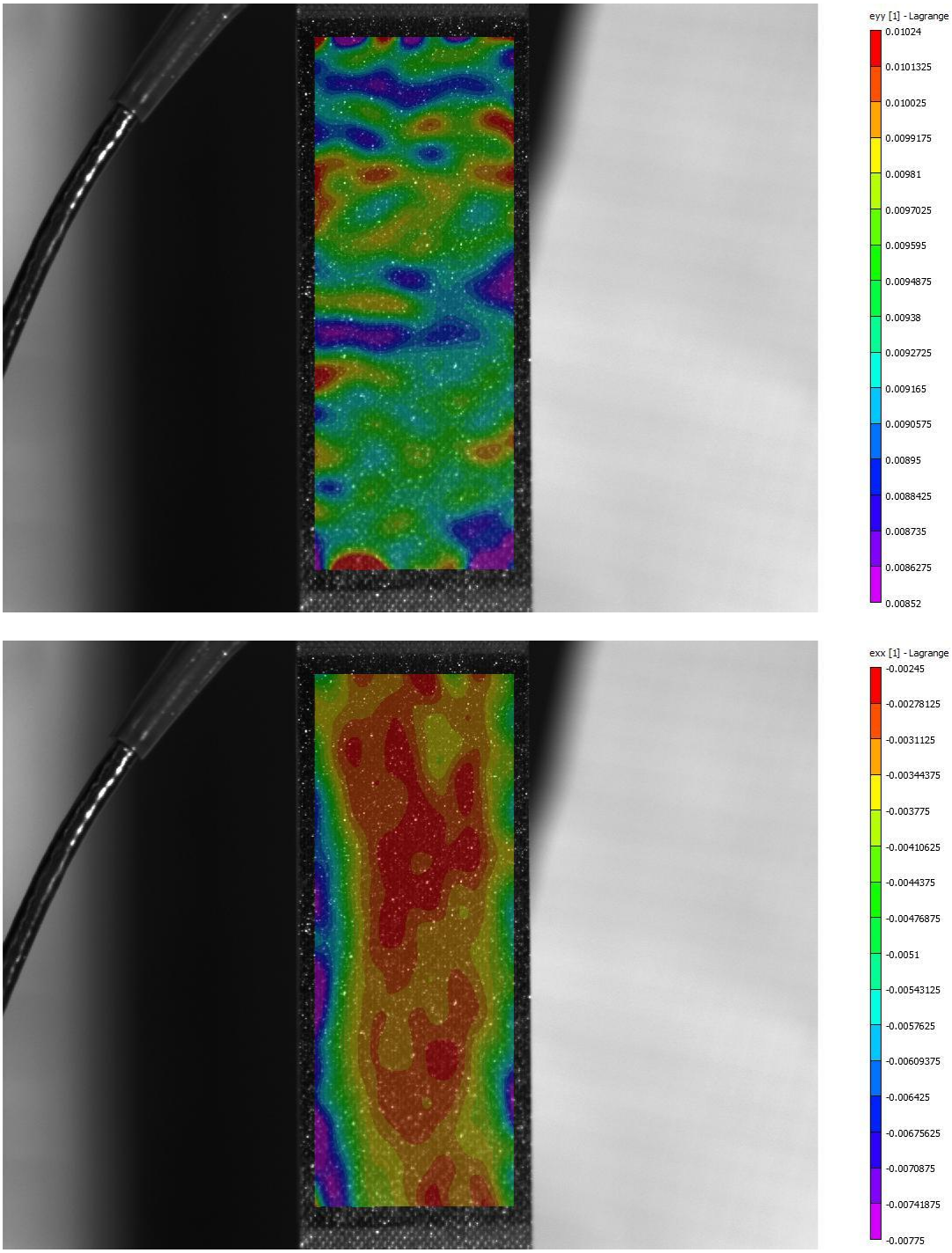

Sample 10 – *Longitudinal and Transversal Strain Maps*

A.1.4. 90^{0} specimen with overlap (specimens 11, 12)

I. Stress vs. Strain curves obtained by DIC analysis

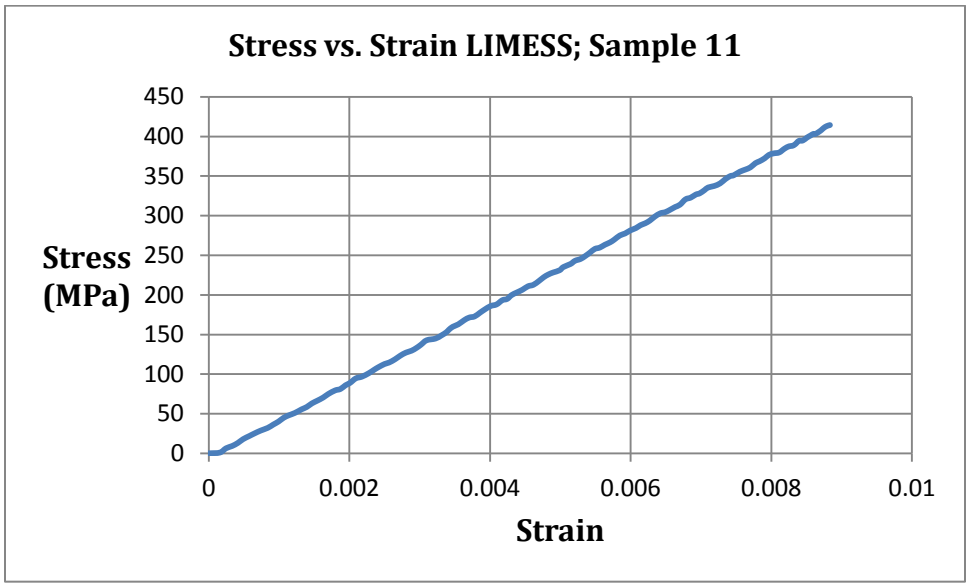

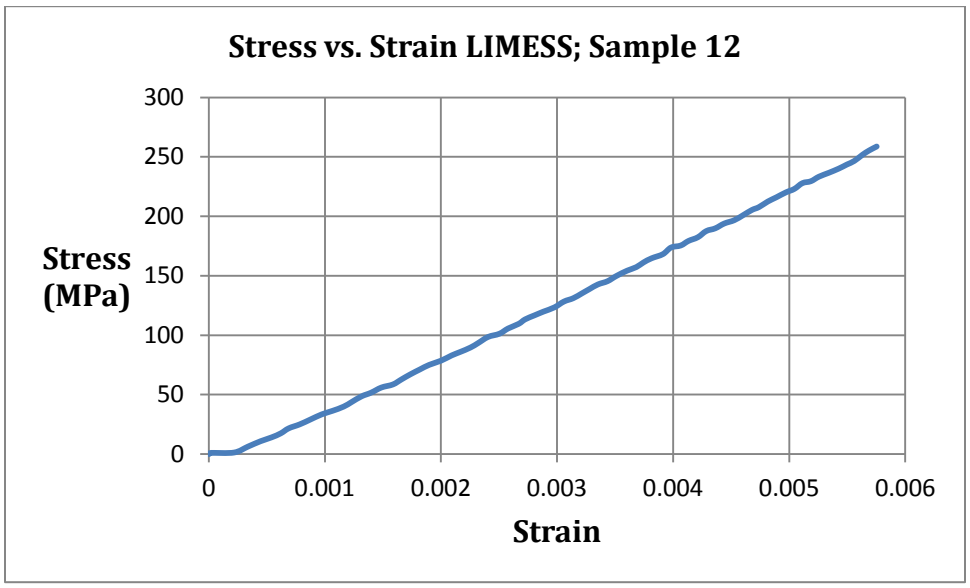

II. Elasticity Modulus vs. Strain curves obtained by DIC analysis

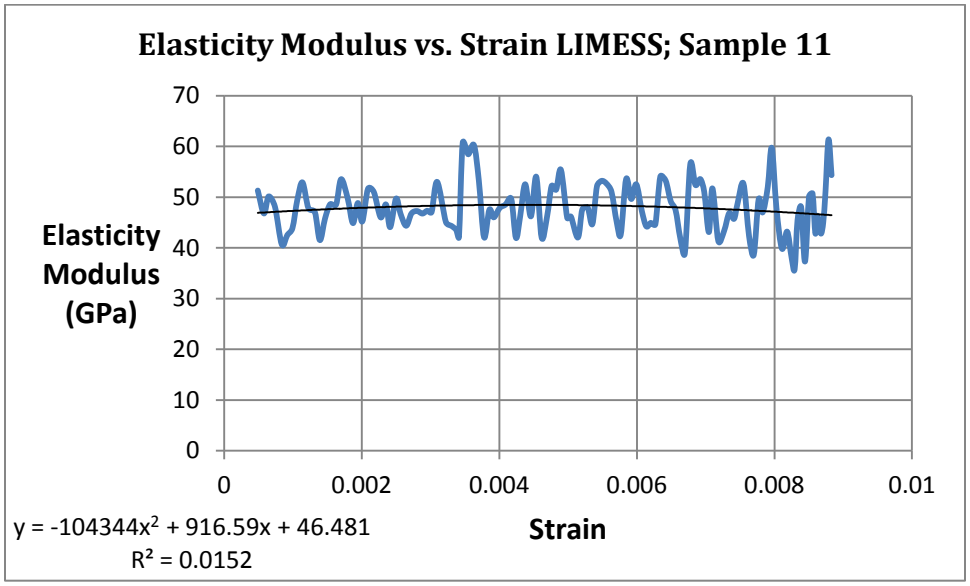

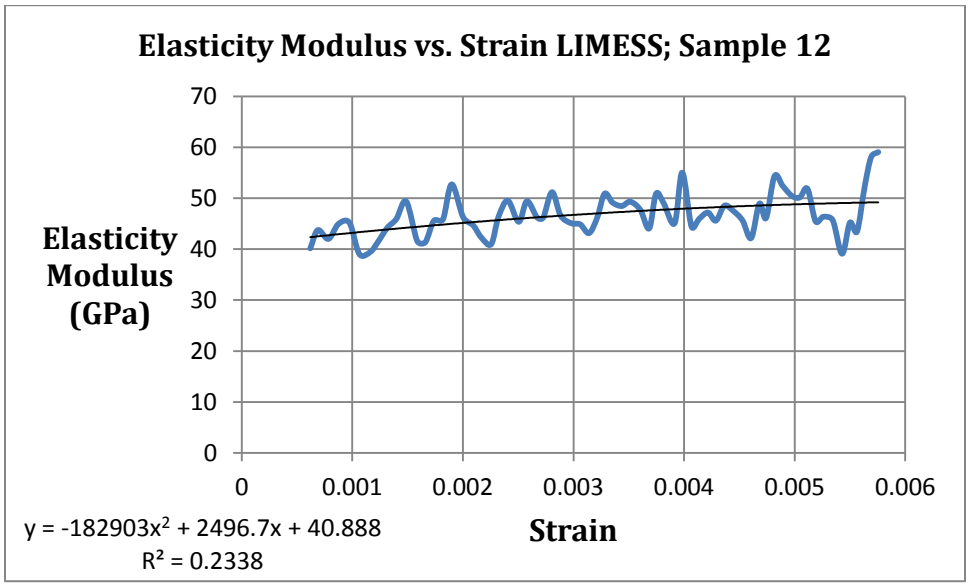

III. Energy – Cumulative Energy – Stress vs. Strain curves obtained by AE analysis

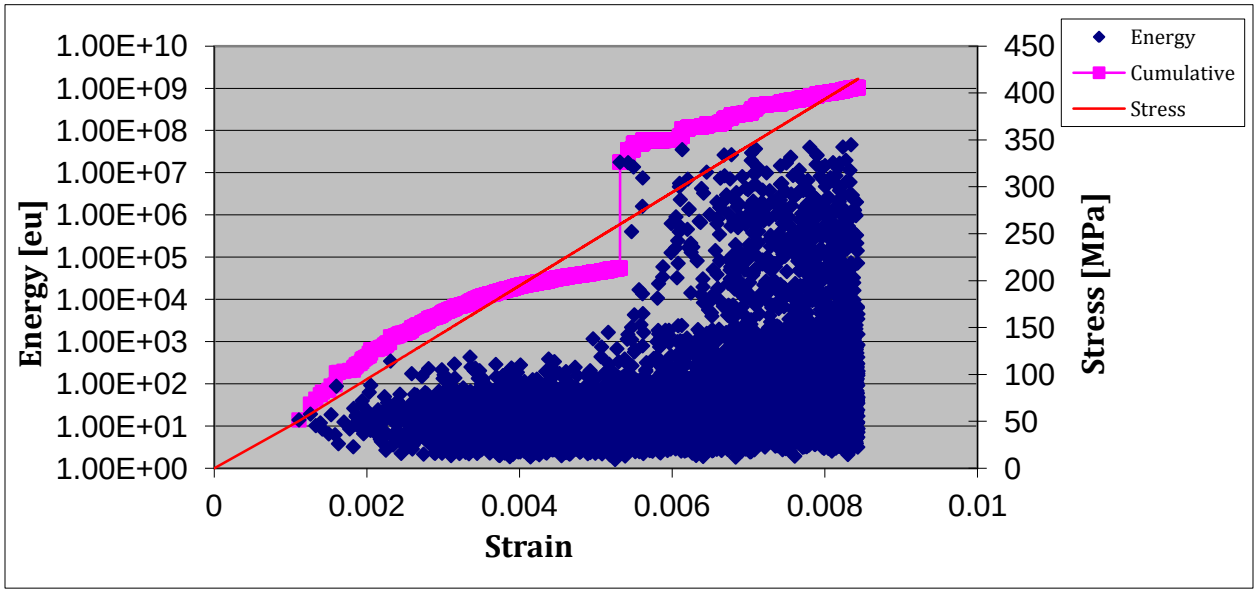

Sample 11

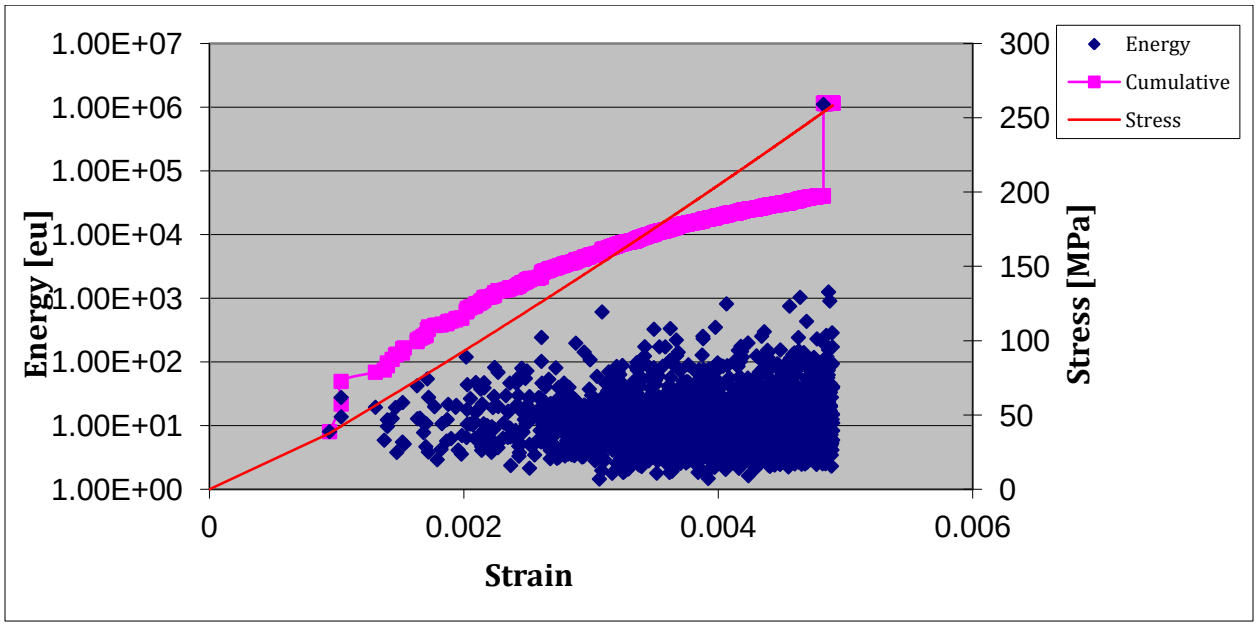

Sample 12

IV. DIC Longitudinal and Transverse Strain Maps at Maximum Strain Level

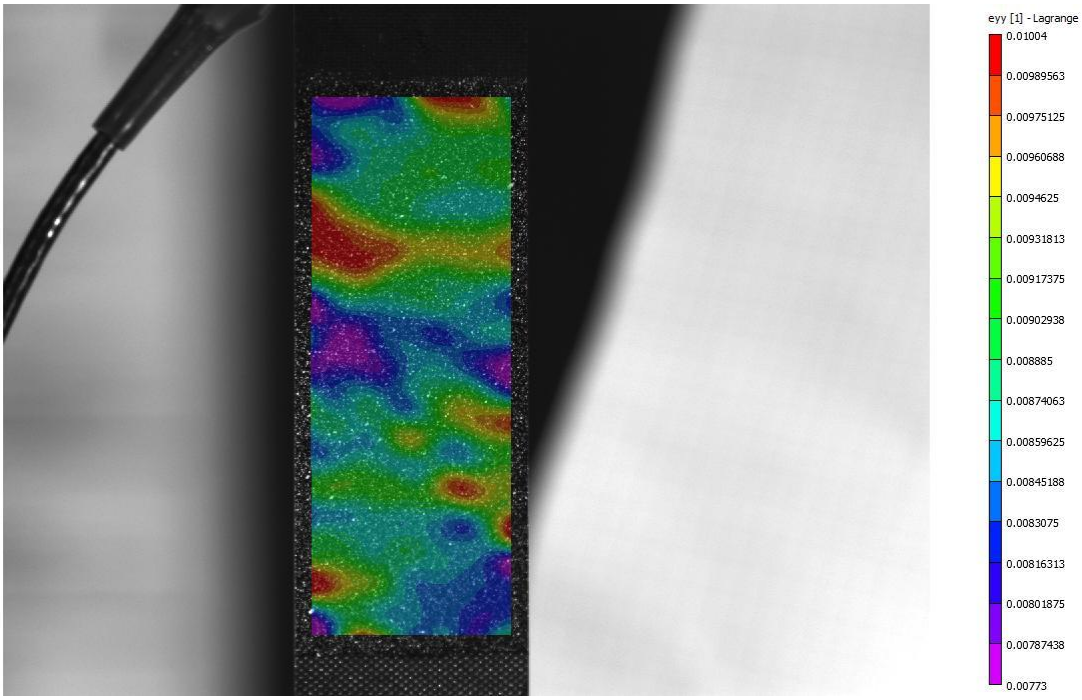

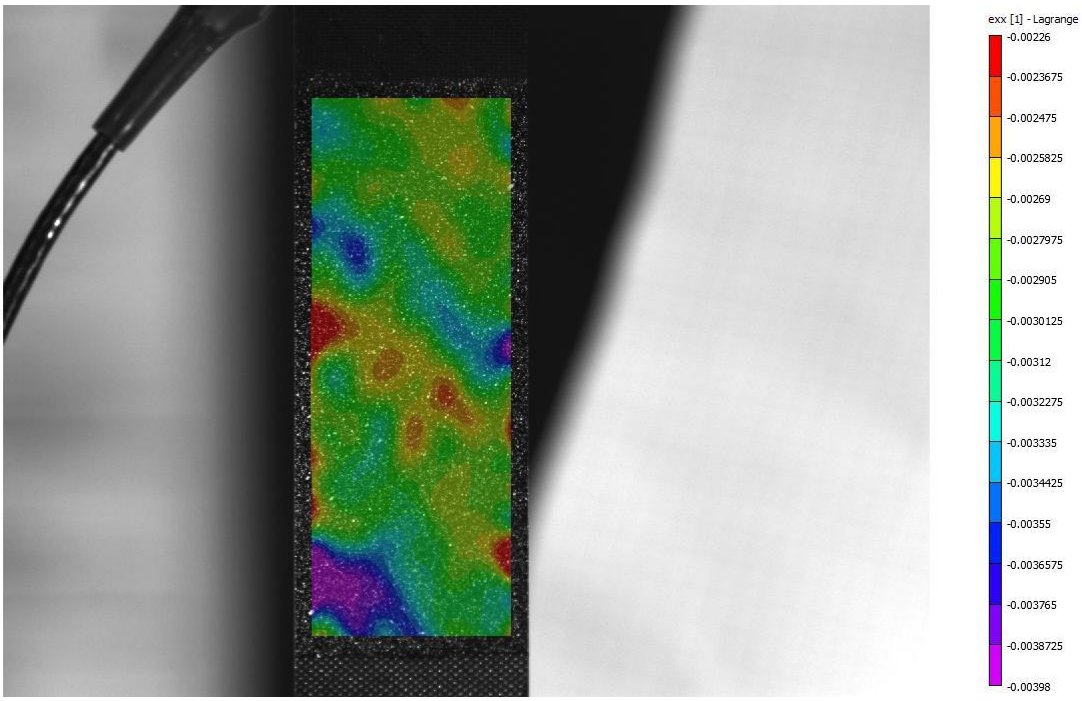

Sample 11 – *Longitudinal and Transversal Strain Maps*

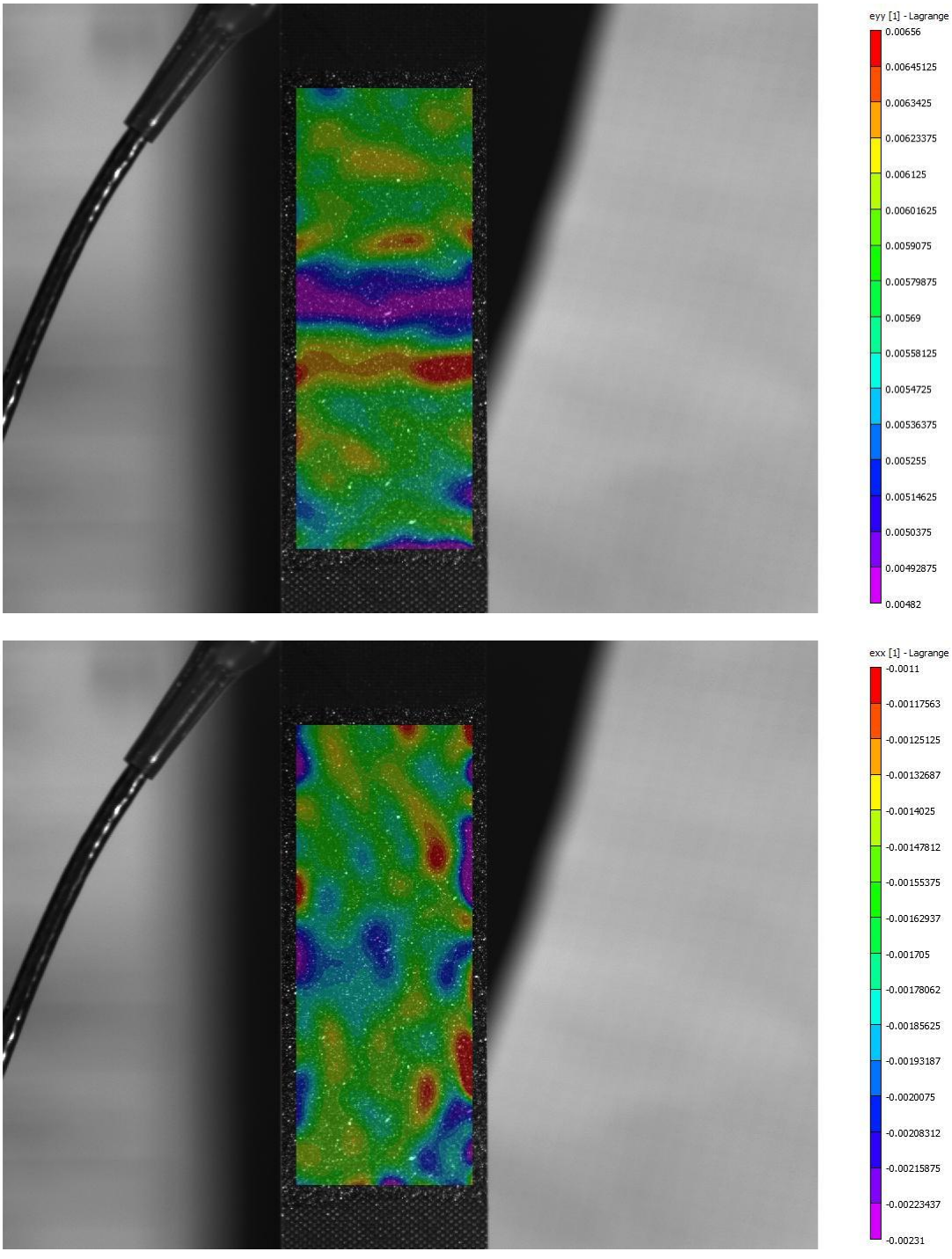

Sample 12 – *Longitudinal and Transversal Strain Maps*

A.1.5. 90^0 specimens with gap

A.1.5.1. Specimens 13, 14

I. Stress vs. Strain curves obtained by DIC analysis

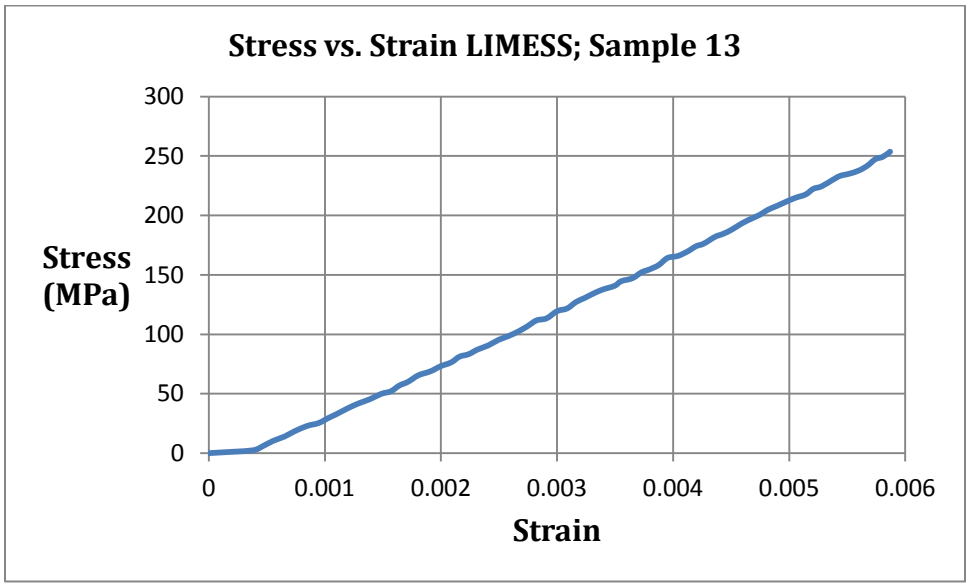

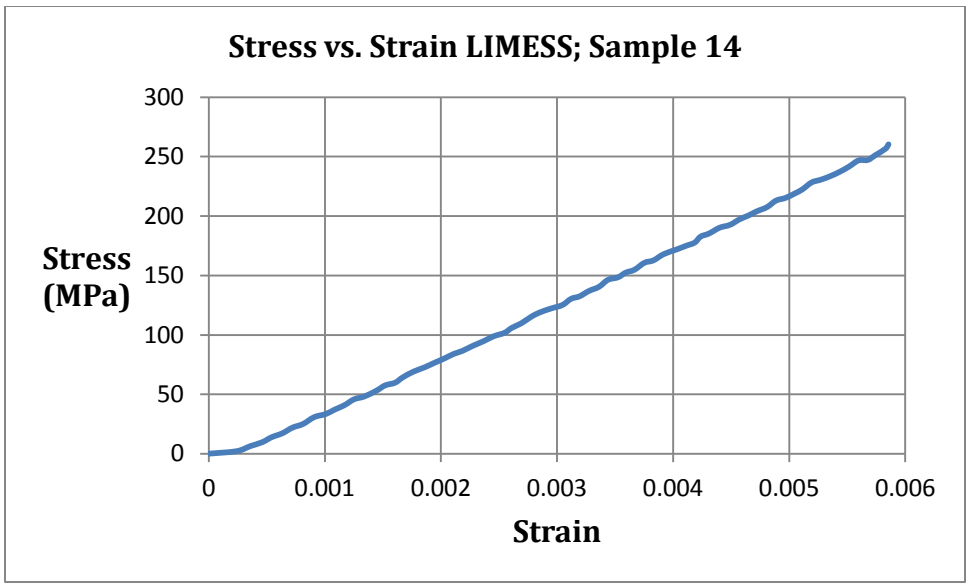

II. Elasticity Modulus vs. Strain curves obtained by DIC analysis

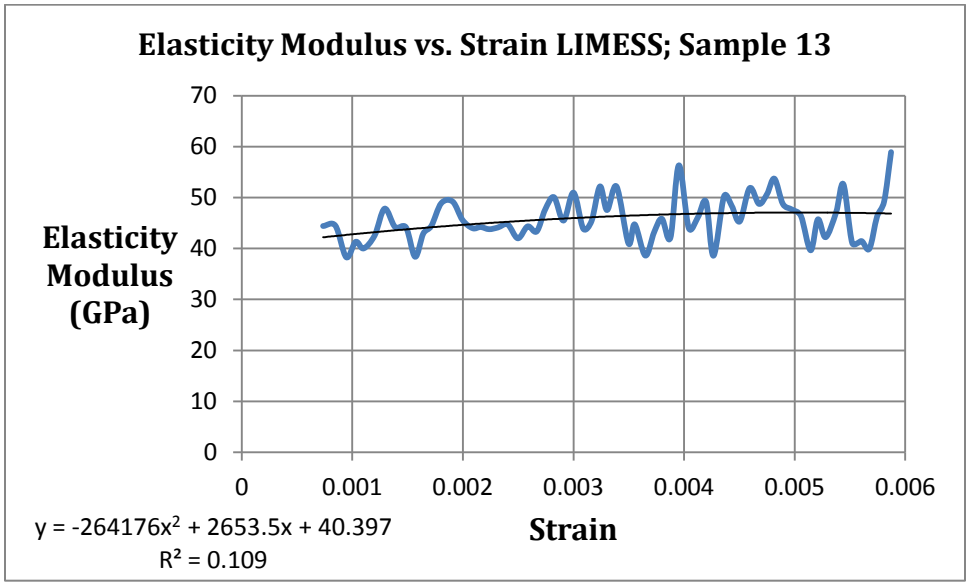

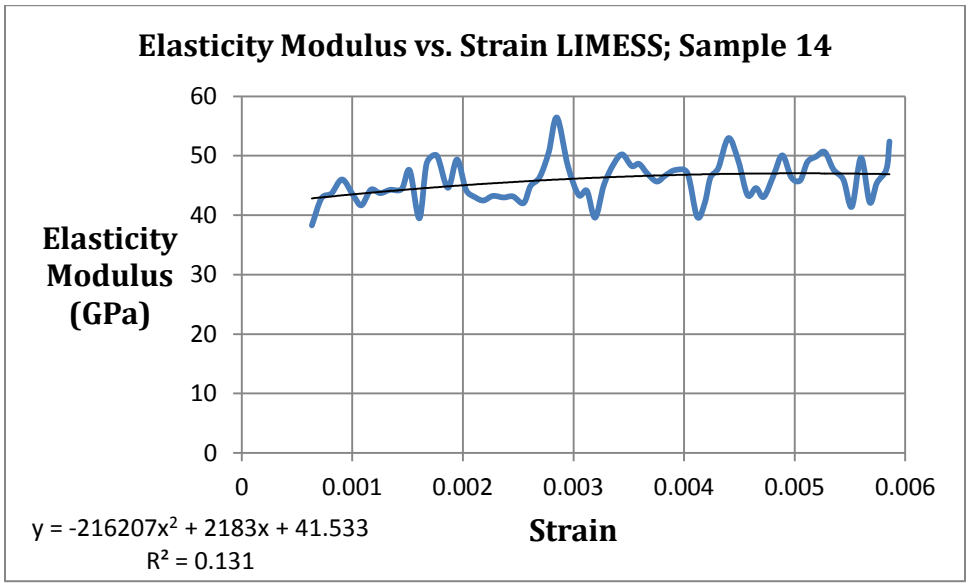

III. Energy – Cumulative Energy – Stress vs. Strain curves obtained by AE analysis

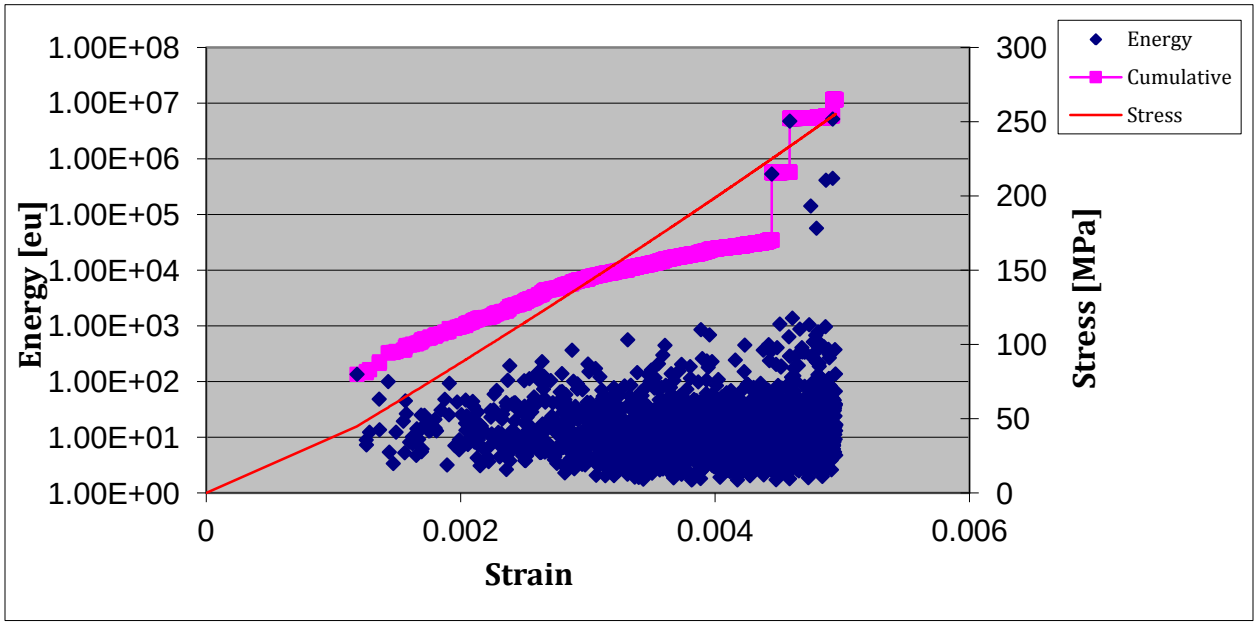

Sample 13

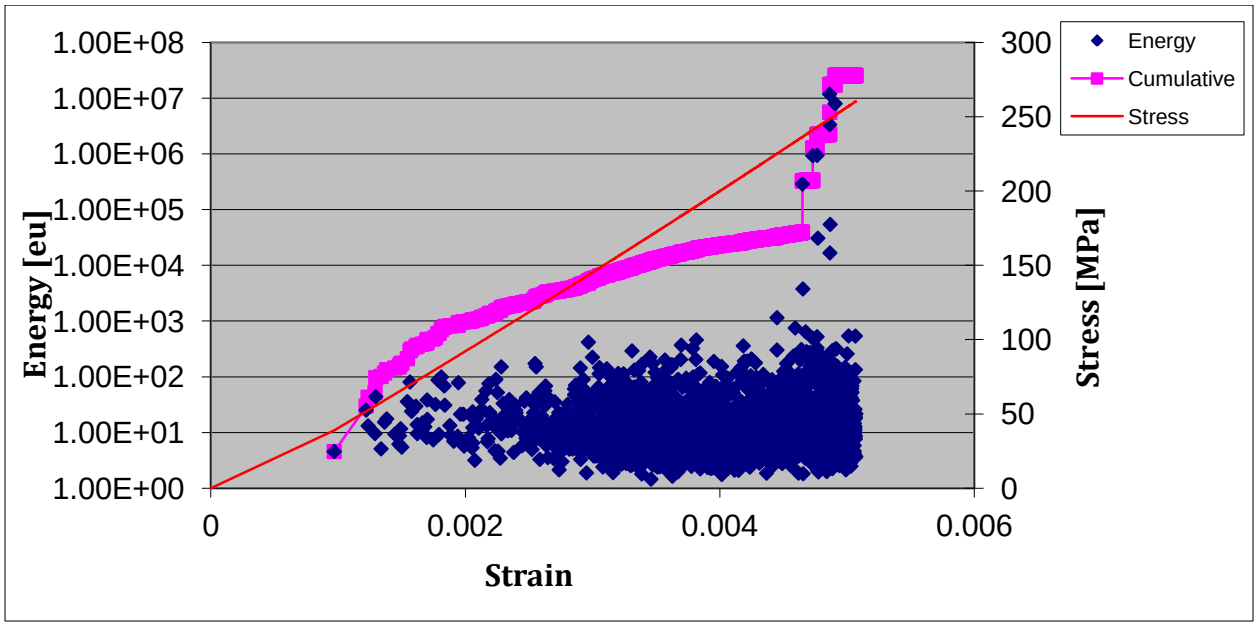

Sample 14

IV. DIC Longitudinal and Transverse Strain Maps at Maximum Strain Level

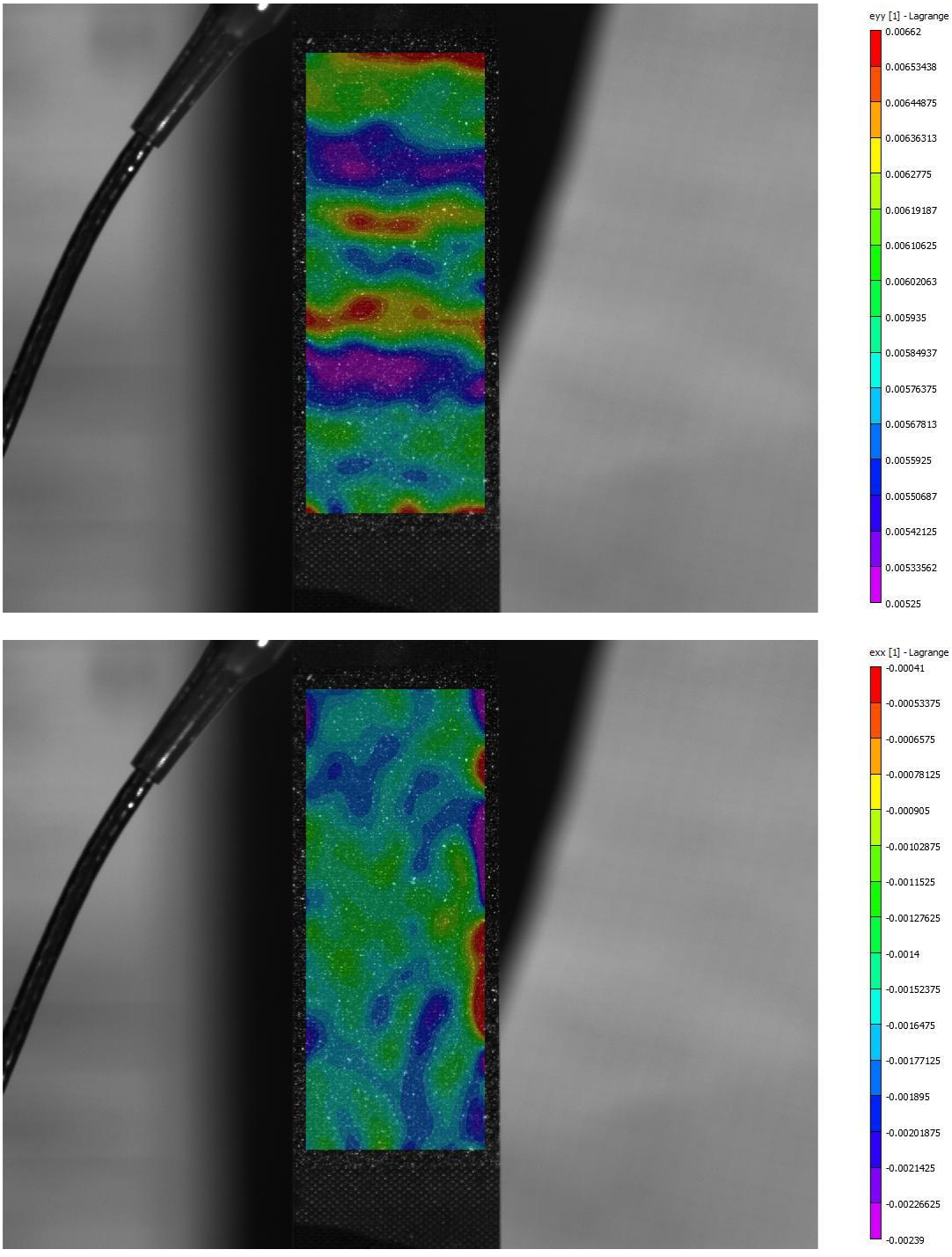

Sample 13 – *Longitudinal and Transversal Strain Maps*

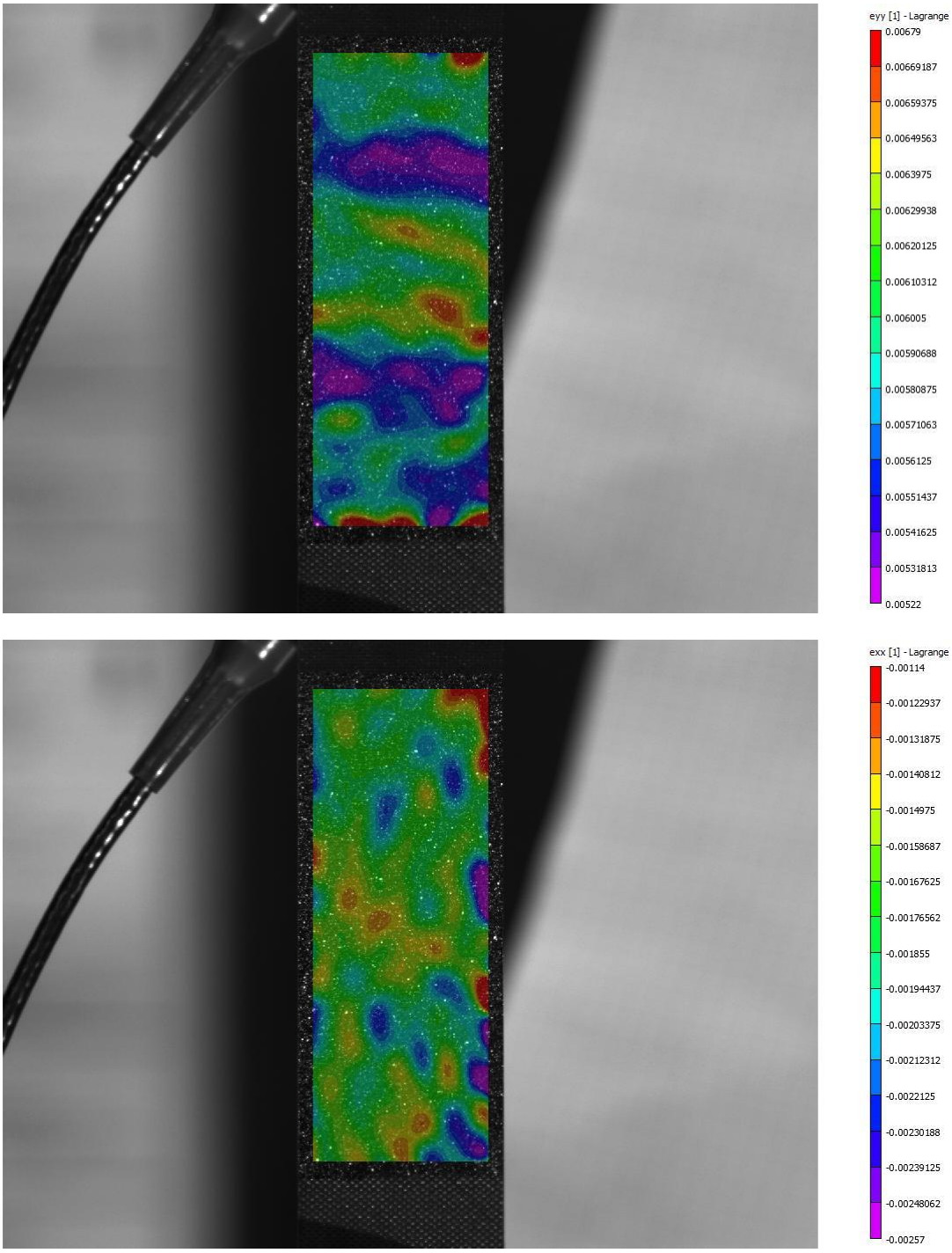

Sample 14 – *Longitudinal and Transversal Strain Maps*

A.1.5.2. Specimens 15, 16

I. Stress vs. Strain curves obtained by DIC analysis

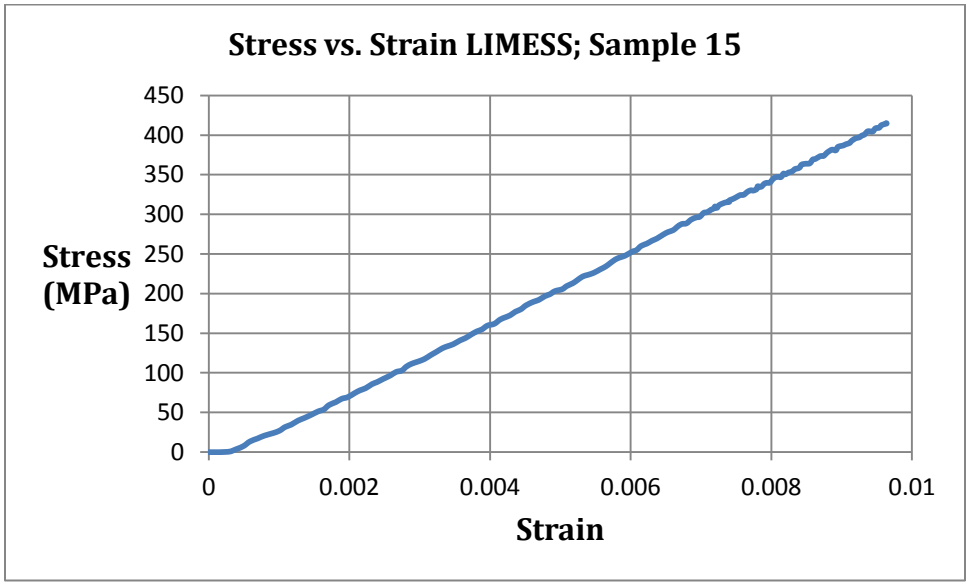

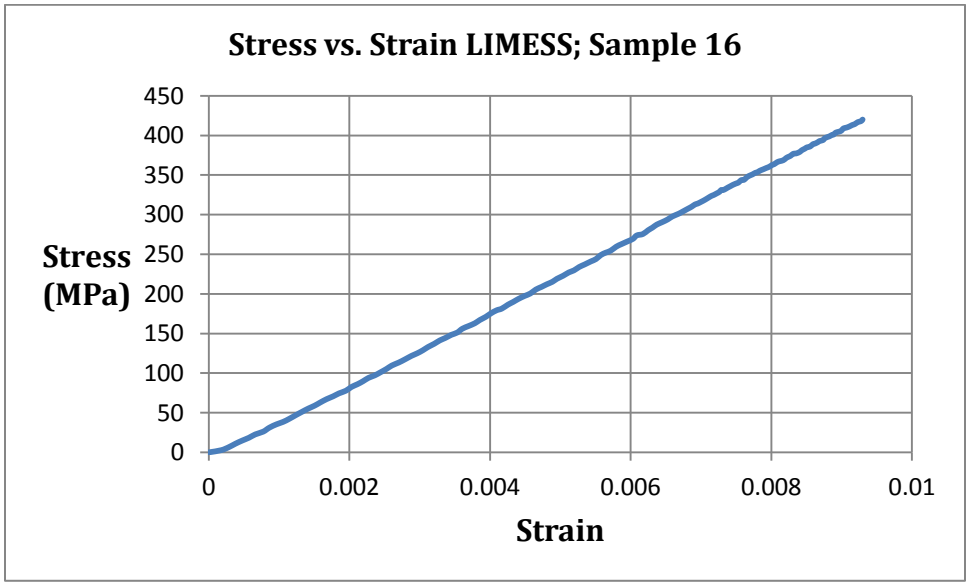

II. Elasticity Modulus vs. Strain curves obtained by DIC analysis

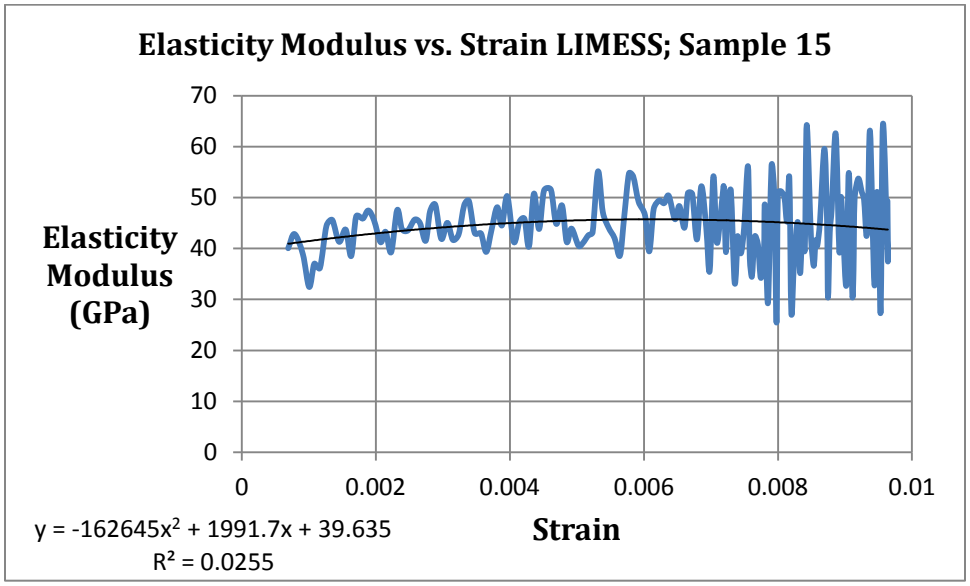

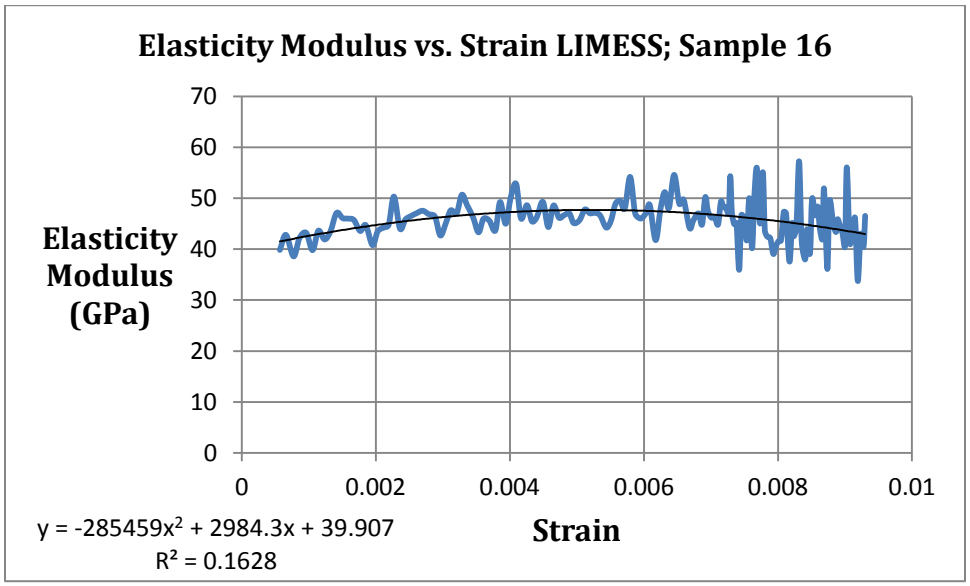

III. Energy – Cumulative Energy – Stress vs. Strain curves obtained by AE analysis

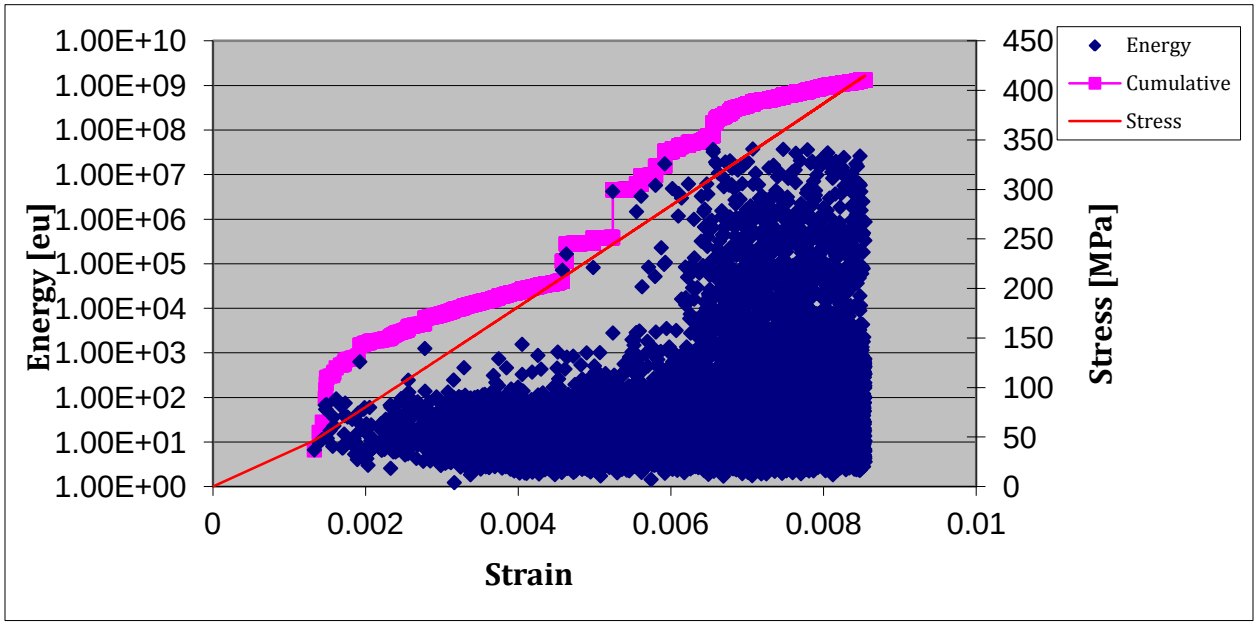

Sample 15

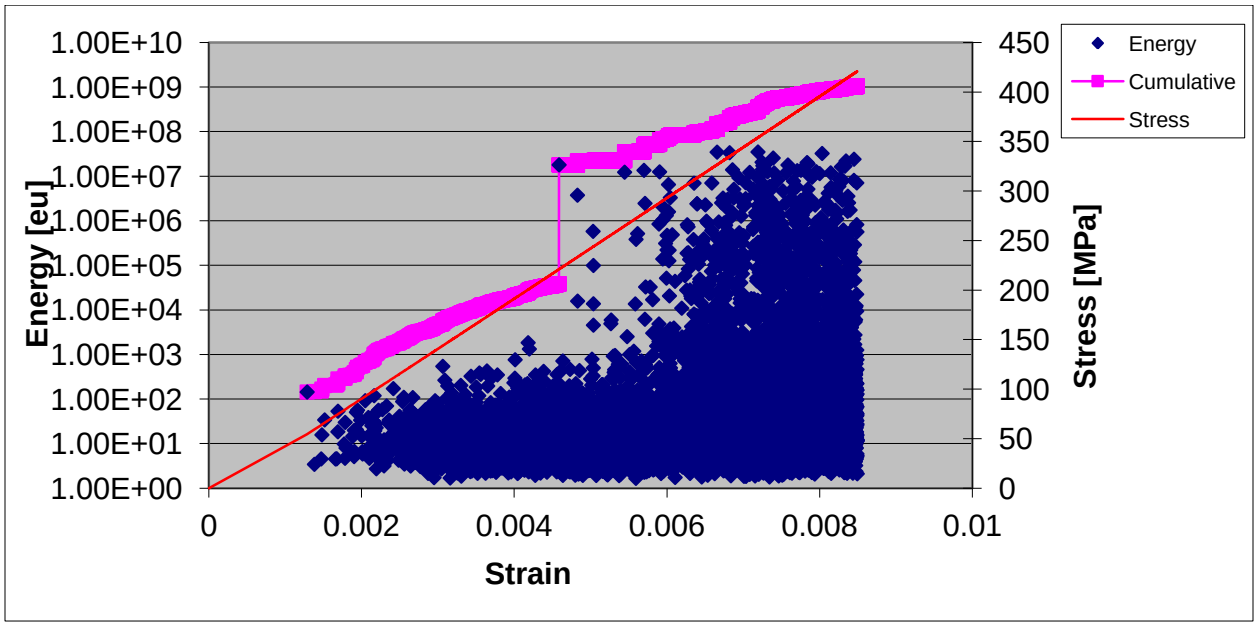

Sample 16

IV. DIC Longitudinal and Transverse Strain Maps at Maximum Strain Level

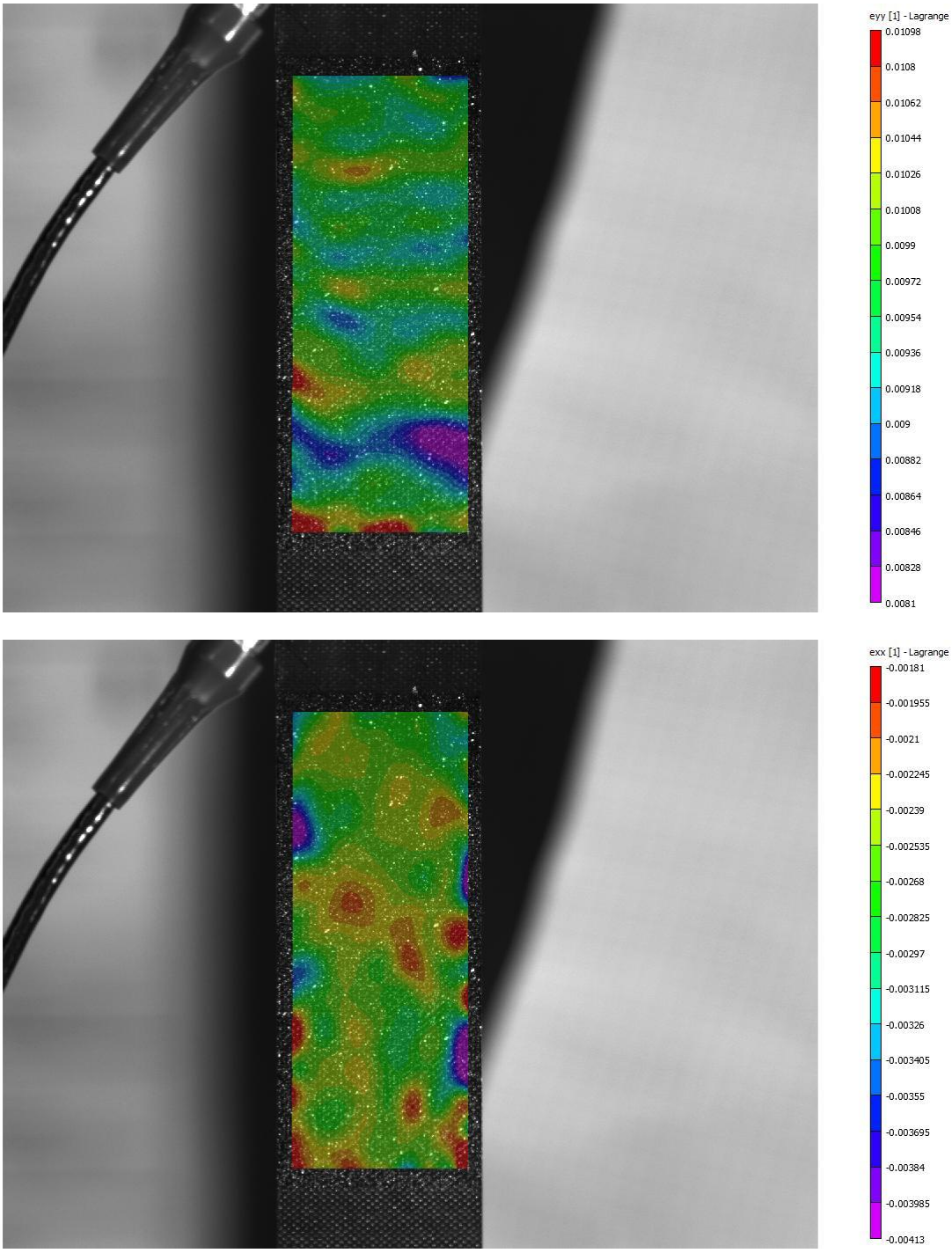

Sample 15 – *Longitudinal and Transversal Strain Maps*

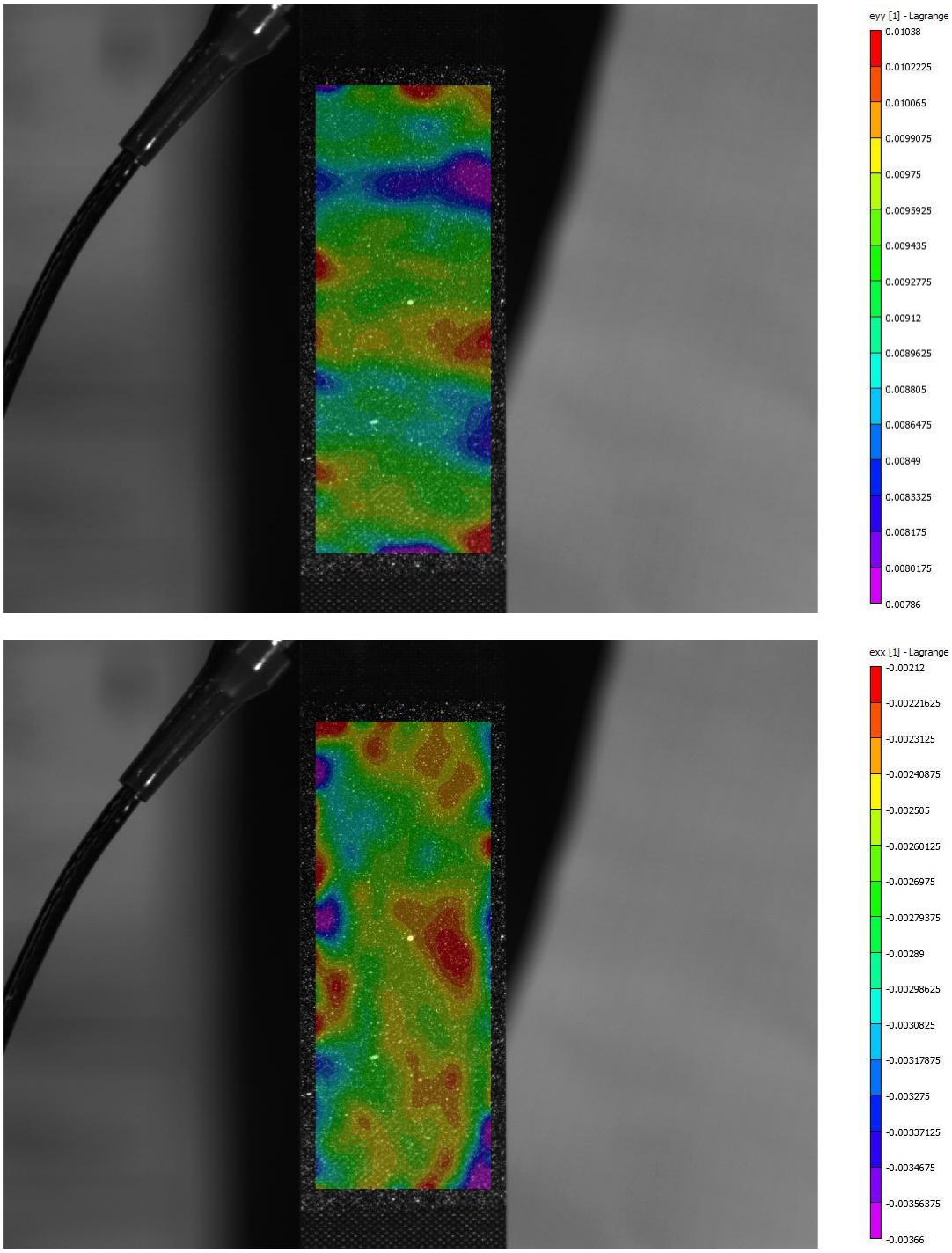

Sample 16 – *Longitudinal and Transversal Strain Maps*

A.2. AP-PLY specimens

A.2.1. 90^0 specimens without defects (specimens 1, 2, 3, 4)

I. Stress vs. Strain curves obtained by DIC analysis

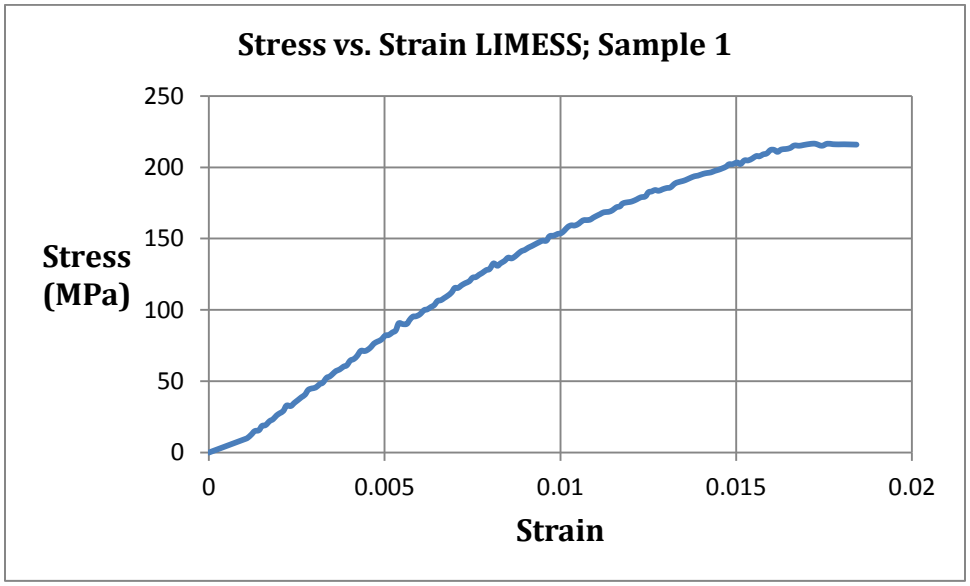

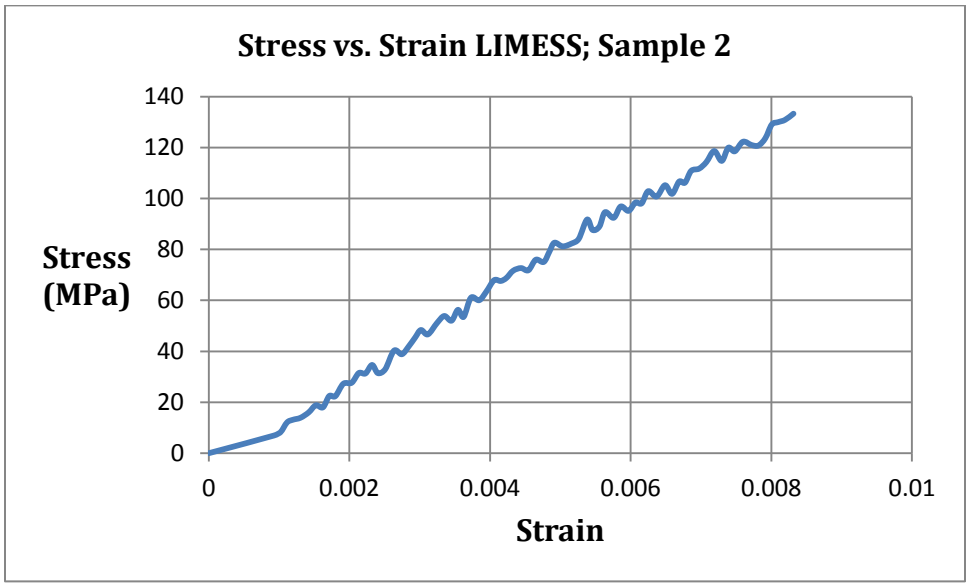

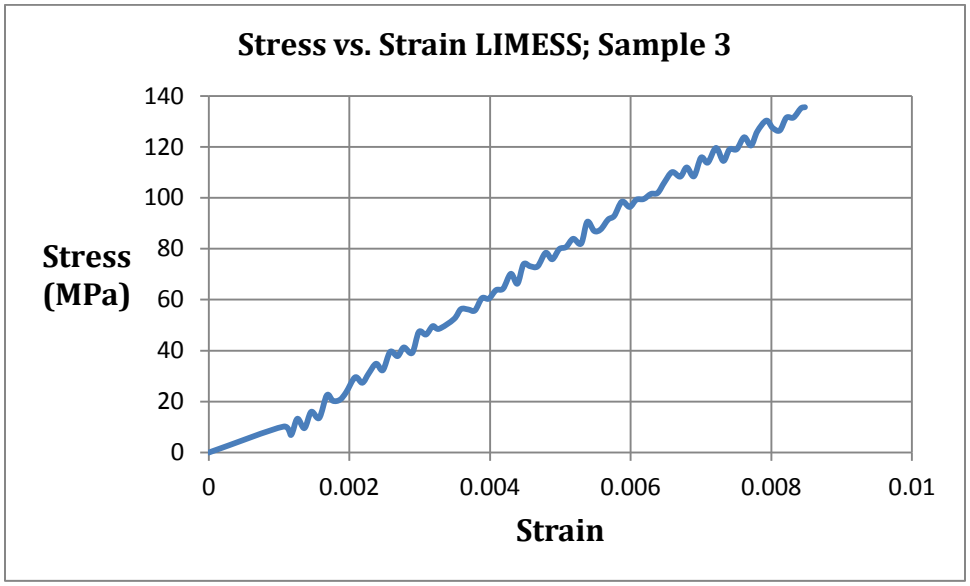
Stress vs. Strain LIMESS; Sample 3
Stress (MPa)
140
120
100
80
60
40
20
0
0
0.002
0.004
0.006
0.008
0.01
Strain

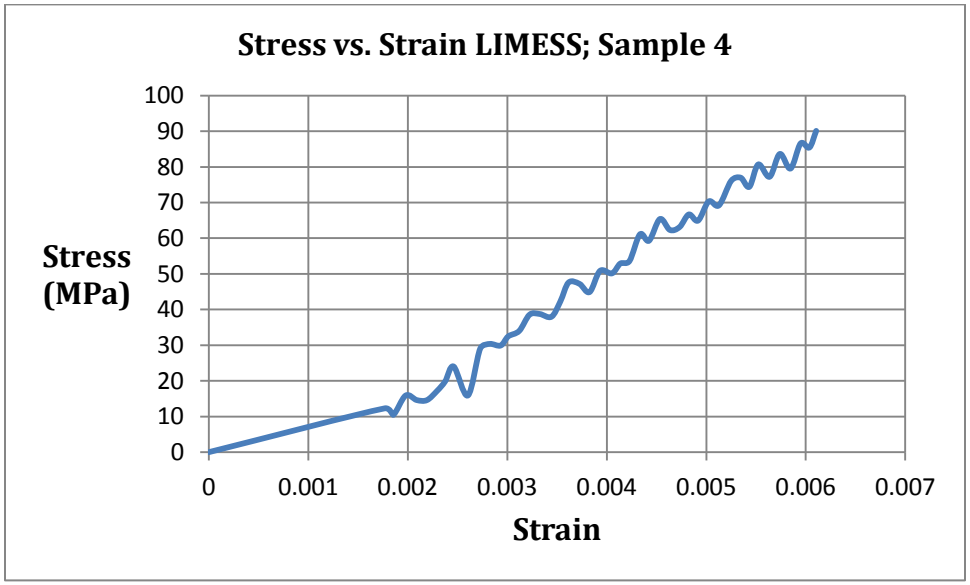
Stress vs. Strain LIMESS; Sample 4
Stress (MPa)
100
90
80
70
60
50
40
30
20
10
0
0
0.001
0.002
0.003
0.004
0.005
0.006
0.007
Strain

II. Elasticity Modulus vs. Strain curves obtained by DIC analysis

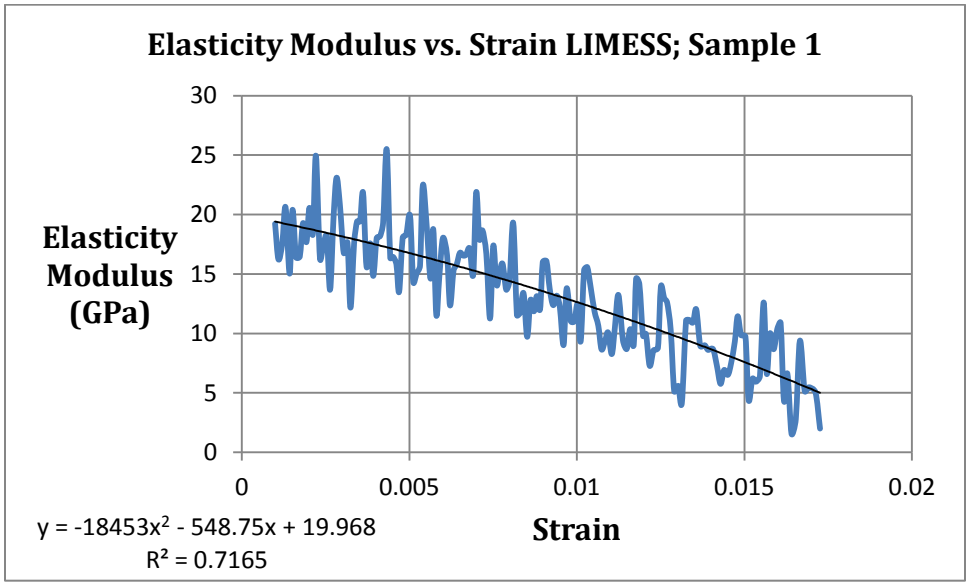

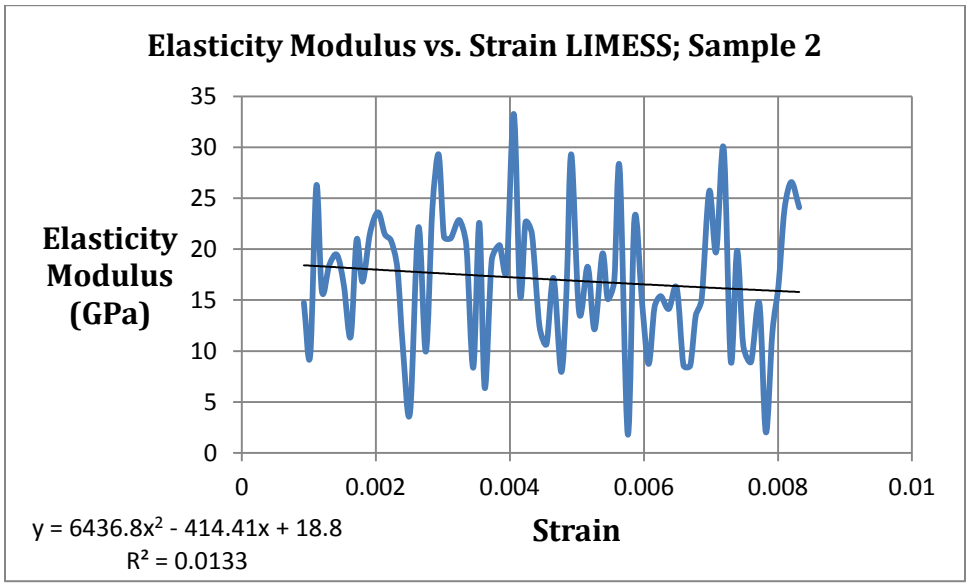

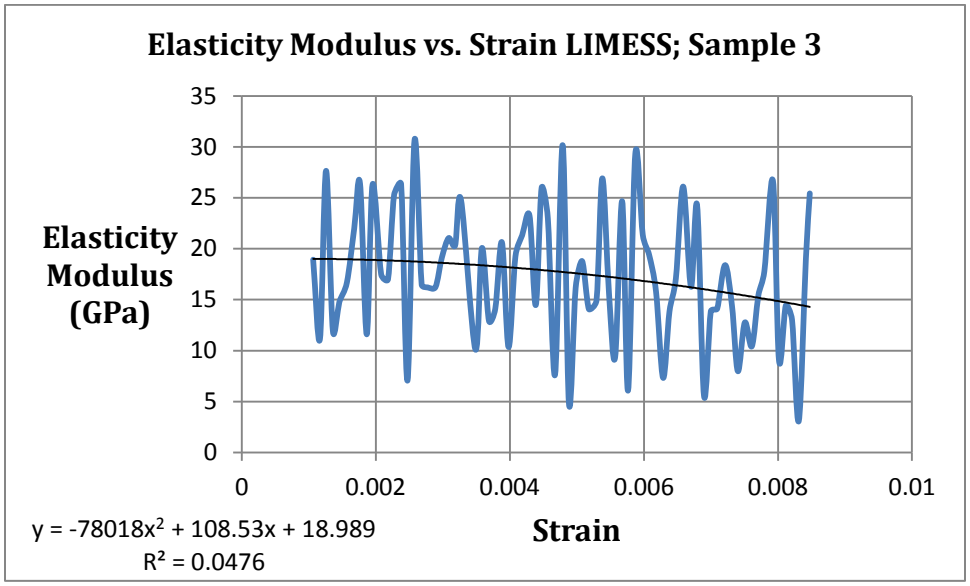
Elasticity Modulus vs. Strain LIMESS; Sample 3
Elasticity Modulus (GPa)
35
30
25
20
15
10
5
0
0
0.002
0.004
0.006
0.008
0.01
Strain
y = -78018x² + 108.53x + 18.989
R² = 0.0476

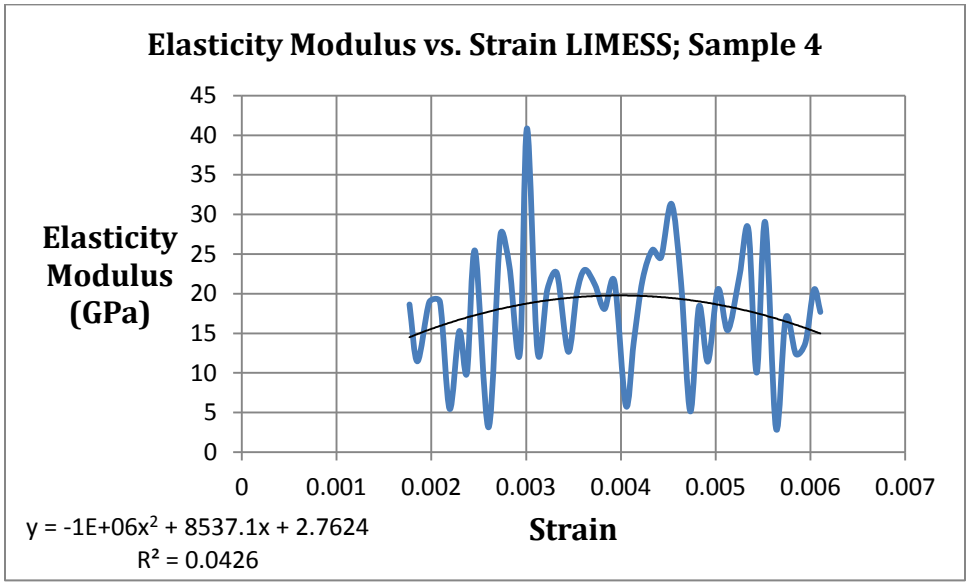
Elasticity Modulus vs. Strain LIMESS; Sample 4
Elasticity Modulus (GPa)
45
40
35
30
25
20
15
10
5
0
0
0.001
0.002
0.003
0.004
0.005
0.006
0.007
Strain
y = -1E+06x² + 8537.1x + 2.7624
R² = 0.0426

III. Energy – Cumulative Energy – Stress vs. Strain curves obtained by AE analysis

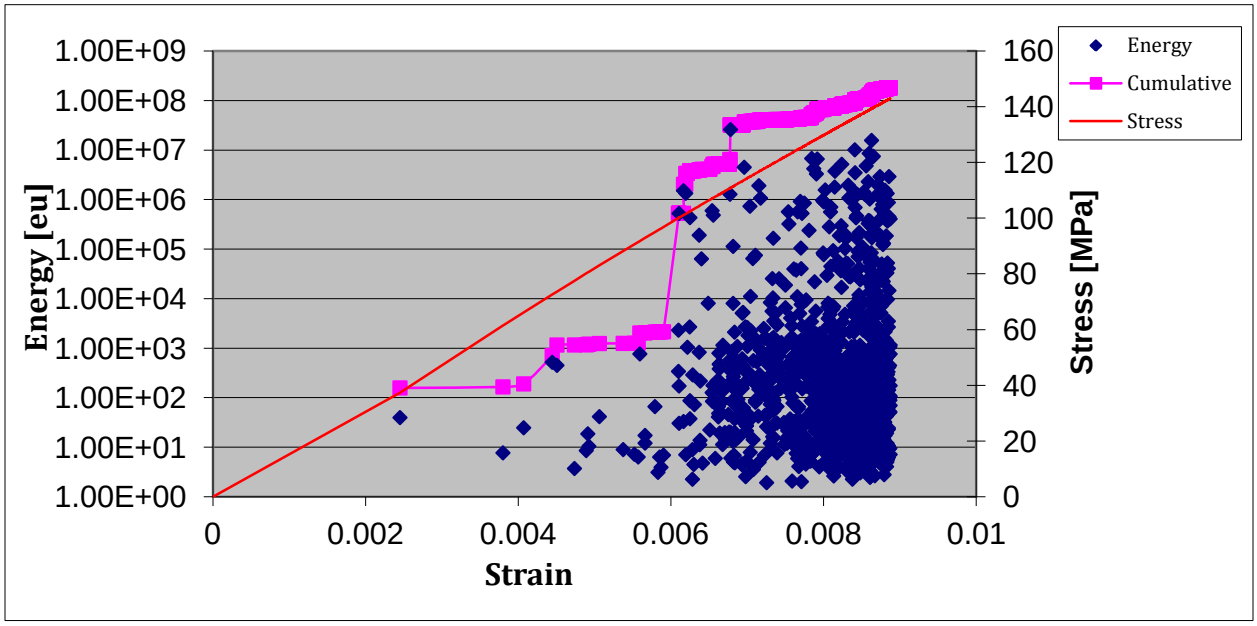

Sample 2

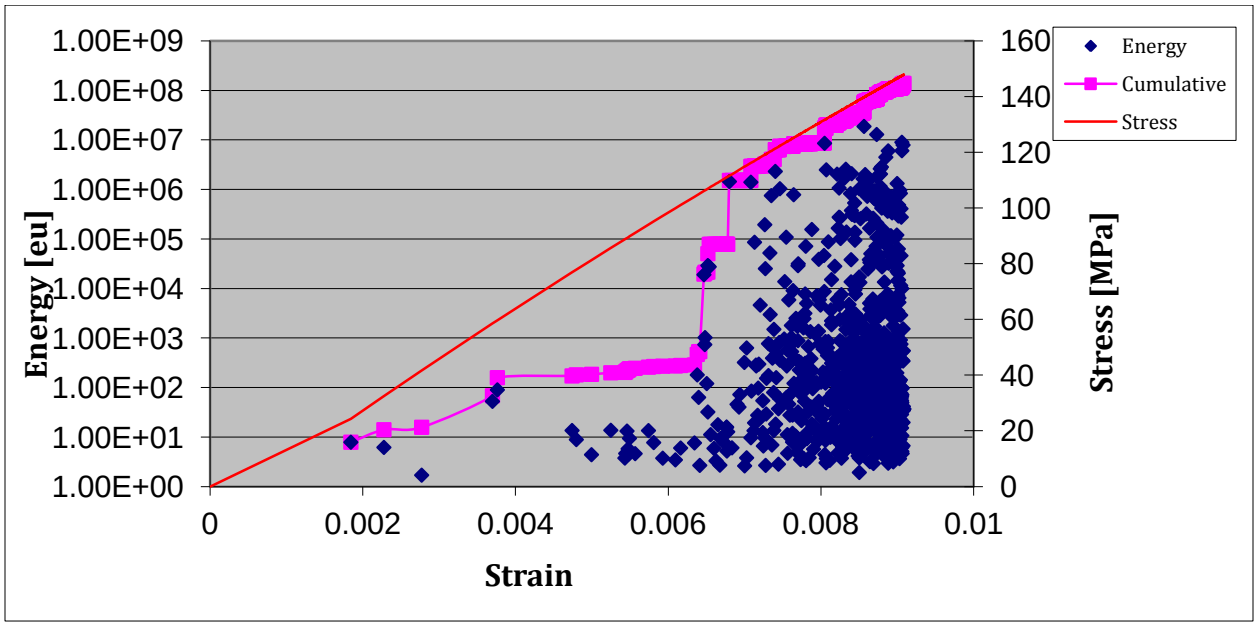

Sample 3

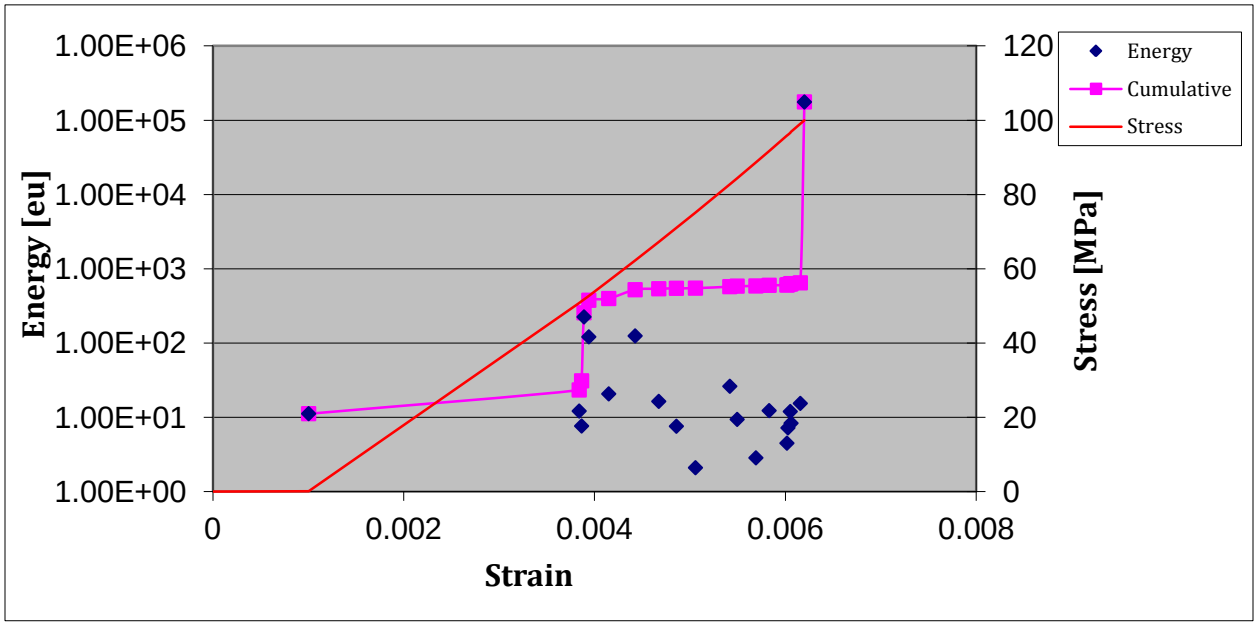
1.00E+06
1.00E+05
1.00E+04
1.00E+03
1.00E+02
1.00E+01
1.00E+00
Energy [eu]
120
100
80
60
40
20
0
Stress [MPa]
0
0.002
0.004
0.006
0.008
Strain
Energy
Cumulative
Stress

Sample 4

IV. DIC Longitudinal and Transverse Strain Maps at Maximum Strain Level

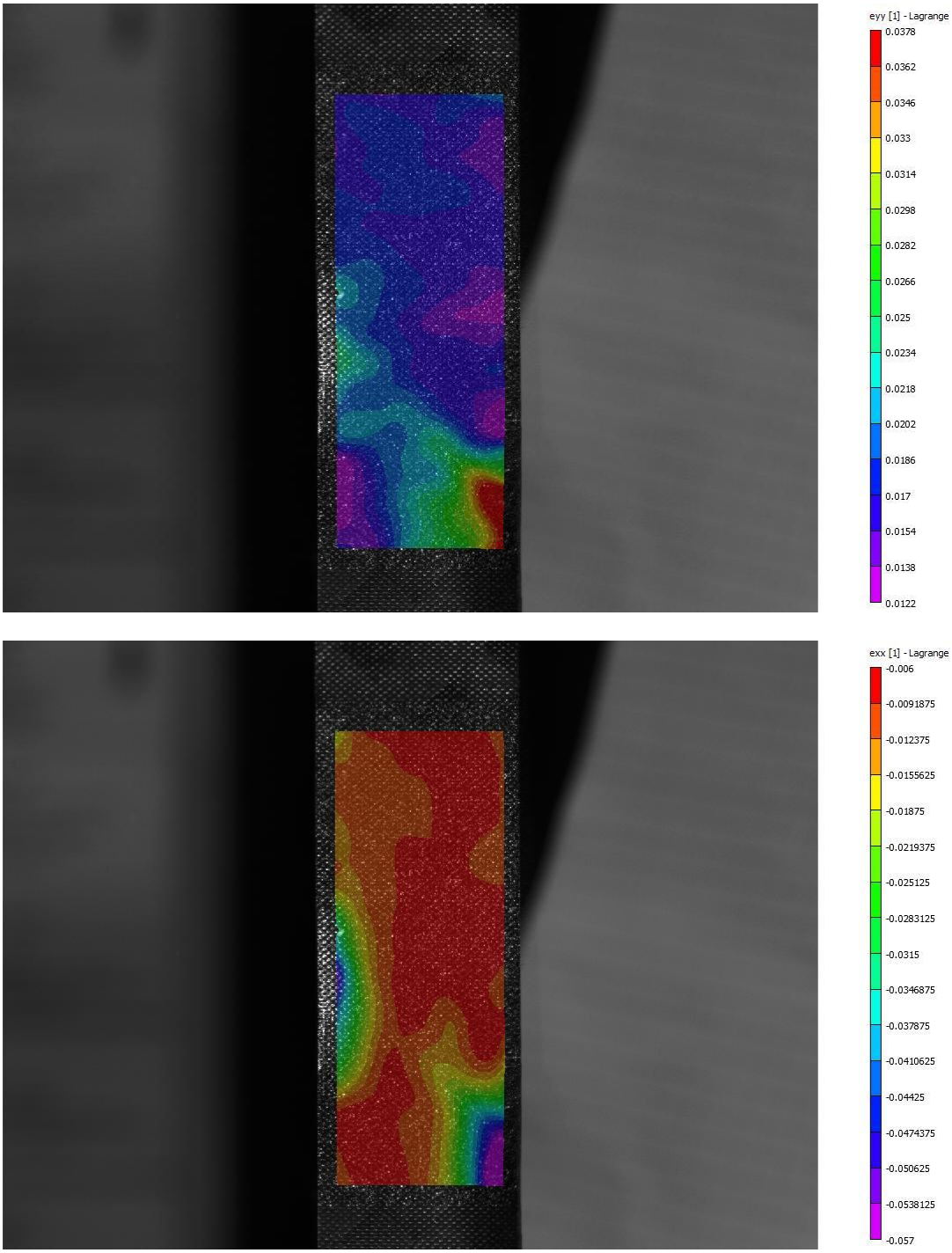

Sample 1 – *Longitudinal and Transversal Strain Maps*

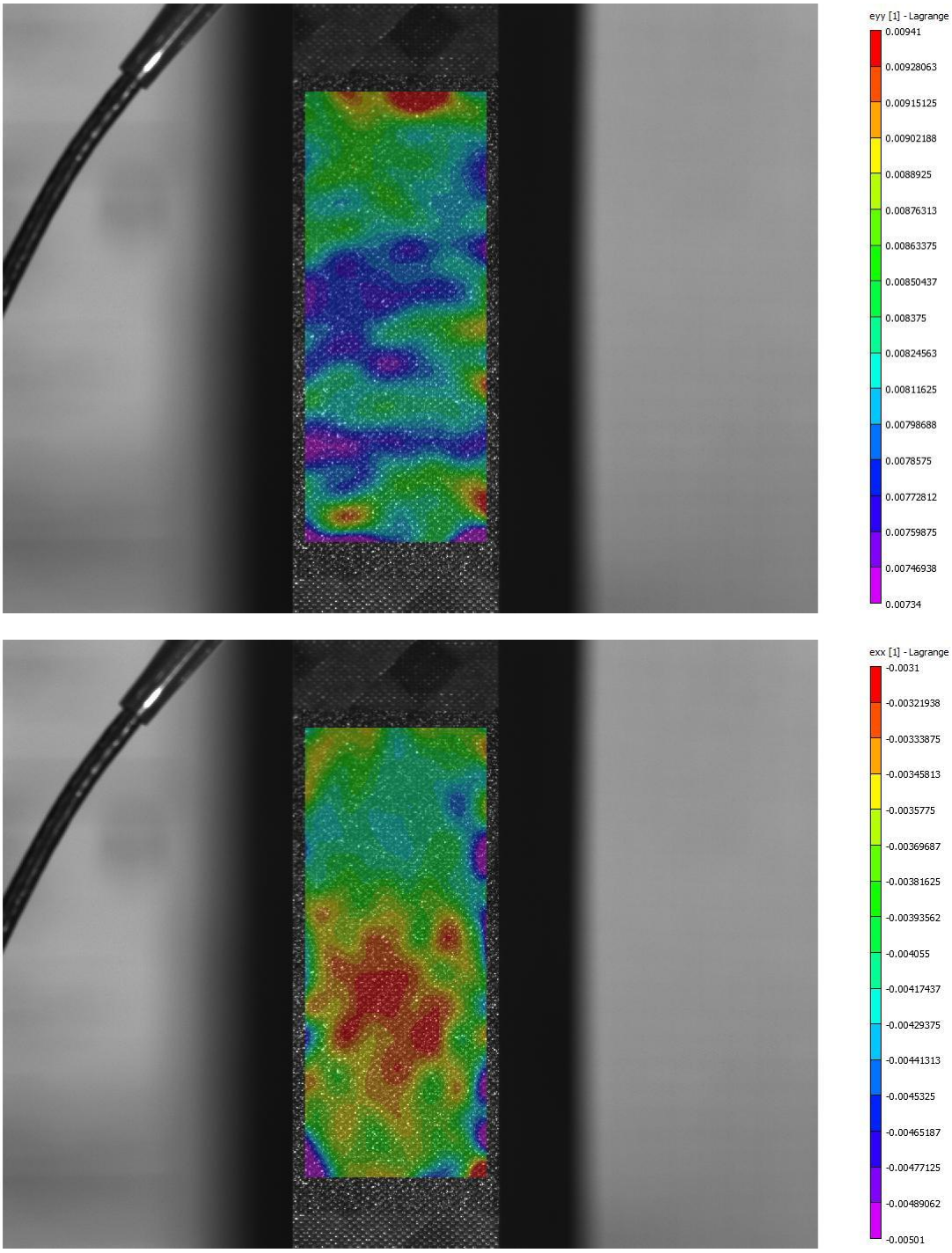

Sample 2 – *Longitudinal and Transversal Strain Maps*

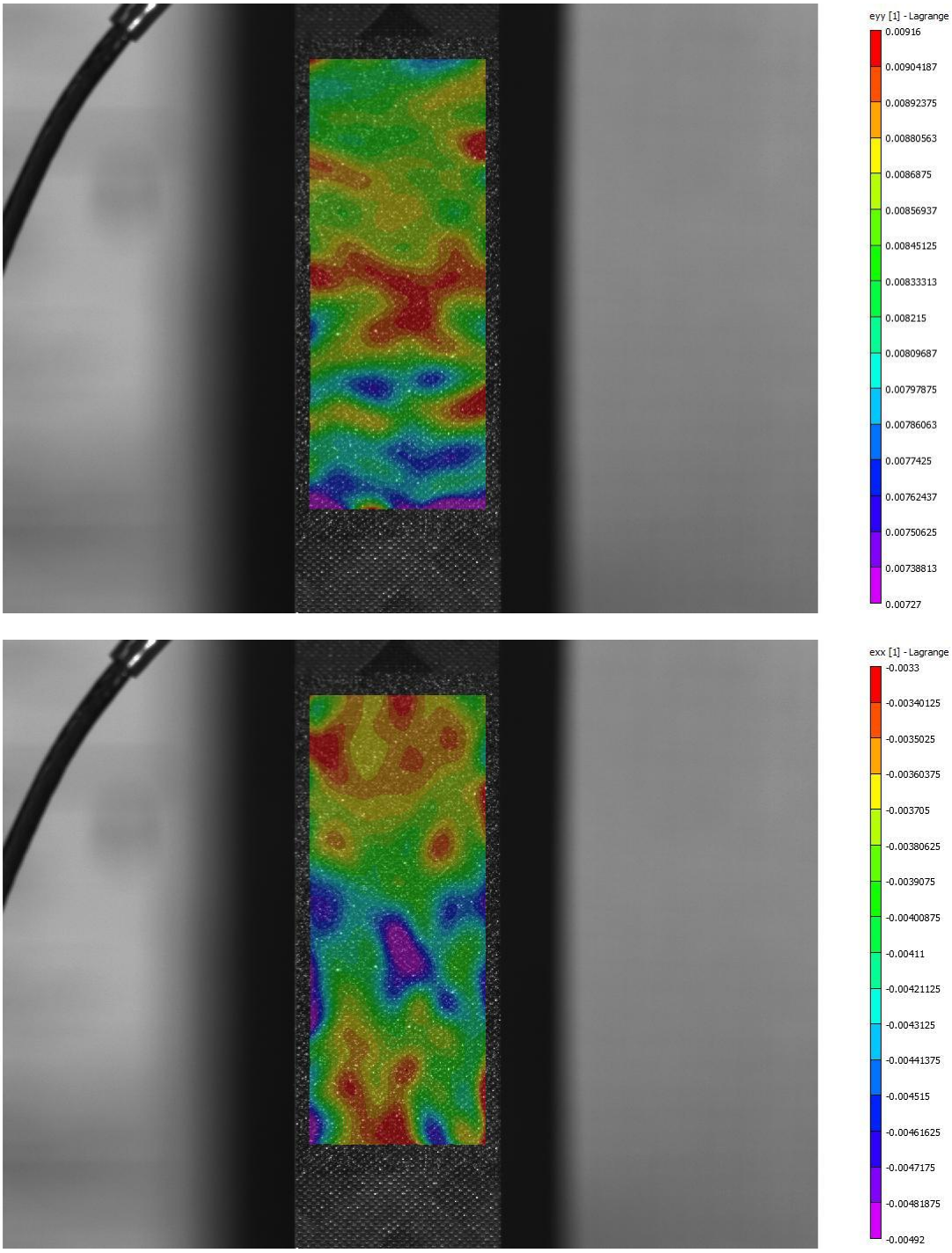

Sample 3 – *Longitudinal and Transversal Strain Maps*

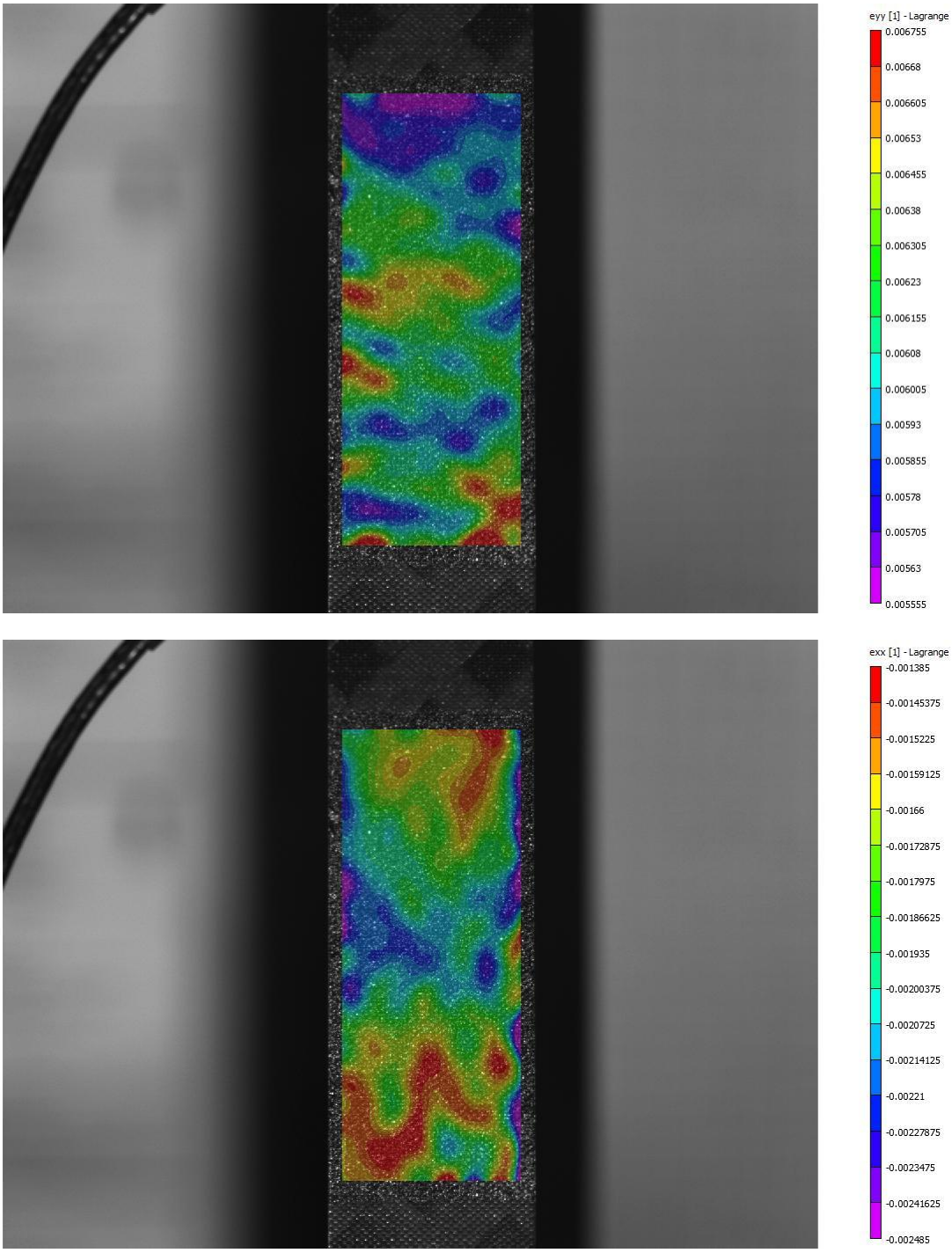

Sample 4 – Longitudinal and Transversal Strain Maps

A.2.2. 0^o specimens without defects (specimens 5, 6, 7, 8)

I. Stress vs. Strain curves obtained by DIC analysis

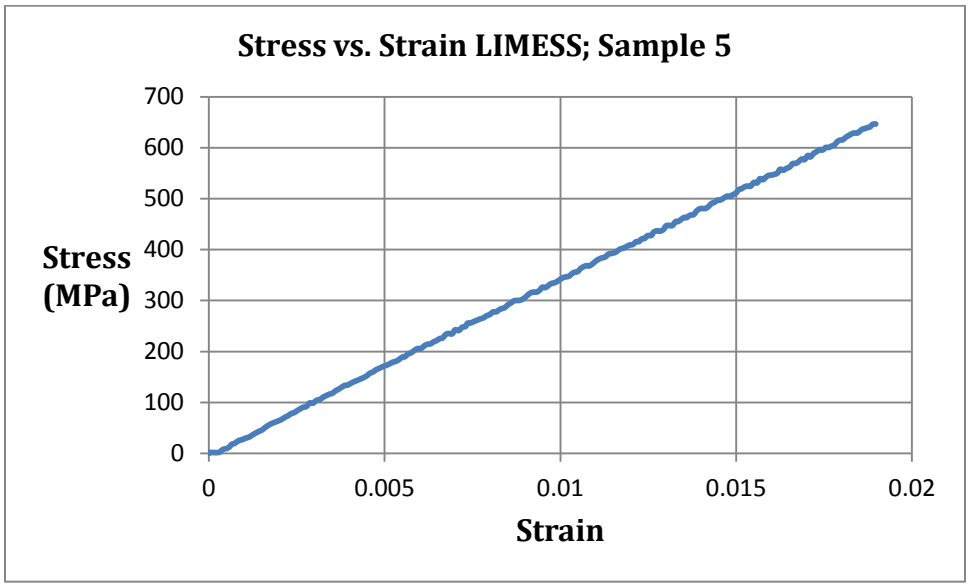

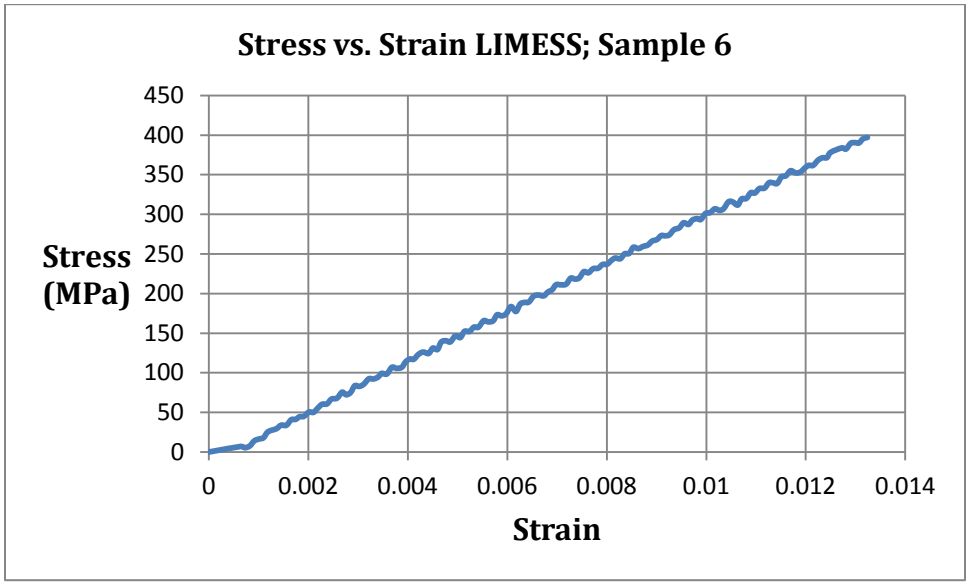

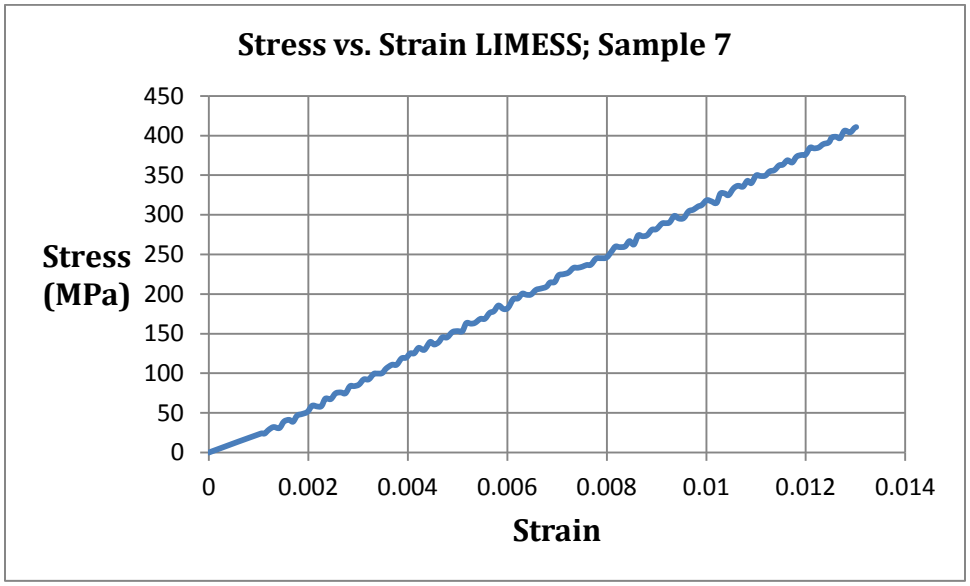
Stress vs. Strain LIMESS; Sample 7
Stress (MPa)
450
400
350
300
250
200
150
100
50
0
0
0.002
0.004
0.006
0.008
0.01
0.012
0.014
Strain

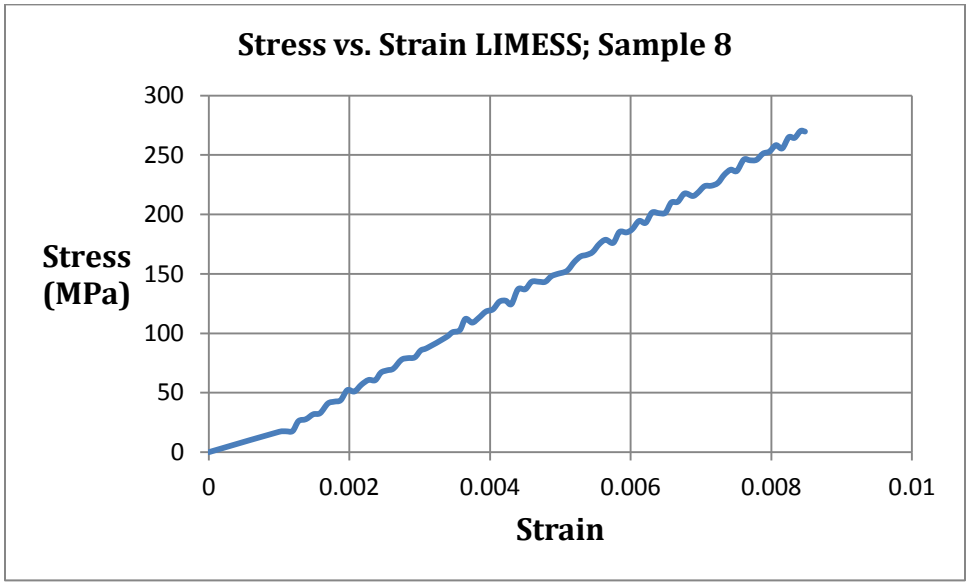
Stress vs. Strain LIMESS; Sample 8
Stress (MPa)
300
250
200
150
100
50
0
0
0.002
0.004
0.006
0.008
0.01
Strain

II. Elasticity Modulus vs. Strain curves obtained by DIC analysis

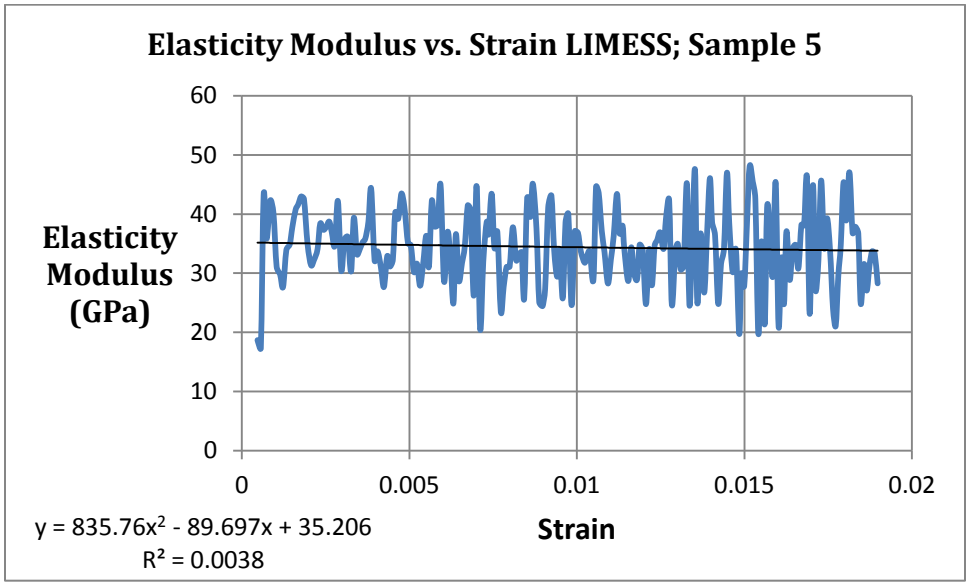

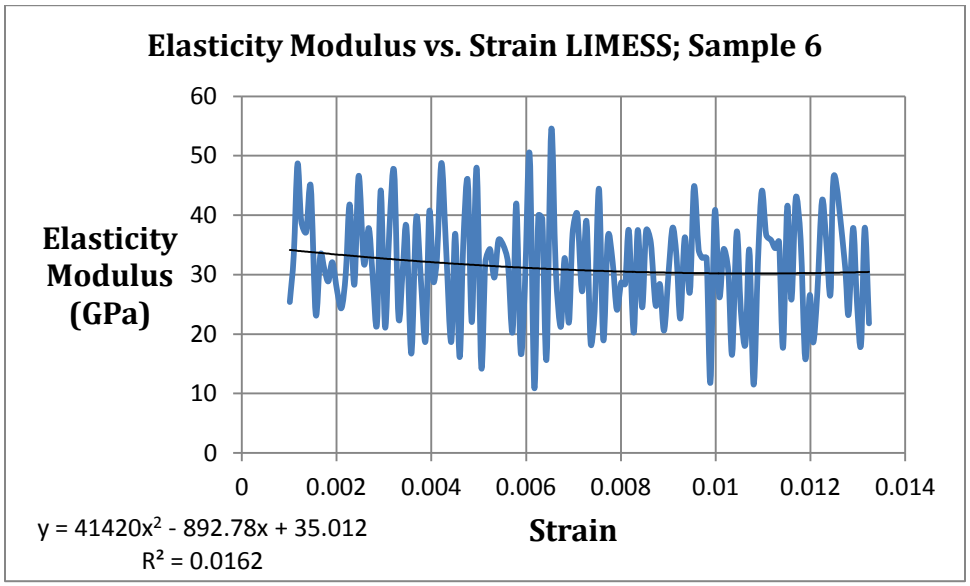

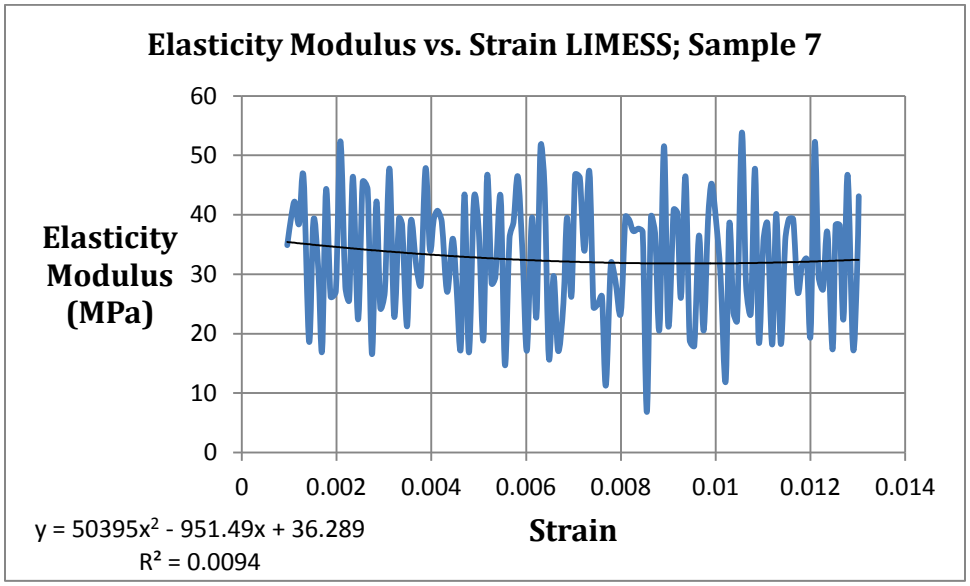
Elasticity Modulus vs. Strain LIMESS; Sample 7
Elasticity Modulus (MPa)
60
50
40
30
20
10
0
0
0.002
0.004
0.006
0.008
0.01
0.012
0.014
Strain
y = 50395x² - 951.49x + 36.289
R² = 0.0094

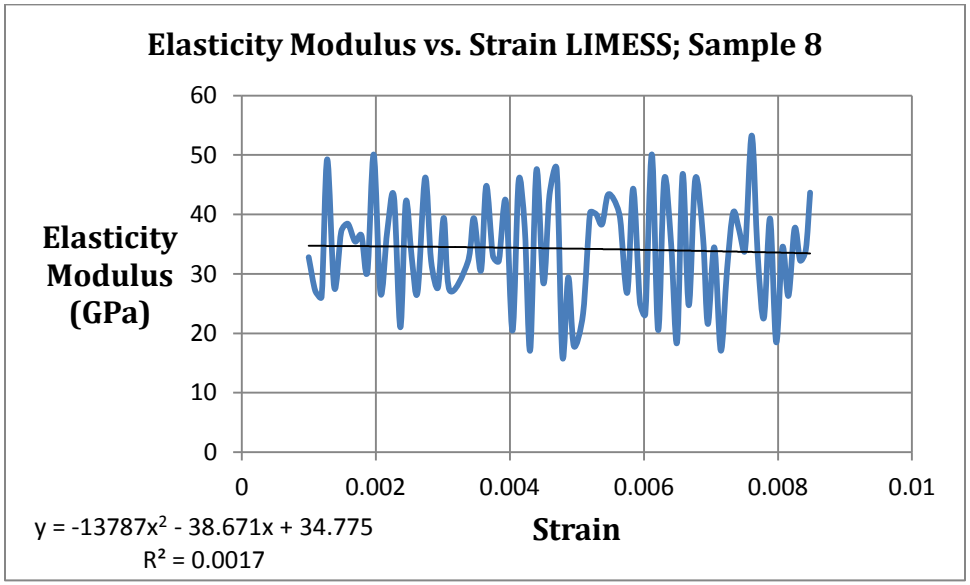
Elasticity Modulus vs. Strain LIMESS; Sample 8
Elasticity Modulus (GPa)
60
50
40
30
20
10
0
0
0.002
0.004
0.006
0.008
0.01
Strain
y = -13787x² - 38.671x + 34.775
R² = 0.0017

III. Energy – Cumulative Energy – Stress vs. Strain curves obtained by AE analysis

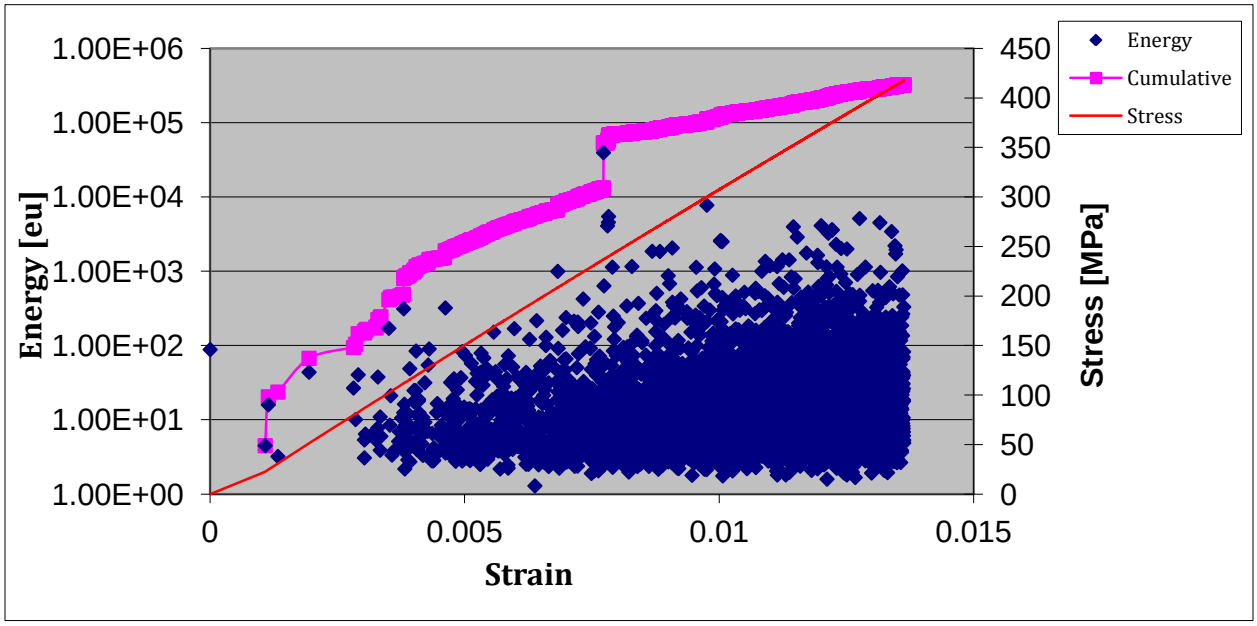

Sample 6

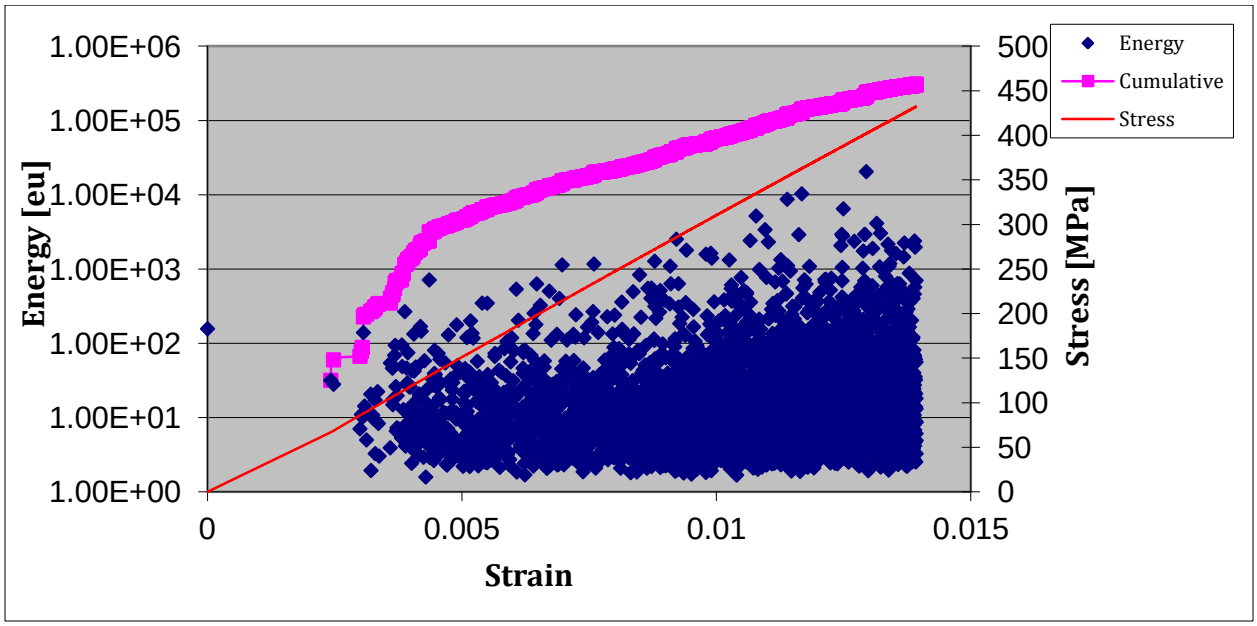

Sample 7

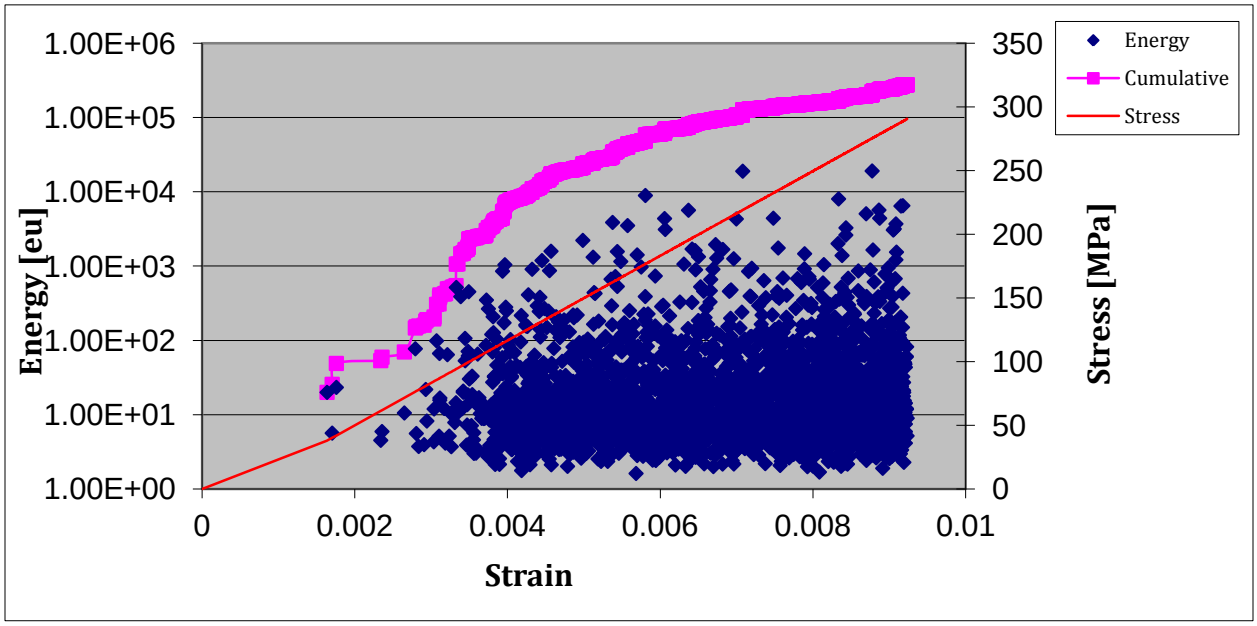
1.00E+06
1.00E+05
1.00E+04
1.00E+03
1.00E+02
1.00E+01
1.00E+00
Energy [eu]
0
0.002
0.004
0.006
0.008
0.01
Strain
350
300
250
200
150
100
50
0
Stress [MPa]
Energy
Cumulative
Stress

Sample 8

IV. DIC Longitudinal and Transverse Strain Maps at Maximum Strain Level

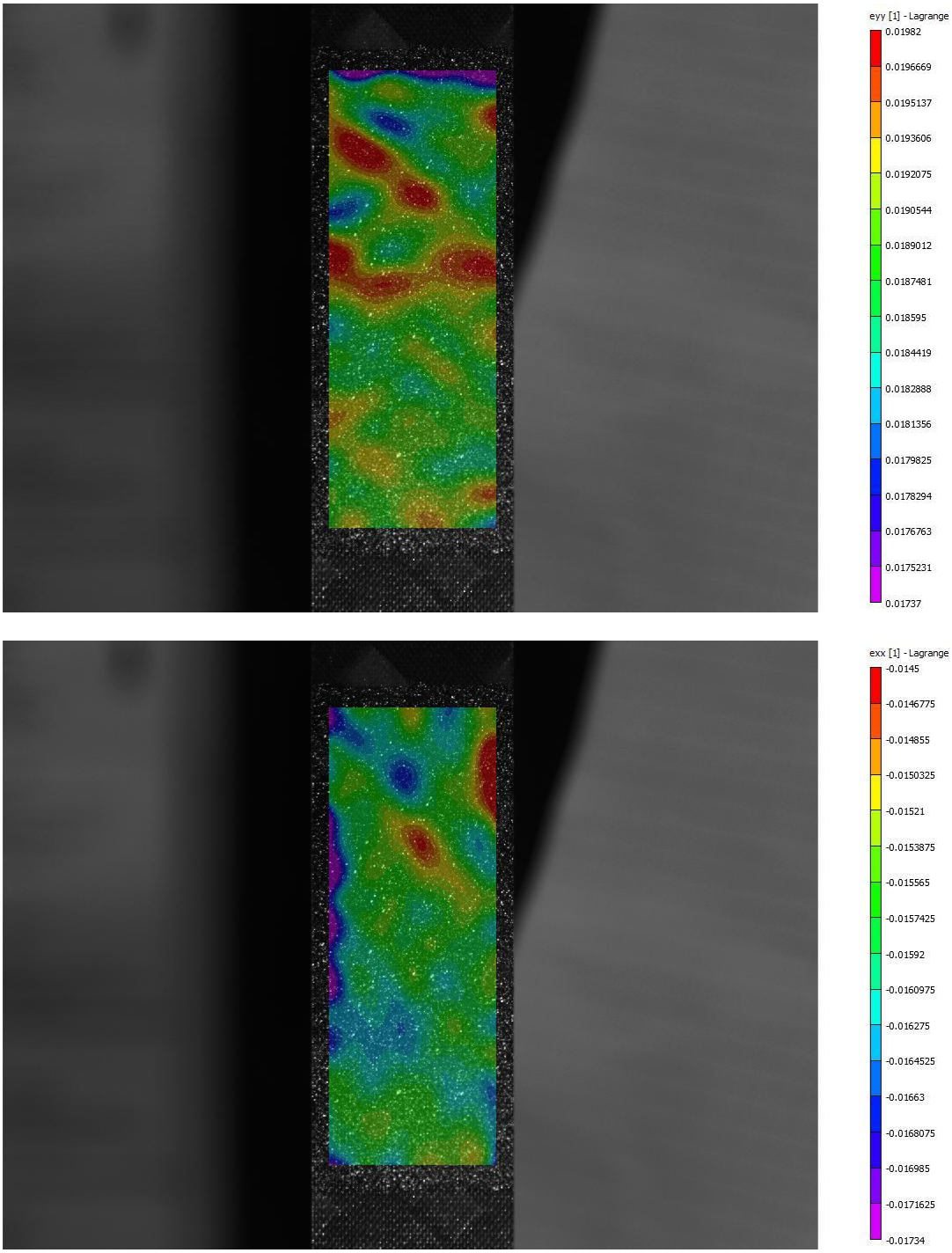

Sample 5 – *Longitudinal and Transversal Strain Maps*

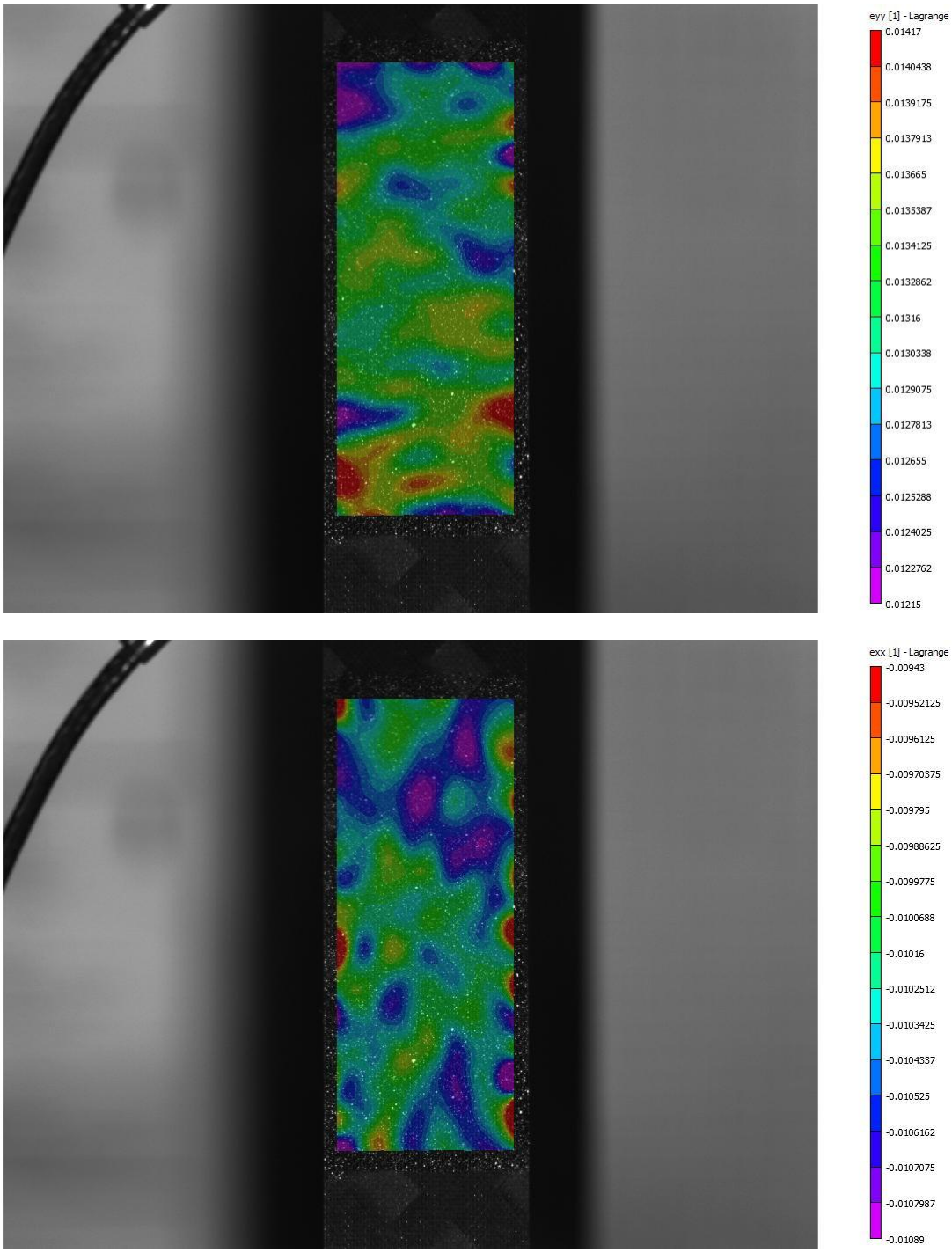

Sample 6 – *Longitudinal and Transversal Strain Maps*

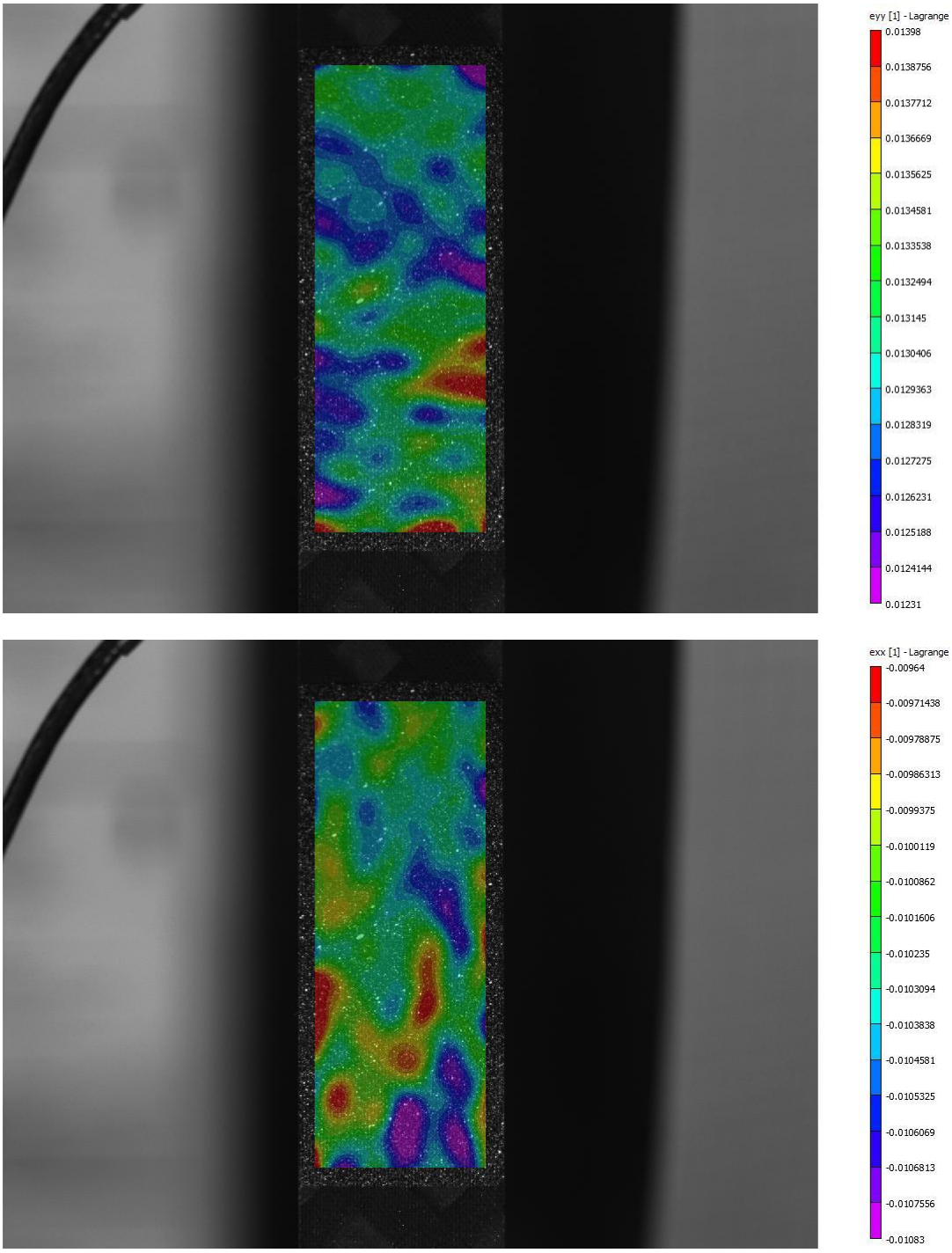

Sample 7 – Longitudinal and Transversal Strain Maps

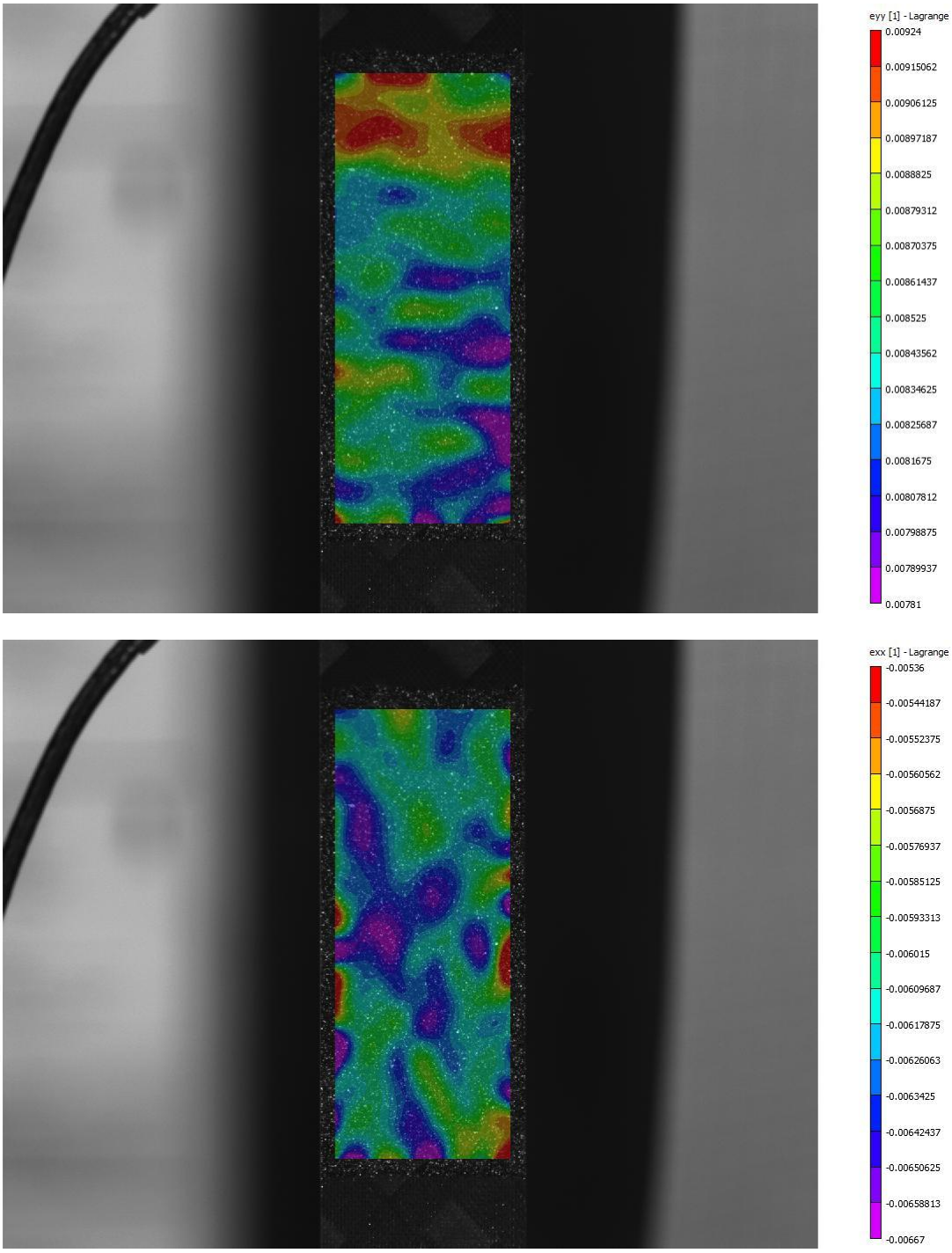

Sample 8 – *Longitudinal and Transversal Strain Maps*

Appendix B

Quasi-Static Compression Test Graphs

B.1. CANAL QI samples; 0^0 specimens without defects (specimens 17, 18)

I. Stress vs. Strain curves obtained by DIC analysis

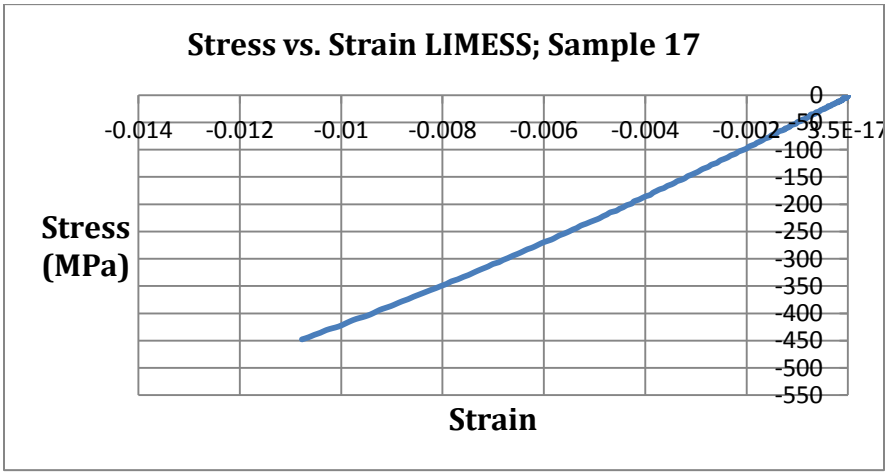

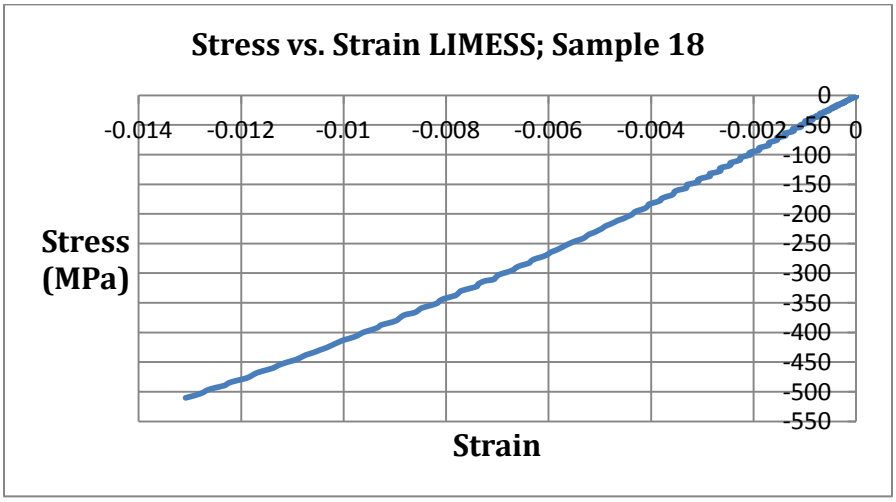

II. DIC Longitudinal and Transverse Strain Maps at Maximum Strain Level

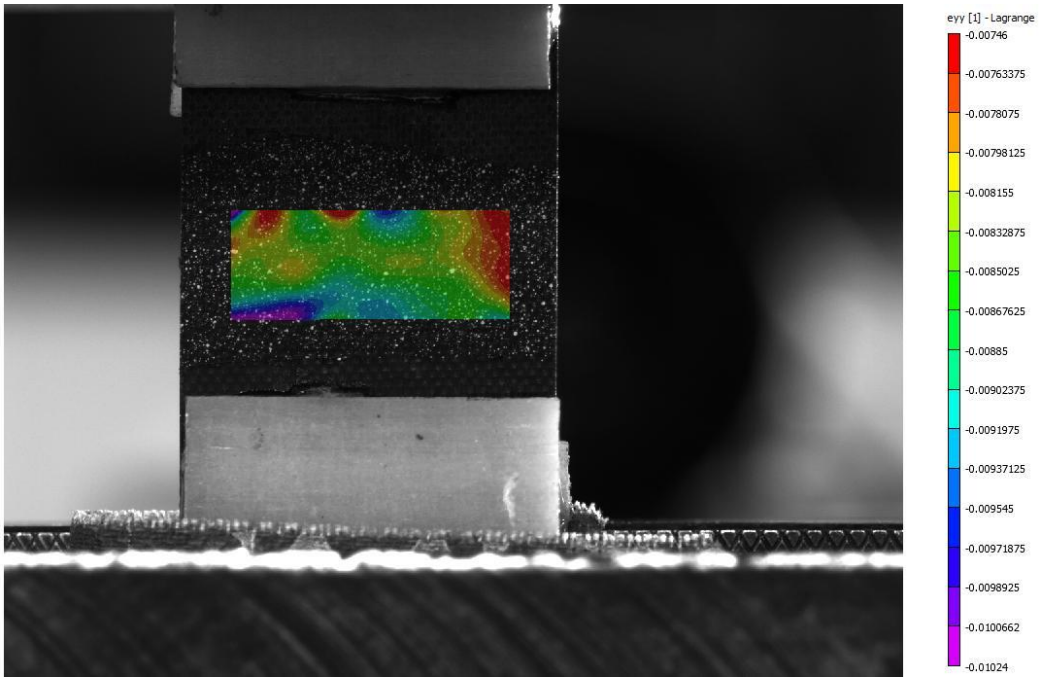

Longitudinal Strain Map, Sample 17, Camera 1

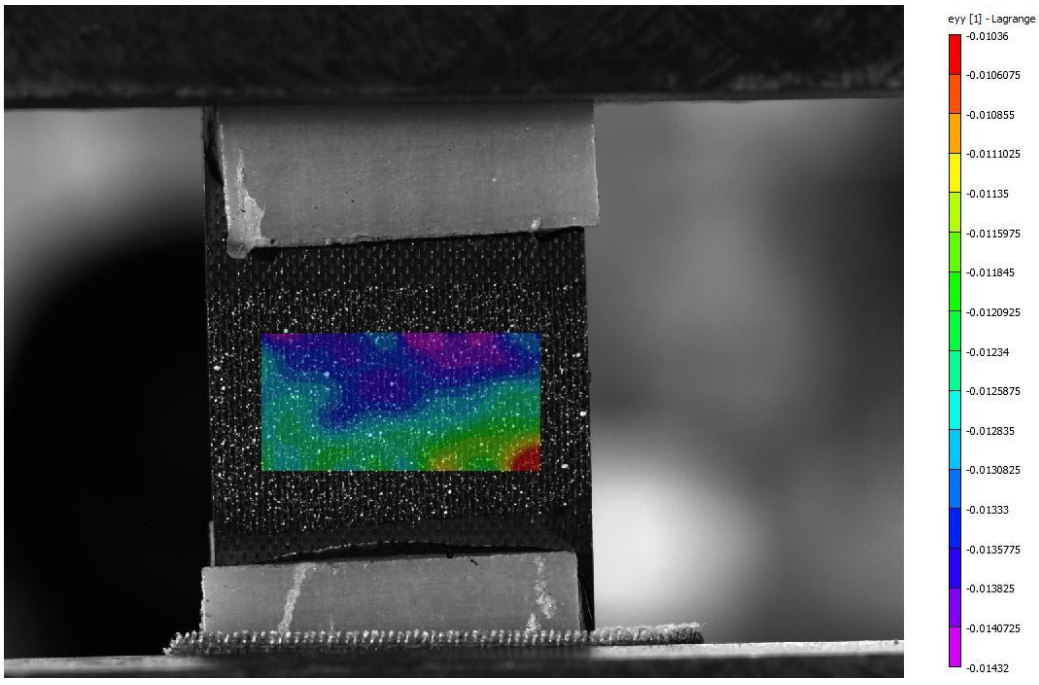

Longitudinal Strain Map, Sample 17, Camera 2

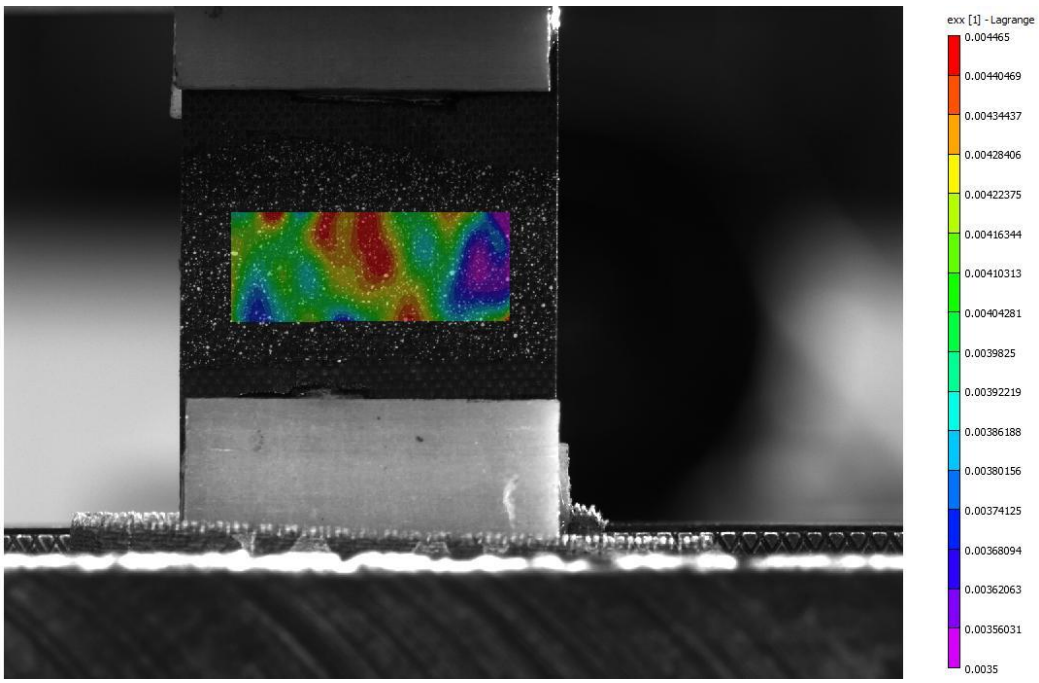

Transversal Strain Map, Sample 17, Camera 1

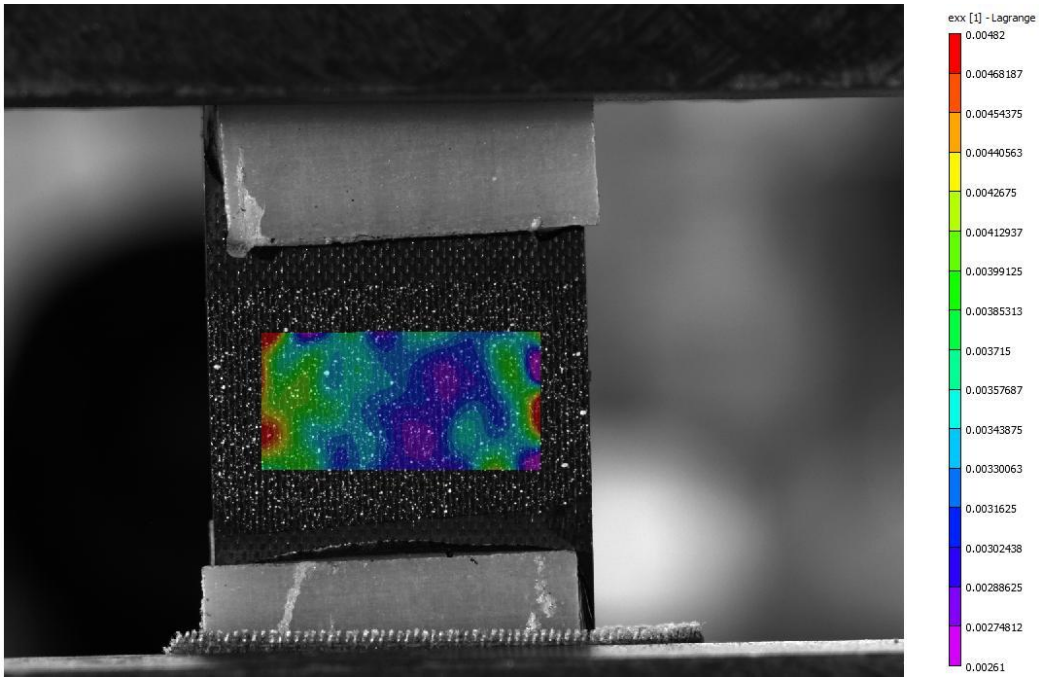

Transversal Strain Map, Sample 17, Camera 2

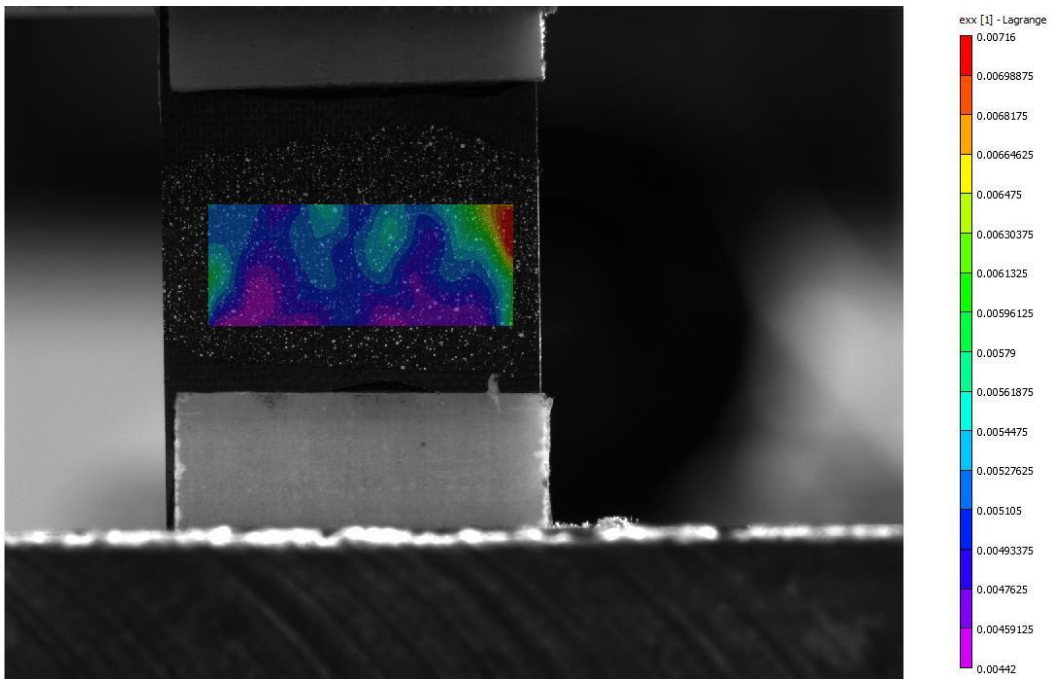

Longitudinal Strain Map, Sample 18, Camera 1

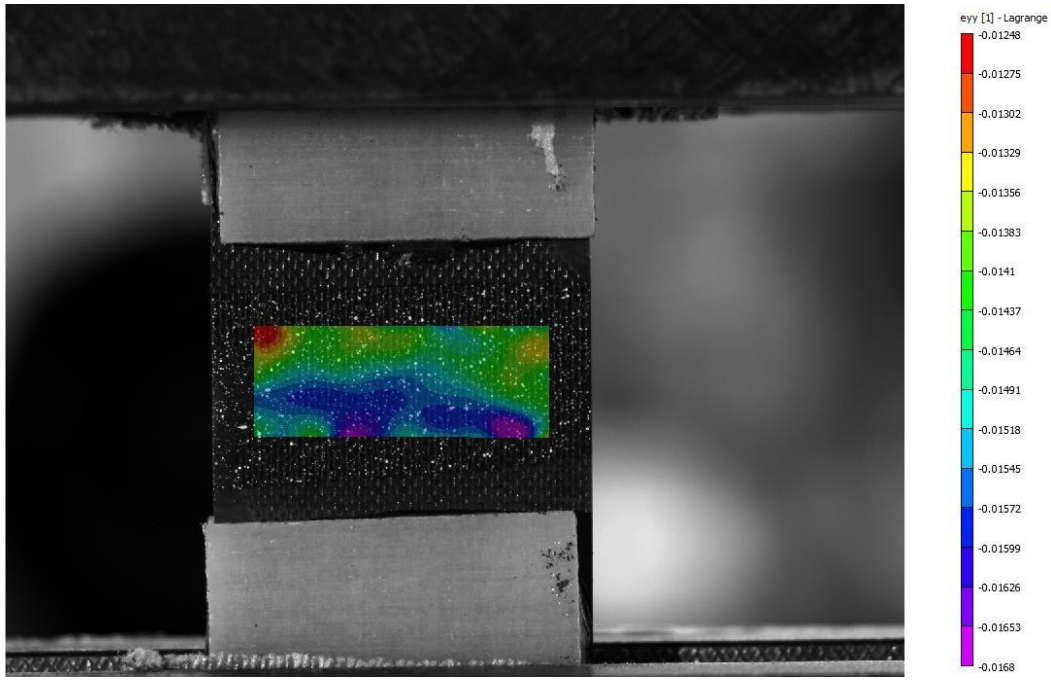

Longitudinal Strain Map, Sample 18, Camera 2

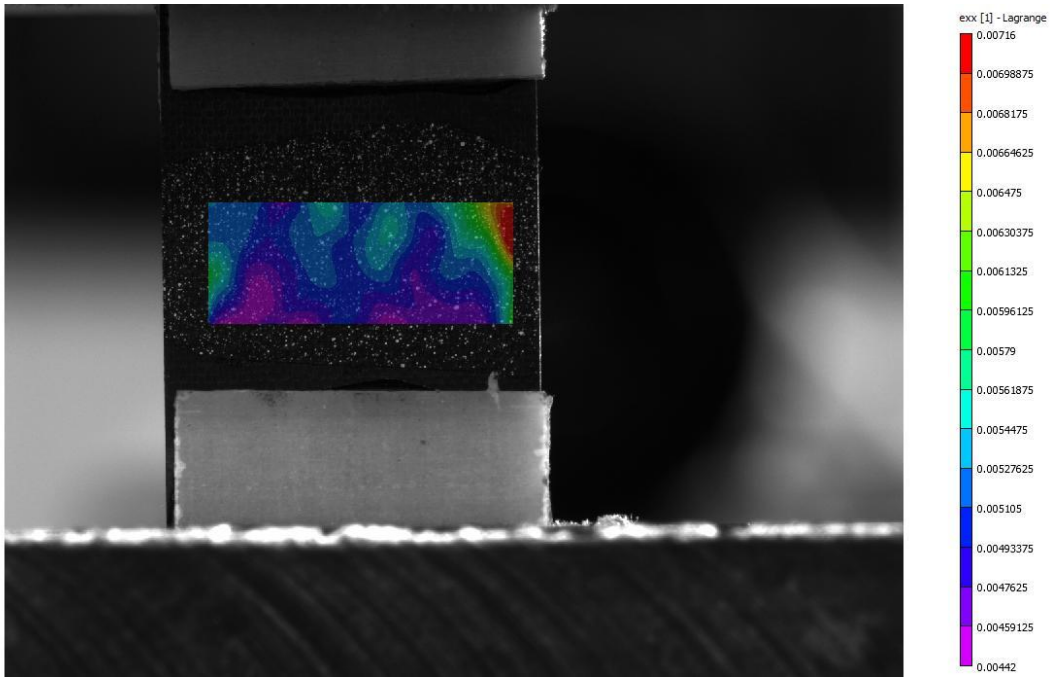

Transversal Strain Map, Sample 18, Camera 1

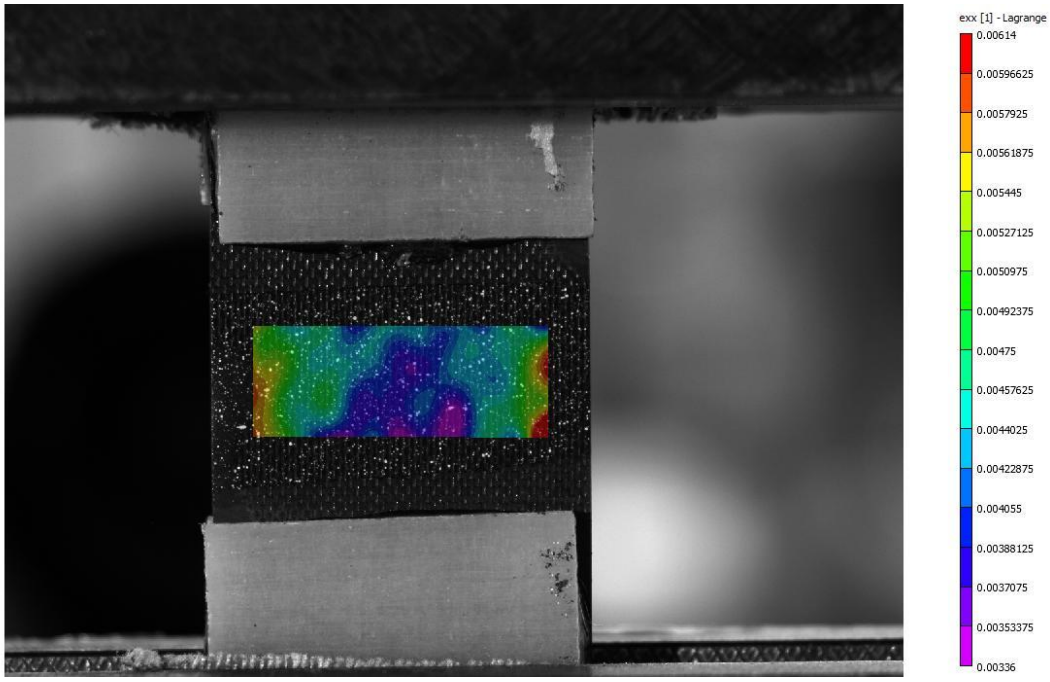

Transversal Strain Map, Sample 18, Camera 2

B.2. AP-PLY samples; 90^0 specimens without defects (specimens 10, 11, 12, 13)

I. Stress vs. Strain curves obtained by DIC analysis

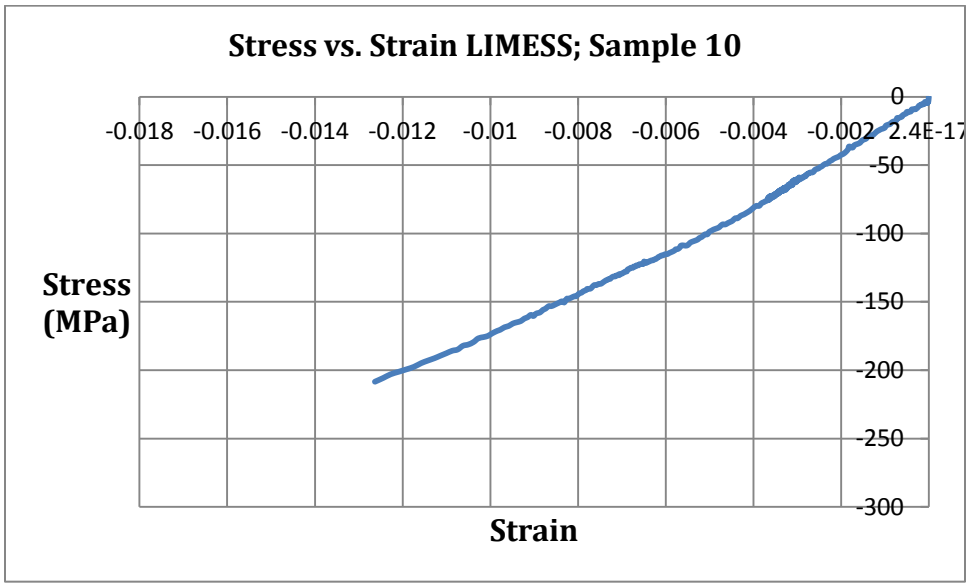

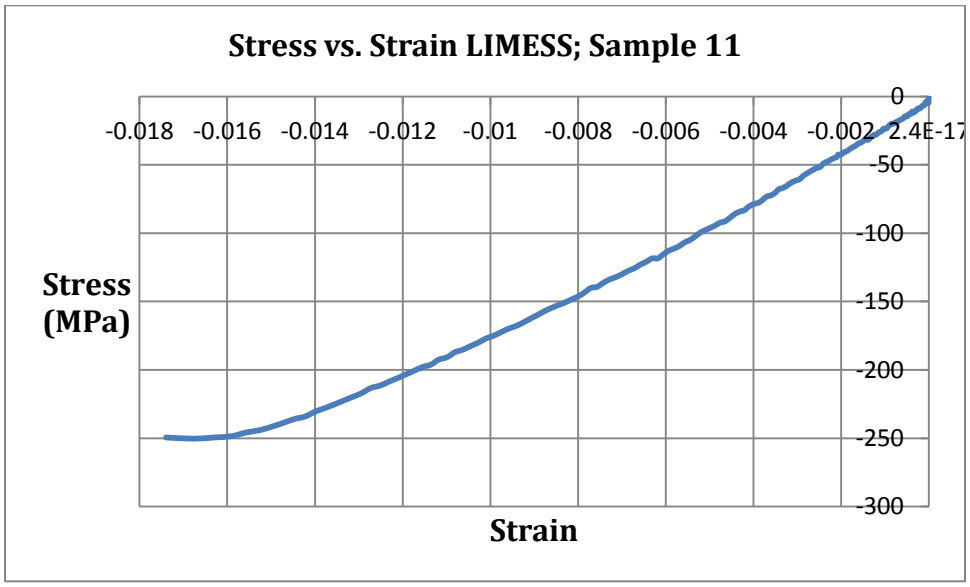

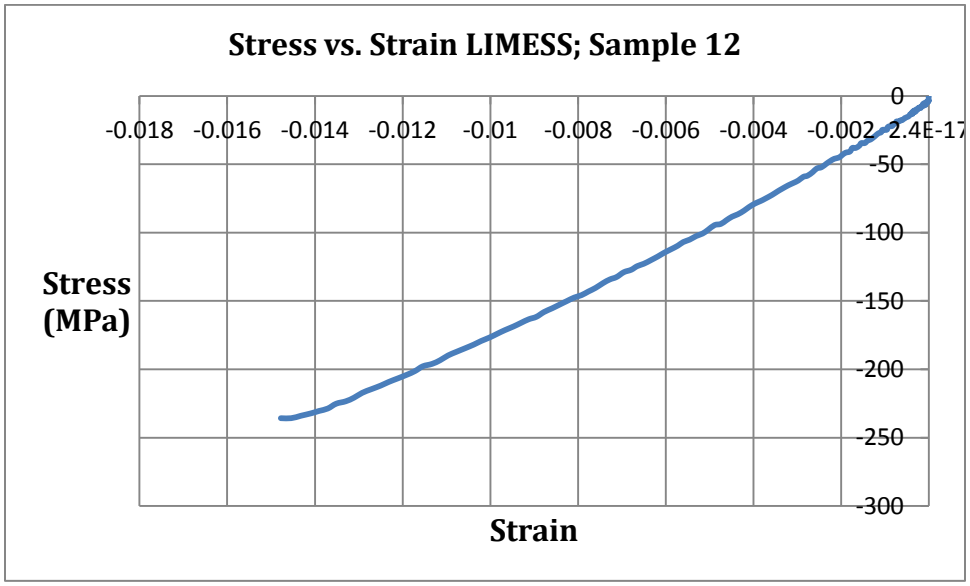
Stress vs. Strain LIMESS; Sample 12
0
-0.018
-0.016
-0.014
-0.012
-0.01
-0.008
-0.006
-0.004
-0.002
2.4E-17
-50
-100
-150
-200
-250
-300
Stress (MPa)
Strain

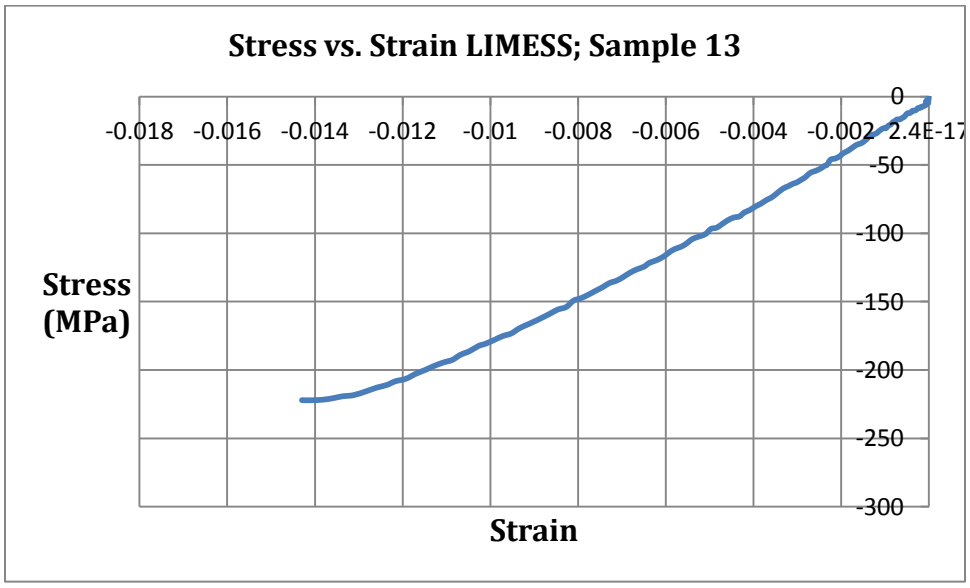
Stress vs. Strain LIMESS; Sample 13
0
-0.018
-0.016
-0.014
-0.012
-0.01
-0.008
-0.006
-0.004
-0.002
2.4E-17
-50
-100
-150
-200
-250
-300
Stress (MPa)
Strain

II. DIC Longitudinal and Transverse Strain Maps at Maximum Strain Level

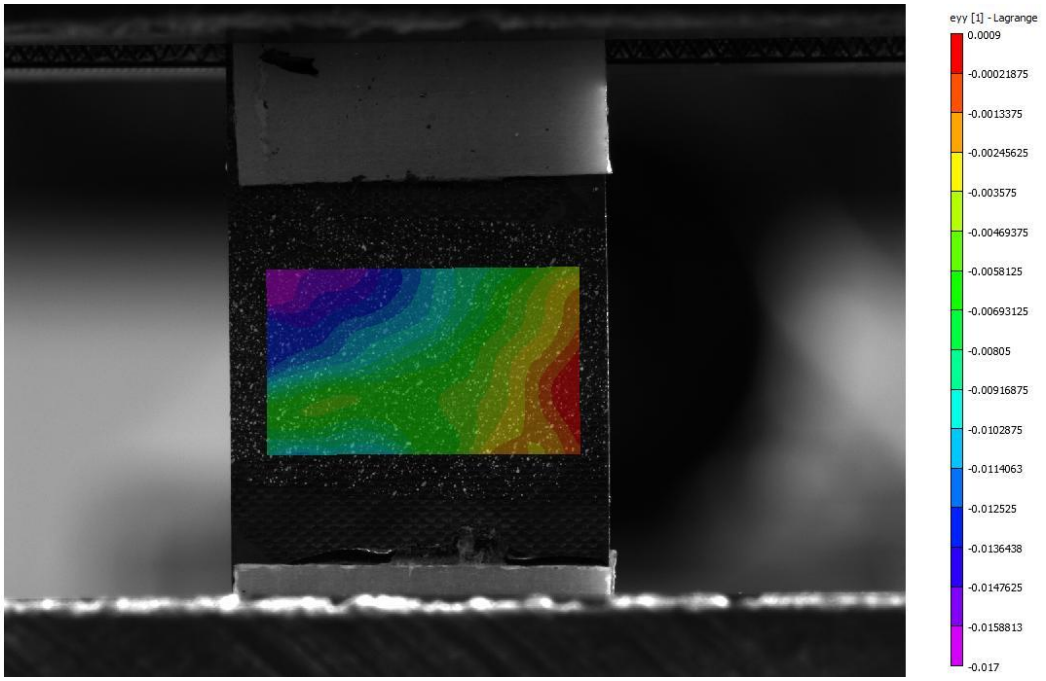

Longitudinal Strain Map, Sample 10, Camera 1

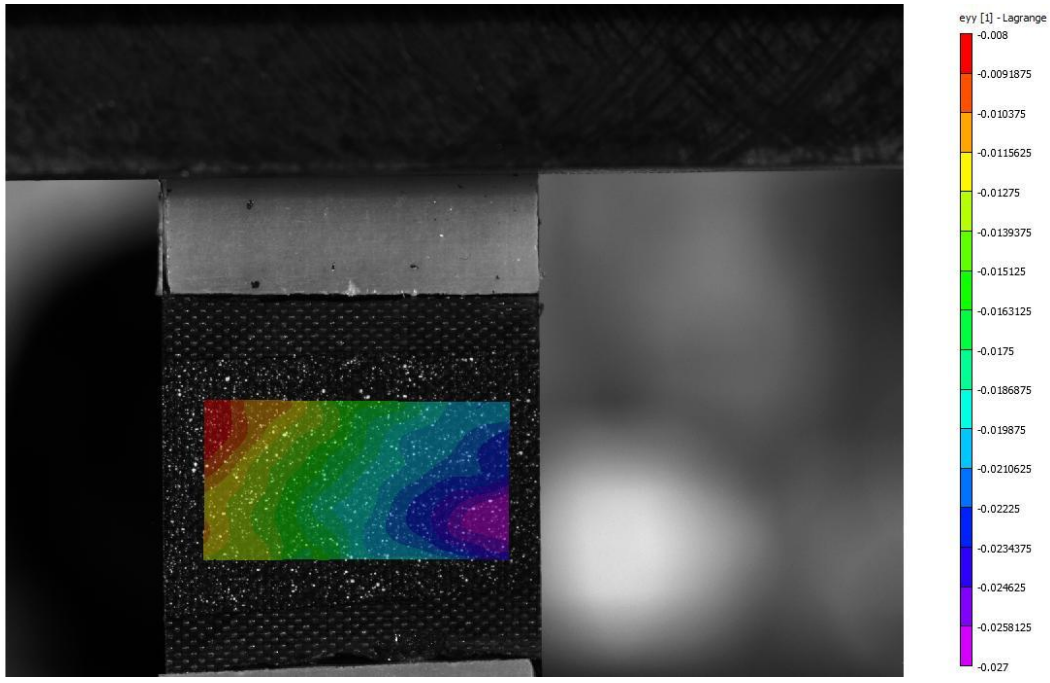

Longitudinal Strain Map, Sample 10, Camera 2

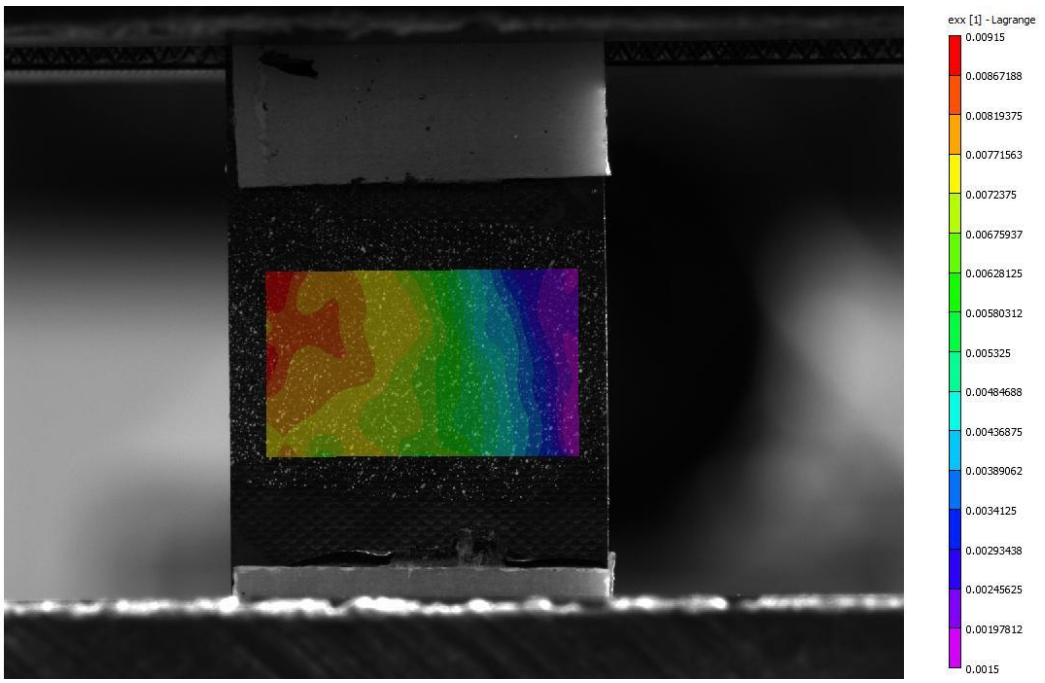

Transversal Strain Map, Sample 10, Camera 1

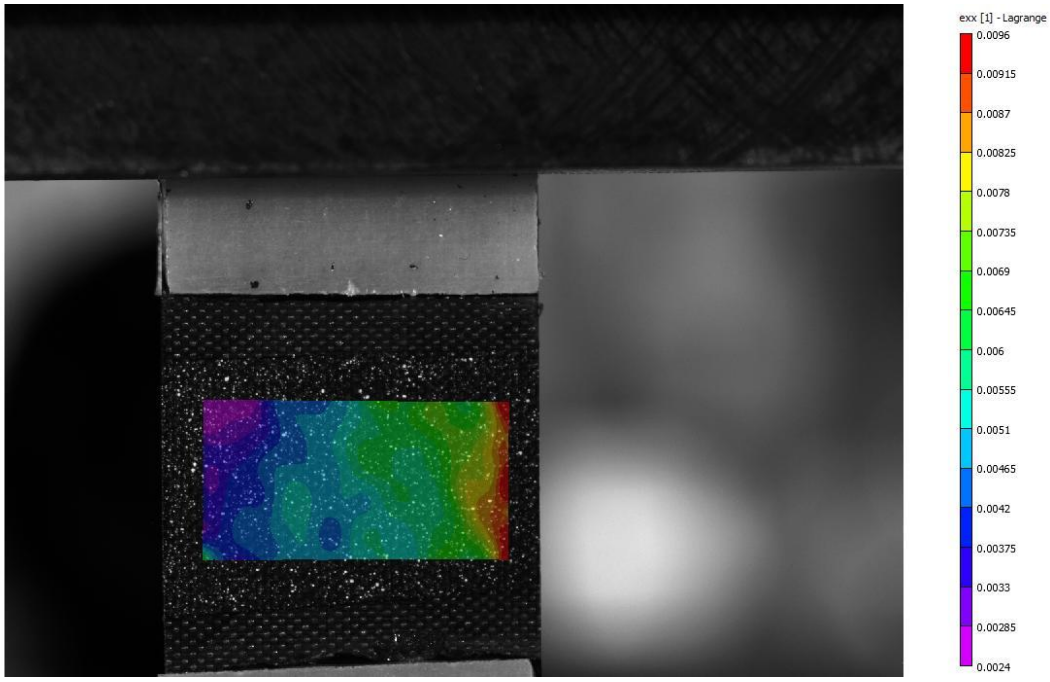

Transversal Strain Map, Sample 10, Camera 2

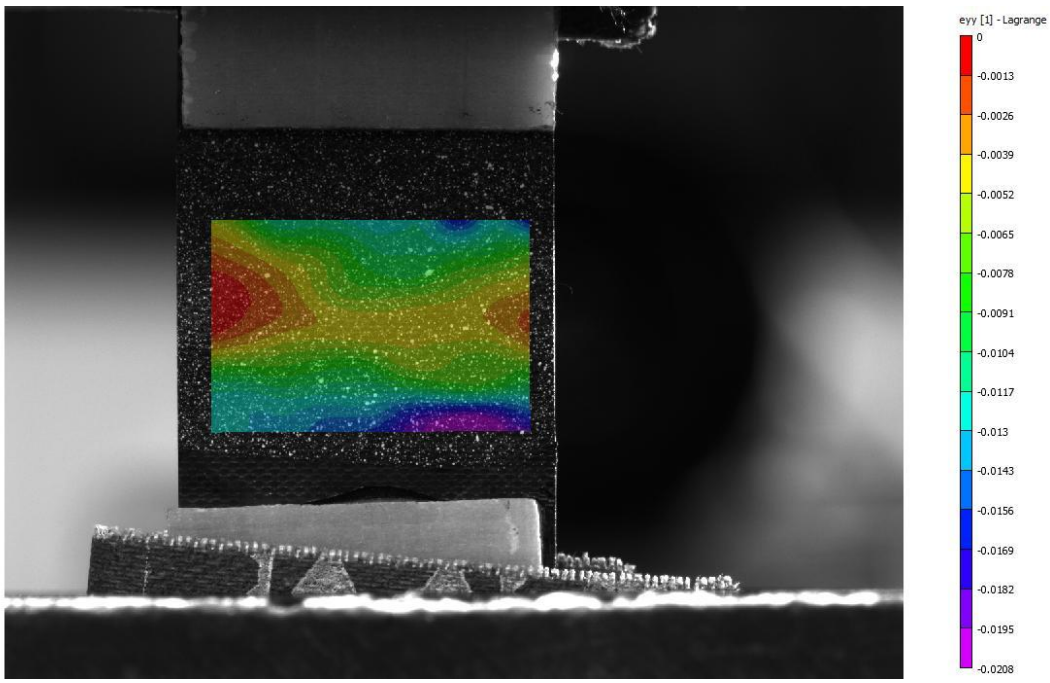

Longitudinal Strain Map, Sample 11, Camera 1

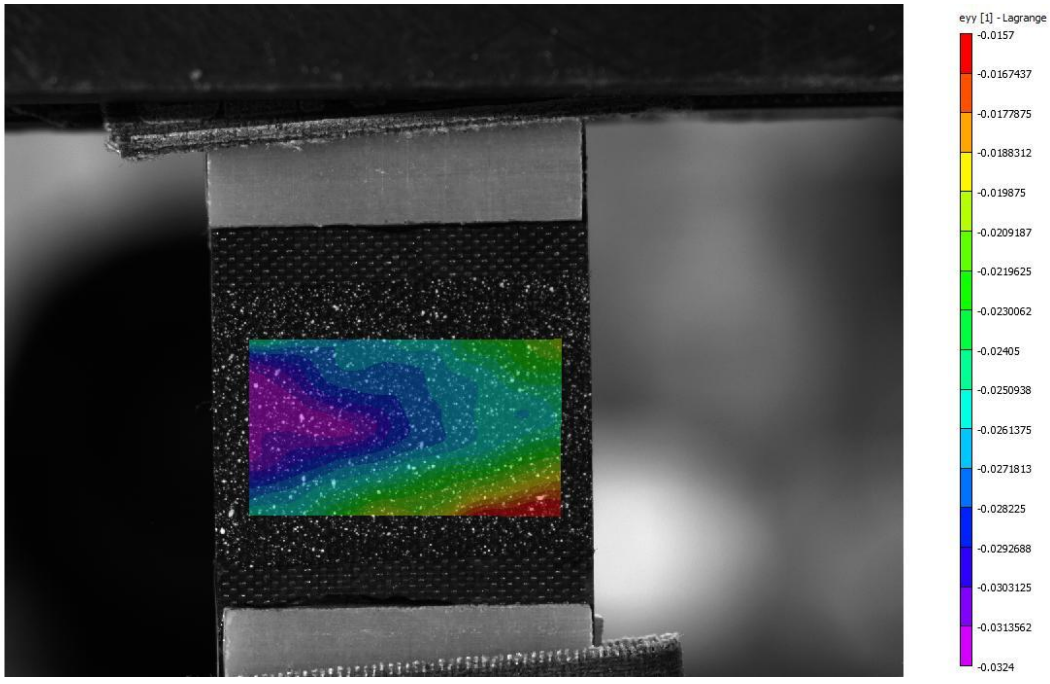

Longitudinal Strain Map, Sample 11, Camera 2

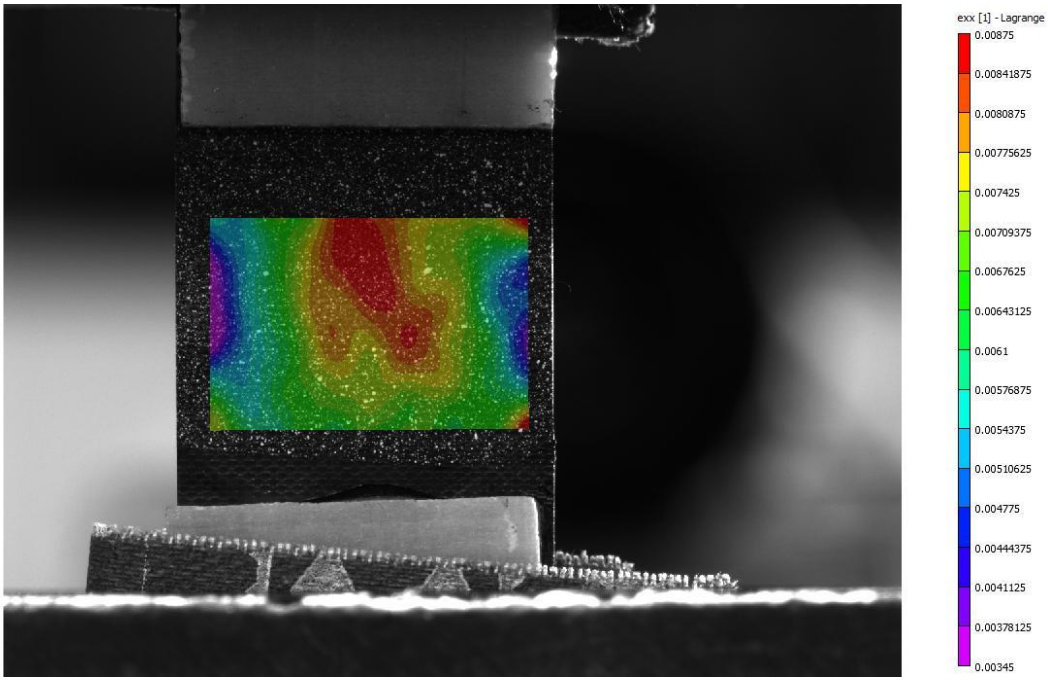

Transversal Strain Map, Sample 11, Camera 1

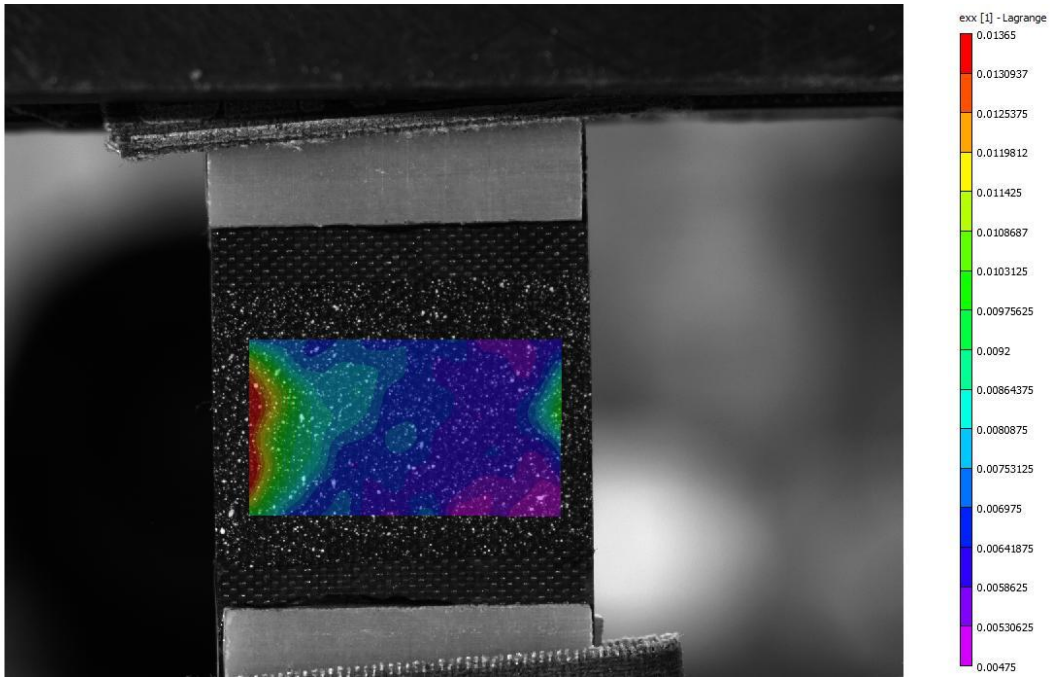

Transversal Strain Map, Sample 11, Camera 2

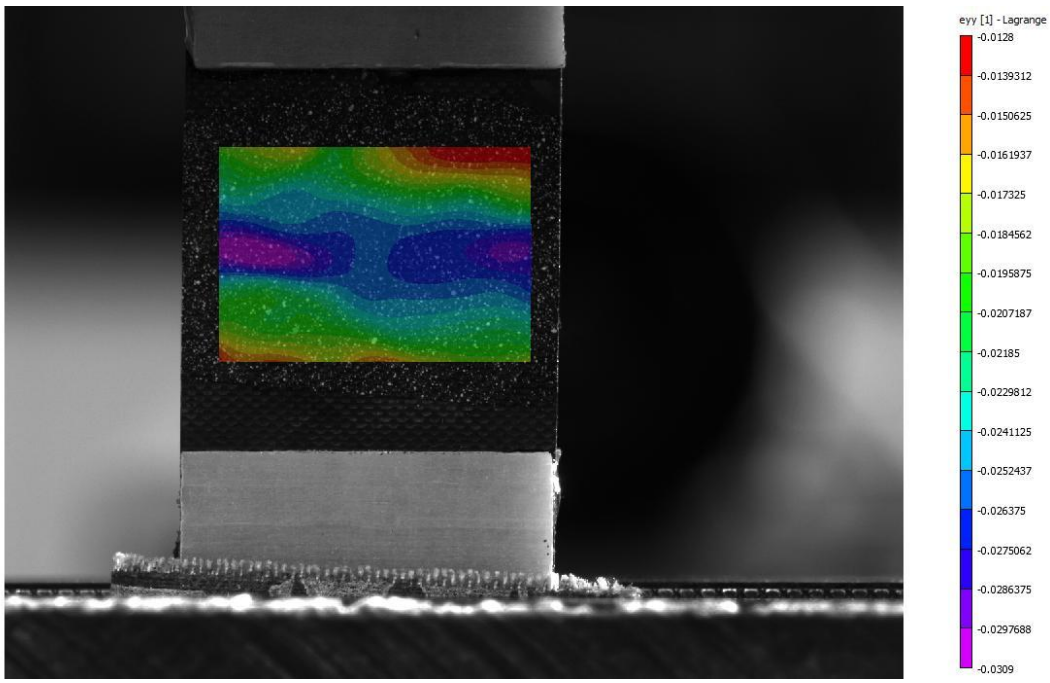

Longitudinal Strain Map, Sample 12, Camera 1

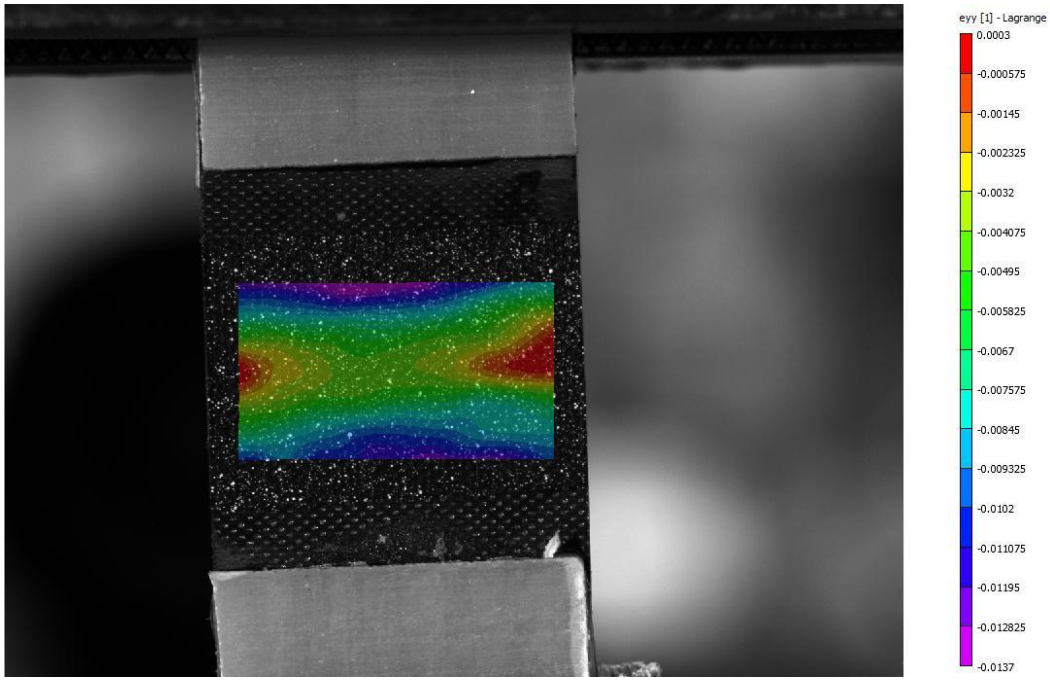

Longitudinal Strain Map, Sample 12, Camera 2

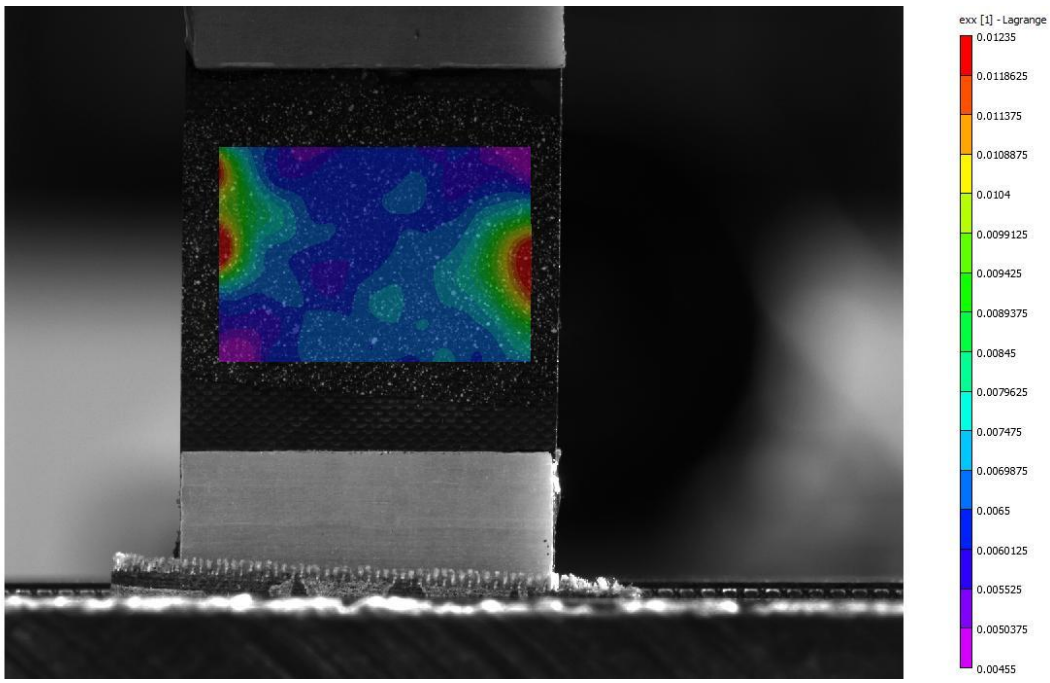

Transversal Strain Map, Sample 12, Camera 1

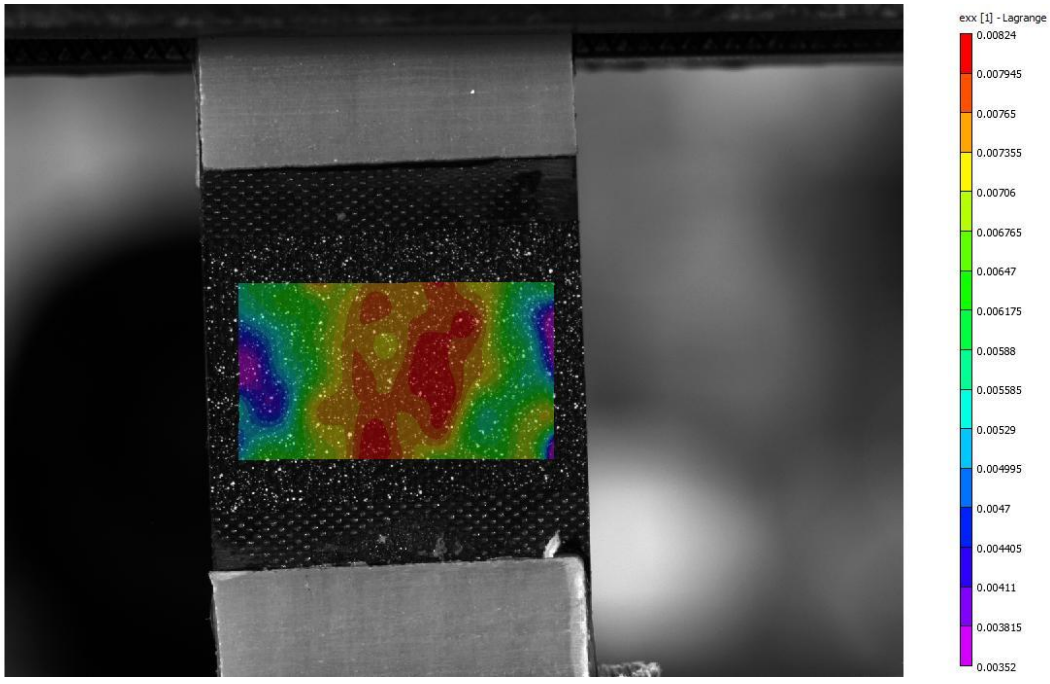

Transversal Strain Map, Sample 12, Camera 2

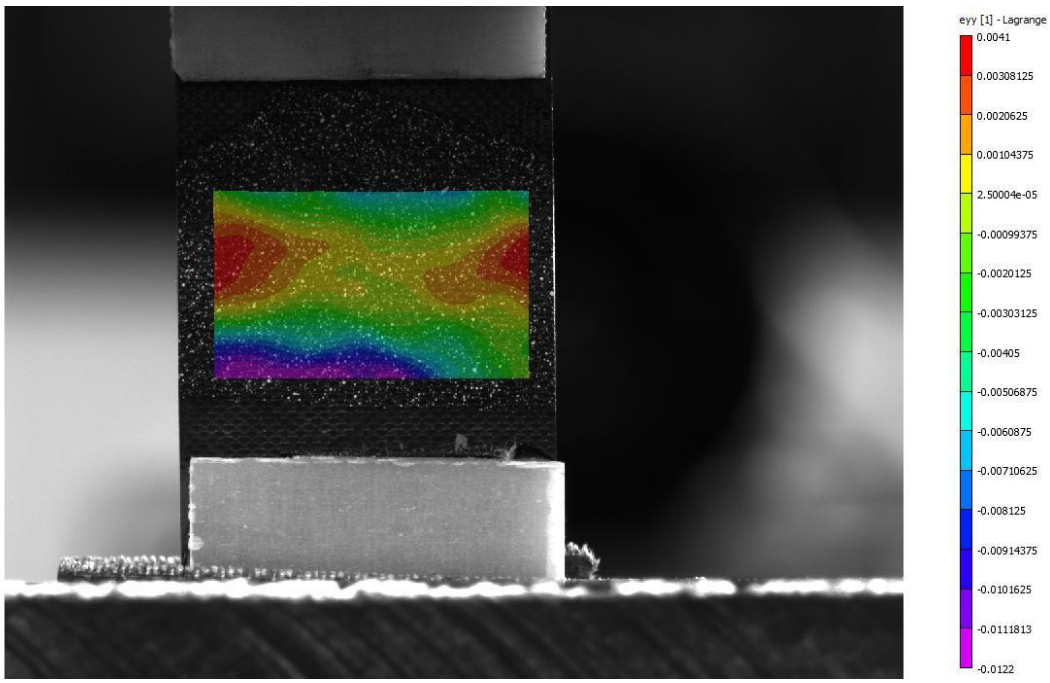

Longitudinal Strain Map, Sample 13, Camera 1

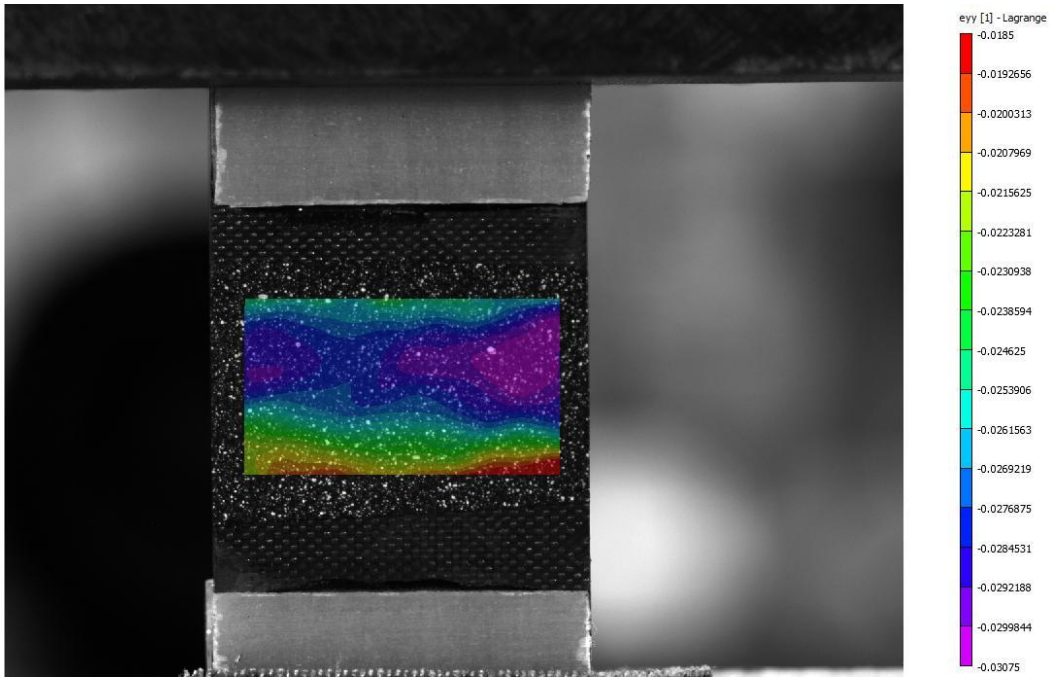

Longitudinal Strain Map, Sample 13, Camera 2

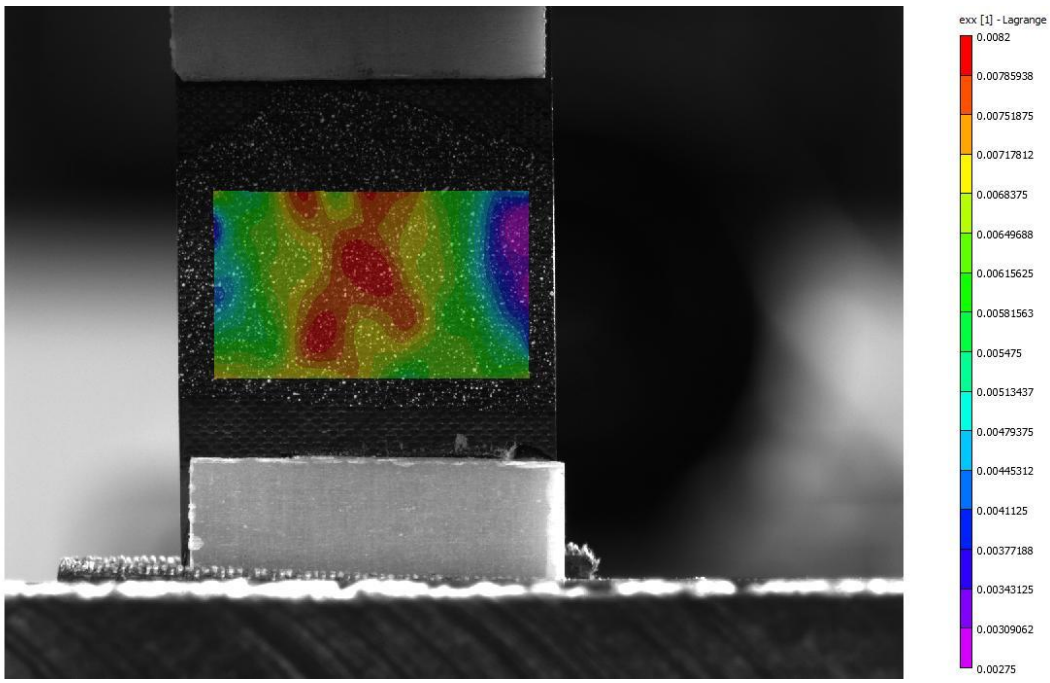

Transversal Strain Map, Sample 13, Camera 1

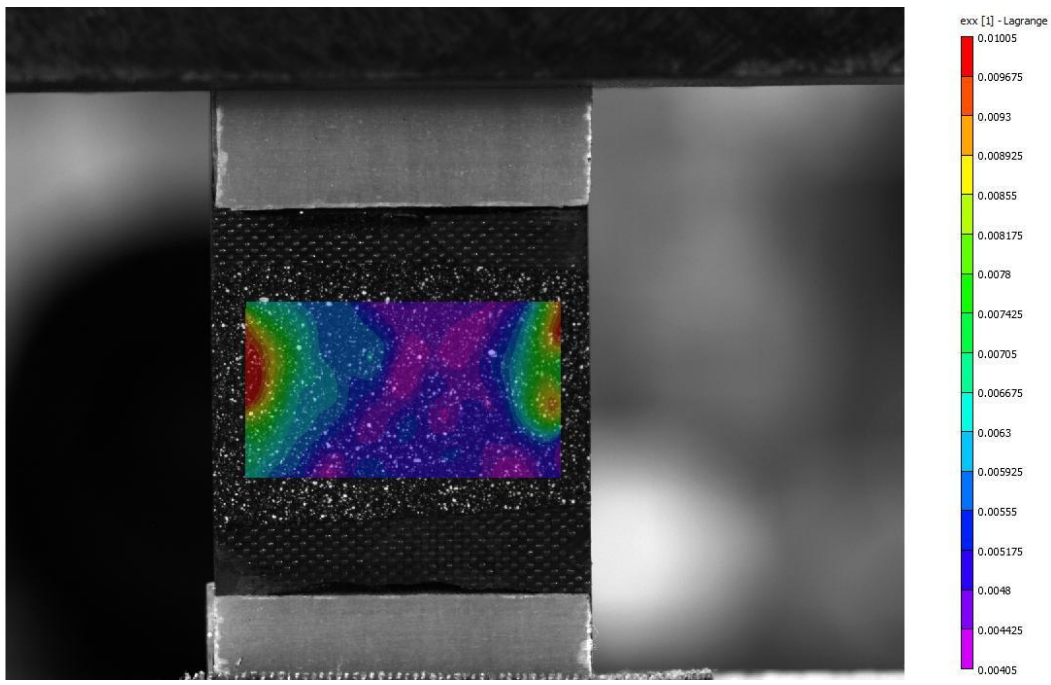

Transversal Strain Map, Sample 13, Camera 2